Creation of a low-cost magnetic resonance system for the early detection of preeclampsia

By

Najlaa Khalfan ALMazrouei

Thesis submitted in partial fulfilment of the requirements of Nottingham Trent University for the degree of Doctor of Philosophy

October 2021

Copyright statement

Declaration

I, *Najlaa Khalfan ALMazrouei*, hereby declare that the work presented in this thesis was conducted by myself. Exceptions to this have been clearly stated in the text.

Abstract

The placenta is a temporary organ that develops after the implantation of a fertilized egg in the uterus, and it functions as an interface between the mother and the foetus to provide sufficient foetus nutrition. Various studies have shown that the magnetic resonance relaxation times of the placenta change during pregnancy, which could be an early indicator of a disease, such as preeclampsia (PE). However, magnetic resonance imaging (MRI) is not a suitable routine for pregnant women due to cost and availability. Low-field unilateral nuclear magnetic resonance (NMR) is a low-cost alternative capable of measuring relaxation times at a single point in space. Although the frequently adopted ultrasound imaging offers an easy technique to locate the placenta, it does not have the potential for early diagnosis of diseases like PE. Therefore, combining the two modalities, (ultrasound and low-field NMR) opens up a novel diagnostic approach at a much lower cost. This thesis aims to develop a low-field unilateral NMR system capable of measuring the relaxation time parameters at a distance from the sensor surface equivalent to the human placenta position.

This study reports the development of a low-field magnetic resonance system, called NMR-CAPIBarA (Clinical Assessment of Patients Implemented with Bar magnet Arrays), capable of measuring spin-lattice relaxation time (T_1) and effective transverse relaxation time (T_2^{eff}) covering the whole range of values relevant to the developing placenta. Two different materials were used to mimic the placental tissue relaxation time values presented in previous literature: PDMS silicone oils representing T_2^{eff} and full-fat milk powder solution representing T_1. The low-field electronic system was operated at a magnetic field of 18 mT and was successful in generating and detecting NMR signals using two types of radiofrequency coils: a solenoid and a printed circuit board surface coil, paired with the constructed planar magnet. The most significant result is the positive correlation between the relaxation times measured on the developed system when compared to the same measurements made by a commercial MRI scanner. In particular, the values obtained from the different silicone oil viscosities showed the capability of the low-field system to provide quantitative relaxation measurements over a range of required values to predict the health of the placenta, assuring that the proposed diagnostic approach is quite promising.

Publications

The following publications and scientific communication have been released as a direct result of this research:

Journal Papers

- Morris RH, Almazrouei NK, Trabi CL, Newton MI. NMR CAPIBarA: Proof of Principle of a Low-Field Unilateral Magnetic Resonance System for Monitoring of the Placenta during Pregnancy. Applied Sciences. 2020; 10(1):162.

  Available from: http://dx.doi.org/10.3390/app10010162

- Parslow S, Almazrouei NK, Newton MI, Dye E, Morris RH. A preliminary study of milk powder hydration using TEDSpiL continuous wave NMR. Magnetic Resonance in Chemistry. 2019;57(9):695-699.

  Available from: http://dx.doi:10.1002/mrc.4845

Conference Papers

- Almazrouei NK, Newton MI, Morris RH. Operational Amplifiers Revisited for Low Field Magnetic Resonance Relaxation Time Measurement Electronics. Proceedings. 2019; 42(1):1.

  Available from: http://dx.doi.org/10.3390/ecsa-6-06645

- Almazrouei NK, Newton MI, Dye ER, Morris RH. Novel Food-Safe Spin-Lattice Relaxation Time Calibration Samples for Use in Magnetic Resonance Sensor Development. Proceedings. 2017; 2(3):122.

  Available from: http://dx.doi.org/10.3390/ecsa-4-04916

Acknowledgements

All the praises and thanks are due to ALLAH Almighty, who always blesses and secures my life and has given me the patience and perseverance to continue my PhD study. In addition, I would like to convey my deep gratitude to every person who has made it possible for me, directly or indirectly, to undertake this thesis.

This thesis is based on work carried out at the Department of Mathematics and Physics in the School of Science and Technology, at Nottingham Trent University (NTU) from 2017 to 2020.

I want to express my gratitude to the Ministry of Education in the United Arab Emirates (UAE) for the financial support, and the Dubai Health Authority (DHA) for granting me study leave to obtain my PhD. Additionally, I am grateful to the UAE cultural attaché office in London for the continuous support and the follow-up with all the subjects I have studied.

Tremendous appreciation goes to my supervisory team for their continuous support, guidance, and motivation; without them I would not have been able to complete this thesis. At the outset, I want to thank the director of my studies, Dr Rob Morris, and my second supervisor, Dr Michael Newton. It was a great privilege for me to meet and learn from them, and I am grateful for their assistance in writing papers and for their feedback regarding my thesis. Additionally, I wish to thank my internal assessor, Dr Martin Bencsik, for the time he devoted to reviewing my annual reports and for his valuable advice.

Moreover, I would like to acknowledge the graduate school team at NTU, which works tirelessly to support all international students academically and technically.

Special thanks to all my colleagues, current and the past members of the CELS003 and ERD274 labs (especially Lizz, Johana, Steve, Abi, Jim, Nic, and Ed) and Dr Christophe Trabi, who helped me in the construction of the planar magnet and advised me regarding the technical issues. I have enjoyed my time with you all at the Clifton campus and appreciate your readiness to help and support me whenever I needed it. Additionally, my thanks go to all physics lab technicians at the ERD building who helped and provided me with everything I needed to realise my NMR-CAPIBarA system.

List of Figures

List of Tables

Contents

Abbreviations

The following notation is used throughout the text; other terms appear less frequently. Symbols used in all equations are defined where they occur.

NMR	Nuclear Magnetic Resonance
MRI	Magnetic Resonance Imaging
SNR	Signal to Noise Ratio
^{1}H	Hydrogen atom
MF	Magnetic Field
B_0	Static magnetic field
B_1	Oscillating magnetic field
T	Tesla, SI unit for magnetic field
T_1	Longitudinal or spin-lattice relaxation time
T_2	Transverse or Spin-spin relaxation time
T_2^*	Observed T_2 or the decay constant of FID
T_2^{eff}	Effective transverse relaxation time
CPMG	Carr-Purcell-Meiboom-Gill sequence
NMR-MoUSE	Mobile universal surface explorer
RF	Radio Frequency
G_0	Static gradient
FID	Free Induction Decay
DOI	Depth of Investigation
NMR-CAPIBarA	NMR-Clinical Assessment of Patients Implemented with Bar Magnet Arrays
US	Ultrasound imaging modality
PE	Pre-eclampsia
FGR	Fetal Growth Restriction

SAG	Small for Gestational Age
AGA	Appropriate for Gestational Age
WHO	World Health Organization
FOV	Field of View
3D	Three Dimensional
IR	Inversion Recovery
FT	Fourier Transform
MOLE	Mobile Lateral Explorer
SD	Standard Deviation
EPI	Echo Planar Imaging
MT	Magnetization Transfer
PDMS	PolyDiMethylSiloxane
CuSO4	Copper Sulphate
NTU	Nottingham Trent University
DSP	Digital Signal Processing
Op-Amp	Operational Amplifier
EM coil	Electromagnetic coil
DDS	Direct Digital Synthesis
DAC	Digital to Analog Converter
GUI	Graphical User Interface
SPIOs	Superparamagnetic iron oxides
PCB	Printed Circuit Board
M_0	Net magnetization
T_E	Echo time
T_R	Repetition time
T_I	Inversion time
A	Amper
V	Volt
dB	decibel

Chapter 1

Introduction

1.1   Research motivation

Nuclear magnetic resonance (NMR) is a powerful and non-invasive versatile technique used to explore the fundamental physical properties of materials. Living and solid materials are composed of a heterogeneous system at a structural and chemical level. Due to the difference in their molecular mobility, they show different characteristic relaxation times and diffusion signals [1]. The low-field NMR technique has received considerable attention in various problem areas, including industry, chemistry, material science, medical research, and diagnosis [2; 3]. High- or medium-field NMR/ magnetic resonance imaging (MRI) systems are available and exhibit various features, ranging from high signal-to-noise ratio (SNR) to high resolution and image quality [4]. However, due to a range of issues, such as a large footprint, highly expensive parts, and the need for a dedicated location (for safety purposes) and high radiofrequency (RF) power, they can be considered infeasible for in-situ applications [4; 5].

Although clinical MRI is a sophisticated medical imaging technique, it has poor availability around the globe, particularly in underdeveloped or developing countries. This is because of the high cost of installation and maintenance, which leads to a costly clinical examination. Globally, the access is limited to one-tenth of the population; even within developed countries, the distribution may not be identical. Therefore, research interest has shifted toward low-field MRI. Despite its inferior image quality or even non-existent in some cases, the capability of providing relevant diagnostic information is acceptable [6].

Advances in magnet development technology, particularly the permanent magnet, have significantly expanded the research fields that require sensitive, portable, and inexpensive measuring systems. The low field can be defined as the range of static magnetic fields (MFs), whose strength corresponds to a B_0 of 10 mT to 1 T, which is equivalent to a Larmor frequency of f_0 = 425 kHz to 42.5 MHz for a hydrogen nucleus

(^{1}H). Moreover, a very low-field NMR system is also available, which corresponds to an MF < 1 mT (f_0 = 42.5 kHz) [7]. The principal advantage of such a system is the flexibility in B_0 magnet design, where the required MF can be generated from a small permanent magnet arrangement: either a single-sided, open-access, or closed system [7; 8]. However, the single-sided system has reduced magnetic field and homogeneity in comparison to the conventional NMR spectrometer. Nevertheless, low-field NMR relaxometry has the potential to measure the water self-diffusion (D_0), spin-spin (T_2) and spin-lattice (T_1) relaxations, and effective transverse relaxation time T_2^{eff} of biological samples. Here, the value of T_1 depends on the field strength, and T_2 relies on the field homogeneity. To enhance the SNR for the NMR measurement applied in a strongly inhomogeneous field, T_2^{eff} is extracted from mixed T_1 and T_2 using a pulse sequence called the Carr–Purcell–Meiboom–Gill (CPMG) sequence [9].

Ex-situ unilateral NMR relaxometry, generally termed inside-out or single-sided, has developed from two main classes of stray-field NMR instruments: the first is oil-well-logging tools, where the concept of inside-out NMR was born in the 1980s for detecting a region outside the RF coil to study the geological formation and core analysis non-destructively inside boreholes [10; 11; 12]. A revolution started in the 1990s when firs, Eidmann et al. [13] and then the Blumich group [14] in Germany developed a similar instrument with a smaller permanent magnet, officially introducing the mobile universal surface explorer (NMR-MoUSE) sensor into the field. This instrument has enabled NMR signal detection for a flat sensitive slice a few millimeters away from the magnet surface. This tabletop system is composed of a U-shaped permanent magnet and a surface RF coil in a single-sided compact design. This type of configuration allows the measurement of different depth profiles into the surface of any arbitrary sample size, by placing the sample outside the magnet and changing the distance between the sample and the sensor [14; 15; 16].

The rapid development of the unilateral NMR system contributed to the increase in the number of applications of low-field NMR that required a portable NMR experiment. In this technique, the external field generated from the permanent magnet arrays projects the static field (B_0) in a volume displaced from the surface of the magnets. Different architectures of surface radiofrequency coil could be paired with a magnet to create the remote oscillating frequency (B_1) field. When the component of these two fields is orthogonal ($\perp$), the sensitive volume or 'sweet-spot' is defined by the shapes of these two inhomogeneous fields [17]. Several geometries of U-shaped magnet have been developed, using different aspect ratios, or by adding magnetic material in a specific position to enhance the field strength or reduce the gradient strength by joining the concentric U-shaped magnet [2]. However, they all share the common characteristic that the polarising field (B_0) is directed parallel to the sensor surface, facilitating an ordinary surface coil to be positioned at the magnet surface to excite and detect RF signals [18].

According to the desired sensitive volume size and application, the existing approaches for the available unilateral NMR sensors can be classified into two groups. The first group, called high gradient magnets, operate in highly inhomogeneous MFs, dominated by a high static gradient (G_0) along the depth direction, and $\perp$ to the device surface. The second group, called sweet-spot magnets, is employed in this thesis. They operate in an approximately homogeneous MF within a sensitive volume with a low G_0 effect, called the sweet-spot [2; 18]. Both methods have their own strengths and limitations. The former has the power of natural slice selectivity and high depth resolution due to its strong B_0 and G_0; which allows profile encoding along the depth direction. However, they are limited to a small sensitive volume and cause high diffusive attenuation in liquid samples.

On the other hand, the latter group provide a larger sensitive volume, more polarised spins, and narrow excitation bandwidth. All of these help to increase the SNR in the spectrum and minimise the diffusive attenuation, which allows liquid sample measurements [18]. Their limitations include operating at a lower MF due to the first or even second order of the G_0 field being cancelled, which prevents the profile measurements possible with the former group.

Since the last two decades, the profile NMR-MoUSE has been available commercially and utilised for different applications that require a detection region near the magnet surface [2; 3]. The depth profile for the sensitive region has been evolved from 2 mm with 5 μM resolution for PM2 up to 25 mm with 100 μM for PM25 [19]. As NMR-MoUSE is limited to a detection region near the magnet surface, it has been used to extract the information available at a shallow depth, such as skin in medicine and wall painting in cultural heritage [3]. Moreover, due to the lower cost of installation and maintenance of such single-sided NMR systems compared to clinical MRI scanners, the applications for medical diagnosis have been developed to investigate different biological tissues, such as tendons [20], contrast enhancement in the skin and subcutaneous fatty tissue [21], human skin [22], articular cartilage [23], T_1-based mammographic density [24], bone-volume–to–total-volume ratio [25; 26], and T_2-based mammographic density [27].

In contrast to NMR-MoUSE, and despite the many potential applications of sweet-spot NMR sensors [28; 29; 30; 31; 32; 33], they are underutilised. Most of the developments stay at the research level, and few have been tested in clinical trials, as is the case for the work of Dabaghyan et al. [5]. A possible reason behind this is that there are no commercial options for such systems [34]. Thus, scientists were encouraged to develop a system that satisfies their application requirements, specifically, when the measurement samples have significant free fluids, such as biological or human tissues [33]. As mentioned earlier, the homogeneous field of sweet-spot magnets offers a larger sensitive volume than high-gradient magnets. In addition, the RF pulse covers a narrower

bandwidth, leading to longer RF pulses with lower peak RF power [18; 33]. However, this field uniformity is not sufficient to measure the free induction decay (FID) due to the inhomogeneities ranging between 1000 and 10,000 parts per million (ppm) across the sweet-spot [2; 32]. Nevertheless, it sufficiently measures the long T_2 characteristic with the CPMG echo train sequence, which is harder to measure with an NMR-MoUSE device.

The depth of investigation (DOI) should be compatible with the application requirements and ensure that sufficient NMR signals are acquired from that region. Thereby, two central elements should be considered: initially, the magnet design, which is the large part of the system, and secondly, the RF sensor design. As described by Blumich and others [2; 18; 35], the RF coil field (B_1) should be $\perp$ to the B_0 field to enable the definition of the sensitive volume. In general, for a U-shaped magnet design, where the B_0 field is parallel to the surface, a single-current-loop RF coil is the most sensitive. For the sweet-spot magnet type, the size of the current-loop RF coil should be larger than the sensitive volume to enhance the SNR and reduce the variation of B_1 along the depth direction.

This research leverages the benefits of the unilateral magnet technique to explore human tissue; specifically the placental tissue. This aids in developing a unilateral NMR system for MR measurements as an assistive tool in addition to the ultrasound (US) imaging to improve the predictivity of diseased placenta. The low-field NMR relaxometry system developed throughout this PhD is called NMR-CAPIBarA (Clinical Assessment of Patients Implemented with Bar magnet Arrays). It is highly anticipated that this new system will contribute to improving the early detection of placenta disorder.

1.2 Medical application of the NMR-CAPIBarA

Non-invasive investigation procedures and proper diagnosis during the early stages of pregnancy is crucial for the development of a healthy placenta. According to researchers [36; 37; 38], 5–8% of pregnancies are affected by preeclampsia (PE) and foetal growth restriction (FGR), which put both mother and the foetus at risk. Globally, one-sixth of maternal deaths, about 60000 per annum, are related directly to PE [39]. This begins at the early stage of pregnancy when the maternal spiral arteries remodel inadequately and cause maternal placental vascular malperfusion [40].

Ultrasound, biomarker profiles, and MRI have been and are still used to monitor pregnant women. Pregnant mothers undergo ultrasound scanning at least twice during the pregnancy period. The sonographer measures the foetus' physical size and placenta's blood flow, relying on neonatal growth charts or simple percentile cut-offs. However, these measurements are not sufficient to indicate PE or FGR. One study by Bamfo

J. et al. [41] showed that morbidity and mortality from FGR are similar whether the baby is small for the gestational age (SGA) or appropriate for the gestational age (AGA). Moreover, the error of undetected cases during routine scans reaches up to 30%, while the incorrect detection rate is up to 50%. Improving placental disorder predictivity requires combining the ultrasound findings with the metabolite profile for blood and urine samples. However, since PE is a heterogeneous disease, "the World Health Organization (WHO) stated that there is no clinically useful screening test to predict the development of the PE" [42]. Thus, a better diagnostic technology is necessary, that includes a combination of different diagnostic tools with informative in-vivo measurements [42; 43].

In contrast, MRI provides reliable information about the placental function at different gestational ages in comparison to ultrasound. This is due to the larger field of view (FOV) and inherently three-dimensional (3D) technique. It is generally applied in cases of high-body-mass-index patients and a posterior placenta with a depth > 8 cm [44; 45; 46]. Several studies in the literature using clinical MRI 1.5T have shown that the MRI relaxation time parameters decrease as the gestational age increases for both healthy and diseased placentas [42; 47; 48], in which the values of the relaxation time for the latter fall below the trend line of the former values. However, despite its early detection capability, MRI is not as routine as ultrasound in terms of cost and availability. Moreover, the closed environment causes patient claustrophobia. Consequently, the proposed NMR-CAPIBarA has the potential to address these issues and provide placental relaxation time.

Therefore, this thesis proposes a novel medical diagnostic approach to assess diseased placenta, such as PE. The NMR-CAPIBarA system will ultimately combine with conventional ultrasound imaging in vivo to co-locate the MR sensitive volume and then the relaxation properties measured with the MR system. However, that is beyond the scope of this project. This additional tool to routine ultrasound imaging aims to improve the predictivity of placenta disease at the early stages of pregnancy. Therefore, it allows the identification of mothers at high risk for close monitoring and consequently a better outlook for both mother and foetus.

1.3 Aims and objectives

Identifying pregnant women at high risk of PE is important for the health of both mother and foetus. PE can lead to several complications, such as preterm delivery or, in a worse scenario, maternal death. Several years ago, clinical MRI showed that for both healthy and compromised placenta, the tissue biomarkers T_1 and T_2 are changed as the gestational age is advanced. However, due to the fact that an MRI scan is considered the most expensive diagnostic modality, a low-cost tool is required that can provide similar quantification for these biomarkers. Therefore, considering a low-field magnetic system that can be used in conjunction with the ultrasound imaging modality could address this issue. The required hardware to accomplish this has been developed and is presented in this thesis.

To accomplish the research aim, the following objectives have been identified:

- Develop and test separate phantoms for T_1 and T_2 measurements, capable of representing the different range of placental relaxation time presented in the literature review in Chapter 2, by employing silicone oil as a material for the T_2 relaxation time and full-fat milk powder for T_1 relaxation time. Reference values for these materials to be generated by means of a clinical MRI 1.5T scanner to characterise the functionality of the developed hardware. A detailed discussion is presented in Chapter 3.

- Develop and examine the low-magnetic-field electronic system. Using a homogeneous magnetic field for B_0 and B_1, as an initial step, their electronic capabilities to be operated at a magnetic field of approximately 18 mT will be verified. A detailed discussion is presented in Chapter 4.

- Construct the magnet: anti-parallel planar magnet arrays inspired by Dabaghyan et al.'s paper [5]. Subsequently, to measure the density flux at different heights to define the position of the sweet-spot. A detailed discussion is presented in Chapter 5.

- Develop and estimate an appropriate RF surface coil to be paired with the planar magnet and optimise the SNR, FOV, and stability. A critical discussion is introduced in Chapter 5.

- Perform MR measurements using silicone oil. These measurements are to be performed at a distance equal to the position of the anterior placenta (24 mm) to determine the sensitivity of the developed system in measuring the different ranges of T_2^{eff}. A critical discussion is introduced in Chapter 5.

1.4 Major contributions of the thesis

The fundamental issue addressed by this research is the possibility to develop a reliable low-field unilateral NMR system capable of measuring the relaxation time parameters at a distance from the sensor surface equivalent to the placenta position. The research explored various paths within the disciplines of the unilateral magnet, which is considered application-specific, in addition to the appropriate electronic system. *The prime novelty of this research is the employment of the technique of a low-field unilateral magnet system to interrogate placental tissue in vivo.* However, because the developed sensor is at the preliminary experimental phase, a phantom study should be performed to characterise the sensitivity of the developed sensor. Thus, the significant contributions of the research were performed in steps.

The first step in the research was to investigate a suitable material that could mimic the values of the placenta tissue relaxation time. *The first contribution in this thesis was a part of the phantom study in Chapter 3, where the use of full-fat milk powder solution as an inexpensive and safe material capable of shorting the spin-lattice relaxation time was investigated.* This result was confirmed in both magnetic fields by the 1.5 T clinical MRI and by a customized magnetic resonance sensor of 0.3 T field strength. To our knowledge, we are pioneers to utilise milk powder to assess the development of the sensors. Moreover, the outcomes from the clinical MRI were used as reference values to demonstrate the suitability of the current system to replace the high-field, as illustrated in Chapter 5, particularly the effective transverse relaxation time for the varying viscosities of the silicone oils' that covered the whole range of placental relaxation time presented in previous literature.

Electronic system hardware is a fundamental factor in a successful NMR experiment. This was the driver behind the second contribution. Therefore, the second step of this research was directed toward developing an effective electronic system capable of operating at a low magnetic field of less than 20 mT. The central concept of the generated electronic design is based on advanced digital signal processing techniques, which are usually employed in telecommunication systems. The commercial spectrometer console SpinCore has a frequency range from 0 to 100 MHz, and is controlled by an in-house MATLAB GUI code to generate the CPMG pulse sequence.

To develop the appropriate electronic system in Chapter 4 a homogeneous field was employed for both static and oscillating magnetic field. Thus, the laboratory electromagnetic coil was used as B_0 with the solenoid coil as the B_1 field. The console was associated with two different external units, commercial units and operational amplifier circuits, as a cost-effective unit. Therefore, *the second contribution of this thesis was successfully producing of an NMR signal from the developed low-field electronic system utilising the different types of external unit, particularly the introduction of the simple*

inverting operational amplifiers circuit as an effective front-end unit for the low-field system.

Usually, the assembly of an entirely new NMR system is conducted gradually to attain reliable information. Hence, the third step in this research was initially focused on combining the new planar magnet with the outcomes from Chapters 3 and 4. However, the NMR-CAPIBarA system was successfully developed after completing the essential steps. To begin with, the unilateral magnet arrays was constructed, which are based on the anti-parallel principle and define the position of the sweet-spot. Subsequently, the integration with the low-field electronic system took several steps of optimisation to enhance the SNR, specifically after the introduction of the planar RF coil as a sensor instead of the solenoid coil.

Furthermore, after the optimum experimental parameters were defined for the required depth (24 mm), measurements of the effective transverse relaxation time were performed for the different viscosities of silicone oils and compared to the values generated from the 1.5 T clinical MRI. Moreover, measurements of the relaxation time were conducted for a model compound that has varying concentrations of full-fat milk powder dissolved in silicone oil. Therefore, *the third contribution of this thesis was successfully measuring the effective transverse relaxation time of different viscosities of silicone oils at a depth equivalent to the position of the anterior placenta, where the measured values cover the whole range of the placental tissue's transverse relaxation time presented in the literature.* Additionally, *the fourth contribution of this thesis was the effectiveness of the full-fat milk powder in suppressing the effective transverse and longitudinal relaxation times for silicone oil utilising a low-field system (NMR-CAPIBarA).*

In conclusion, the proposed NMR system in this thesis is an open-access, low-cost, portable magnetic resonance relaxometry system. It has the potential to appropriately measure the effective transverse relaxation time at a distance from the sensor surface equivalent to the position of the anterior placenta. It could be utilised as an add-on tool to the ultrasound imaging modality for MR measurement after the placenta has been localised. The system introduced in this thesis is an affordable instrument, both for developing and developed countries, in places where clinical MRI is expensive or does not exist.

1.4.1 Specific contribution by chapter

In this subsection, the contributions made by the candidate and supervisory team are explicitly described for each experimental chapter. To provide further clarity, initials will be used to attribute the effort replicating author contribution statements in journal publications: NKA – PhD candidate, RHM – Director of Studies, MIN – second supervisor.

Chapter 3. Sample selection and preparation – NKA. MRI scan protocol creation – RHM, scan parameter optimisation and data analysis and interpretation - NKA using a combination of in-house MATLAB software originally written (not for this PhD) by RHM and other tools as identified by NKA. Closed-loop magnet used in 3.2.2.2 originally constructed (not for this PhD) with commercial off-the-shelf equipment (COTS) – RHM; all experiments and data processing and interpretation - NKA.

Chapter 4. RF coil preparation – NKA. Identification of suitable components and assembly, including tuning and matching circuit and operational amplifier circuits – MIN. MATLAB software for the control of SpinCore spectrometer originally produced (not for this PhD) by RHM and modified by RHM as needed. All parameter optimisation and measurements – NKA. Sample preparation – NKA. Experimental work – NKA. Data analysis and interpretation – NKA. Parts of this chapter have been published (in reference [71]); these remain referenced as copyright has been transferred to the publisher. All figures other than 4.7 – NKA; Figure 4.7 – RHM from publication.

Chapter 5. Planar magnet construction - NKA supported by former PDRA. Acrylic field mapping guide, measurements, and analysis – NKA. All RF coils – NKA. Improvements to the front end – NKA. MATLAB software for control of SpinCore spectrometer originally produced (not for this PhD) by RHM and modified by RHM as needed, including the addition of composite pulses. Sample preparation – NKA. Tuning and matching of coils – NKA. Figure 5.33 and Figure 5.36 – RHM (from publication [142].

1.5 Thesis structure

This thesis is divided into six chapters and ends with an appendix. These chapters are organised as follows:

Chapter 2 presents three main sections: the necessary information that allows the reader to understand the basic principle of NMR theory and NMR pulse sequences, which will be used in the subsequent chapters. The following sections provide two topics: a general overview of the traditional unilateral magnet hardware and its application in the medical field, and a review on both the placenta thickness and the measured relaxation time, which will be utilised as criteria for the developed system in Chapter 5.

Chapter 3 involves two practical experiments conducted in a clinical MRI (1.5 T) to mimic the placenta tissue relaxation time separately. This is done by means of employing different viscosities of two separate materials: the silicone oil to mimic T_2^{eff} and a novel food substance, full-fat milk powder, to mimic T_1. The results of this chapter will be used as a reference value for the measurements demonstrated in Chapter 5.

Chapter 4 shows how the electronic system has been developed to efficiently operate in a homogeneous and low magnetic field, approximately 18 mT. The development involved utilising two different RF pulse power amplifiers: the high-power TOMCO and the lower-power operational amplifier (Op-Amp). The Op-Amp was also used as a signal pre-amplifier. The results of this chapter will determine which electronic circuit should be used for the developed magnet arrays, which are characterised as less homogeneous in Chapter 5.

Chapter 5 reports the developmental stages of the unilateral magnet (NMR-CAPIBarA), starting with the construction of the permanent magnets, flux density map, developments of RF coil, and finally, the MR measurements for silicone oil at a distance equal to the position of the anterior placenta. This chapter outcome will define the outlook for this project.

Chapter 6 concludes this thesis with a summary of the findings of this research, collected from each conclusion provided in the previous chapters, including a brief synopsis of the potential future works.

Chapter 2

Theory and Literature Review

2.1 Introduction

The NMR phenomenon is the basis for both MRI and NMR scanning. The resulting NMR signal from a hydrogen (^{1}H) nucleus in tissue can be characterised by several parameters, e.g. the relaxation time constants T_1 and T_2. These constants are sensitive to ^{1}H population in a local environment. Thus, these parameters should be investigated carefully to attain an accurate representation of their chemical composition and structural organisation within biological tissues.

This chapter has three main sections. It begins with the basic NMR principles required to understand the experimental study presented in this thesis. Different parameters related to the time domain MR measurement are discussed, such as nuclear spins, spin polarisation, the Zeeman splitting theorem, and precession; additionally, the relaxation time constants are discussed. The main pulsed NMR experiment used for this project is discussed along with the parameters that might affect the measurement sensitivity (SNR).

The following section reviews relevant literature on various low-field NMR relaxometry designs and how a different approach of the unilateral NMR sensors inspired the development of the hardware system presented in this thesis. The final section of this chapter discusses the placental thickness and relaxation time values extracted from several studies utilising ultrasound imaging and clinical MRI scanners, respectively. This section will help establish the criteria for the system in this project.

2.2 NMR theory

NMR is a phenomenon that strongly depends on the intrinsic properties of atomic particles. Therefore, spin angular momentum (aka nuclear spin) has a magnetic dipole moment (μ). The presence of magnetic dipole moment is associated with the electron spin observed by Stern and Gerlach in 1922 [49] during a study on the effect of the magnetic field gradient on a beam of a silver atom. They observed that the path of the molecules changed and the beam split, if their nuclei had a magnetic moment (μ) [50; 51; 52]. This experiment is shown in Figure 2.1.

In 1936 [53], Rabi developed the theory for the use of a field gradient to create and destroy signals by applying electromagnetic radiation with different directions at the resonance frequency to induce a successive transition between nuclear spin states of the atom in the molecular beam. Later, in 1946 the first NMR experiment was successfully performed independently by two scientists, Bloch [54], who observed protons in water and Purcell [55], who observed protons in paraffin samples. They used different experiment that relied on the net nuclear magnetisation. For the success of their experiments, the net magnetisation required to build up at an appropriate relaxation rate, which was initiated from the instability between the spin states of different magnetic quantum number values [52].
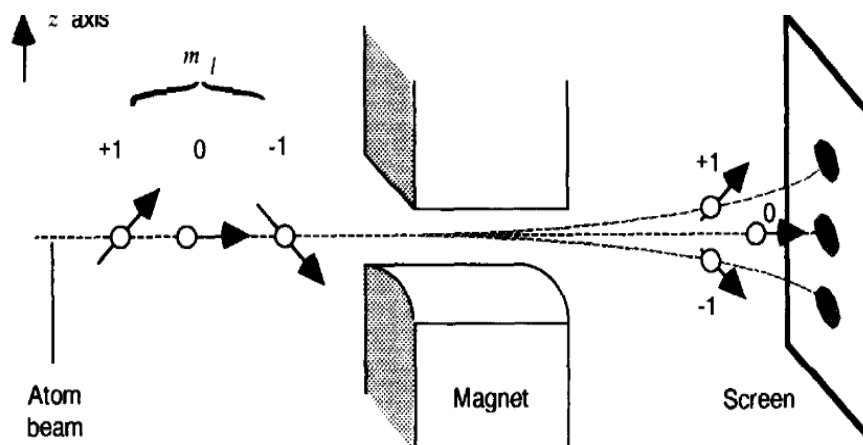
Figure 2.1: Diagram of the Stern–Gerlach experiment.
(Adapted from [51])

2.2.1 Nuclear Spins

Nuclear spin is an intrinsic quantum property of protons in all elementary particles. It results in two classical properties: nuclear angular momentum and nuclear magnetic moment. The latter can be considered to produce a similar effect to a small bar magnet aligned along the rotation axis of the spin [56] (Figure 2.2). A nucleus with an odd mass

number such as ^{1}H and an angular moment property (L) is characterised by a non-zero spin quantum number($I=\frac{1}{2}$). Generally, I can be zero, an integer, or a half-integer, depending on the physical property of the nucleus.

The proton's two properties, *angular momentum and magnetic moment*, enable the proton to be affected by an applied external magnetic field and electromagnetic waves [57]. A non-zero spin loses the random orientation when it is exposed to an external magnetic field. This interaction results in two potential orientations for the spins, parallel or anti-parallel to the Z-direction of the applied magnetic field [27]. These two created energy levels are characterised by a magnetic quantum number (m), with values strictly equal from I to -I in integer steps [58].
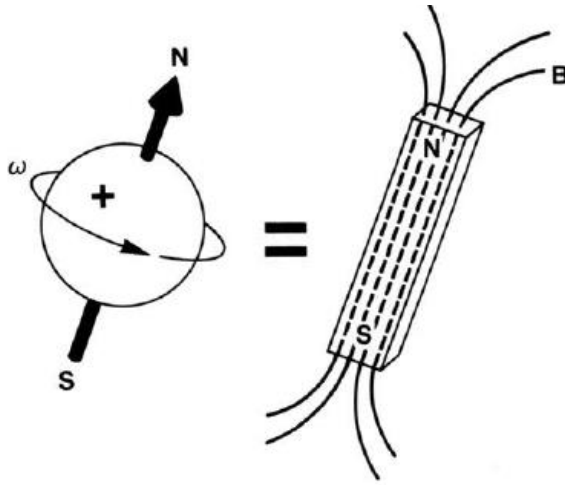
Figure 2.2: Positively charged nucleus rotating with angular frequency ($\omega=2\pi$ ν) around its axis and has a magnetic field B equal to a tiny bar magnet which has a similar spin rotation axis (Adapted from [56])

The nuclear spin magnitude and direction are quantised and described because they are vector quantities [58]. The magnitude of the **spin angular momentum (L)** is

$$L= \sqrt{I(I+1)}\hbar, \tag{2.1}$$

where $\hbar$ is Plank's constant and is equal to $\frac{h}{2\pi}$ (6.63 x 10^{-34} J.s) [56]. $I= 0, \frac{1}{2}, 1, \frac{3}{2}$,...., and the angular momentum vector direction I onto z-axis is

$$I_z = m\hbar, \tag{2.2}$$

where m has $2I+1$ values, for example, $m= I, I+1$,....,$-I+1,-I$. As an example, ^{1}H atom has two values of m: $-\frac{1}{2}$ and $\frac{1}{2}$ (Figure 2.3b).

The **spin magnetic moment (μ)** is also a vector quantity and related to I through

the gyromagnetic ratio γ[1] of the nucleus; therefore, the length or magnitude is

$$\mu = \gamma\sqrt{I(I+1)}\hbar, \tag{2.3}$$

Thus, the nuclear magnetic moment can be parallel to the angular momentum or anti-parallel for negative γ nuclei. As a result, the magnetic moment has both magnitude and direction, which are quantised.

2.2.2 Spin Polarisation and Precession

Based on the previous discussion, if B_0 is removed, all the spin states or energy levels of the nucleus collapse, and all spins have the same energy, causing an uneven distribution for the direction of the quantised axis (Figure 2.3a). In the application of a stronger magnetic field B_0, the spins will be quantised along the axis of B_0, often the Z-axis, and gain an energy

$$E = -\mu.B_0 = -\mu_z B_0, \tag{2.4}$$

Considering that $\mu_z = \gamma I_z$ and $I_z = m\hbar$, the energy is

$$E = -m\hbar\gamma \, B_0, \tag{2.5}$$

Thus, the $2I+1$ of the spin states has different energy values and splits equally with an energy gap equal to $\Delta E = \hbar\gamma \, B_0$ (Figure 2.3c).
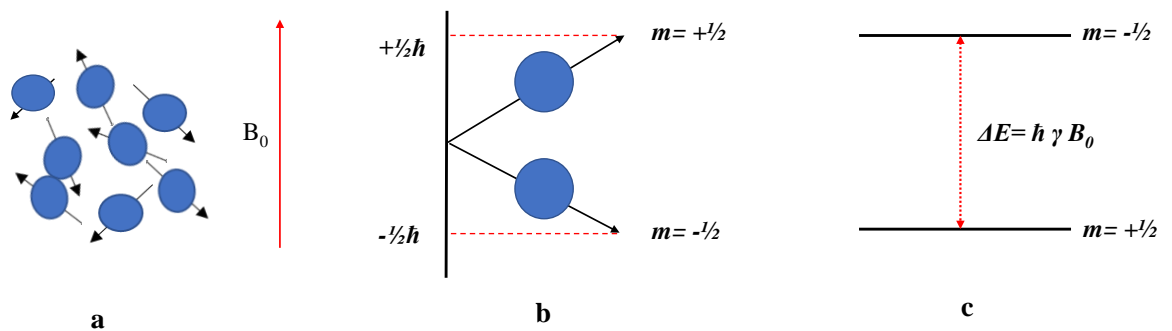
Figure 2.3: Space quantisation and energy level for ^{1}H, spin$\frac{1}{2}$. a) Random motion of the atoms, b) space quantisation, and c) energy level splitting depending on the values of B_0 and γ.

---

[1] A specific constant for a particular nucleus that is directly related to the strength of the tiny nuclear magnet (e.g. ^{1}H γ is 42.58 MHz/T at $B_0 = 1$ T) [57]

The difference in energy level between two spin states is defined as Zeeman splitting, which involves the spin populations at each energy levels. As mentioned in the previous section, splitting between states is linearly related to the strength of the external B_0. The higher the difference between the population of two spin states, the more the net magnetisation (M) along the direction of B_0 will be observed [27]. Therefore, a higher sensitivity enables the NMR signal to be acquired. This process is known as **spin polarisation**. Figure 2.4 shows the increase in the difference (ΔE) between the spin states as a function of an external B_0 strength.
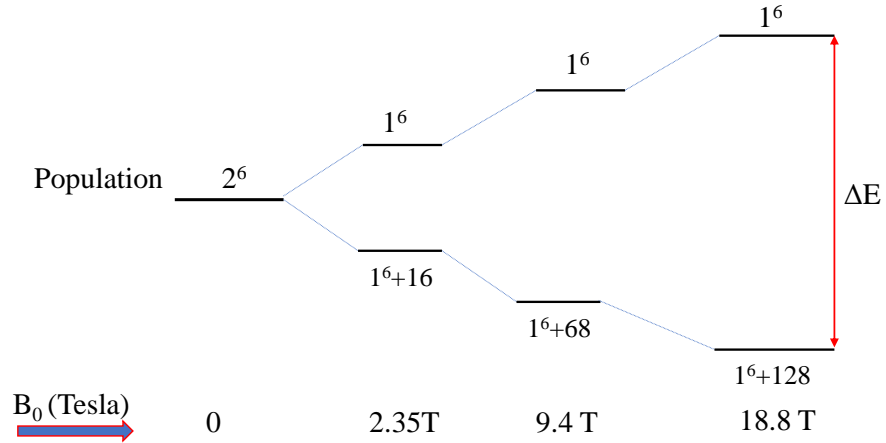
Figure 2.4: Energy level splitting increasing linearly with the B_0 strength, for a spin $\frac{1}{2}$ nuclei of a relative number of population equal to 2 million protons in a sample.
[56]

At thermal equilibrium and room temperature, the undisturbed protons are distributed in the energy states according to the Boltzmann equation [59]:

$$\frac{Nupper}{Nlower} = \exp^{-\frac{\Delta E}{kT}} = \exp^{-\frac{hF_0}{kT}}, \tag{2.6}$$

where N_{lower} and N_{upper} represent the number of populations in the lower and upper energy levels, respectively. T is the temperature in Kelvin (K), and k is the Boltzmann constant ($1.38{\times}10^{-3}$ JK^{-1}). Bohr's condition states that $\Delta E = h\, f_0$, as shown in Equation 2.6; thus, the frequency f_0 for a spin transition to be expressed as

$$F_0 = \frac{\gamma B_0}{2\pi}, \tag{2.7}$$

Moreover, the above equation defines the Larmor frequency (ω_0), where $\omega_0 = 2\pi f_0$, which describes the proton precession at a specific frequency when the external magnetic field is applied [57].

2.2.3 Sensitivity (SNR)

The sensitivity (SNR) is directly proportional to the total magnetisation, where the net magnetisation ($\mathbf{M}_0$) is a consequence of the population difference between the two energy states. The relationship between them assumes the form

$$\mathbf{M}_0 = \frac{N\gamma^2\hbar^2 I(I+1)B_0}{3\mu kT} \tag{2.8}$$

where N is the number of system population, and μ is the permeability.

Figure 2.4 shows an excess number of protons in the lower state, which they are parallel to the B_0 direction at thermal equilibrium. The population ratio for protons under 18.8 T ($f_0 = 800$ MHz) is 0.99987, as the number of protons in the lower energy level is exceeded by the upper level by 128 protons. These small excesses in the protons number are the major key to observing NMR signals [56].

As Equation 2.6 indicates, the population ratio increases with the B_0 strength. Therefore, the small population ratio will reduce the sensitivity, and consequently, the NMR signal is hardly observed. However, other approaches can be used to increase the sensitivity, such as increasing the sample volume or concentration (number of protons per volume) [56].

2.2.4 B_1 magnetic field

As described earlier, the protons influenced by B_0 are precessed along the z-direction, longitudinally (M_z), but with irregular phases, and the associated transverse magnetisation (M_{xy}) is zero. To build a phase coherence within the precessed spins, another type of magnetic field should be applied on the M_{xy} for a short period, and it should be oscillating at the Larmor frequency to move the spins down away from the z-direction [27; 60]. B_1 represents this magnetic field pulse applied along either the x or y-axis, and it is generated through RF coils.

Thus, the spin system will absorb energy when it is irradiated by the RF pulse at an appropriate ω_0, where the amplitude of the B_1 field should be $\perp$ to the Z-axis and B_0 field. This pulse will simulate spins in the two energy levels as follows. The upper-level spins are dropped, and lower-level spins are raised. Hence, a sum of energy absorption is obtained when the low energy level obtains more spin numbers [61].

The bulk magnetisation ($\mathbf{M}_0$) behaviour after the RF pulse can be described by two frames. The laboratory frame, which represents the flipping of the bulk magnetisation to the x-y plane, occurs after a conical spiral trajectory (Figure 2.5a). The other frame is called the rotating frame, which is a 3D coordinate system (x', y', and z') representing the trajectory of flipped spins on a plane $\perp$ to the (x-y) plane, and rotating at ω_0 along

the z-axis (Figure 2.5b). [27; 60].
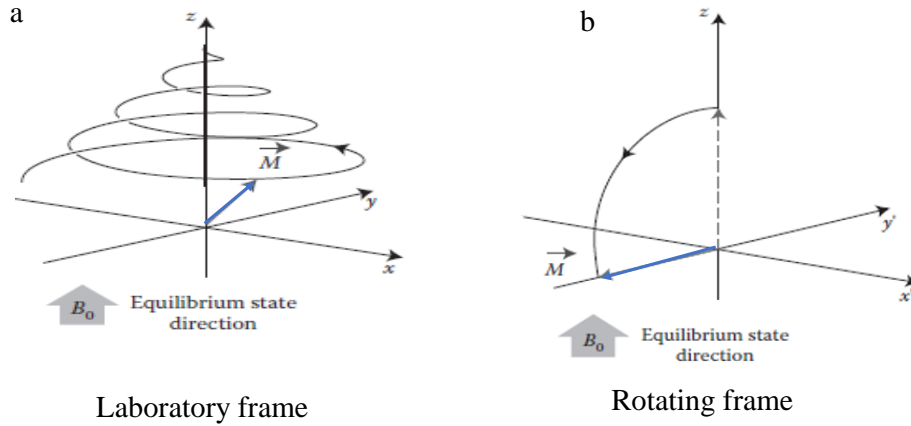
Figure 2.5: Bulk magnetisation behaviour after excitation by an RF pulse: a) laboratory frame and b) rotating frame
[60]

The rotating frame is the common reference frame utilised to describe the RF pulse effect on the $\mathbf{M}_0$ behaviour [27; 56; 60].

2.2.5 Bloch Equation

The rate of change in $\mathbf{M}_0$ with respect to time is described by the Bloch equation

$$\frac{d\vec{\mathbf{M}}}{dt} = \vec{\mathbf{M}} X \gamma \vec{\mathbf{B}}, \tag{2.9}$$

where the $\vec{\mathbf{M}}$ experiences a torque caused by the magnetic field $\vec{\mathbf{B}}$ and raised by γ. Therefore, the $\mathbf{M}_0$ time-dependent behaviour after RF pulse (B1) is described as follows [27; 60; 61]

$$\frac{d\vec{\mathbf{M}}}{dt} = \vec{\mathbf{M}} X \gamma \vec{\mathbf{B}}_1 - \frac{\mathbf{M}_x x}{T_2} - \frac{\mathbf{M}_y y}{T_2} - \frac{(\mathbf{M}_z - \mathbf{M}^0)z}{T_1}, \tag{2.10}$$

where $\mathbf{M}^0$ is the thermal magnetization value for $\mathbf{M}_z$ that is built up from the B_0 field. $\mathbf{M}_x$ and $\mathbf{M}_y$ are the magnetisation components of $\mathbf{M}$ along the x-axis and y-axis, respectively. The spin system relaxation process begins after the perturbation by the B_1 field is complete, and it is characterised by two time constants: T_1 and T_2.

In summary, there are two steps to analyse the $\mathbf{M}$ behaviour; first, during the RF pulse excitation, and the second is the relaxation after the RF pulse is turned off.

During the period of the RF pulse excitation, the form of the Bloch equation becomes

$$\frac{d\vec{\mathbf{M}}}{dt} = \vec{\mathbf{M}} X \gamma \vec{\mathbf{B}}_1, \tag{2.11}$$

the part of the x-y magnetisation is cancelled owing to the short period of the applied RF pulse compared with the time constants T_2 and T_1.

B_1 angular frequency (ω_{rf}) is preferred to be applied similar to the spin system resonance frequency (ω_0), where $\omega_{rf} = \omega_0 = \gamma \, B_0$. This is important to enable the spin transition between the energy levels.

When the spin system magnetisation (**M**) irradiated by B_1 along the x$'$ axis, only the protons that shared a similar resonance frequency will be tipped away from the z-axis to the transverse plane, as described by the following equations [27]

$$\mathbf{M}_{x'}(\mathbf{t}) = \mathbf{0} \;, \tag{2.12}$$

$$\mathbf{M}_{y'}(t) = \mathbf{M}_Z^0 \sin(\int_0^t \gamma B_1(\hat{t}) d\hat{t}), 0 \le t \le \tau_p \tag{2.13}$$

$$\mathbf{M}_{z'}(t) = \mathbf{M}_Z^0 \cos(\int_0^t \gamma B_1(\hat{t}) d\hat{t}), 0 \le t \le \tau_p \tag{2.14}$$

where τ_p represents the duration of the RF pulse. Now, the bulk magnetisation is precessing around the x$'$ axis with an angle created between the **M** and z/z$'$ axis. This angle is known as the flip angle (α) and is formed as follows:

$$\alpha = \int_0^{\tau_p} \gamma B_1(t) dt, \tag{2.15}$$

The flip angle depends on both the exposure length (τ_p) and B_1 values [27]. The flip angles that were used in the practical experiments of this thesis were 90° and 180°, which are common for most measurements.

2.2.6 Relaxation time

Several relaxation processes constantly occur within all samples. We generally become aware of the influence of these processes directly after the RF excitation is turned off, and the bulk magnetisation begins to return toward the equilibrium state (z-axis). In this process, the length of the magnetisation vector along the x-y plane decreases while the magnitude increases along the z-axis. This is due to the interactions of the spins between the surrounding environment, known as the lattice [27; 60]. The rotating transverse magnetisation is responsible for the appearance of the MR signal in the receiver coil. As mentioned earlier, the time constants that represent spin system relaxations in the Bloch equation are the longitudinal relaxation time and the transverse relaxation time. Additionally, according to their decay mechanism, they are known as spin–lattice and spin–spin relaxation times (T_1 and T_2, respectively) [60]. These two parameters are the principle to generate the contrast between tissues. They are independent processes, although they occur simultaneously.

2.2.6.1 Longitudinal relaxation (T_1)

T_1, also known as the recovery longitudinal relaxation time, in which the magnetisation vector along the z-axis ($\mathbf{M}_z$) begins to recover gradually as the transverse magnetisation in the x-y plane ($\mathbf{M}_{xy}$) decays to rebuild the thermal magnetisation ($\mathbf{M}_0$). This process is obtained through an efficient energy transfer to the medium, where the excess energy that is absorbed from the RF pulse should be dissipated to the medium. Hence, the simulated protons are permitted to return to the ground states. This energy is generated from the interaction of the resonating protons with other protons and with the magnetic nuclei in the surrounding environment [57; 60].

This time constant is dependent on the strength of the static magnetic field (B_0) and the molecular internal motion (Brownian motion). T_1 assumes the following form after a 90° RF pulse is applied along the x-axis [57; 62]

$$\mathbf{M}_z(t) = \mathbf{M}_0[1 - \exp{(\frac{-t}{T_1})}], \tag{2.16}$$

Figure 2.6 shows the required time for T_1 to reach 63% of the $\mathbf{M}_0$ value. An exponential function results in this decay.
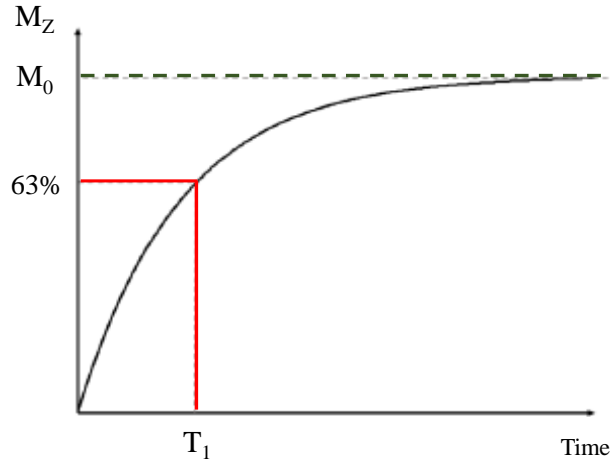
Figure 2.6: T_1 magnetisation vector growth to reach 63% of $\mathbf{M}_0$ value (Adapted from [62])

2.2.6.2 Transverse relaxation ($\mathbf{T}_2$)

T_2 or spin-spin relaxation time is obtained when the transverse magnetisation decays in the x-y plane. Unlike T_1, T_2 decay has different mechanisms; it results from spin interaction and exchange of energy. This causes a scrambling of relative phases between spins of the same group, dephasing until they fade out gradually. The reason behind the spin scrambling is that, on their circular precessional path, one of the spins moved forward while the other moved backwards. The spin moment precedes at a different speed. Thus, instead of adding, the magnetisation vectors begin to cancel each other until the transverse magnetisation disappears [57].

The loss of coherence that occurs between the spins has a main reason: as mentioned in Section 2.2.1: spins have small magnetic moment properties, which causes a variation in the local magnetic field; thus, they interact with each other randomly. Therefore, each spin is exposed to a different magnetic field; they precede differently (faster or slower), which results in phase loss.

The intrinsic inhomogeneity resulting from the external magnetic field generator and the sample scanned also causes phase scrambling. However, this effect could be fully or partially reversible depending on the presence of molecular diffusion. This type of exponential decay is faster than T_2 and is represented by a time constant T_2^*, where $T_2^* \leq T_2$. Moreover, it reflects the free induction decay (FID) signal, and it can be avoided through a spin-echo sequence, which is discussed in the next section.

T_2 is less dependent on the strength of B_0. T_2 assumes the following form after a 90° RF pulse is applied along the x-axis [57; 62]:

$$\mathbf{M}_{xy}(t) = \mathbf{M}_0[\exp{(\frac{-t}{T_2})}], \qquad (2.17)$$

20

The total transverse relaxation time includes the two effects of dephasing and is called the apparent relaxation time. It can be expressed as follows:

$$\frac{1}{T_2^*} = \frac{1}{T_2} + \frac{1}{T_2'},$$ (2.18)

where $T_{2'}$ is the dephasing caused by the inhomogeneities in the magnetic field over the sample volume.

Figure 2.7 shows signal loss due to T_2^* relaxation. T_2^* is the time required for $\mathbf{M}_{xy}$ to decay to 37% of its initial $\mathbf{M}_0$ value, and it is leading by an exponential function. This envelope represents the NMR signal detected by a receiving coil.
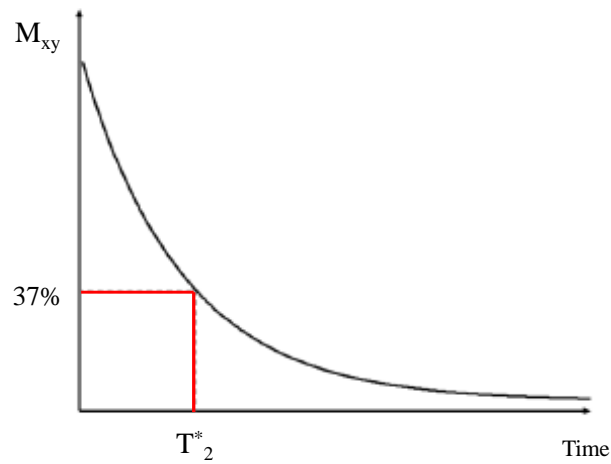
Figure 2.7: T_2 of transverse magnetisation ($\mathbf{M}_{xy}$) decaying from maximum to background. (Adapted from [62])

Most of molecular motions in biological tissues are considered to be in a slow interaction mode, therefore, T_2 relaxation is more favourable for tissue characterisation because of its interaction mechanism, reflecting the slow motions of macromolecules. Moreover, T_1 is considered to be tissue specific at low B_0 fields. In human tissue, the T_1 value is significantly longer than T_2 values, and the time difference between them is the key to the MR measurement. T_1 values rang from 0.5 to 5 s, while T_2 values rang from 20 to 300 ms at 1.5 T, and they are shorter in solids than in liquids [57; 60; 62].

2.2.7 NMR pulse sequence

The primary use of the pulse sequence is to investigate sample properties, which is achieved through a proper measurement for the relaxation time constants. Frequently, this type of experiment consists of a series of RF pulses permeated with a time delay, resulting in a signal acquisition [63]. Furthermore, in the MR image, a gradient pulse is introduced between the RF pulses for signal localisation, where the gradient coil is positioned orthogonally in each direction (x, y, and z). There are several types of NMR pulse sequencing methods; this section will discuss only the pulse sequences utilised for an experimental part in this thesis.

2.2.7.1 Spin echo pulse

This method was discovered by Hahn in 1950 [64] and developed by Carr and Purcell in 1954 [65], and it is considered a fundamental method of measuring spin–spin relaxation time. As explained earlier, an excitation pulse 90° is applied for a short time (τ), and the net magnetisation rotates from the z-direction into the x-y plane. After a while, the spins experience phase scrambling and begin dephasing. This process produces the FID signal that is detected via the receiver coil as a sinusoidal voltage. The observed decay constant of the FID is indicated by T_2^*. This method is considered the most basic technique in the measuring of spin system properties. In homogeneous samples, the signal is decayed mono-exponentially, whereas in actual samples, it is decayed multi-exponentially; this is because actual samples contain more than one environment. This technique is often utilised with an external magnetic field (B_0) higher than 1 T [66]. However, it is inconvenient in an inhomogeneous field or even to measure the information for T_1 relaxation time. Thus, other techniques should be employed to obtain this information.

Assuming the spins experience similar interactions, the signal can be recovered by reducing the sign of the processional rotation. This is most often achieved by a complete inversion of the spin system using a 180° pulse. Therefore, after the FID signal is produced, the 180° pulse is applied to refocus the dephased spins for a particular time (τ). Precisely, this pulse flips the collection of the dephased magnetic moment about an axis in the x-y plane. The overall group of the magnetic moment begins to precess continually in the same direction, and they re-phase together to recover the FID signal [67]. This refocusing generates an echo. The total time for this process is called the echo time (TE= 2τ) (Figure 2.8). The total TE is defined as the time from the first excitation pulse to the formation of spin echo.

The amplitude for the generated echo is given by Equation 2.19, where t = TE

$$\mathbf{M}_{xy}(TE) = \mathbf{M}_0[\exp{(\frac{-TE}{T_2})}], \tag{2.19}$$

22
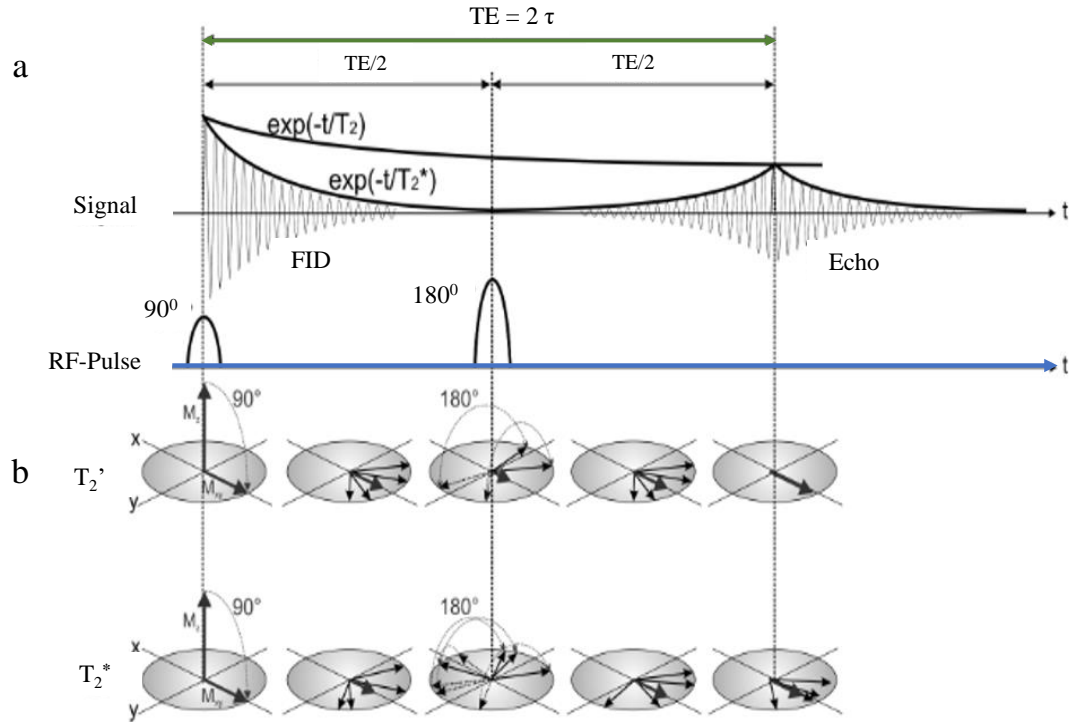
Figure 2.8: Spin echo pulse sequence in an ideal magnetic field. a) The echo signal acquired at TE = 2τ after a 90° RF pulse and 180° refocusing pulse, controlled by the exponential function for both FID and T_2 decay; b) the top part reflects the spin isochromat re-phased at TE under the effect of local magnetic field variant only and is called T_2', while the lower part is the rephased of isochromat under the effect of the additional variant of the magnetic field and is called T_2^*; the signal amplitude of T_2^* is shorter than T_2'.

(Adapted from [67])

2.2.7.2 Carr–Purcell–Meiboom–Gill (CPMG) sequence ($\mathbf{T_2^{eff}}$)

There are several pulse sequences which extend this echo refocusing further such as the Carr-Purcell (CP) and CPMG sequences. The CPMG sequence is an improvement of the CP sequence as it corrects the imperfection of the 180° pulses [65; 68]. This technique is used to measure long T_2 relaxation times by minimizing the effect of molecular self-diffusion. Additionally, it is less affected by the inhomogeneity of B_0, but is sensitive to the nuclei motion [66].

In the CPMG sequence, the 90° RF pulse is applied on the x-axis while the 180° pulses are applied on the y-axis; the sequence can be expressed as 90_x^o- $(\tau - 180_y^o - \tau)^n$. The selected time between 180° excitation pulses should be as short as the hardware system permits; this is to reduce the effect of the molecular diffusion. Generally, the CPMG sequence generates a train of spin echoes by refocusing the magnetisation continually. The first two pulses ($90^o\tau180^o$) are the same as in the spin-echo sequence and then followed by a train of refocusing 180° pulses at a specific time (Figure 2.9).

The excitation pulse (180°) is applied to produce the next spin echo but with lower peak magnetisation. The molecular self-diffusion causes a decrease in the magnitude of the echo peak signal as protons that have diffused into areas of different field strength will not be refocused. This is because of the variation in the local magnetic field of each moment over time. Consequently, only a part of the initial magnetisation percentage is recovered each time. Therefore, the decrease in the spin echo amplitude is covered by an exponential envelope. A new spin system property is described owing to this process, and it is characterised by the time constant effective T_2 ($\mathbf{T_2^{eff}}$). Thus, by tracking the height of each spin echo's as a function of delay time, T_2^{eff} can be estimated. The longer the protons are permitted to diffuse between the refocusing pulses (called the echo time), the more likely they are to have moved into a different magnetic field, and they all be not refocused. Therefore, the echo amplitude at a particular time after excitation is dependent on the echo time.
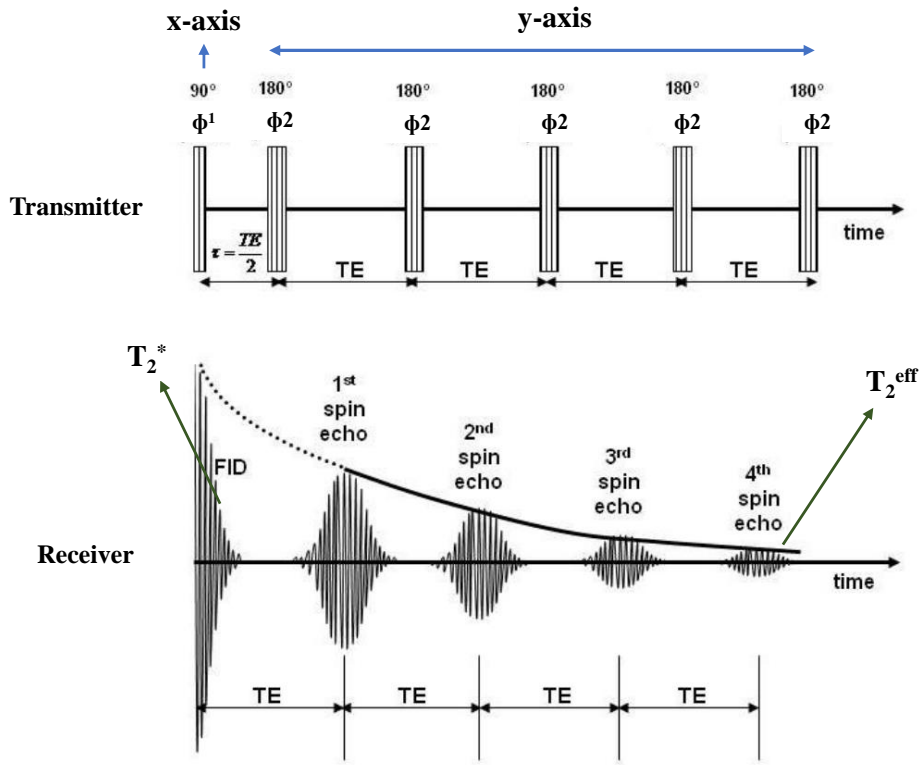
Figure 2.9: CPMG pulse sequence, 90° RF applied on the x-axis, and FID signal decay with T_2^* envelop, then a train of 108° refocusing pulses applied on the y-axis; the maximum signal value reaches TE = 2τ and generates the first spin echo, then the subsequent echoes decay under the envelope of T_2^{eff}.
(Adapted from [69])

The combination of T_2 and the inhomogeneity of the MF (T_2^*) generates an effective T_2. In an ideal MF $T_2^* = T_2$, but in an inhomogeneous MF $T_2^* < T_2$. This pulse sequence can be repeated after a while; repetition time (TR $\approx$ from $3T_1$ to $5T_1$)); this time includes the delay time and the acquisition time (TR = delay time + acquisition time). The several repeating and averaging scans improve the SNR, where the signal

is linearly proportional with the number of averaging (NA), whereas the noise is scaled with the square root of the NA; thus, the SNR relies on NA/ $\sqrt{NA}$. The more number of averages, the better the SNR. In contrast, more averages results in a longer scan time [57].

Moreover, in water molecules, the magnetisation behaviour will not follow Equation 2.19 because of the high self-diffusion. Thus, the diffusion effect on the sample can be estimated from the echo amplitude as a function of TE, while the gradient field is active during the pulse sequence [70]:

$$\mathbf{A}(TE) = \mathbf{M}_0[\exp{(\frac{-TE}{T_2})}][\exp{\frac{-\gamma^2 DG^2 TE^3}{T_2}}], \qquad (2.20)$$

here, A(TE) is the echo amplitude, G is the magnetic field gradient (G = $\frac{\partial B}{\partial Z}$), and D is the diffusion coefficient.

2.2.7.3   Measuring T_1

The actual pulse sequence designed to measure T_1 is inversion recovery or saturation recovery in a homogeneous magnetic field such as clinical MRI. The measurement consists of three periods: first, a preparation period in which one or more RF pulses are applied to invert the longitudinal magnetisation from equilibrium state + Z- direction into the - Z-direction; Second, a free recovery period to enables the spin system to relax to the equilibrium state to pass through the transverse plane; third, a detection period when the relaxed spin system is measured by rotating the longitudinal magnetisation into the x-y plane. The time between the inversion pulses is called the inversion time (TI). The duration period for the recovery times can be varied to cover a range of times for the T_1 [3].

In an inhomogeneous magnetic field, and specifically in this thesis with low-field magnetic systems, B_0 = 18 mT, it is difficult to fully invert or saturate the spin system across the entire sample. Hence, a CPMG sequence is applied to extract T_1. The signal integral is measured over a range of repetition times (TR) and fitted with an exponential function to extract the estimated T_1 value [71]. For a reliable measurement, the repetition time should be ranged from minimum value almost equal to $\frac{1}{10}$ T_1 to a maximum value (3–5)T_1, with more values at the beginning and fewer at the end [72] (Figure 2.10). Some systems used in this study adjusted the repetition time by changing the inter-experimental delay (T_{RN}), which is the time after the last acquisition to the beginning of the next excitation pulse (Figure 2.10).
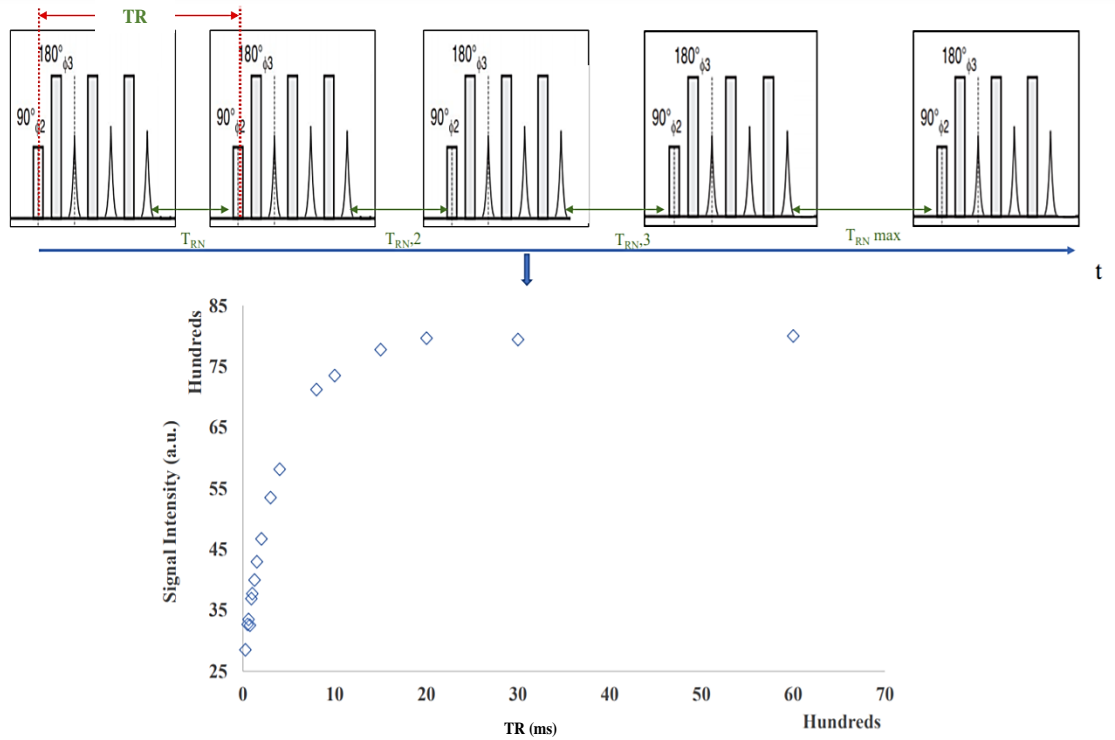
Figure 2.10: CPMG pulse sequence to estimate T_1 via a range of TR values; plot showing the collect signal intensity for each CPMG measurement as a function of TR.

2.2.8   Fourier Transform (FT)

FT is applied to the detected signal from the receiver coil to divide it into discrete frequency components, where each quantity in the frequency component is represented. This conversion occurs by using a mathematical process that converts the detected FID signal, which was produced as a time-domain function into a spectrum in the frequency-domain function (Figure 2.11).

The detected FID signal comprises the x and y components of the net magnetisation (M_x and M_y) and they are proportional to these two equations

$$\mathbf{M}_X = \mathbf{M}_0\cos(\Omega t), \tag{2.21}$$

$$\mathbf{M}_y = \mathbf{M}_0\sin(\Omega t), \tag{2.22}$$

Where Ωt is the angle of rotation vector, where Ω is the offset, and both are describing the phase (ϕ) and this signal can be expressed as a function of time as follows:
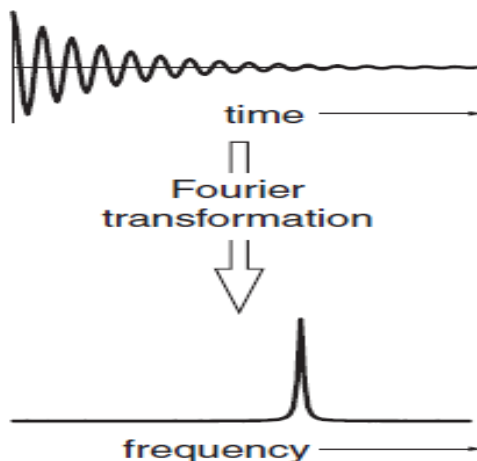
Figure 2.11: Fourier transformation of the FID signal from the time-domain to the frequency-domain.
(Adapted from [73])

$$\mathbf{S}_X(t) = \mathbf{S}_0\cos(\Omega t), \qquad (2.23)$$

$$\mathbf{S}_y(t) = \mathbf{S}_0\sin(\Omega t), \qquad (2.24)$$

where S_0 is the size of the overall signal, and it is a function of time since it is expressed as $S_x(t)$ or $S_y(t)$.

For the FT, these two components are considered as the real and imaginary parts of the complex function, similar the time domain $\mathbf{S(t)}$; where $\mathbf{S(t)} = \mathbf{S}_y(t) + i\ \mathbf{S}_y(t)$. Thus, by substitution in Equations 2.23 and 2.24, the S(t) can be expressed as

$\mathbf{S}(t) = \mathbf{S}_0\ \cos(\Omega\ t) + i\ \mathbf{S}_0\ \sin(\Omega\ t),$

$$\mathbf{S}(t) = \mathbf{S}_0\exp{(i\Omega t)}, \qquad (2.25)$$

As mentioned earlier, $\mathbf{M}_{Xy}$ decays exponentially over time; thus, the equation can be expressed as follows

$$\mathbf{S}(t) = \mathbf{S}_0\exp{(i\Omega t)}\exp{\frac{-t}{T_2}}, \qquad (2.26)$$

In the frequency domain, the real and imaginary parts are a spectrum; the real part is called the absorption mode, and the imaginary is called the dispersion. The absorption mode is always positive while the dispersion has both positive and negative values (Figure 2.12).

Only by integrating the area under the line in the absorption spectrum, can the relative
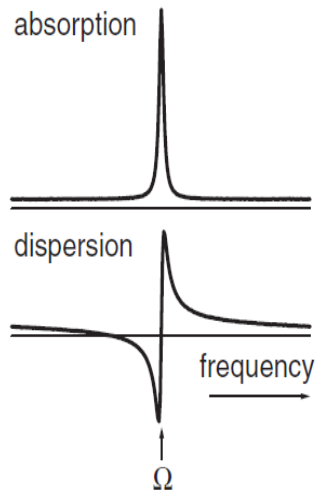
Figure 2.12: Spectrum line shape showing the absorption and dispersion modes for the real and imaginary parts.
(adapted from [73])

number of protons be determined. Thus, it is a direct relationship between the size of the signal in the time domain (S_0) and the peak height of the spectrum [73].

Therefore, to efficiently compute the entire signal, the number of points in the signal series should be in the order of $N = 2^n$, where n is a small integer. Moreover, to represent the received signal correctly, the spectrum should be digitised properly by the spectrometer, and the sampling rate should be twice the highest frequency of the received signal based on the Nyquist theorem condition [74] or sampling theorem. Frequently, quadrature detection is used in the NMR spectrometer, enabling sampling at the same rate as the highest frequency. For instance, if the received signal is under sampled, the spectrum will no more represent the position of the frequency peaks correctly and cause aliasing [75].

2.3   Literature review

This section is devoted to reviewing two topics: the significant development in the unilateral magnet designs utilised in a wide range of applications, specifically in the medical field, and the placental relaxation time to generate reference values to evaluate the constructed system presented in this thesis.

2.3.1   Unilateral low field magnet system

As mentioned in the introduction chapter, there are two types of unilateral magnet designs: high gradient and sweet-spot magnets. When designing the magnet, the type of the required information is essential; this is because each design has its strength and weakness. Therefore, several magnet designs had been reported over the past years in various fields, and according to their geometry, they were classified into U-shape, bar, and barrel magnets. Additionally, the categorization into gradient or sweet-spot magnets depends on the direction of the B_0 to the surface of the magnet or field line shape [76]. Therefore, reviewing the high gradient magnet designs aids in illustrating the project perspective, although the system developed in this project utilised the sweet-spot type.

2.3.1.1   High Gradient magnet design - NMR-MoUSE

The portable NMR-MoUSE was investigated in the medical field several years ago because of the advances in permanent magnet technology and lower installation/maintenance cost. The U-shape geometry is a conventional design and is composed of two block magnets with anti-parallel polarisations placed on an iron yoke, and the static field is parallel to its surface and enables the combination of the sample and surface RF coil [16]. The early version of the NMR-MoUSE provides a 1 mm depth resolution with maximum depth penetration of 5 mm [13]. The poor resolution for this early version is caused by the high variation in the static magnetic field (ΔB). Thus, efforts have been made to improve the uniformity of the static gradient (G_0) to reduce ΔB along the lateral direction by modifying the magnet geometry. Additionally, to minimise the variation at the depth resolution, the ratio ($\frac{\Delta B}{G_0}$) should be optimised without affecting the inherent sensitivity measurement by limiting the minimum value of the MF strength to 0.1 T [77].

Evolution occurred with the profile NMR-MoUSE, constructed in 2005 by Perlo et al. [16], who presented a new geometry of a U-shaped NMR sensor with a maximum depth profile of 10 mm and spatial resolution better than 5 μm by re-positioning the sensor with respect to the sample. It consisted of four permanent magnet blocks positioned on an iron yoke. Magnets with the same polarisation were separated by a small gap d_s (2 mm), while magnets with the opposite polarisation were separated by a gap d_B

(14 mm) that produced an MF of $B_0 = 0.4$ T at a depth of 10 mm with $G_0 = 20$ T/m. Figure 2.13b shows the schematic diagram for this sensor. In addition, they could reach a depth of 18 mm by maintaining the same magnet size and increasing the gaps, and keeping their proportions fixed ($d_S = 3$ mm, $d_B = 30$ mm), thereby achieving an MF of $B_0 = 0.25$ T with static gradient 11.1 T/m. This sensor was placed on a lift to position the thin sensitive volume inside the object. The system was equipped with a low inductance surface RF coil to avoid re-tuning when changing the loading during the scan. The slice thickness ranged from a few μm to 100 μm.

<div align="center">

(a)   (b)

</div>
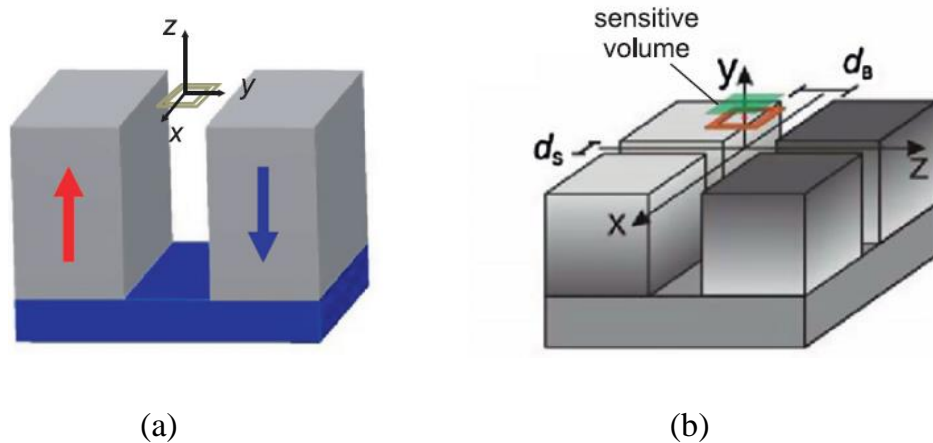
Figure 2.13: Schematic diagram for the NMR MoUSE. a) An early version of the U-shape NMR MoUSE; b) Profile NMR MoUSE.
(Adapted from [77])

Therefore, a few studies focused on the pathologies of near-surface tissue, which is a few millimetres under the skin, such as tendons and skin [78]. Moreover, the U-shaped NMR-MoUSE was observed to be a useful follow-up system, particularly for patients whose region of interest is known. As an example, for breast cancer, which is a common cancer type affecting women worldwide, follow-up is vital after operation or radiation therapy. In addition, the integrity of cancer was observed to be assessed faster after contrast agent injection to enhance the SNR [3].

A 2005 study [21] measured the T_1 relaxation after administering a contrast agent to explore the skin and subcutaneous fatty tissue using NMR-MoUSE. They observed that malignant tissue has a faster signal recovery than scar or healthy tissue does. Hence, the changes in the relaxation time can be differentiated between the skin structures. However, they admitted that before clinical application, more cases were required as their study was only performed on three patients.

Moreover, recent studies that employed the profile NMR-MoUSE in medicine were conducted, such as the 2015 study of articular cartilage diseases such as osteoarthritis [23] to monitor a flat sensitive volume aligned horizontally in human joints. The joint degeneration caused by early-stage osteoarthritis can be diagnosed since the relaxation

times and diffusion coefficients are expected to deviate significantly from that of healthy tissue. Additionally, two studies were conducted ex-vivo on mammographic density in 2018 [24] and in 2019 [27] to measure T_1 and T_2 using NMR-MoUSE PM5, respectively. This is because the mammography density is considered a risk factor for breast cancer and a source of masking in the X-ray examination. In the T_2 based study, tissue composition, fat, and water were quantified, and in T_1 based study, high and low breast densities were distinguished. For both studies, this was a promising approach for in-vivo clinical applications.

2.3.1.2 Sweet-spot magnet design

The sweet-spot was defined by Pulyer and Perlo J. [79; 80] as a point in a space at which at least all the first-order derivatives of the constant gradient field magnitude are zero. This approach was developed to compensate for the low-field associated with reducing the G_0 effect, thereby, resulting in an increase in the size of the excited sensitive volume (V_s). Thus, the sensitivity of the NMR signal will be maximised, where the product of $V_s B_0^2$ defines the sensitivity of the magnet. This technique narrows the variation in the resonance frequencies among the spins inside the object, resulting in a large excited volume for a fixed excitation bandwidth and an increase in the interrogated depth. Therefore, the numbers of polarised spins in the sensitive volume depend on the gradient strength and excited bandwidth of the RF pulse [77; 80].

The magnet geometry that achieves this gradient cancellation combines two units of anti-polarised magnets blocks and different magnet sizes. As a rule of thumb, the condition to generate a sweet spot for the planar magnet depends on the distance ratio between the two magnet blocks (a) and the magnet height (h), and it should be higher than one ($\frac{a}{h} > 1$). For the barrel magnet type, the magnet height should be larger than the diameter, and the depth of sweet spot depends on the inner diameter [5; 79; 80]. Figure 2.14 depicts these two types of magnet geometry.
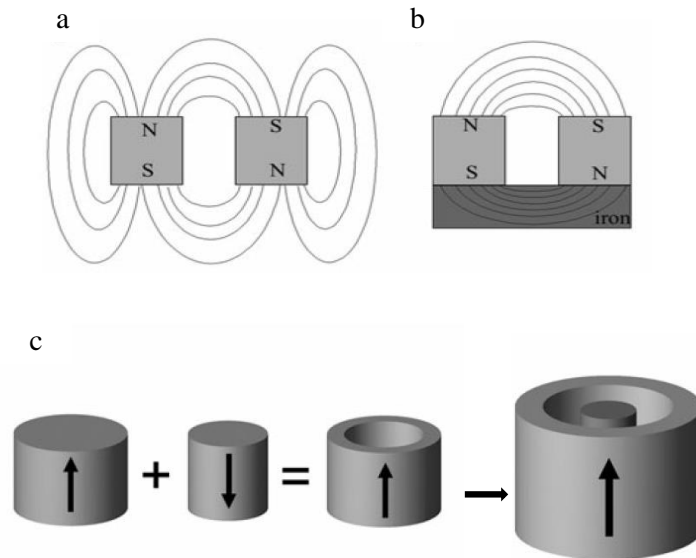
Figure 2.14: Two geometries for sweet spot magnets. a) Two blocks of anti-polarised magnet blocks without an iron yoke, b) U-shape magnet is similar to the NMR-MoUSE, and it has an iron yoke to direct the filed lines, and c) barrel magnet, where the arrows on the cylinders indicate the direction of magnetisation.
(Adapted from [3])

The two magnets described in Figure 2.14 do not differ only in the geometry but also in the direction of the B_0 field. In U-shape geometry, the field is parallel to the sensor surface, while in the barrel magnet, the field is perpendicular to the surface. Thus, they have to pair with a different type of RF coil to create a B_1 field $\perp$ to B_0. For the first geometry, a simple loop current surface coil is sufficient to provide an NMR signal from the sensitive volume, whereas for the second geometry, a relatively complex surface coil is required, such as a figure-eight surface coil. Figure 2.15 shows these two types of the surface RF coils. The common characteristic for both coil designs is that the coil size should be greater than the sensitive volume, which can be determined by 3D spatial variation measurement of the B_0 field [3].
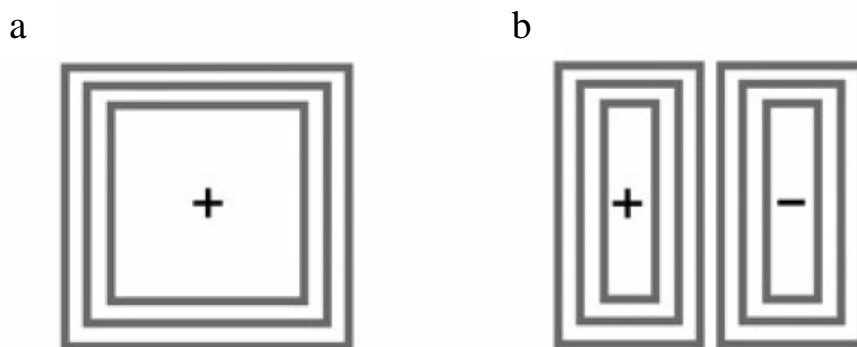
Figure 2.15: Surface RF coils. a) Single current loop RF coil produces a B_1 field perpendicular to the coil surface; b) Figure-eight coil produces a B_1 field parallel to the coil surface.
(Adapted from [3])

For both types of coils, the SNR decreases as a function of the depth. The SNR degenerates with the inverse square for the depth. A larger depth requires a larger coil as a larger number of turns are required to maintain the inductance. Moreover, the sensitivity for a single current loop is higher than that of the figure-eight coil by a factor of 2 [2; 3].

A new version of the barrel magnet, called MObile Lateral Explorer (MOLE) and operating at 3.3 MHz, was introduced by Manz et al. [28], for which the homogeneous field is 76.7 mT at 15 mm away from the surface. The device diameter is 200 mm and consist of eight discrete barrel magnet spaced uniformly inclined at an angle of 11.5^o with a central magnet positioned to provide a uniform region (Figure 2.16). The sweet-spot can be adjusted by tilting the angle of the bar magnets. They achieved a field uniformity of 15,000 ppm over a range between 4 to 16 mm from the device surface, with maximum sensitivity at a depth of 10 mm. This system was coupled with a figure-eight surface coil to transmit and detect the NMR signal.

a   b
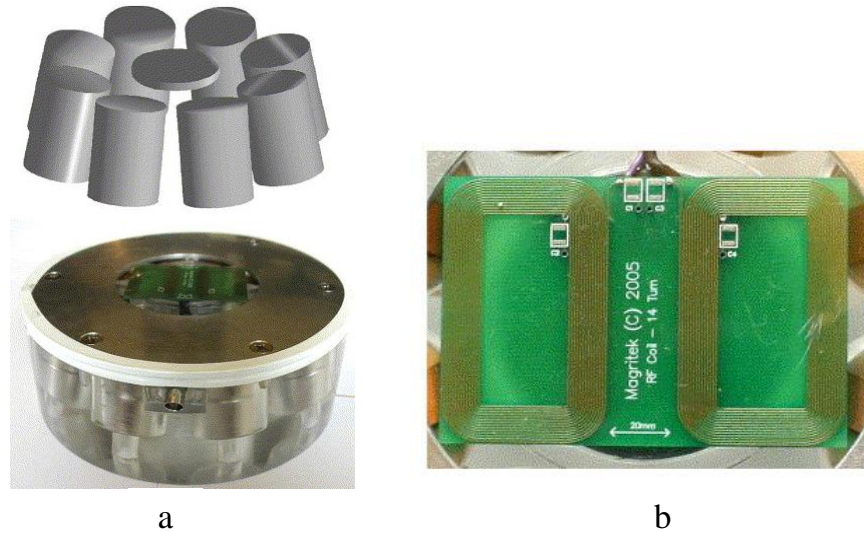
Figure 2.16: NMR-MOLE, a)top figure is a schematic diagram for the 8 bar magnet with a magnet in the central axis, while the bottom figure is the entire assembly for the magnets array and the surface coil; b) a printed circuit board (PCB) figure-eight coil, composed of two-loop with 14 turns and separated by 12 mm.
(Adapted from [28])

As previously mentioned, one of the advantages of using sweet-spot magnets is the studying of liquids and biological tissues because of the lower diffusion attenuation. A 2018 study by Barbieri et al. [26] utilised the unilateral NMR to diagnose osteoporosis. The NMR experiment was performed by employing two types of instruments, namely NMR MoUSE PM10 as a constant MF gradient and NMR mobile lateral explorer (MOLE) to present the sweet-spot because of the homogeneous field. NMR-MOLE was used to perform the diffusion-weighted (DW) T_1 - T_2 (DW -T_1-T_2) experiments, because of the higher SNR and larger sensitive volume compared with NMR MoUSE. The sensitive volume was 26 mm x 26 mm x 6 mm for NMR-MOLE and 16 mm x 16

mm x 0.330 mm for NMR MoUSE PM10.

In 2006, Perlo et al. [81] proposed a high uniformity U-shape magnet design up to 8 ppm using the shimming approach. The design was composed of two anti-polarised magnet blocks positioned on an iron yoke and separated by a gap. The difference was that the field homogeneity was controlled via shimming units. These small magnets bar were positioned in the gap between the two main blocks, but with opposite magnetisation directions to the main magnets (Figure 2.17a). This approach assists in matching the spatial B_0 variation with the B_1 field and reduces the strength of the G_0. The system was paired with a single rectangular loop RF coil and weighted 36 Kg. The chemical shift was observed when the system was operated at a magnetic field close to the sensor surface, which was equal to 0.25 T with a gradient field of approximately 0.4 T/m.

The previous configuration was criticised in 2007 by Marble et al. [18], as it requires large magnet arrays relative to the sensitive volume to enable the vertical field lines over the magnet to reorient themselves horizontally in the sweet-spot. In addition, zeroing the second spatial derivative of the B_0 results in a negative effect on field strength and array size. In contrast, Marble et al. proposed a different geometry composed of three magnets, two axially magnetised with a shim bar in between and having a similar magnetisation direction (Figure 2.17b). This configuration generated a B_0 parallel to the surface with a sweet-spot at 10 mm from the sensor, and the magnetic field strength was 0.11 T. It enabled a simple loop RF coil to be employed; thus, sensitivity is increased dramatically compared with designs paired with special surface coils. Their system measurements were 100 mm x 115 mm x 6 mm, weighting 5 Kg.
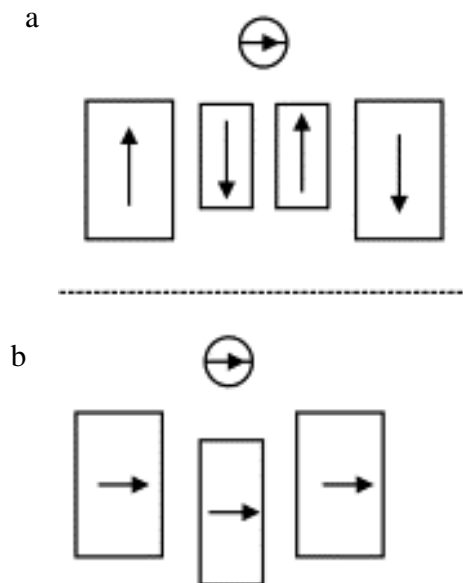
Figure 2.17: Schematic diagram for the magnet designs of a) Perlo et al. and b) Marble et al. (Adapted from [18])

In 2007, Perlo et al. [31] improved the magnet design of 2006 to be very highly homogeneous and reached up to 0.25 ppm at an MF of 0.2 T situated 5 mm from the RF coil surface. This improvement was achieved using eight shim components placed in the gap (Figure 2.18a). The main magnet bar had a dimension of 280 mm x 280 mm x120 mm, and the surface RF coil had an outer diameter of 7 mm. The sensitive volume size was 5 mm x 5 mm x 0.5 mm. Such a high homogeneous field enabled Perlo et al. to clearly realise the chemical shift, such as in water/crude oil mixtures. This design of Perlo et al. was adopted in the medical field in 2011 by Van et al. [22] to profile human skin. The adoption was with a slight modification to the inner edge of the main magnet unit, along with movables shim units (Figure 2.18b). This is because most of the skin layer exists within the first 2 mm from the body surface and is composed of wavy interfaces between layers. Thus, the profile NMR-MoUSE with a resolution better than 20-30 μm would not reveal the fine structural detail for the skin layers due to the high gradient, which would result in a flat sensitive volume of few hundreds of μm. For skin profiling, a sensitives volume of size 2 mm was required, and this was achieved by using a sensor with a low gradient, which is sufficient to excite the interesting area with acceptable uniformity at the required depth. Therefore, with the modification of the design by Perlo et al. a resolution of 25 μm at the central region from 0.5 to 1.5 mm up to 50 μm at the border was obtained with a G_0 of 2 T/m. The application of in-vivo NMR-MoUSE for humans is promising for skin pathology, skincare, and diagnosis at tissue depth ranging from 10 to 15 mm.
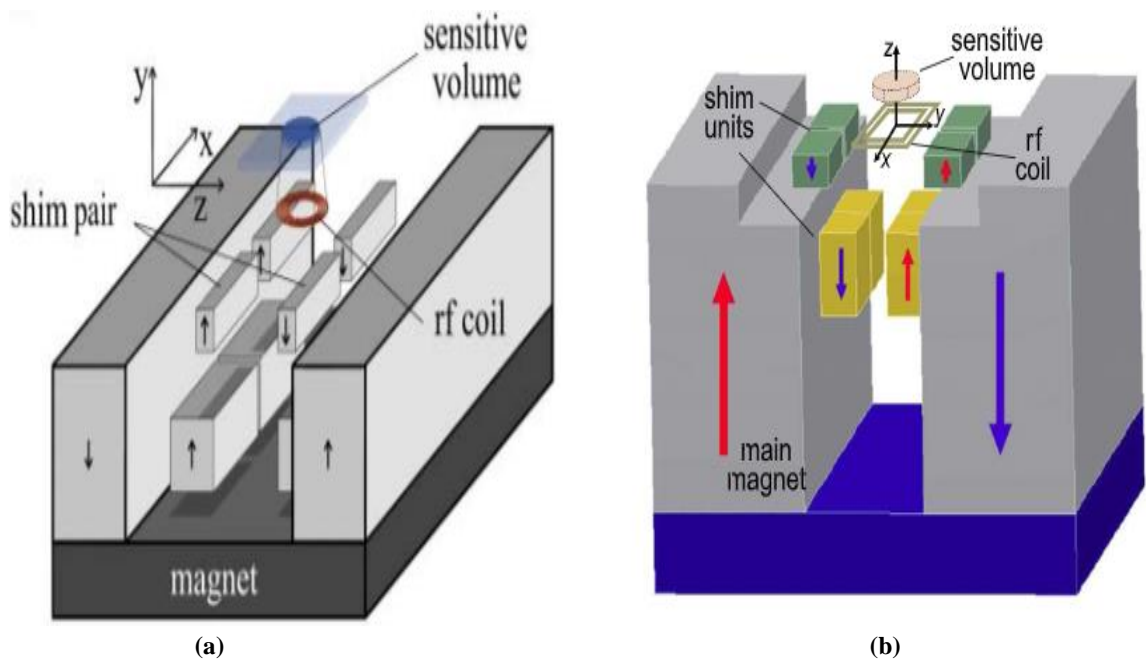
Figure 2.18: Schematic diagram for a) Perlo et al's. highly homogeneous magnet design and b) Van et al's. magnet design to profile human skin.
(Adapted from [22; 31])

In 2002, Pulyer et al. [79] proposed a planar or unilateral magnet design, in which the magnet source was placed to one side, providing more open access. This was because the target region was not enclosed by the magnet source and could relatively efficiently generate remote saddle points in the field profile. A paper in 2014 by Dabaghyan et al. [5] adopted the Pulyer et al. principle [79]. They demonstrated a prototype system applying the design of remote NMR measurement for bedside pulmonary density measurement; they used a low-field unilateral magnet design to measure the NMR signal from the lung, a notoriously challenging tissue to MRI, with a target volume of the order of 30 cm^3. Their system was similar to the NMR-MoUSE concept, where the B_0 is parallel to the surface of the magnet. Magnet geometry was constructed from two equal and opposite antiparallel dipole rectangular arrays composed of 240 small NdFeB magnets. The distance between the inside array end edges was approximately 300 mm. The saddle point was generated at approximately 80 mm above the magnet surface. Figure 2.19a shows the geometrical configuration of the Dabaghyan et al. permanent magnet system, and Figure 2.19b shows the system prototype. The field strength at the sweet-spot was 8.8 mT (it was more than an order of magnitude smaller than the 0.25 T and above of the profile NMR-MoUSE family). This was achieved using a short solenoid coil of height and radius 50 mm in the centre between the magnet arrays. To solve the problem of low MF and the sensor sensitivity (SNR $\approx B_0^{7/4}$), they selected a target volume larger than the imaging voxel size in a 1.5 T clinical scanner.

(a)   (b)
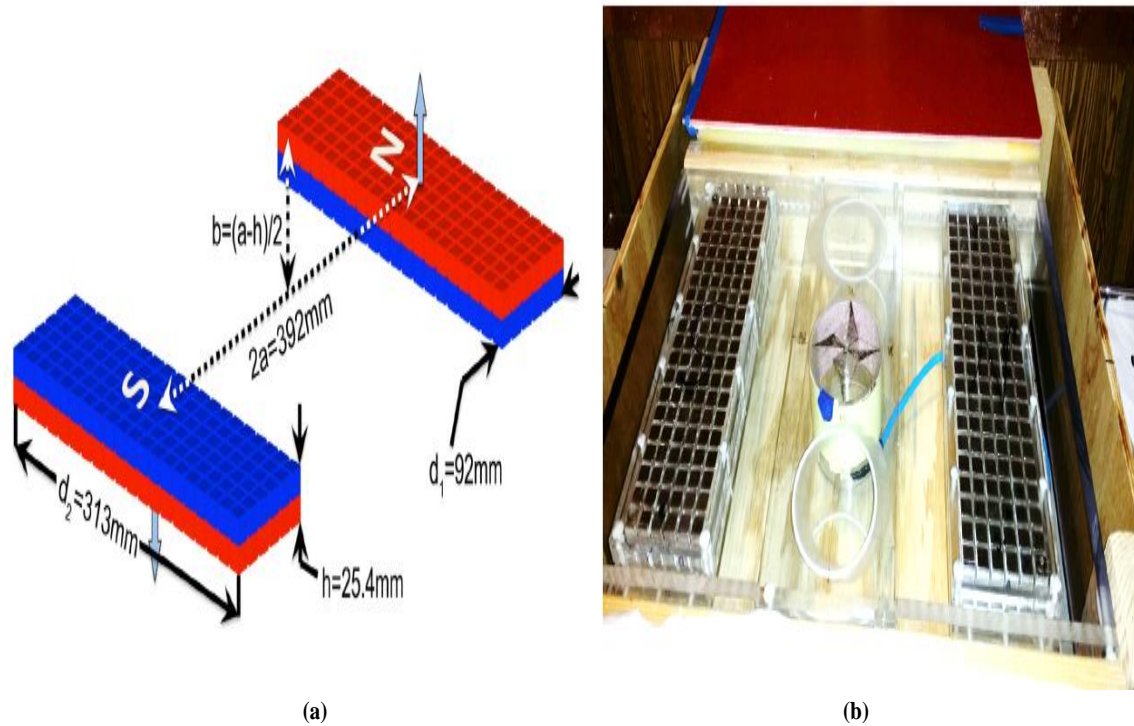
Figure 2.19: a) Geometrical configuration of the anti-parallel permanent magnet system; the arrows indicate the field direction at each magnet face, the distance between the centres of the two magnet assembly is 2a, and the field uniformity region is located at distance b above the magnet surface. b) Prototype of MRI lung-density monitor.

In 2019, two studies were published on the potential application of the unilateral MRI sensor for medical diagnosis. The first study was conducted by McDaniel et al. [82], in which they developed a lightweight MR cap (8.3 kg) for 3D brain imaging to monitor patients at the point-of-care (Figure 2.20a). Their prototype was operated at 64 mT over an average FOV of 30 mm x 80 mm x 80 mm for a sensitive volume at a depth of 30 mm beneath the scalp. The device was composed of 37 blocks of permanent magnets arranged in the 3D printed acrylic former in a cap shape that fit an adult head. The cap also included a build-in gradient for slice selection and an external pair of gradient coils for phase encoding located outside the magnet assembly. In addition, the RF coil for transmitting and receiving the signal was located inside the magnet (Figure 2.20b). The system depth profiles for the phantom study obtained a high resolution of 0.89 mm, and the multi-slice images were acquired with a resolution of 2 mm in-plane and 6 mm slice thickness for a total experimental time of 11 minutes. However, McDaniel et al. acknowledged the truncation boundary and image artifacts due to the inhomogeneous B_0 map that resulted in a reduction in the size of the region of interest. They conducted all experiments in a shielded environment using laboratory-grade instruments for RF amplifiers that cost \$15,000 and a console that cost of \$35,000. In contrast,the MR cap with a T/R switch and gradient power amplifier/pre-amplifier was cost-effective and highly compact.
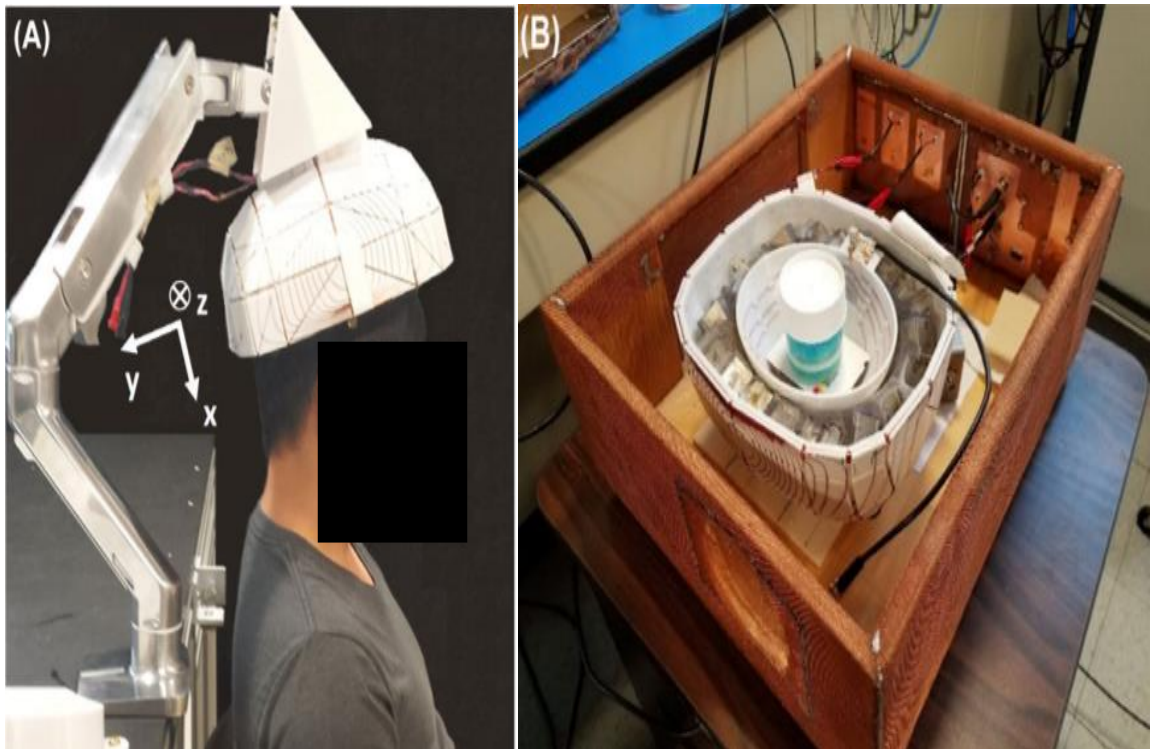
Figure 2.20: Photographs for a) Drawing for the concept of the 'MR cap' showing the possible position and movement of the system around the head. b) Shielded box containing the prototype system with a tested phantom at the centre of the RF coil.

Greer et al. [34] had proposed a hand-held portable unilateral MRI sensor with potential applications in various fields such as medicine. The sensor was contained in 3D printed housing and PCB manufactured to include all other components such as the RF coil, gradients, and matching network (Figure 2.21). The sensor was composed of five permanent magnets and three copper shields. To optimise the SNR and field uniformity, they swept the positions of the main magnets at the top and along the y and z directions. The optimal geometry was at a z-separation of 45.7 mm and y-separation of 5.4 mm. The RF coil was composed of three turns, with an inner diameter of 9 mm and an outer diameter of 13.1 mm. Their FOV was approximately equal to the size of the RF coil inner diameter, and the sensitive profile was at depth ranged from 4 to 8 mm. The depth of investigation was at 6 mm at an MF of 0.186 T with a G_0 strength of 2.2 T/m. The experimental time to acquire the images for 3D phantom was 108 minutes with a resolution of 0.33 mm over a FOV of 9 mm x 9 mm for ten images per scan. Hence, they suggested that the experimental time could be reduced by reducing the resolution.
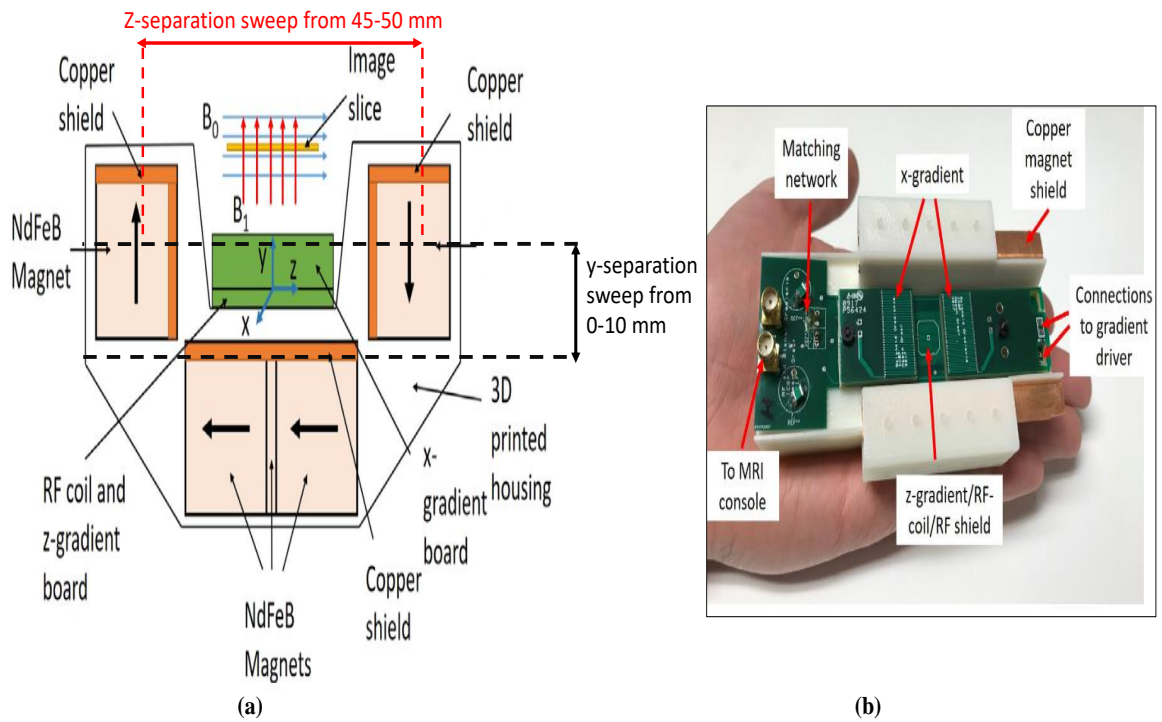
Figure 2.21: a) Schematic diagram of the proposed hand-held sensor, indicating all components. b) The complete assembly for the hand-held MRI sensor.

In this project, the objective is to probe the placental tissue, located several centimetres in-depth within the mother's uterus. According to Victoria et al. [83], the average thickness for anterior healthy placenta is 25 mm using the ultrasound and 29 mm using MRI, and it is > 80 mm for the posterior placenta. Therefore, the constructed unilateral magnet should provide a sufficient depth of investigation to reach the position of the placenta.

Among the reviewed unilateral prototypes in this section, the model by Dabaghyan et al. [5] was with some modifications selected to satisfy the project objectives. Dabaghyan et al. proposed a system characterised by an open-access, low-MF system, portable, and unnecessary RF shield room. There is no use of gradient coils and their associated power supplies, which result in a relaxation measurement approach in which the measurement of spins from the localised region is acquired. Overall, these features produce an inexpensive device because image construction is not used.

2.3.2   Placenta

The placenta is a temporary foetal organ that functions as an interface for maternofoetal exchange between the mother and embryo. This organ evolves from the fertilized egg shortly after implantation and is composed of the foetal tissue (chorion) and maternal tissue (decidua basalis), the inner layer of the uterus, and is shed during delivery. The placenta connects to the foetus via the umbilical cord, and on the other side to the maternal uterus [84; 85].

The development of a healthy foetus strongly depends on the adequate function of the placental. Thereby, the process of placenta development involves a precise and tight remodelling of the maternal spiral arteries in the uterine wall to provide the developing placenta with sufficient maternal blood [85]. The placental tissue is primarily formed from the foetal trophoblast, an embryonic stem cells representing the outer layer of the fertilized ovum (blastocyst), and it develops into a large part of the placenta, including chorionic villi. Villi are finger-like structures that are metabolically active tissue producing hormones, absorbing nutrients, gas exchange, and eliminating unwanted waste [41; 85].

Trophoblasts are divides into two layers: the underlying layer called the cytotrophoblast (proliferative stemlike cells) and the overlying layer known as syncytiotrophoblast, a multinucleated cell layer that covers the placenta surface resulting from the differentiation and fusion of the cytotrophoblast cells. Syncytiotrophoblast covers the villi, completely lines the intervillous space, and becomes in direct contact with the maternal blood and anchors into the decidua [85].

The extravillous trophoblast develops an invasive cell (endovascular trophoblast) which drills into the maternal decidua tissue and uterine wall to replace the maternal endothelial cell and change the characteristics of the blood vessels. Subsequently, spiral arteries in the decidua are remodelled to becomes wider and less resistant, facilitating increased blood flow to the intervillous space to ensure sufficient supply for the foetus during the pregnancy period [85].

In compromised pregnancies, abnormal cytotrophoblast differentiation and extravillous trophoblast invasion of the maternal decidua occurr early in the first trimester. The trophoblast is more proliferative and less invasive, and these events result in a comparatively week invasion of uterine spiral arteries, causing an increase in uteroplacental resistance and the release of placental material into the maternal circulation [37; 84].

A common maternal complication from abnormal placentation is PE; moreover, common foetal complications are FGR, preterm delivery, and perinatal death [36]. Hence, understanding the placental structure is important. Figure 2.22 shows the difference between healthy and PE placentas. The poor invasion may result in early PE associated with FGR or pure FGR. Moreover, a *stereological*[1] study indicated differences between PE and FGR in placental morphology, primarily at the villous membrane, related to diffusive conductance, which reduced in the FGR group (both pure and associated) compared with the pure PE and normal group [86]. Furthermore, cellular senescence, the gradual deterioration of function characteristic of most complex life forms, is accelerated in both diseases because of placental oxidative and endoplasmic *reticulum*[2] stress. Moreover, differential DNA methylation analysis has shown that late PE does not accelerate ageing, but early onset PE does do [39].
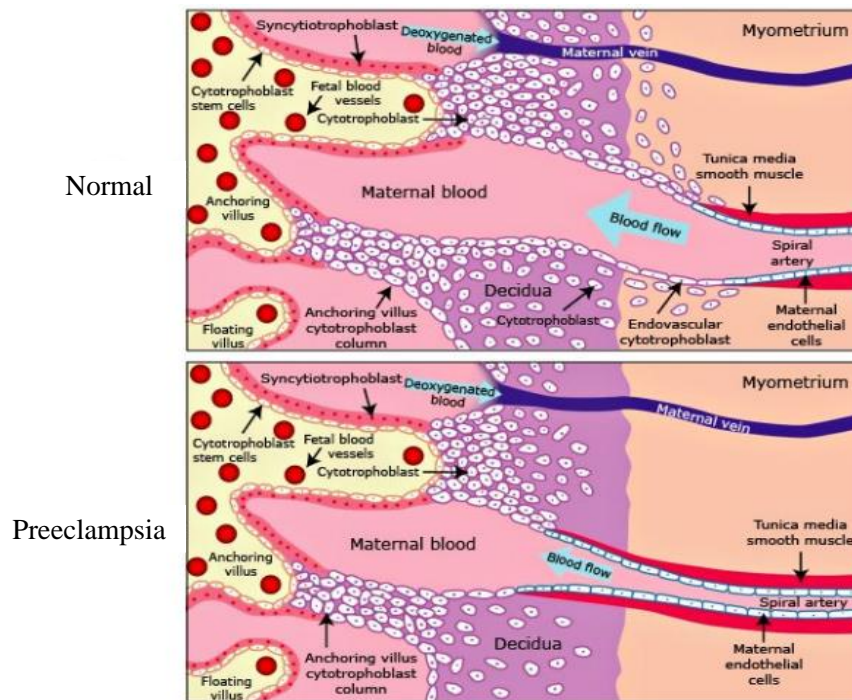
Figure 2.22: Placentation. Normal placentation shows in the top image, showing foetal cytotrophoblasts invade the maternal decidua and transform the spiral artery from low to a high capacitance vessel to provide adequate placental perfusion for the growing foetus. The image below illustrates the preeclamptic placenta; the cytotrophoblast fails to invade the decidua, and the spiral artery remains with a small capacitance.
(Adapted from [88])

---

[1]Applied to randomly generate thin sections, facilitating minimally biased and economical quantitation of the three-dimensional [3D] structure of the placenta from molecular to whole-organ levels [86].

[2]A multifunctional organelle required for lipid biosynthesis, calcium storage and protein folding and processing [87].

2.3.2.1   Preeclampsia (PE)

Clinically, PE manifestation begins after the 20th week of gestation and may result in morbidity and mortality for both the mother and neonate [37; 38]. In severe PE cases, women develop HELLP syndrome (*haemolysis*[1], elevated liver function enzymes, low platelets density), eclampsia, and other end-organ damages [37]. Several studies have been conducted to understand the evolution pathophysiological and morphological of the PE disorder (e.g. stereological placenta analysis) [37; 38; 84; 89]. However, the causative factor for this disorder is not yet known. Stereological analysis has revealed that pure PE has a limited effect on the placenta morphological structure, vascular development, and total volumes. In contrast, it affects the intervillous space and terminal villi volume compared with healthy groups [84; 89]. First-trimester metabolic detection results have shown that early and late PE are different disorders, as ranked by variable important in projection (VIP) analysis [90]. A clear separation between early and late PE stages is essential for understanding the progression of this disease; hence, researchers have suggested that early PE is < 34 weeks and commonly associated with FGR, while late PE is ≥ 34 weeks and associated with moderate maternofoetal complication. Thus the outcome from late-onset PE is more favourable [43; 89; 91].

2.3.2.2   Foetal Growth Restriction (FGR)

FGR is a failure of the foetus to reach the determined potential of genetic growth. This potential complication is clinically suspected if an estimation of foetal weight, size, or symmetry during the routine sonography has abnormal results [92]. It affects up to 10% of pregnancies, and there are several causes, including foetal, maternal, environmental, and placental factors. This foetal condition is less common, and up to 40% of the cases occur due to mothers suffering from PE or gestational hypertension (GH) [41]. The stereological analysis for pure FGR or FGR with PE has shown that the total diffusive conductance is lower than controls or pure PE cases; this is due to the decrease in the total volumes and surfaces of trophoblast in peripheral villi, causing uteroplacental hypoxia [86].

---

[1]Destruction of red blood cells by the rupture of the cell envelope and release of the contained haemoglobin.

2.3.2.3   Placenta thickness

Placental thickness is considered an additional indicator of a healthy pregnancy. A thick placenta is associated with increased perinatal mortality and morbidity, as well a higher incidence of either large or SGA babies at term 40. Thick placentas have been observed in perinatal infections, maternal diabetes, and maternal anaemia, while thin placentas have been observed in FGR, PE, foetal infection, and chromosomal abnormalities [93].

In 1994–1998, 17254 pregnant women underwent ultrasound screening for severe thalassemia [94]. The screening was performed at mid-pregnancy, from 18 to 21 gestational weeks, and the placental thickness was measured and recorded. The values of normal placenta for 18, 19, 20 and 21 gestational weeks were 24.1 ± 0.45, 24.2 ± 0.54, 25 ± 0.55 and 25.2 ± 0.6 millimetres (mm), respectively, while the suggested cut-off thickness for abnormal placenta was above 3 cm. Furthermore, a study performed in 2000 included 561 singleton pregnant patients screened in 1996–1998 [95]; the results indicated that the criteria for diagnosing thick placenta using 40 mm as a cut-off might may indicate normal placentas as abnormal if the gestational age group is not defined. Moreover, the researchers claimed that the 90th percentile from each group could be used as a cut-off. They used a cut-off for the second trimester (20–22 weeks) of 35 mm and the third trimester (32–34 weeks) of 51 mm.

In 2004, a clinical ultrasound study was conducted on 333 normal pregnant women in the first half of pregnancy between 8 and 20 weeks of gestation [96]. The data indicated that the placental thickness was directly related to gestational age; using linear regression modelling, the following equation was obtained: placental thickness (in mm) = gestational age (in weeks) × 1.4–5.6 (r = 0.82); Table 2.1 listed these values.

Table 2.1: Measurements of placenta thickness in normal pregnancy by Tongson et at.in 2004.

Weeks	Cases	Mean $\pm$ SD (mm)
8	9	5.9 ± 2.1
9	23	6.4 ± 2.3
10	28	8.4 ± 2.5
11	24	9.2 ± 3.0
12	37	11.2 ± 3.1
13	29	14.2 ± 2.5
14	35	15.5 ± 2.7
15	36	17.0 ± 3.6
16	28	17.8 ± 3.8
17	28	18.4 ± 3.8
18	18	20.5 ± 3.3
19	27	20.3 ± 4.0
20	11	21.8 ± 3.3

In 2011 [83], an evaluation for the thickness of a normal placenta was conducted using clinical MRI for 53 patients in the second trimester and seven patients in the third trimester, and the data were correlated with ultrasound measurement. These values are presented in Table 2.2. Moreover, the researchers reported that a placental thickness above 4 cm is considered abnormal.

Table 2.2: Normal placenta measurements using MRI and ultrasound in the second and third pregnancy trimesters by Victoria et al. in 2011.

Modality	Overall thickness(mean) mm	2nd trimester(22 ± 2) weeks	3rd trimester(31 ± 3) weeks
Ultrasound	10–40 (25 ± 0.05)	13–37(24 ± 0.05)	21–34 (29 ± 0.04)
MRI	17–59 (29 ± 0.08)	17–59$(28 \pm 0.08$)	24–40(33 ± 0.06)

Another study was conducted in 2012 on the placental thickness in the second trimester (18–22 gestational weeks $\pm$ 6 days), for the posterior and anterior placenta. This study included 114 cases, 57 for each group [97]. The measurements for each case and overall values are listed in Table 2.3.

Table 2.3: Measurement of normal placenta thickness for posterior and anterior cases by Lee et al. in 2012.

Week + days	Anterior (mean±SD)mm	Posterior (mean±SD)mm	Overall (mean±SD) mm
18 +6	18.2 $\pm$ 6.34	26.7 $\pm$ 7.64	23.9 $\pm$ 8.04
19 +6	20.2 $\pm$ 6.44	27.1 $\pm$ 7.00	23.8 $\pm$ 7.52
20 +6	21.1 $\pm$ 4.89	28.8 $\pm$ 5.54	24.6 $\pm$ 6.35
21 +6	23.6 $\pm$ 4.54	27.3 $\pm$ 5.44	25.3 $\pm$ 5.17
22 +6	20.3 $\pm$ 9.37	33.7 $\pm$ 14.49	28.0 $\pm$ 13.62
Average	21.7 $\pm$ 5.73	28 $\pm$ 7.12	24.6 $\pm$ 7.29

A further study was conducted in 2013 [98] using ultrasound to investigate the correlation of placenta thickness to gestational age in normal and FGR placentas at the umbilical cord insertion in the late 2nd and 3rd trimester. A total of 498 patients were investigated, and the finding was divided into two groups: group A (foetal weight < 2.5 kg, n = 122) and group B (fetal weight $\geq$ 2.5 kg, n= 376). Placenta thickness indicated statistical significance (p-value > 0.05) for group A between weeks 26–27 and 30–31 compared with group B (Table 2.4).

Table 2.4: Placenta thickness in normal and FGR cases by Mathai et al. in 2013

Gestational age(weeks)	Cases	Normal (mean ±SD)mm	Cases	FGR(mean ±SD) mm
26–27	4	30.4 ± 0.03	2	24.8 ± 0.01
30–31	11	31.3 ± 0.02	7	27.6 ± 0.05

Another study in 2015 [99] was performed in the first trimester to analyse placenta volume in pregnant with PE. Pregnant women between 11 and 14 weeks were included, and 84 cases with PE versus 904 that were normal were presented. They observed that the placenta volume of PE patients was lower than the normal ones. Table 2.5 shows these differences between normal and PE (early onset + late onset).

Table 2.5: Placenta volume in normal and PE cases, 1st trimester by Plasencia et al. in 2015

Gestational age(weeks)	Cases	Normal (mean ±SD)cm³	Cases	PE(mean ±SD)cm³
11–14	904	63.62 ± 20.74	84	50.49 ± 21.35

A study in 2018 investigated the relationship between the placental thickness and gestational age of the foetus in normal pregnancy in the second and third trimesters [93]. The study was performed on 100 pregnant women. Table 2.4 shows the mean placental thickness in relation to the gestational age in weeks. The study concluded that placenta thickness could be used as an additional parameter to correlate with the gestational age during routine ultrasound measurements if the last menstrual period (LMP) was not defined and to detect developing intrauterine growth restriction. Moreover, this measurement is not for any specific disorder; it is an assessment tool to monitor foetuses at risk [93; 95].

Table 2.6: Mean placental thickness values in relation to gestational age by Sinha et al. in 2018.

Gestational age (weeks)	Cases	Thickness (mean ±SD) mm	Range (min–max)
14–18	20	19.82 ± 3.4	14.6-23.7
19–23	17	26.21 ± 1.0	24.9- 27.4
24–28	16	27.52 ± 3.3	22.3-30.4
29–33	23	35.65 ± 3.3	30.4-38.2
34–38	24	38.9 ± 0.04	38.1-38.2

In conclusion, all the mentioned studies indicated a positive correlation between the placental thickness and foetus gestational age. We can observe that this is a linear relationship. Moreover, the placenta thickness is lower in compromised pregnancy, such as those affected by PE and FGR, compared with the normal pregnancy. This review on placenta thickness helped to identify criteria for the depth of investigation for this project.

2.3.2.4 Placenta relaxation time

Different MRI techniques are increasingly used to investigate the human placenta in-vivo, particularly in compromised pregnancies. MRI relaxation times, both transverse (T_2) and longitudinal (T_1), are considered biomarkers for biological tissue. Different body tissues have specific characteristic relaxation times that depend on the number of free or bound protons [100]. Hence, healthy and diseased tissues can be identified using this technique. In 1998, the first in-vivo studies by Gowland et al. and Duncan et al. [101; 102] demonstrated the measurements of placenta MR relaxation time $(T_1$ and $T_2)$ and perfusion estimation for 41 normal and 11 abnormal pregnancies. The researchers used the inversion recovery and Look–Locker echo-planar imaging (EPI) sequence technique to measure T_1, while for T_2 measurements, a spin echo EPI sequence was used at 0.5 T. The researchers observed a significant decrease in T_1 and T_2 from the 20th week of pregnancy in normal pregnancies, which they related to the natural tissue changes of the placenta during pregnancy and possibly changes in the blood oxygenation level. A reduction was also observed in the abnormal group of the same gestational age, but the sample size was too small to be verified statistically. Such results could be obtained using a low-cost alternatives to MRI; such observations could be made in a clinical setting, thereby preventing the requirement for a costly MRI scan.

Table 2.7 shows data extracted from the graphs of a 1998 study [102] that investigated the placental relaxation time for normal and compromised pregnancy using echo planer MRI, and it is clear that there is a negative relationship with gestational age.

Table 2.7: Mean placental relaxation time for T_1 and T_2 for normal and compromised pregnancies, using 0.5 T MRI by Duncan et al. in 1998.

Gestational weeks	Normal T_1(ms)	Normal T_2 (ms)	Compromised T_1(ms)	Compromised T_2 (ms)
20, n_{T1}=5, n_{T2}=7	1364	259	-	-
25, n_{T1}=3, n_{T2}= 7	1247	226	-	-
30, n_{T1}=4, n_{T2}= 7	1295	205	n=3, 1038	n=5, 137
35, n_{T1}=5, n_{T2}= 13	1220	189	n=4, 1120	n=7, 175
40, n_{T1}=2, n_{T2}= 2	1120	165	-	-

In 2004, Ong et al. [103] analysed and compared placentas at 16–36 gestational weeks for normal and compromised pregnancies (PE and FGR). The researchers used a 0.5 T EPI scanner using the magnetisation transfer (MT) technique and stereological analysis method. MT was used to quantify the ratio of bound protons to the total number of protons in a given sample, and stereological analysis was used to estimate the ratio of residual non-vascular volume to the total placental volume. The researchers observed that MT was not altered significantly in either normal or abnormal placentas. In addition, in the cross-sectional studies on the foetal capillary to total placenta volume, the residual to total volume (R:T) ratio did not change. According to the findings, the changes in the relaxation time in the 1998 studies [101; 102] were not because of the vascular and non-vascular modification, but instead possibly because of placental morphology changes. These changes include the volumes, surfaces, and lengths of the placenta's main functional compartments.

In a 2005 review study on placental MRI, Gowland [47] mentioned the findings of Duncan et al. [102] on the relaxation time (T_1 and T_2) in normal pregnancy. They observed a shorter relaxation time in pregnancies affected by PE and FGR, but the values were not reported. Table 2.8 shows the T_1 and T_2 values for normal pregnancy using a 0.5 T MRI scanner.

Table 2.8: Mean placental relaxation time for T_1 and T_2 for normal pregnancy at a 20 week gestational age and term using MRI 0.5 T by Gowland in 2005

Gestational weeks	T_1 (ms) , n=48	T_2 (ms) , n=36
20	1350	250
Term (42)	1200	175

Further research was conducted in 2011 by Wright et al. [100] to verify the findings of the 1998 studies [101; 102] using higher-field 1.5 T MRI. The study included 30 normal pregnant females between 22 and 42 gestation weeks. They observed the same behaviour for both relaxation times, which decreased as gestational age advanced. Moreover, they observed that the T_1 values declined significantly because of the stronger MF applied. Seventeen placentas were investigated serologically; seven placentas that were collected in the same week as delivery indicated a significant correlation between the fibrin volume densities and ratio of fibrin to villous volume density and T_2. They concluded that T_1 and T_2 are influenced by the change in placental structure. Table 2.9 shows the data for the normal placenta relaxation time.

Table 2.9: Mean placental relaxation time by gestational age using 1.5 T MRI by Wright et al. in 2011.

Gestational weeks + Days	T_1 (ms)	T_2 (ms)
20–23 + 6, n = 1	1407	217
24–27 + 6, n = 7	1170	225
28–31 + 6, n = 8	1000	195
32–35 + 6, n = 2	935	198
36–39 + 6, n = 10	904	194
40–41 + 6, n = 2	1017	163

In 2013, Derwig et al. [48] performed a study to measure placental perfusion using a 1.5 T echo-planar MRI scanner to determine the relation between the placental T_2 relaxation time and uterine artery Doppler ultrasound pulsatility index (PI). The study included 40 singleton pregnancies in the second trimester (24–29 weeks); the PI was measured using Doppler ultrasound and T_2 was measured using a 1.5 T echo-planar scanner. T_2-weighted structural images were used to visualise the details of the placenta and foetus, and single-shot fast spin-echo scans were acquired in both the sagittal and axial orientation. The researchers observed that, in all 40 cases, the T_2 was significantly affected by whether the foetus was small for gestational age (SGA) or appropriate for gestational age (AGA). Additionally, the median T_2 relaxation time was lower in 25 cases of SGA (88 ms) compared with AGA (149 ms).

Moreover, the PI was significantly affected by the SGA or AGA status; the PI in SGA (1.96) was higher than that in AGA (1.0). Hence, the researchers concluded a significant association between T_2 and the degree of the uterine perfusion measured using ultrasound. Additionally, a lower T_2 in delivery was associated with SGA, as opposed to uncomplicated pregnancy. Moreover, they suggested that the MR T_2 measurement is more sensitive than PI for predicting SGA at birth. Table 2.9 shows the T_2 values for normal and abnormal placentas. The study selected only T_2 because this measurement is faster than T_1 and less sensitive to movement artifacts.

Table 2.10: Results of T_2 mean values using 1.5 T MRI scanner, for the 2nd trimester of pregnancy for the normal and abnormal placenta. The SGA group was divided into those with and without PE and those with and without low estimated foetal weight (LFW) at the time of the MRI examination by Derwig et al. in 2013.

Gestational weeks (24–29)	T_2 (ms)
Normal placenta, n = 15	149 (137–160)
SGA group, n = 25	88 (69–100)
PE, n = 7	90 (46–92)
No PE, n = 18	86.5 (69.8-113.5)
LFW @ MRI scan, n = 11	69 (46–82)
Normal foetal weight @ MRI scan, n = 14	93 (89.5–113.5)

As a summary for the placenta relaxation section, the reviews has indicated how both T_1 and T_2 decreases as the gestational ages increases for both healthy and compromised pregnancies. In compromised pregnancies, the biomarker values are lower than in normal pregnancies. This decrease is expected as these parameters are affected by placenta morphology and oxygenation (Figure 2.22). The presented values in this section for both T_1 and T_2 were used as a references to select a safe tissue mimicking substance for the experimental parts, as described in Chapter 3. Subsequently, they were employed to evaluate the sensitivity of the constructed system, as described in Chapter 5.

2.4 Conclusion

The brief overview of the NMR basic principle indicates how the NMR phenomenon depends on the intrinsic property of the nuclei. The most important nucleus the hydrogen proton, which is present in the water molecule and thus in all biological tissue. Generation of NMR signals in biological tissues depends on three types of magnetic field: B_0 for polarisation and precession, and the radiofrequency field (B_1) for flipping net magnetisation into the x-y plane, and the linear field gradient (G) for phase encoding and imaging. The literature review on the unilateral magnet designs assists in adopting the required magnet configuration. The review section on the placenta provides the basis for the expected trends of the tissue relaxation time. This project focused on simple and portable hardware to acquire the NMR signal spectroscopically. Thus, no gradient coils were included.

The field of application is the major driver for adopting an adequate magnet configuration. Moreover, the leading criteria that have to be considered are the depth of investigation, and the system's appropriate sensitivity. The following table indicates the required specifications for the developed system in this thesis.

Table 2.11: Developed hardware specifications

Specification	Justification	Criteria
Low magnetic field	No shielding room	<20 mT
Cost-effective	Affordable examination	As much as ultrasound cost
Open access	Accessible for pregnant women	Planar magnet
Portable	Employed at a clinical setting	Ultrasound clinic
Depth of Investigation	Anterior placenta	24 mm
Sensitivity	Measure T_2 and T_1 relaxation time	217–80 ms and 1407–1017 ms

Chapter 3

Tissue mimicking study

3.1 Introduction

This chapter describes the identification of materials to mimic the relaxation time parameter of the placenta; subsequently, the materials for each relaxation time were identified separately. Such experimentation is essential because it would assist in evaluating the efficiency of the newly developed system in this project. NMR systems have been evaluated in different studies for quality control or pulse sequence optimisation based on sample viscosity [104; 105; 106; 107]. The viscosity of a solution is one of the factors that is affected the MR relaxation time of a material in that viscosity relies on the molecular size and physical and chemical environment of the nucleus [3; 108; 109; 110].

Thus, various substances have been employed as phantom to measure spin–spin and spin–lattice relaxation times. For instance, copper sulfate-doped agarose gel [111], copper sulphate-doped agar gel [105], nickel-doped agarose gel [107], and copper sulphate [104] have been used to shorten both T_1 and T_2 values. For T_2 measurement, polydimethylsiloxane (PDMS) has been used [106]. However, the materials used to shorten the spin–lattice relaxation time are not safe. The safety data sheets for both copper sulphate [112] and nickel sulphate [113] indicate that they are toxic and carcinogenic. Thus, special precautions is required when manipulating such materials. Therefore, it was preferable to develop a range of safe and repeatable reference material to test the developed sensor.

In this study, a safe and non-expensive material was employed to simulate placenta relaxation times T_2 and T_1. For T_2, a range of silicone oils (PDMS) viscosities were employed. The PDMS safety data sheet [114] indicates that the PDMS ingredients are not hazardous nor carcinogen. For T_1, a novel-safe food substance was utilised, which is full-fat milk powder. In food science, water self-diffusion in dairy products have been observed to rely on the volumes of the protein, lactose, and fat in the sample

[115; 116; 117; 118]. Therefore, the concentration of milk powder in distilled water can be manipulated to produce different viscosities. The spin–lattice time is influenced by the molecular self-diffusion, as mentioned in Chapter 2; thus, the high concentration results in a decrease in the T_1 values.

Unlike a healthy placenta, the relaxation time of a compromised placenta (PE) in each period of gestational age was not discussed in previous studies. The most examined gestational age was the second trimester, which begins approximately from week 24 to 29, and the T_2 values were ranged from 46 to 92 ms with a mean value of 90 ms [48]. However, all previous studies indicated that the relaxation time of PE follows the same trend, but with lower values. Hence, the placenta relaxation time was mimicked depending on the value extracted from the research on healthy placentas by Wright et al. [100]. For T_1, the values were 1407, 1170, 1000, 935, 904, and 1017 ms, and the T_2 values were 217, 225, 195, 198, 194, and 163 ms, where each value represents a different gestational age, namely 20–23, 24–27, 28–31, 32–35, 36–39, and 40–41 weeks, respectively.

3.2 Method

A clinical MRI scanner (1.5 T MAGNETOM Avanto, Siemens, Erlangen, Germany) was used to generate reference values for both spin–spin and spin–lattice relaxation times. These values indicated the eligibility of the developed system in this project to replace high-field clinical MRI. The experimental details to achieve this objective are described below.

3.2.1 Silicone oil for T_2 measurement

Silicone oil (PDMS) is considered a perfect candidate for spin–spin relaxation time measurements. This is because of its physical structure, which forms a proton-rich environment with low-frequency motions, and the polymer chain is composed of two methyl groups on each unit [119].

3.2.1.1 Sample preparation

Eight silicone oils bottles (Schumacher Racing, Northampton, UK) with different viscosities (300, 600, 900, 2k, 5K, 10k, 15K, 30k) of centipoise (cP) were collected to obtain different effective transverse relaxation times (T_2^{eff}). Each bottle contained 60 ml of silicone oil, and all metallic stickers were removed before being positioned inside the MRI scanner. Figure 3.1 shows one of the PDMS bottles that was used in this experiment with a silver sticker on the back.

Figure 3.1: Silicone oil with a viscosity of 2k cP. This metallic sticker on the back of the bottle should be removed before the MRI scan.

3.2.1.2 MRI Measurement

In the clinical scanner, all samples were measured parallel to each other using the spine coil to receive the radiofrequency signals. Spin echo (SE) imaging sequence was performed similarly to the CPMG pulse sequence to extract the T_2^{eff} value for each viscosity on a later stage. This experiment was performed using a range of echo times (TE) (12.4, 20, 25, 30, 35, 40, and 50 ms) with a 1230 ms repetition time and coronal orientation. For each echo time, the scan was acquired using 16 echoes and 32 slices, and the total scan time lasted 7.54 minutes. A total of 16 images were acquired and transferred to an in-house MATLAB software (MathWorks, Natick, MA, USA) to produce a T_2^{eff} map. Figure 3.2 shows the images of the PDMS samples at different TE values, and the viscosity of each sample is indicated in the first image.

A region covering the centre in each of the samples was selected from the image in Figure 3.2 to observe the T_2^{eff} data and determine its numerical value. The region of interest was averaged in each of the 16 echo images in MATLAB over the same area and plotted against the centre line of the echo. A mono-exponential fit was then used to determine the value of the T_2^{eff}. Maps of the T_2^{eff} were also produced using the same fitting method but for each individual voxel rather than an average. These are shown in Figure 3.3.
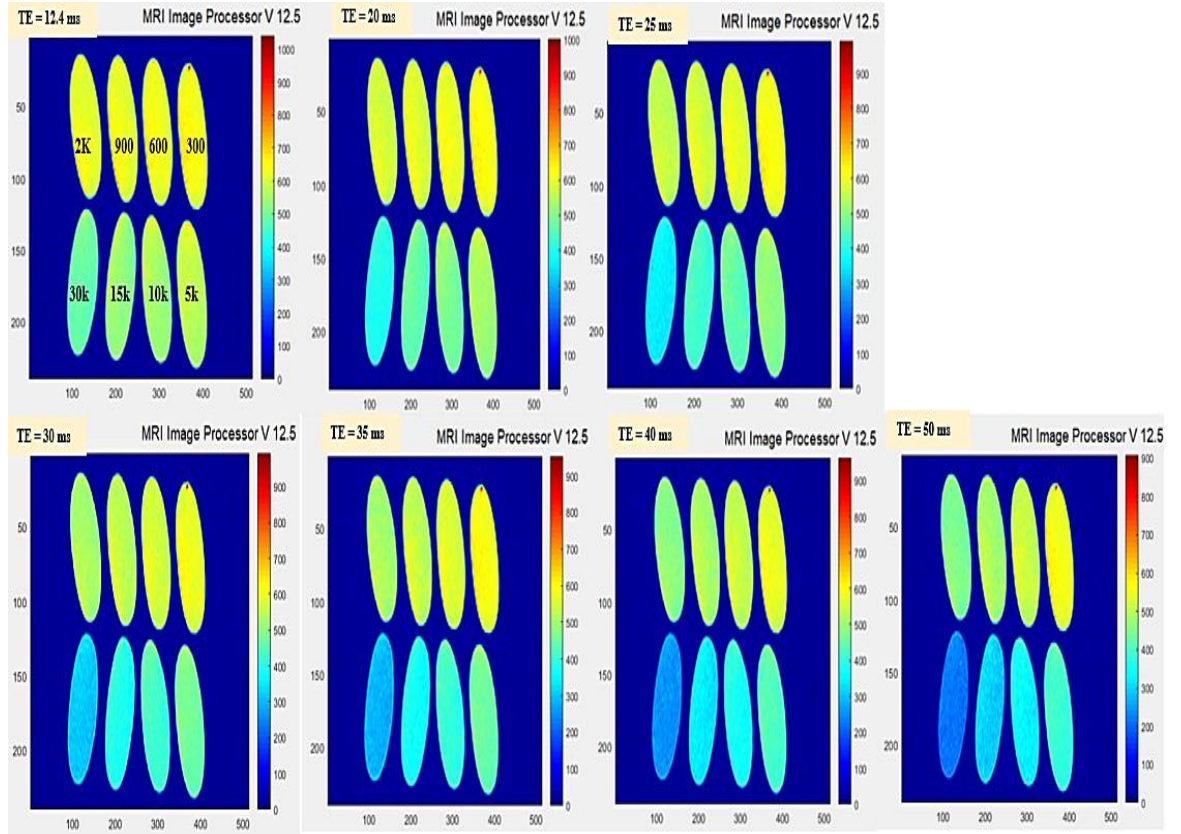
Figure 3.2: Images showing the final echo image from PDMS samples at different TE values. The annotation on the first image on the left side indicates the viscosity for each sample.
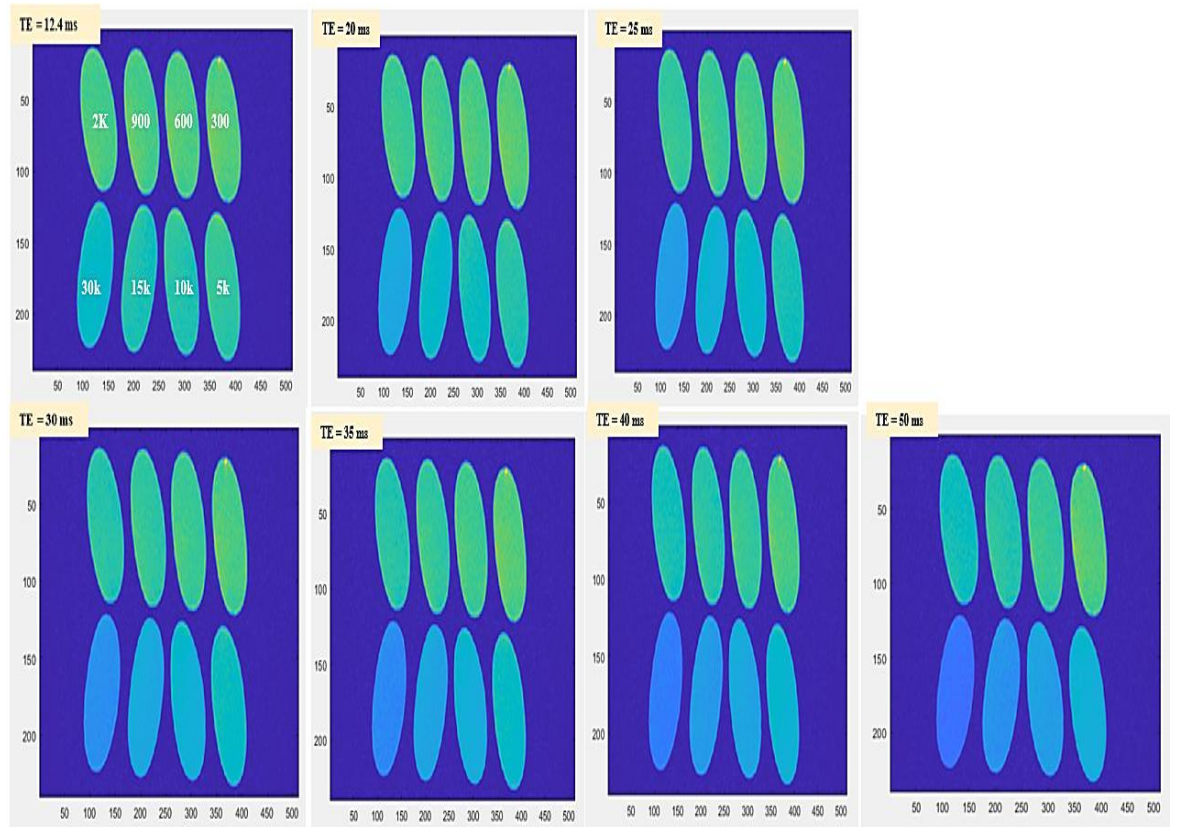
Figure 3.3: PDMS T_2^{eff} image maps created in MATLAB for each echo time.

3.2.1.3 Results and discussion

This study investigated different T_2^{eff} values for each PDMS concentration, and it was clear that the PDMS affected spin–spin relaxation time. These values covered the entire range of the placental tissue transverse relaxation time. It has been observed that as the PDMS concentration increased, the values of T_2^{eff} decreased, which was expected and agreed with the observation of previous studies [106; 107; 120]. Table 3.1 shows T_2^{eff} values for each PDMS viscosity, and Figure 3.4 depicts the relationship between the T_2^{eff} values and PDMS viscosity.

Table 3.1: T_2^{eff} as a function of increasing the PDMS viscosity using a 1.5 T clinical MRI

PDMS viscosity (cP)	T_2^{eff} (ms)	Standard Deviation ($\pm$ ms)
300	340	7
600	240	5
900	190	2.5
2K	165	2
5K	140	1.7
10K	130	1.5
15K	120	1.5
30K	105	1.5
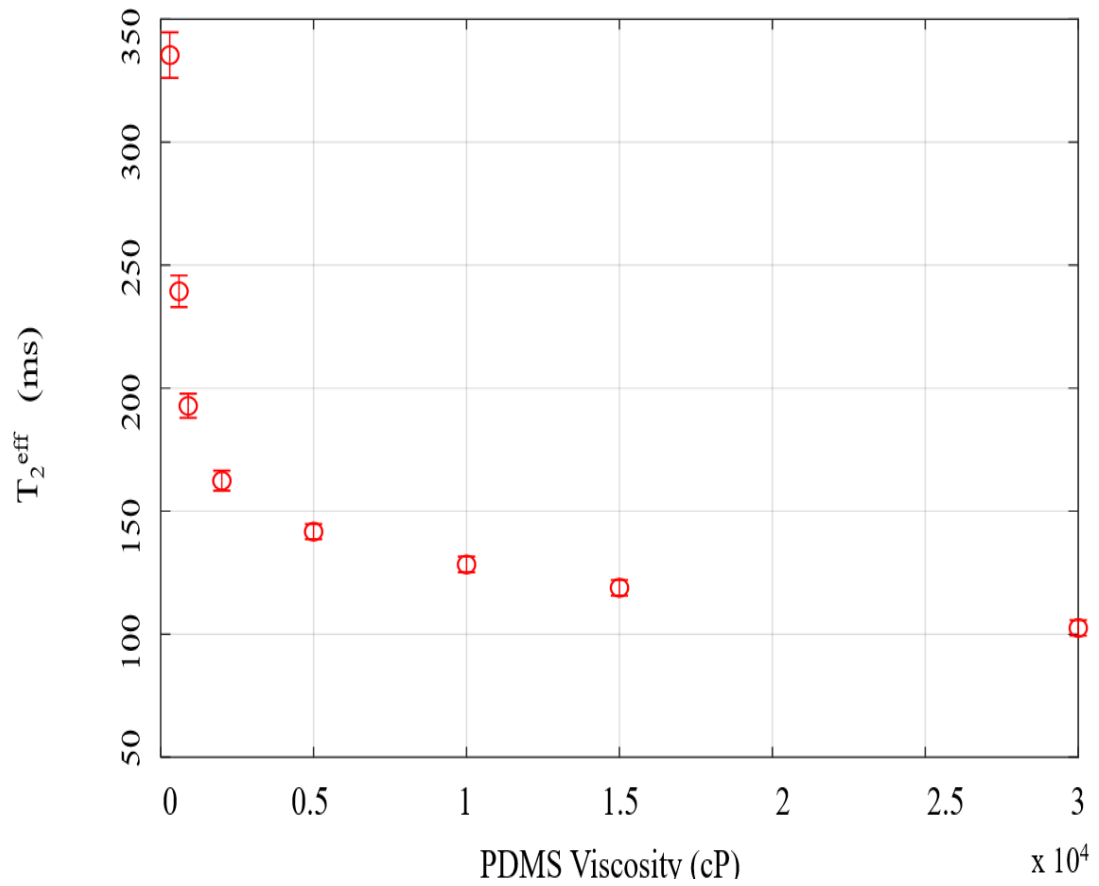
Figure 3.4: T_2^{eff} value against PDMS viscosity using a 1.5 T clinical MRI.

3.2.2 Full-fat milk powder for T_1 measurement

In this study, full-fat milk powder was used to shorten the T_1 over a wide range of values. This novel food material is considered safe, affordable, and repeatable samples can be prepared as required [110]. Therefore, the effectiveness of the full-fat milk powder was evaluated using two different magnetic fields strengths: 1.5 T clinical MRI, and 0.3 T magnetic resonance sensor.

3.2.2.1 1.5 T MRI Measurement

The preliminary experiment was conducted with an ankle coil to illustrate the suitability of the prepared concentrations as T_1 calibration samples and to verify that full-fat milk powder does indeed affect the spin–lattice relaxation time [110]. Subsequently, similar concentrations were freshly prepared and measured with spine coil, as explained in the next subsections.

3.2.2.1.1 Sample preparation

The required materials to prepare the samples were only full fat milk powder (NIDO, Nestle, Vevey, Switzerland) and distilled water. The milk powder was dissolved in distilled water at seven different concentrations, all as weight per volume (w/v), of 5%, 11%, 18%, 23%, 38%, 50%, and 64% in sample tubes and were mixed thoroughly before the clinical MRI images were collected.

An example of the preparation of 11% concentration: a 0.95 g of full fat milk powder was dissolved in 7 ml distilled water, yielding a total solution volume of 8.5 ml, and the concentration was calculated as follows:

(MATERIAL WEIGHT/TOTAL VOLUME) X 100 = (0.95 / 8.5) X 100 = 11.2 %

Each concentration was very well mixed in a 15 ml plastic tube, then dispensed in a selected well. This dispensing took the form of the acronym of 'NTU' (Nottingham Trent University) in three well plates composed of 24 wells in each plate (Figure 3.5).

Figure 3.5: Full-fat milk samples with different concentrations in the form of the letters NTU, each row representing different concentrations as indicated on the image.

3.2.2.1.2 MRI Measurement

The spine coil was used to receive RF signals for these samples as inherently flat. The well plates were imaged using an inversion recovery pulse sequence with the following applied varying inversion times: 100, 500, 750, 1000, 1250, 1500, 1750, 2000, 2250, 2500, 3000, 3500, 4000, and 4500 ms with a 5000 ms repetition time and 68 ms echo space. Coronal orientation was employed, and the total experimental time was 1.54 hour. The T_1 values were extracted using the previously mentioned in-house MATLAB software to produce an inversion recovery T_1 map; the values of T_1 were encoded on the colour scale.

Nevertheless, as a preliminary step to verify that the milk powder varied the values of the T_1, seven concentration were prepared in 15 ml plastic tubes and examined in two patches utilising ankle coil (Figure 3.6). The experimental procedure was similar to the spine coil measurements, except that the orientation was sagittal. The inversion time commenced from 500 ms for concentrations 5%, 11%, and 18%, while for the remaining concentrations, the inversion time began from 100 ms, as with the spine coil.
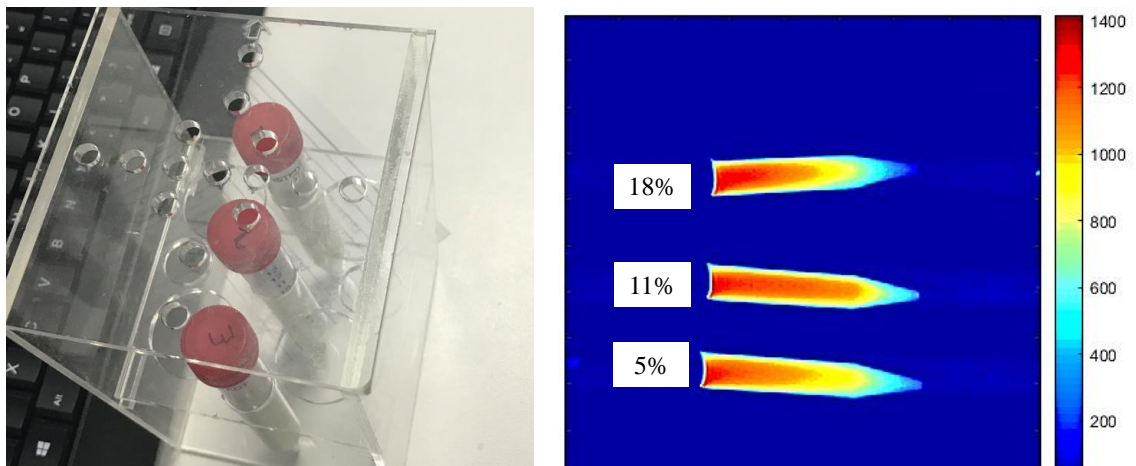
Figure 3.6: T_1 inversion recovery map for the first three milk concentrations using an ankle coil in 1.5 T MRI. The left-hand image shows the prepared samples of different concentration, and the right-hand image represents the T_1 map for each tube. The colour bar scale is T_1 in ms

As shown in Figure 3.7, the inversion time variation affected the image contrast for each section in the NTU letters that had different milk concentrations. After the inversion recovery T_1 map was obtained, the T_1 value was extracted by selecting a region inside the centre of each well and then averaging the value for each concentration. Figure 3.8 shows an example of T_1 values obtained for the concentrations of 5% and 50% of the 15 ml plastic tube samples that was measured using the ankle coil.
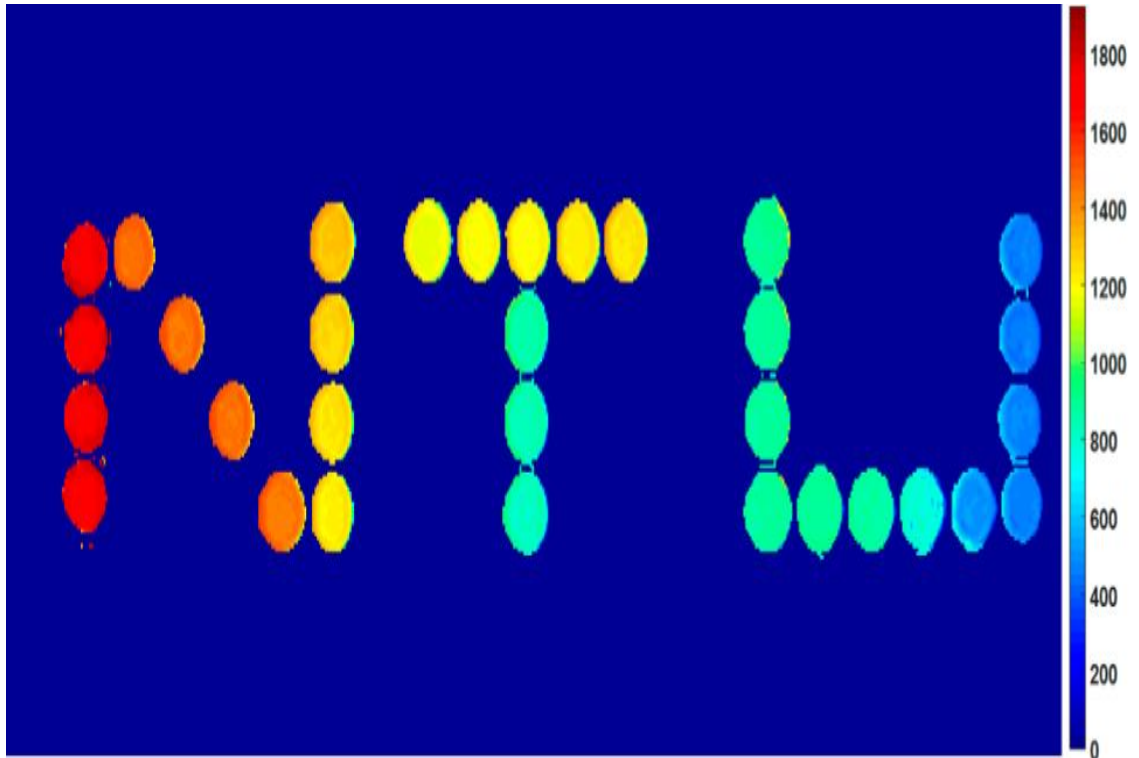
Figure 3.7: T_1 map of different milk concentrations using inversion recovery sequence in 1.5 T MRI. Concentration is increasing from left to right, four for each sample. The colour bar scale is T_1 in ms.
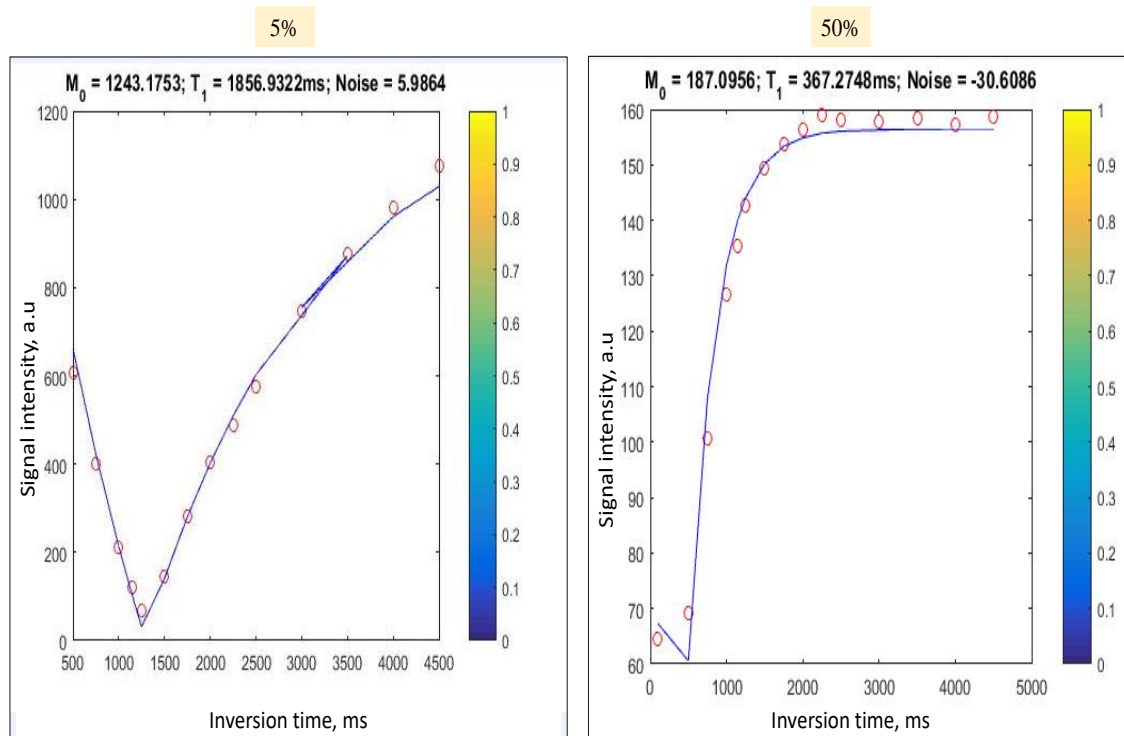
Figure 3.8: T_1 values for two concentration of full fat milk-powder solution measured using the ankle coil and produced by the MATLAB software.

3.2.2.2   0.3 T magnetic Resonance Sensor Measurement (MRS)

3.2.2.2.1 Sample preparation

Fresh solutions of full fat milk powder were prepared for the measurements in the 0.3 T MRS. For each of the seven concentrations, three samples were extracted and dispensed in separate standard NMR 5 mm glass tube to collect average measurements for each concentration. The tested concentration was similar to the concentration used with the clinical MRI, which were 5%, 11%, 18%, 23%, 38%, 50%, and 64% w/v.

3.2.2.2.2 MRS Measurement

A customised magnet was used as a magnetic resonance sensor, and it could be described as a closed-loop, iron yoke magnet (Figure 3.9). The magnetic field generated from this sensor was 0.3 T, equivalent to a resonance frequency of 19.38 MHz. For the transmitting and receiving RF signals, an RF coil, as a part of a commercial NMR probe (Part 514 606, Leybold Didactic GmbH, Huerth, Germany) was positioned over the two permanent magnets. The NMR probe ensured a homogeneous field in the sample region, and the sample was placed in the RF coil for signal detection [110].
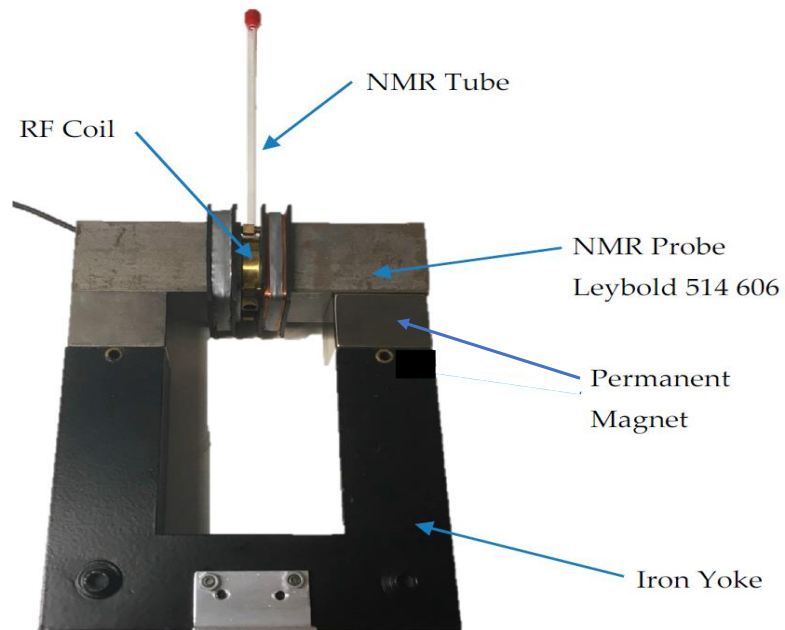
Figure 3.9: Snapshot of the customised close-loop 0.3 T magnet used as a sensor, showing the setup parts.

Data was collected using Prospa software (Version 3.22, Magritek, Wellington, New Zealand), for which the RF coil was connected to a Kea^2 spectrometer (Magritek, Wellington, New Zealand) through a standard series-parallel tuning and matching circuit.

T_1 measurements were achieved using a T_1 inversion recovery sequence with seventeen inter-experimental repetition times (T_{RN}) that were incremented non-uniformly as follows: 25, 1000, 50, 400, 60, 3000, 75, 1500, 100, 6000, 800, 125, 90, 300, 150, 2000, and 200 ms. The maximum recovery time was set at 10000 ms, a 7 T_1 value as estimated by the 1.5 T MRI scanner. The SNR intensity was improved through the summation of eight echoes with the shortest enabled TE. The entire MRS was placed in a bench-top Faraday cage to reduce external noise (Figure 3.10).
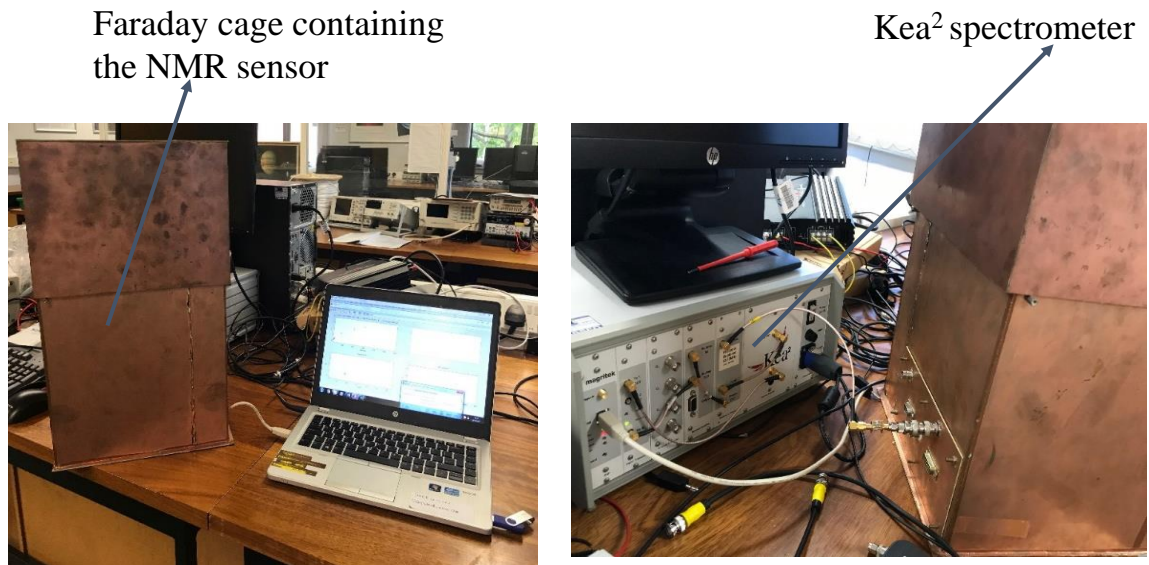
Figure 3.10: Faraday cage containing the customised 0.3 T MRS and connected to the Kea^2 spectrometer through a cable.

The collected data via the Kea^2 were manipulated through an online program (mri-Toolbox website, © 2011-13 Alan McMillan) [121]. The mono-exponential fit for the signal intensity against the inversion times was performed to extract the T_1 values. Figure 3.11 depicts the T_1 values for 5% and 64% full-fat milk powder concentration processed using the mriToolbox website. The online program used the non-linear least-squares fit and the fact that 180^0 is never perfect. The equation to estimate the T_1 value has the following form:

$$\mathbf{M}_z = \mathbf{M}_0[1 - 2A\exp{(\frac{-TI}{T_1})} + \exp{(\frac{-TR}{T_1})}] + C, \qquad (3.1)$$

where A is equal to (1 - cosθ), θ is the inversion pulse angle, and C represents the noise. The signal to noise ratio of the data exceeds 2; therefore, a simple offset to represent the noise is suitable, as discussed in [122].

5%

$$T_1 = 1610 \text{ ms}$$

Parameters

$M = M_0 \, (1 - 2 \, A \, e^{-TI/T_1} + e^{-TR/T_1}) + C$

T1 IR (imperfect 180) ▾

☑ Include Constant in Fit

TIs (ms)

1500
2000
3000
6000

Measurements

5376.05
6275.04
7253.63
8373.23

TR (ms)

10000

T1-IR Data and Fit

— Meas.
— Fit

Messages

Fit is excellent (r^2=0.9996)
T1 = 1609.6473 ms
M0 = 12373.0379
A = 0.3187
C = -3868.8929
Operation took 29 ms

64%

$$T_1 = 426 \text{ ms}$$

Parameters

$M = M_0 \, (1 - 2 \, A \, e^{-TI/T_1} + e^{-TR/T_1}) + C$

T1 IR (imperfect 180) ▾

☑ Include Constant in Fit

TIs (ms)

1500
2000
3000
6000

Measurements

7966.81
7943.35
8003.17

TR (ms)

10000

T1-IR Data and Fit

— Meas.
— Fit

Messages

Fit is excellent (r^2=0.9984)
T1 = 426.4597 ms
M0 = 6632.6965
A = 0.4025
C = 1325.5516
Operation took 42 ms

Figure 3.11: Example of T_1 values for two full-fat milk powder concentration (5% and 64%) using the online program (mriToolbox); the right corner of each concentration indicates the T_1 value.

3.2.2.3 Result and discussion

Different concentrations result in an alteration in the sample's viscosity, and as a well-known result, this has a prominent effect on the spin–lattice relaxation parameter. This study demonstrated that as the concentration increases, the viscosity increases, and as anticipated, the T_1 relaxation time values decrease. This decrease is due to the relationship between the viscosity and molecular size of the sample; as mentioned earlier, full-fat milk powder consists of lactose, protein, and fat, and both fat and protein have comparable molecular sizes. Hence, the higher concentration of these components results in more abundance of these molecules, and thus, a slower nucleus rotation. Consequently, the relaxation time decays rapidly [117; 118].

Samples measured using the 1.5 T MRI indicated the decrease in the values of T_1 as the viscosity increased. The T_1 values using the ankle coil for the different milk concentrations in the 15 ml tubes are presented in Appendix A. Table 3.2 shows the T_1 averaged values for each milk concentration using the spine coil.

Table 3.2: T_1 averaged values as a function of the increasing full-fat milk powder concentration using 1.5 T clinical MRI with a spine coil.

Milk concentration %	Averaged T_1 (ms)	Standard Deviation ($\pm$ ms)
5	1707	7
11	1464	20
18	1249	38
23	1187	28
38	837	34
50	887	8
64	528	13

Moreover, Figure 3.12 shows the relationship between the T_1 relaxation time values as the milk concentration increased using the spine coil. The figure of T_1 corresponds to the increase in the milk concentration using the ankle coil is presented in Appendix A.

$$y = 1888.2e^{-0.022x}$$
$$R^2 = 0.998$$
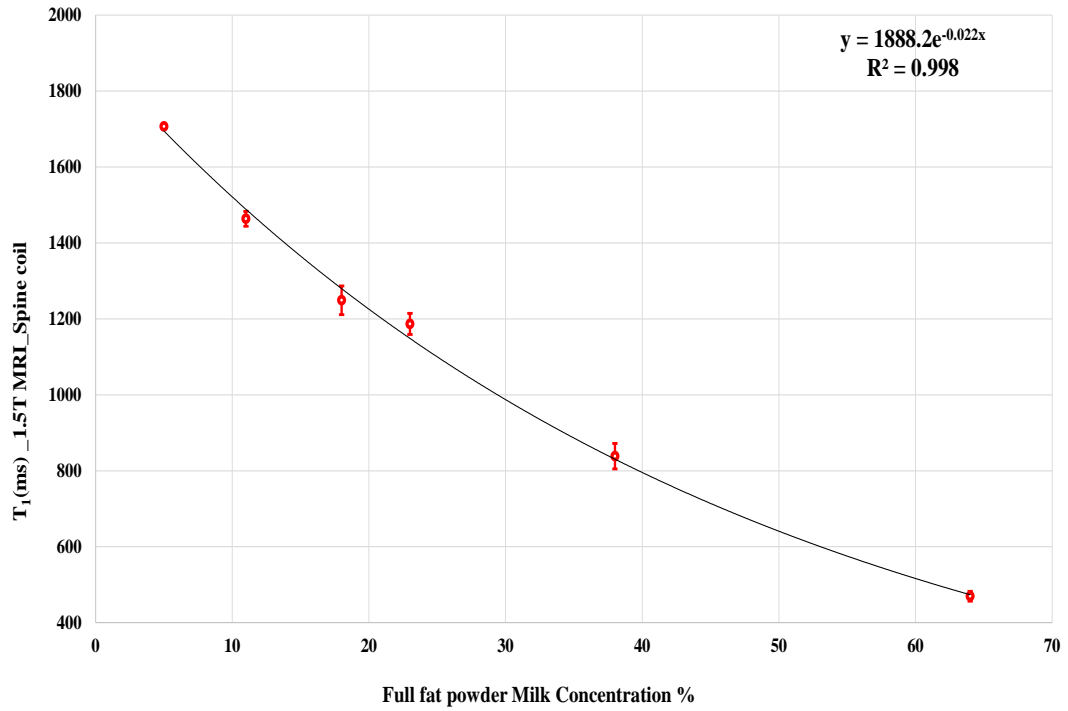
Figure 3.12: T_1 values as a function of full-fat milk powder concentration using 1.5 T MRI with a spine coil.

A similar results was observed for the samples measured using the 0.3 T MRS. It was clear that, as the concentration increased, the T_1 value decreased. The values of T_1 were estimated by averaging the values of three samples for each concentration. Table 3.3 shows the averaged values of T_1 relative to the milk concentration. Figure 3.13 shows the inverse relationship between milk concentration and T_1 values. The repeatability of the measured sample was evaluated using the error bars of the standard deviation of the T_1 values.

Table 3.3: T_1 averaged values as a function of the increasing full-fat milk powder concentration utilising 0.3 T customised closed-loop magnet.

Milk concentration %	Averaged T_1 (ms)	Standard Deviation ($\pm$ ms)
5	1682	223
11	1322	43
18	1063	64
23	939	26
38	724	23
50	540	21
64	431	5

65
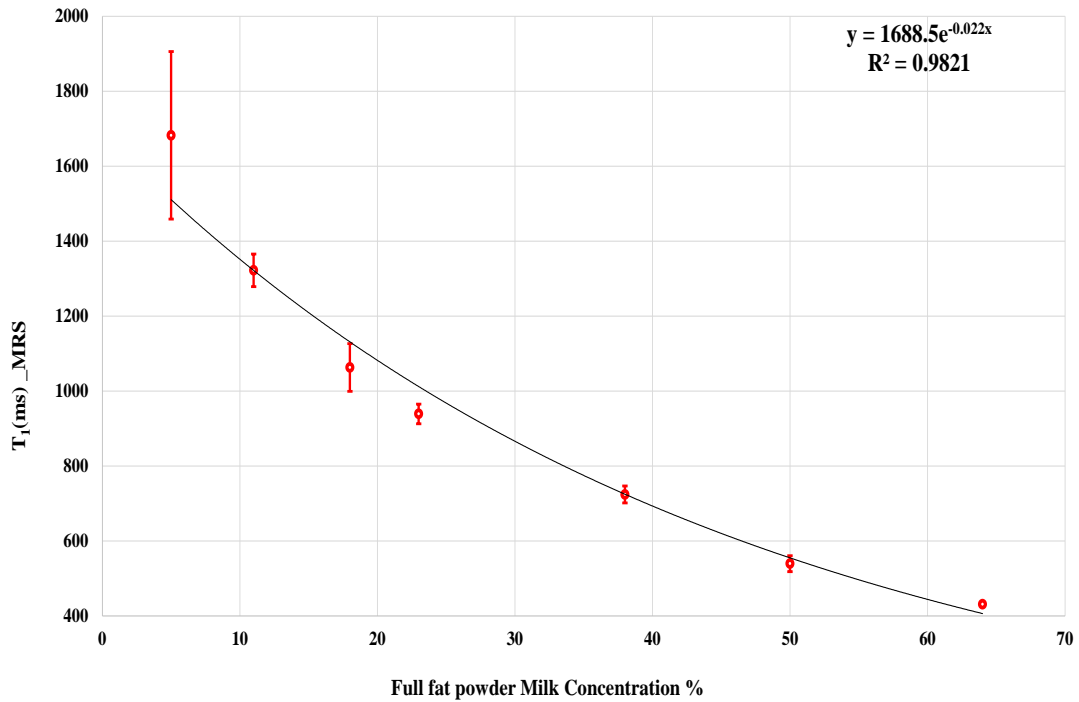
Figure 3.13: T_1 values as a function of full-fat milk powder concentration using the 0.3 T MRS. The error bars represent the standard deviation of the measurements.

Despite the large difference in the strengths of the magnetic fields of the customised closed-loop sensor (0.3T) and the clinical MRI using the spine coil (1.5T), the full-fat milk powder samples exhibited approximately similar values for the spin–lattice relaxation time. This similarity was observed from the fitting coefficient for the exponential curve, which was -0.022X in both systems. The reason for this similarity in values might be due to the fat in the full-fat milk powder having a comparable size to the protein and the fat is weakly dependent on the intensity of the magnetic field [118; 123].

Generally, this study succeeded in the use of full-fat milk powder samples as a standard calibration substance for the development of a magnetic resonance sensor.

3.3 Conclusion

The results in this study reveal the safe and inexpensive wide range for both T_2 and T_1 that can be extracted from silicone oil and full-fat milk powder, respectively. The viscosities demonstrated in this study encompass the entire range of placenta relaxation times at different gestational ages. The various viscosities of the silicone oil and full-fat milk powder that were tested using clinical MRI indicated an excellent relationship with the spin–spin and spin–lattice relaxation times, respectively. For the spin–lattice relaxation time, the full-fat milk powder dissolved in distilled water exhibited an efficient outcome in both clinical MRI and low-field magnetic sensors in having a similar exponential fitting coefficient. This material is considered a safe, affordable, and easily replicated tool to calibrate MR sensors. A freshly prepared sample is recommended to be used within 0–4 hours to avoid substance separation and, consequently, fluctuation in the T_1 values. These materials were used separately as a safe tool to validate the development of a low-field NMR system, as explained in Chapter 5. Moreover, the possibility of combining these materials to create a tissue-equivalent phantom is discussed in Chapter 5.

Chapter 4

Electronics system for a low-field NMR spectrometer

4.1 Introduction

This chapter presents the development of an electronic system that can be operated at an RF below 1 MHz. Although most low-field NMR spectrometers are operated at a frequency ranging from 10 to 20 MHz [3; 8] or at Earth's field [124], the operating frequency used in this study has become more common [5]. This range of frequency is considered a motivating cross over, and although it is above the audio domain (20 Hz – 20 kHz), the RF electronics design is economical.

However, the main challenge in low-NMR MF systems is extremely low SNRs, as the SNR depends on the strength of the static MF (B_0), sample volume, and characteristics of the detection coil. For instance, when using an electromagnetic coil as a B_0 field, a stabilised power supply is fundamental for establishing a constant field value and, therefore, resonance frequency. Moreover, an enhancement in signal processing is essential to overcome the SNR problem [4; 125]. Moreover, a low noise pre-amplifier is considered one of the key elements for receiving the NMR signal in a low magnetic field [126].

The SNR in a low-NMR MF system can be enhanced by using a digital signal processing (DSP) system, as demonstrated by earlier researchers [4; 127; 128; 129]. The DSP system functions as a controller and an interface between the frequency translator and digital synthesiser. The primary components of the NMR spectrometer are the magnet, console, and host computer. The DSP operates similarly to a radio system in that it has components such as a transmitter, synthesiser, and receiver.

In this study, the electronic system used was a commercial magnetic resonance console called SpinCore (RadioProcessor^{TM}, SpinCore, Gainesville, FL, USA), which is a digital RF excitation and broadband data acquisition system with spectrometer frequencies

ranging from 0 to 100 MHz [130]. The RadioProcessor board combines three major units: the data acquisition core, excitation core, and PulseBlaster timing core, which provides high-resolution timing control for the entire system. This commercial spectrometer does not comprise the required signal amplifiers, which are the pulse power amplifier, transcoupler (duplexer), and pre-amplifier, as these depend on the applied frequency. Therefore, this chapter will discuss the employment of two different RF power amplifiers and pre-amplifiers: the off-the-shelf components as a typical system and the existing generation of the operational amplifier (Op-Amp) as cost-effective parts.

Moreover, as a preliminary step to verify the efficiency of the electronic system for the low MF-NMR spectrometer, a relatively homogeneous MF for both B_0 and B_1 was used. The aim of this step was to avoid the variation in the magnetic field that could be generated from the single-sided NMR sensor and surface coil and to focus on developing the low-field NMR electronic system.

4.2 NMR spectrometer system

The entire system was composed of three main parts: the MF source, which was an electromagnetic (EM) laboratory coil, the SpinCore console, and the host computer. Each part of this spectrometer system had an essential role in acquiring the nuclear magnetic resonance signal, as is explained further below.

The first part included the EM coil and NMR probe. The EM coil functioned as the main static MF source (B_0). The produced MF was controlled using a programmable DC power supply to ensure power stabilisation and determine the actual current (A) that generated the required MF to satisfy the resonance frequency of the RF coil. The NMR probe was a resonance-frequency circuit composed of a home-made solenoid coil and fixed high-voltage capacitors. A solenoid coil in the probe circuit was used to generate the EM field (B_1) to interact with the nuclei of the sample. This coil was used to transmit and receive the NMR signal simultaneously.

Since the characteristic of the detection RF coil is very important for the SNR, the coil was fabricated from Litz wire (500 g, 81 strands of 0.04 mm copper warped in silk, 0.67 mm wire diameter) to reduce coil resistance at low frequencies and provide a high-quality factor [4]. Moreover, a winding machine was used to build the RF coil to ensure that all the layers were superimposed correctly. The diameter and height of the RF coil were 20 mm, composed of 3 layers of 30 turns of Litz wire. Subsequently, the RF coil and fixed high-voltage capacitors were contained in an aluminium box and inserted in between the poles of the EM coils (Figure 4.1).

The gap between the two poles was 5 cm, the EM coil was driven to 0.0189 T, which corresponded to a frequency of 0.8075 MHz using a 0.332 A current provided by the

programmable DC power supply set at 20 V.
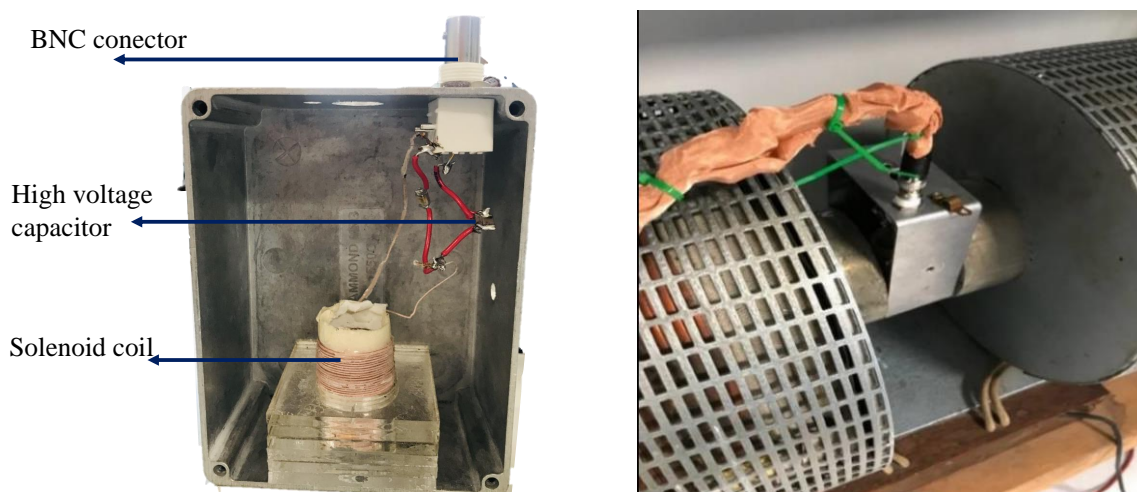
Figure 4.1: Electromagnetic coil with the aluminium box inserted between the iron poles. The right-hand image shows the probe parts inside the aluminium box.

The NMR probe was connected to a transmitter/receiver (T/R) switch or duplexer, which was used to blank the pre-amplifier to avoid the overloading and destruction caused by the high power excitation pulses. It also isolated the transmitter from the receiver during the receiving period to prevent electrical noise from the transmit channel [4].

4.2.1 Electronic system with off-the-shelf units

The second part of the low-field NMR spectrometer was the electronic system, represented by the SpinCore console. Figure 4.2 depicts the block diagram of the electronic system of the low-MF NMR spectrometer using the off-the-shelf components such as front-end electronics. These components were the RF power amplifier (BT00500-AlphaS, TOMCO, 100 kHz–30 MHz, Stepney, Australia), a duplexer (custom built transcoupler, nmr-service.de, Germany) which operated from 0.7 to 1 MHz, high gain and low noise ZFL-500LN-BNC pre-amplifiers (MiniCircuits, 0.1-500 MHz, GND+15v, Brooklyn, NY, USA), and the low pass filter of 1 MHz (EF508, Thorlabs, Newton, NJ, USA).

The excitation core of the RadioProcessor board generated both RF analogue signals and digital outputs. It was represented by a direct digital synthesis (DDS) board, which controlled the digital transmitter channel of the spectrometer system. The function of the transmitter was to provide a short RF pulse. These pulses irradiated the sample in the probe with the desired frequency and pulse length at the correct phase and power level [131]. The digital transmitter channel included a frequency synthesiser, RF signal generator, and transmitter controller. The RF amplifier was not part of the DDS board
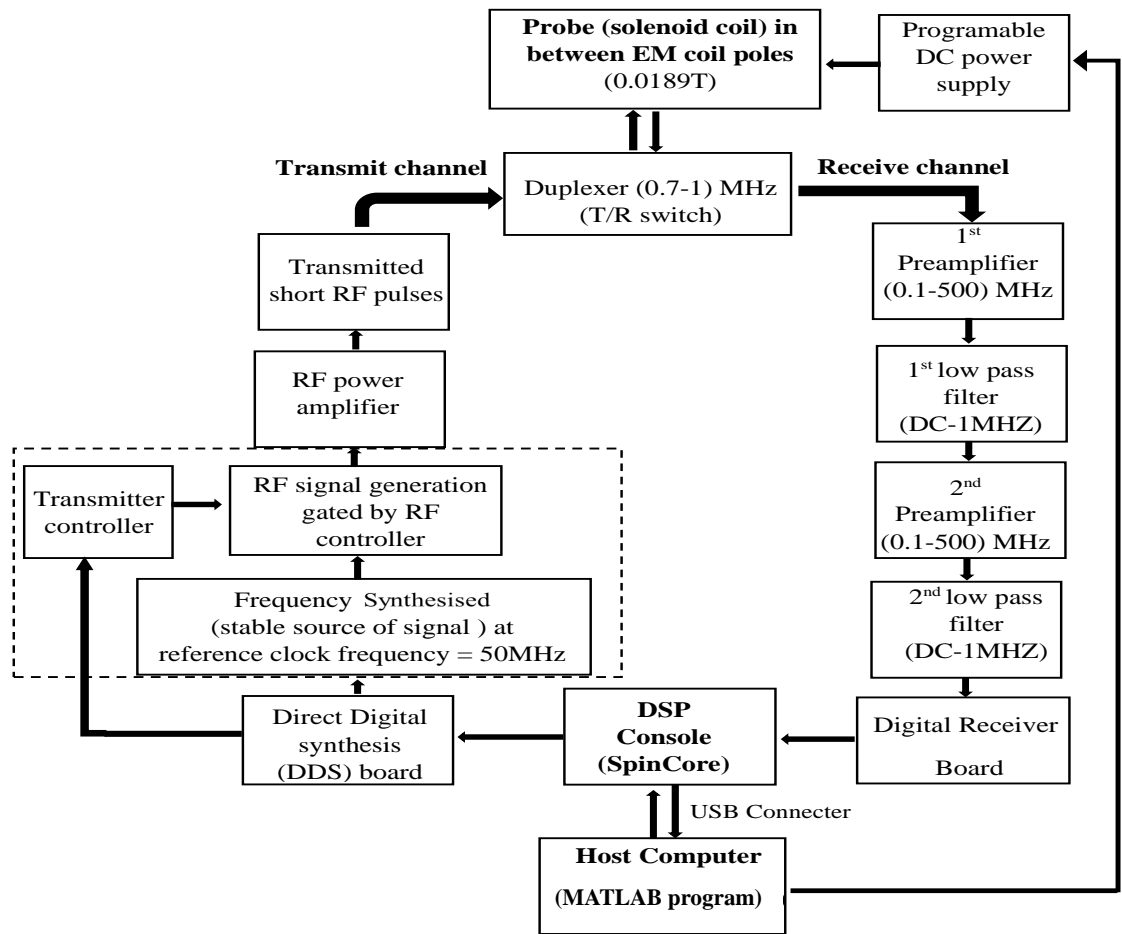
Figure 4.2: Block diagram for the low NMR spectrometer electronic system.

but of the transmitter channel. The DDS board synthesised the excitation pulse and amplified the pulse generated by an RF power amplifier (TOMCO) at 125 mV.

Moreover, signal coherence was maintained between the acquisition and excitation cores by deriving the detection of the acquisition core [130]. First, the frequency synthesiser was the source of a stable RF signal with the required frequency using a standard reference frequency of 50 MHz. Second, the RF controller, under the computer interface control, gated the output of the synthesiser generated signal to form short timing pulses at a low amplitude level. Third, the transmitter controller was used to create the modulated phase, pulse power, and pulse switching. Subsequently, the digital-to-analogue (DAC) converted the information obtained in digital form, the generated signal that was controlled by the host computer, to analogue information in the form of a voltage and current (sine wave signal).

This pulse was sent to the RF coil through the duplexer, and when the pulse was turned off, the NMR signal was detected by the same coil and transmitted to the digital receiver via the same duplexer. The receiver channel included a pair of high gain and low noise

ZFL-500LN-BNC pr-amplifier mini circuits with two of the 1 MHz low-pass filters to filter the noise outside the frequency bandwidth, and the digital receiving board (DR). The DR represented the acquisition core and captured the received signal through a high-resolution analogue-to-digital converter (ADC) [130]. The received signal was demodulated digitally using digital quadrature detection and filtered to reduce the signal to baseband. These demodulated signals transmitted to the DSP for digitizing by an ADC (75 MHz) for data processing and display such as the Fourier transform of the time domain data, which was performed by the hosted computer.

The PulseBlaster timing core was used to simplify the creation of complex pulse sequences via robustly designed instruction set. This timing core controlled all system features functionality, for instance, the triggering data acquisition, frequency, and gating RF output in addition to the control of the digital outputs.

The third part was the host computer, a tool used for communication between the user and spectrometer via the MATLAB program. An in-house MATLAB (MathWorks, MA) program was used as a graphical user interface (GUI) to program and control the RadioProcessor board, in which the program controlled the digital pulse and RF generation of the board. It also enabled the end-user to design the operating window as required (Figure 4.3). The designed panel had different sections to control the NMR signal parameters: the hardware, echoes, and experiment sections. The SpinCore controlled the entire operation by appropriately synchronising the excitation and internal acquisition core parameters.

These sections contained parameters that were related to both excitation pulse and acquisition time. The parameters that related to the excitation pulse were the NMR frequency (f) (MHz), 90 lengths (pulse length), phase shift, amplitude, echo time (TE), and repetition time (TR). The ones related to the acquisition time were the ADC f, dwell time (DW), number of echoes (NE), number of echo points (PPE), and number of average scans (N Reps). These input parameters were required to be set correctly to obtain useful CPMG data, and the experimental procedure could be repeated as required to improve the SNR.

The function of the input parameters is explained as follows: **ADC f** is a sampling clock frequency fixed at 75 MHz. At this sampling frequency, the input signal can be sampled up to 37.5 MHz (the Nyquist frequency (fmax) = ½ the sampling frequency) [130]. The function is to convert the obtained analogue information such as the amplitude of the input signal to digital information, defined in numerical values concerning a reference signal produced by a DAC. The process includes digitisation and encoding, in which the signal is digitised by converting the electric voltage of the input signal into a set of coded binary electrical levels, and the digitised input signal is output in series (pulse-train) form and a parallel (simultaneous) form with the most significant bits first [131].
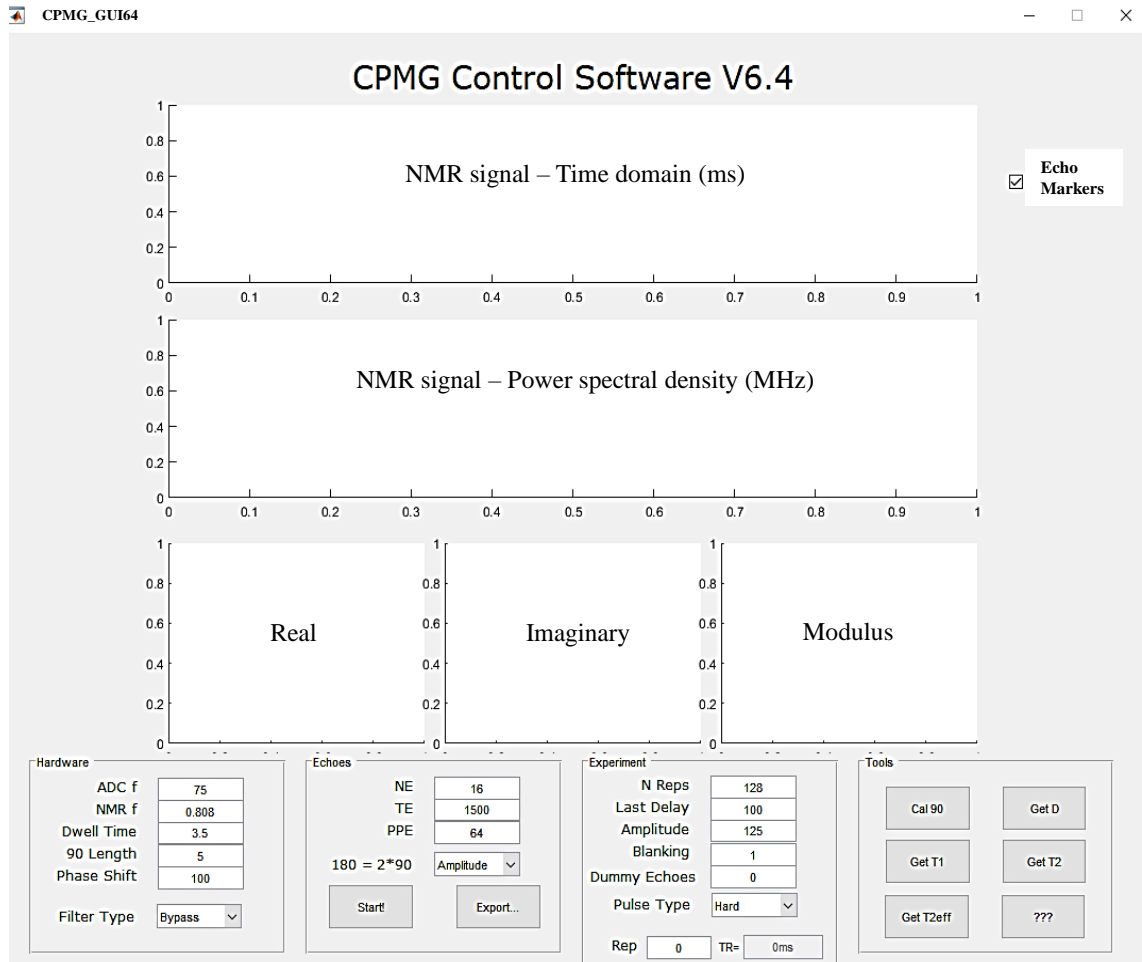
Figure 4.3: MATLAB GUI main front panel illustrates the basic parameters used to generate an NMR signal. The top two sections represent the plots for the time of and spectral density domains, respectively. The third section depicts images of the real, imaginary and modules components of the spin echo.

NMR frequency (f) is the desired spectrometer frequency in MHz, reflecting the NMR probe tuning circuit output (resonance frequency). The **DW** is the interval time between the sampling point ($\Delta = 1/ (2{*}\mathrm{f}_{max})$); a signal at f_{max} will have two data points per cycle and the sampling rate = (1/DW) KHz [73].

The **PPE** sampled per echo must be a binary number (2n) to be able to process the data using the fast Fourier transform (FFT) algorithm. Based on these acquisition parameters (DW and PPE), calculation of the acquisition time (AT) can be performed for the total amount of the time that the data are sampled for each experiment (AT= DW X PPE). An important means of obtaining a good spectrum is setting the desired spectral width (SW) of the stored baseband data. It represents the range of frequencies that are measured or the bandwidth of the measured baseband data. The SW begins from 0 kHz to 1/2 the sampling rate (SW= 1/2DW).

90 lengths (pulse width) represents the time duration of the excitation pulse in μs. This time should be calibrated each time there is a new probe and a different sample. The objective of this pulse is to rotate the net magnetisation from the equilibrium state (Z direction) into the x-y plane, where the magnetic moment loses the coherence and the FID signal produced. Moreover, it determines the bandwidth of the excited frequency.

Phase shift is the phase of the output signal in degrees. It determines the appearance axis of the applied magnetic field (B_1), which caused by the oscillating RF current in the coil [73].

The dialogue has two **filter types**: bypass (BP) and narrow. The BP filter permits the signals within the accepted frequency band to pass through and the signals above or below the cut-off frequency will be attenuated. The narrow bandpass filter isolates the spectrum's narrow region and has a bandwidth of less than 6% of the centre of the wavelength value.

NE represents the spin echo train in an experiment, reflecting the number of 180° pulses applied in the experiment. The optimum number of echoes to acquire the whole decay of the echo signal is equal to $((5T_2)/TE)$. This NE is separated by the **TE**, which is the time from the centre of the 90° RF pulse to the echo peak in μs. This time is equal to the delay time required for the FID to completely dephase and the delay time for the spin echo rephase after the 180° pulse. This parameter is related to the T_2 relaxation measurements.

N Reps. is the number of repeated scans, which are averaged at the end of the experiment.

TR is the time between 90° excitation pulses (refer to Figure 2.10). It is adjusted by the 'last delay', which is the time parameter between the end of the pulse sequence and the beginning of the next pulse sequence, consecutive scans, in a millisecond. It should be sufficiently long to facilitate a comfortable long recovery time, which is equal to 5 T_1.

Amplitude is the scaling factor for the excitation signal amplitude, which is the amplifying power applied to the RF signal before it is sent to the RF coil. **Blanking** is the span time before the excitation pulse, enabling the RF power amplifier to warm-up [130].

Pulse type: The hard pulse is a short and robust time pulse that rotates the total net magnetisation from the equilibrium state. The soft pulse is soft with a long time pulse that rotates part of the net magnetisation; it is used as a selective pulse.

4.2.1.1 Materials and methods

Part 1: The system was investigated using a sample of olive oil in a plastic transparent transfer pipette with a diameter of 14 mm placed in the coil. The experimental measurement was obtained using the CPMG pulse sequence in the MATLAB GUI window. The hardware section parameters were a B_1 frequency of 0.8705 MHz with a DW of 3.5 μs. The 90° pulse length was 5 μs, and the phase shift was 100 degrees. For the echo section, the parameters were 16 echo numbers, 6000 μs for the echo time, and the points per echo were 256. The experimental parts involved the number of the averaged scans, which was 256 to improve the SNR, the delay time was 100 ms, the total time for repetition was 196 ms, and the amplitude was 125 mV. The amplitude of the 180° pulses was twice the amplitude of the 90° pulses, but with a similar duration for both.

Part 2: The capability of the electronic system in differentiating between different materials was inspected. The tested materials were pure sunflower oil (Sainsbury Ltd., London, UK), olive oil (Sainsbury Ltd., London, Spain), $CuSO_4$ dissolved in distilled water (100 millimolar (mM)), superparamagnetic iron oxides dissolved in distilled water (SPIOs 0.1%) and still smart water (vapour distilled spring water with added electrolytes, Coca-Cola Enterprises Ltd., UK). Similar transparent transfer pipettes were used for each material. The CPMG pulse sequence was used to measure T_2^{eff} as it is a well known method for such measurements [3; 5; 34]. This process was repeated to create a train of echoes with an exponential envelope of time-constant T_2^{eff}. The use of this experiment and the averaging of results resulted in an improvement in the SNR. Thereafter, the value of the T_2^{eff} was calculated by first defining the modulus for the real and imaginary components of the spin echoes and then the modulus integration for each of the echoes. The T_2^{eff} was calculated as the decayed time constant using the mono-exponential fit to the time decay by adopting the Levenberg–Marquardt least-squares minimization.

The CPMG experiment parameters were 5 μs long RF pulses for both 90° and 180°, and the B_1 frequency was 0.8075 MHz with a 180° phase shift. The amplitude was 125 mV and an average of 256 scans was obtained. The NMR echo signal intensities were acquired using an interval time of 25 μs, with 8 points per 250 echoes. The echo time was 500 μs for the sunflower, olive oil, and $CuSO_4$, and 5000 μs for the SPIOs and still water. The repetition time was 225 ms for the sunflower, olive oil, and $CuSO_4$, 2250 ms for SPIOs, and 4750 ms for still water.

4.2.1.2 Results and discussion

The measured NMR quantities of a sample are restricted by the instrument noise limit and the permitted experimental time. Therefore, NMR experiment parameters should be set appropriately to acquire useful outcomes [63]. Numerous NMR experimental parameters trials were conducted until the first successful experimental test for the above described electronic system was obtained. The outcome was promising, and the NMR signal was produced from the olive oil sample, as shown in the time domain section in Figure 4.4, for which 16 spin echoes produced successfully.

One of the essential factors that produced this result was to assure that the magnetic field across the solenoid coil precisely matched the frequency of the resonating circuit, which was set at 0.8075 MHz in the GUI panel. This matching was achieved by measuring the MF inside the coil using a Gauss meter (Hirst Magnetics Instruments Ltd., GM08-2476, Probe PT11651, Cornwall, UK), and accordingly adjusting the current flow through the EMC to attain an MF equal to 18.9 mT at the centre of the coil. Moreover, the use of the correct pre-amplifier and low-pass filter permitted only the signals below 1 MHz to pass.
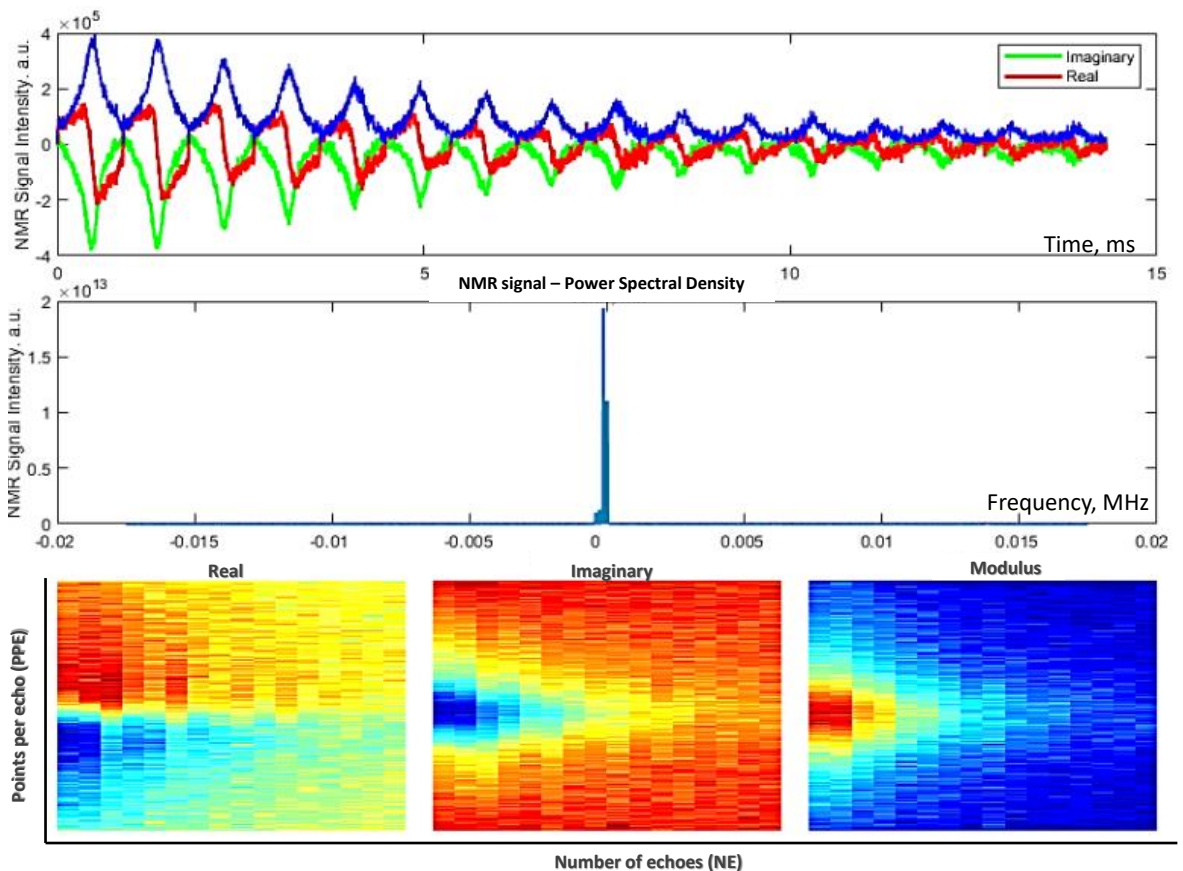
Figure 4.4: NMR signal obtained from olive oil sample using an EMC operated at 18.9 mT, which corresponded to $B_1 = 0.8075$ MHz. The SpinCore was connected to the TOMCO as the RF power amplifier and pairs for each of the off-the-shelf components: mini circuit ZFL-500LN-BNC and low-pass filter as the pre-amplifier. In the time domain section, the blue colour of the spin echoes represents the modulus integration for the real and imaginary components echoes.

Moreover, the efficiency of the electronic system in differentiating between different materials was investigated. Figures 4.5 and 4.6 show an example of the NMR signals that were acquired for the different sample viscosities: sunflower oil, olive oil, $CuSO_4$ (100 mM), SPIOs 0.1%, and still water. The right-hand side of the figure presents the echoes train generated by the CPMG sequence using the MATLAB GUI. The modulus of the real (red) and imaginary (green) components are represented as a blue overlay. The left-hand part shows the integrals of produced echoes in a red circle and the fit curve is in blue; the fit parameter is shown above the plot and the T_2^{eff} shows in μs. The time constant T_2^{eff} was extracted from the average of three measurements for each of the materials using the CPMG pulse sequence. Furthermore, Table 4.1 shows the averaged T_2^{eff} values for each material with the standard deviation (SD).
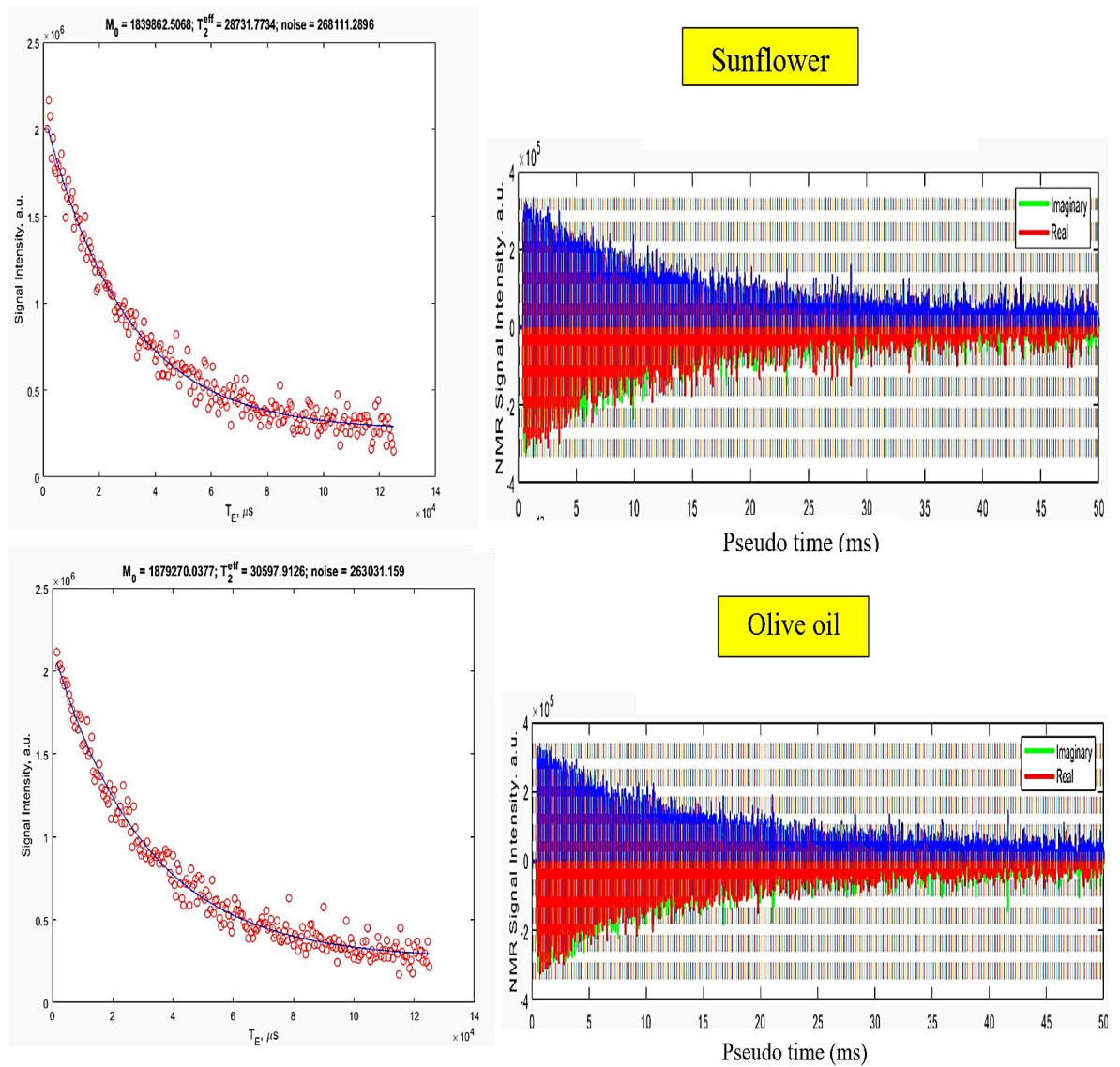
Figure 4.5: Estimated T_2^{eff} for sunflower oil and olive oil using the EMC operated at 18.9 mT and solenoid coil for NMR signal detection with a TOMCO RF power amplifier.
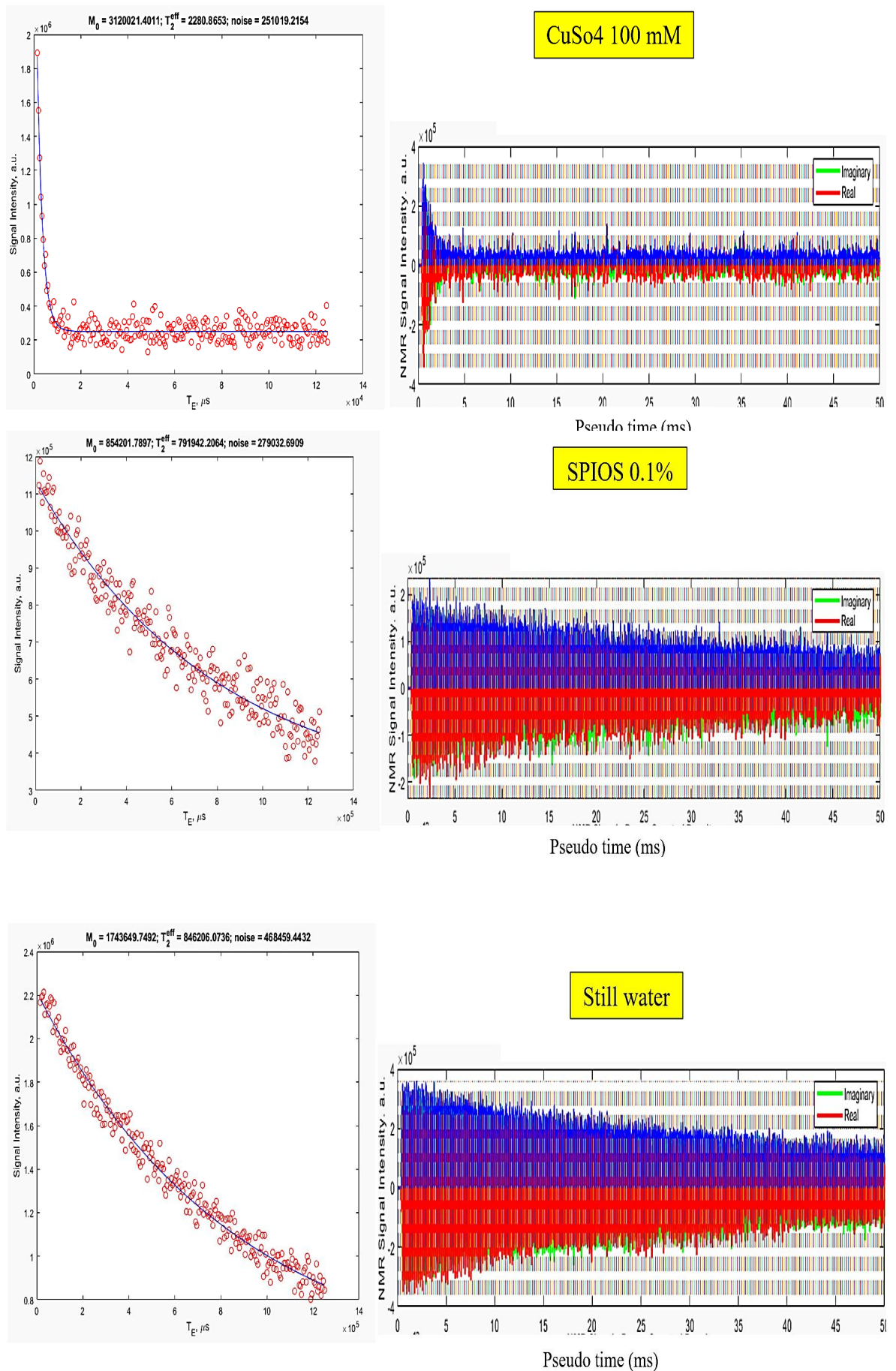
Figure 4.6: Estimated T_2^{eff} for different materials using the EMC operated at 18.9 mT and solenoid coil for NMR signal detection with a TOMCO RF power amplifier.

Table 4.1: T_2^{eff} values for different materials using the EMC operated at 18.9 mT with a TOMCO RF power amplifier

Material	T_2^{eff} (ms)	$\pm$SD (ms)
$CuSO_4$ (100 mM)	2.34	0.21
Sunflower oil	29	0.52
Olive oil	31	0.1
SPIOs (0.1%)	777	16
Still water	843	23

The estimated values of the T_2^{eff} for the different samples in this study were reasonable relative to their molecular compositions. The proton mobility of the sample was the main key factor affecting the effective spin–spin relaxation time. The T_2^{eff} values for olive and sunflower oils were relatively similar. However, they have different percentages of fatty acids, as indicated by Popescu et al. [132]. The results of this study agreed with those of Xu et al. [133], which indicated that both oils are relatively similar, but theirs had higher values, with the T_2 values being 65.5 ms and 67.5 ms for sunflower and olive oil, respectively. Nevertheless, the T_2 value of the sunflower was in agreement with another study [134], with the value ranging from 28 to 32 ms for the linoleic type of sunflower oil. Moreover, Santos et al. [135] indicated a T_2 value for olive oil of 44 ms using a Halbach array with a solenoid coil as a sensor. In this study, the T_2^{eff} lower values were most likely due to the different gradient strengths in the different types of sensors used and different echo times used in the different experiments, both of which contribute to the value of the T_2^{eff} (Equation 2.20). The precession of the system used here was observed to be effective in previous experiments where consistent values were observed for the same samples.

For $CuSO_4$, the acquisition time was set to be exceedingly long, resulting in higher noise and a lower SNR. Accordingly, a lower T_2^{eff} was obtained compared with the value obtained by Melville et al. [136], which was 9.6 ms. For SPIOs and still water, the transverse relaxation of protons in the sample that contained the SPIO nanoparticles had a lower value than water, and this was due to the nonuniform field generated by magnetic particles and consequently a faster dephasing of precessing spins in the x-y plane.

In summary, the developed electronic system sufficiently discriminated between the different compositions of the tested materials. These values are compared with the NMR measurement that was performed using the constructed single-sided NMR system in Chapter 5.

4.2.2 Electronic system using an operational amplifier

An Op-Amp is a versatile electronic device widely used in instrumentation applications owing to its low cost and high performance. It is a high-gain directly coupled voltage amplifier with differential voltage inputs and a single-ended output [137]. The differential inputs have opposite polarities, where the voltage V_{IN+} is the non-inverting input and the voltage V_{IN-} is the inverting input. Unlike the ideal Op-Amp, a practical Op-Amp is characterised by a finite gain for a defined bandwidth of frequencies, and outside this bandwidth, the gain will decline. Additionally, it has a finite input impedance and a low output impedance [138].

This section describes the employment of a modest Op-Amp in a simple form of an inverting design. The design involves only two resistors and a decoupling capacitor (Figure 4.7). The desired gain of the circuit can be controlled by selecting the correct values for the resistors, and the voltage gain can be calculated using the equation A_v= -(R(feedback)/R (in)) [137]. This design can effectively provide the front-end electronics for both an RF power amplifier and signal pre-amplifiers for frequencies below 1 MHz.

Figure 4.7: Schematic diagram of an inverting Op-Amp

4.2.2.1   Materials and methods

Similar to the experiment described above, the EMC, NMR probe, and SpinCore RadioProcessor have been used to produce the signal from an olive oil sample in a 14 mm diameter tube. All the measurements were performed using a CPMG sequence with the amplitude of the 180° pulses being twice that of the 90° pulses but with a similar pulse length durations. Figure 4.8 depicts the schematic diagram for the front-end electronics circuit; an inverting Op-Amp (Linear Technology LT1363 [139]) was used as an RF power amplifier and inverting Op-Amp (Linear Technology LT1222 [140]) as a pre-amplifier. The LT1363 Op-Amp is characterised by a high speed, low supply current, and significant slew rate with an outstanding DC gain performance. The LT1222 Op-Amp is characterised by low noise and high speed with a higher DC gain; however, it has a smaller current sourcing capability than LT1363 [71]. LT1222 circuit is stable in a noise gain of $\geq$10 without compensation. Both circuits of a voltage feedback amplifier (LT1363 and LT1222) provide excellent settled features with a single gain stage that makes them ideal options for data acquisition system, buffer, and cable driver applications owing to the capability of driving any capacitive load [139; 140]. Moreover, Figure 4.8 shows the use of a pair of back-to-back Germanium (Ge) diodes, which functioned as an effective duplexer owing to the low power requirement and appropriateness for battery-powered applications.

Figure 4.8: Schematic diagram for the inverting Op-Amp that represents the power amplifier (LT1363) and pre-amplifier (LT1222). All capacitors are of 0.1 μF, and the Ge diodes act as a duplexer. The NMR probe comprises the inserted sample coil, and tuning and matching circuit are marked by a dotted line.

The entire electronic system functioned as follows: the signal generated by the SpinCore

exited the RF output of the Radioprocessor board and was fed to the inverting Op-Amp circuit (LT1363) via a decoupling capacitor. The LT1363 circuit has a gain-bandwidth product of 70 MHz, and according to the value of the resistors used in this circuit, the produced gain is approximately 12, and the frequency bandwidth is 5.7 MHz. The required operational power supply for the RF power amplifier and the pre-amplifiers was $\pm$ 15 V. Therefore, the supply voltages for both amplifiers were a pair of Traco Power TSRN 1-24150 DC-to-DC converter/switching regulators. This power regulator enables a single dc supply from 16.5 to 42 V, which is an advantage of the application of battery power. These regulators were connected to a digital control DC power supply (TENMA^{TM}, 72-2630, UK) to supply the required voltage.

The output signal from the LT1363 amplifier was again decoupled and fed to the pair of the back-to-back Ge diodes, which formed a part of the duplexer that sufficiently isolated the transmitter output from the probe tuning circuit and pre-amplifier during the sequence of the receiving process. Additionally, it prevented the signal leakage from the SpinCore RF output from disturbing the detection circuit [71].

The olive oil sample was inserted in the coil of the previous home-built NMR probe, where the tuning and matching capacitor was fixed to yield a resonant frequency of 0.808 MHz. Similar to the previous setting, the NMR probe was placed in between the poles of an electromagnet coil to guarantee the accurate field for the tuned frequency at a current of 0.335 A.

Since the returning NMR signal from the coil was an order of magnitude smaller than the signal generated from the LT1363, other pairs of back-to-back Ge diodes were grounded to protect the pre-amplifier. Hence, the maximum voltage input to the pre-amplifier was restricted to 0.2 V, which offered efficient protection than the 0.6 V provided by Silicon (Si) diodes. The signal from the Ge diodes was fed to a simple inverting Op-Amp circuit (LT1222) through a decoupled capacitor. The LT1222 has a 500 MHz gain bandwidth product, and owing to the value of the resistors used in this circuit, the produced gain is approximately 340, and the frequency bandwidth is 1.47 MHz. Consequently, this circuit effectively served as a low-pass filter to prevent the noise of the high frequency from returning to the SpinCore. Moreover, this circuit was investigated by adding 1 MHz low-pass filters (ThorLabs, EF508) on the input and output of the LT1222 terminals, and an insignificant difference was observed.

An optimum 90° pulse duration length should be selected to obtain an optimal performance for the new front-end electronics. Therefore, a 90° calibration in the tool section in the GUI window was run to determine the optimum value, for which the amplitude power level was increased to 500 mV. The pulse duration was from 10 to 80 μs with eight increments, each increment being equal to 10 μs. The following experiment parameters were employed: a proton resonance frequency of 0.808 MHz with an interval time of 20 μs spaced by an echo time of 2000 μs. The PPE was 32, with

an echo number of 64. The TR was 228 ms with 128 average scans with a 270° phase shift. After the optimum 90° pulse duration was obtained, the NMR signal could be acquired.

4.2.2.2 Results and discussion

Since the 90° pulse is responsible for flipping the net magnetisation from the equilibrium state to the x-y plane, an accurate value for the pulse duration is critical. The pulse duration is primarily influenced by the following factors: the probe (type, dimension, and age), tuning (wrong tuning results in longer 90° pulses), voltage power supply to the front-end electronics (for which a higher power results shorter pulses), amount of the RF power delivered to the probe, type of power amplifier, and interrogated nucleus [141].

Therefore, for the current hardware configuration, a 90° calibration was used (Figure 4.9). The plot shows the optimum 90° pulse length value for the measured signal integral over a range of duration times. The peak value represents the optimum pulse duration value used in the NMR experiment, which was 40 μs in this scenario. As a first attempt, the LT1222 was used as an RF power amplifier with a power supply of $\pm$ 12 V, and the optimum value was 45 μs. As expected, when the RF power decreased, the pulse length increased.
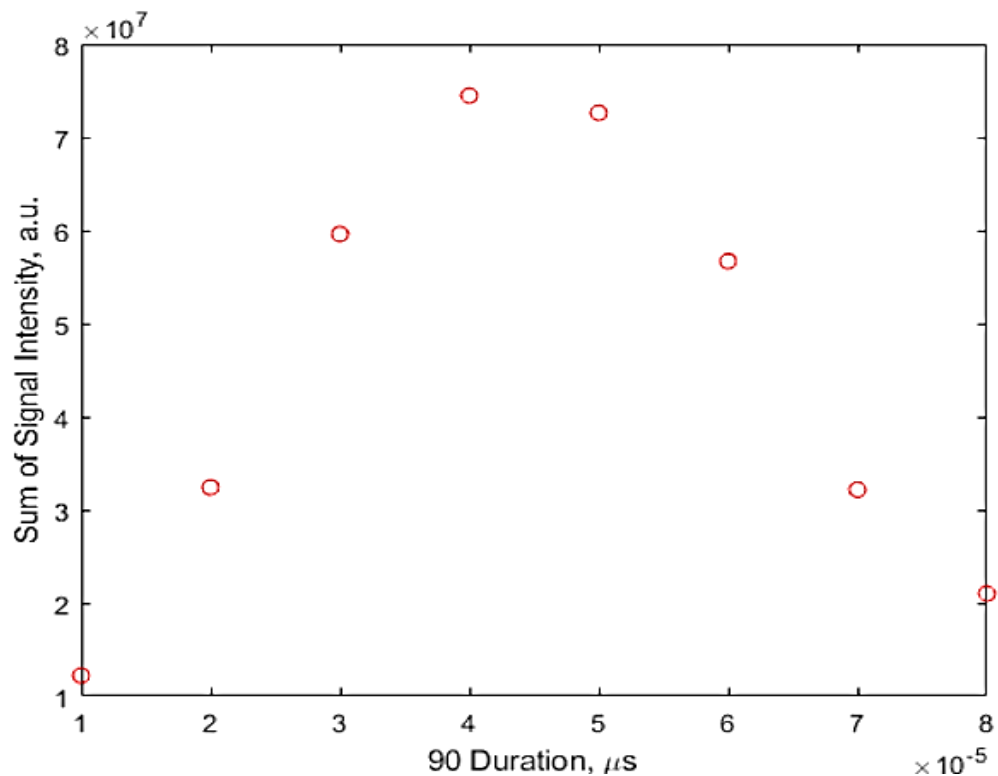
Figure 4.9: A 90 degree calibration demonstrating the optimum pulse length duration value at the peak (40 μs) using the LT1363 circuit as a power amplifier and the LT1222 circuit as a pre-amplifier.

Other trials were conducted with the LT1222 as an RF power amplifier, and the receiving channel circuit was similar to that described in Section 4.2.1. The optimum pulse duration was obtained at 57.5 μs (Figure 4.10). In this trial, the echo time was 1500 μs, PPE was 32 for 128 echoes, TR was 292 ms, and 64 average scans had a 180° phase shift. Again as expected, the hardware configuration affected the pulse duration.
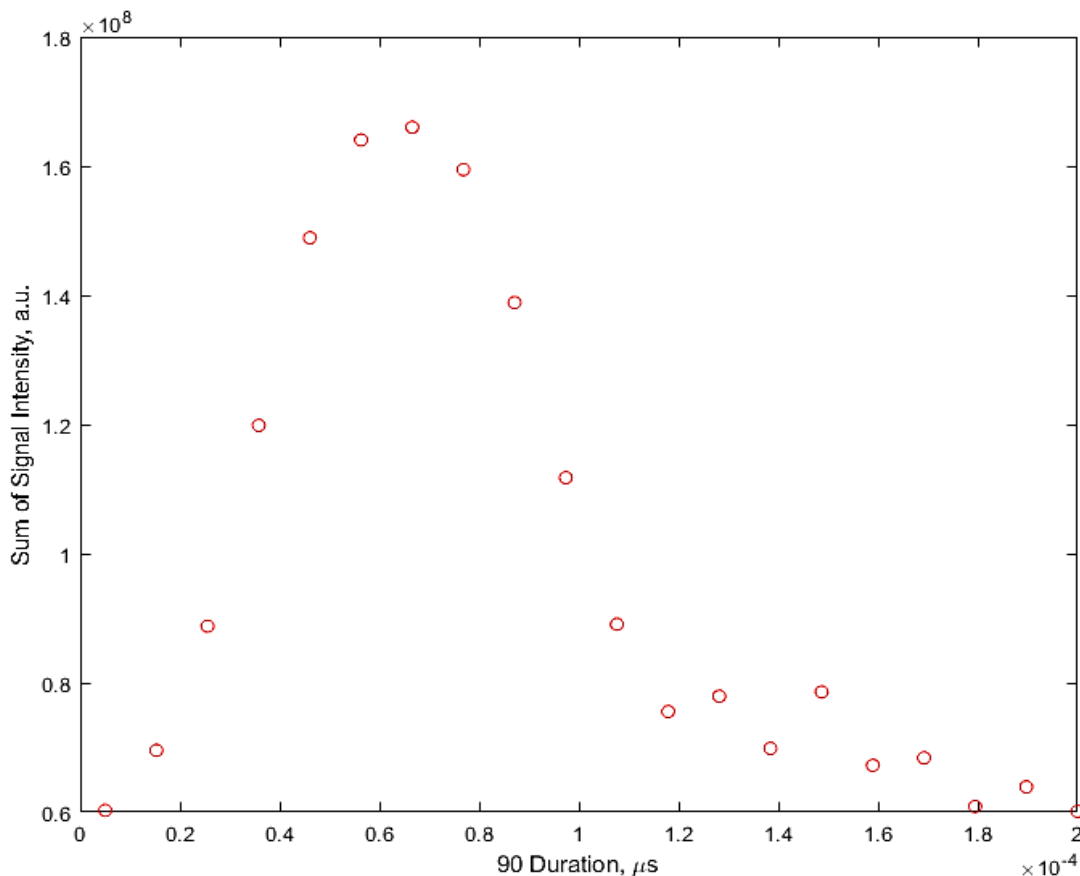
Figure 4.10: 90° pulse length calibration for the LT1222 as an RF power amplifier and off-the-shelf electronics as a pre-amplifier; the optimum value at the peak was 57.5 μs

After the optimum 90° pulse duration was obtained for the simple inverting Op-Amp electronic circuit, the NMR signal was produced with a pulse length of 40 μs (first section of Figure 4.11). Furthermore, similar to the method in Section 4.2.1.1, the effective spin–spin and spin–lattice relaxation times were extracted for the olive oil sample. Moreover, the echo train indicated that the first Hahn echo was slightly lower than the subsequent echoes, which is a common phenomenon for pulse NMR at low frequencies [71].
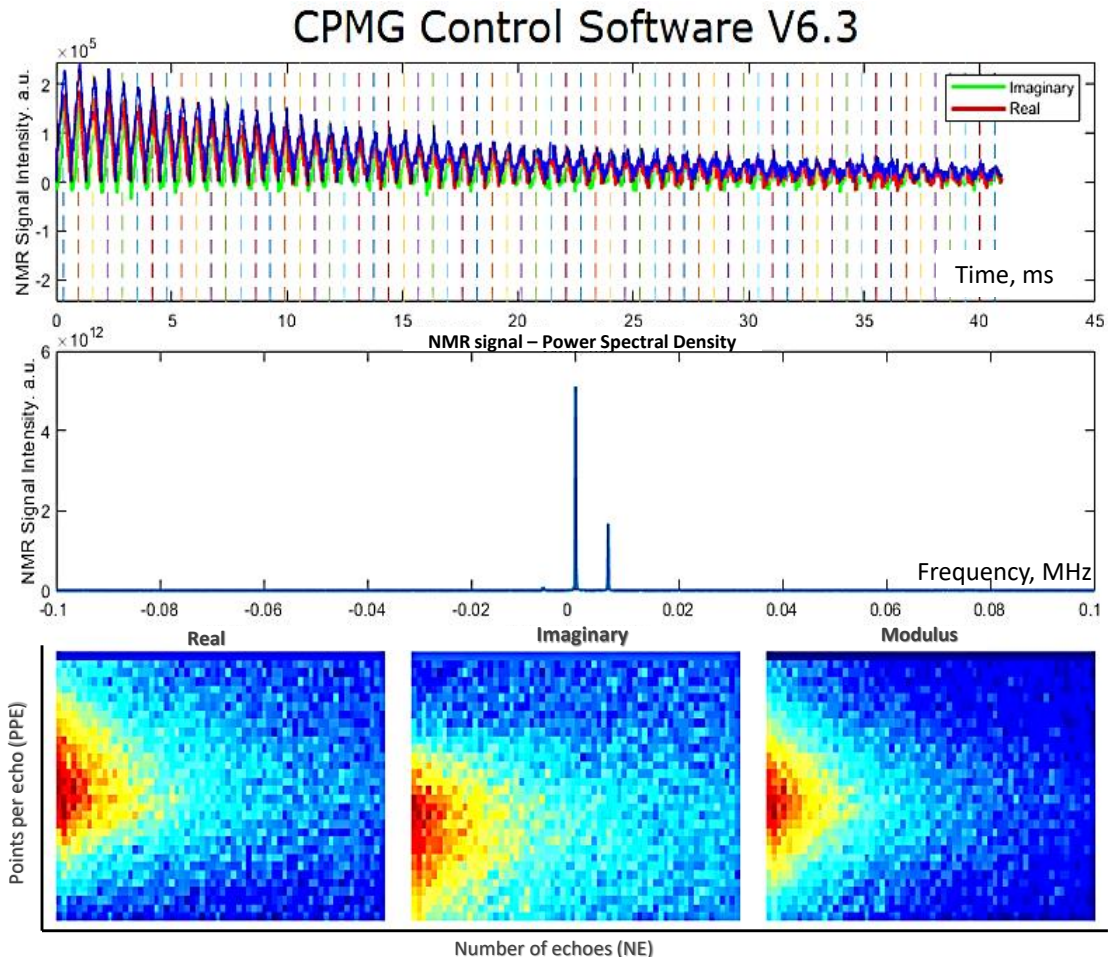
Figure 4.11: NMR signal of an echo train of 64 spin echoes with a T_E of 2000 μs obtained using the simple inverting Op-Amp LT1363 circuit as a power amplifier and LT1222 as a pre-amplifier at a pulse length of 40 μs.

The NMR signal in Figure 4.12 was obtained using a CPMG sequence with front-end electronics composed of LT1222 as a power amplifier and the off-the-shelf electronics as a pre-amplifier. The employed pulse duration was 57.5 μs. Moreover, the initial Hahn echo was similar to one observed in Figure 4.11. Additionally, the reader can notice that in the time-domain section, the real and imaginary components are flipped to the negative direction; this was because a different phase shift was applied, which was 180°.

Moreover, to verify the capability of the Op-Amp electronic circuit to be operated only with the power of the battery, the experiment was conducted using two different power supplies to produce the NMR signal. Therefore, a battery power of $\pm$ 18 V and the TENMA^{TM} digital DC power supply were used for this experiment (Figure 4.13). As shown in the time and frequency domain sections in Figure 4.13, the generated NMR signal intensity via battery was similar to the NMR signal intensity produced by the digital DC power supply. The experimental parameters used for this comparison were identical to those in Figure 4.10, but with a higher number of points per echo (64)

and lower echo numbers (16) that were spaced by 2000 μs. The pulse duration was increased to 45 μs owing to the increased distance between the EMC poles, which was 10 cm instead of 5 cm, as in the previous setting.

As a consequence of the distance increase between the poles, the EMC current power supply was increased to 0.795 A, to maintain the magnetic field of 0.804 T at the coil centre. The repetition time was 132 ms, and the number of the averages scans was 512. The result shows that the Op-Amp circuit can be employed in the fields where battery power is required.
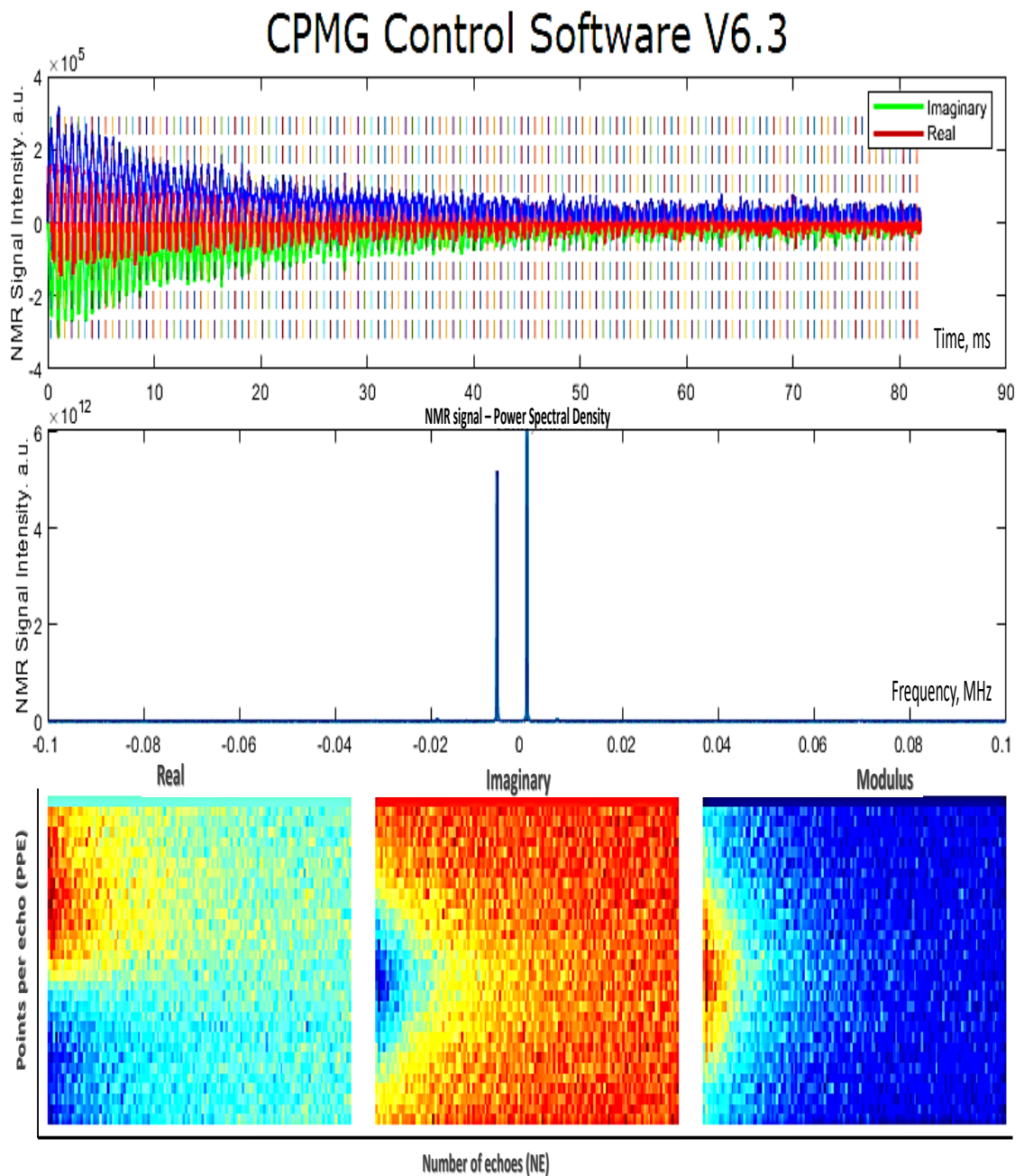
Figure 4.12: NMR signal of an echo train of 128 spin echoes with a TE of 1500 μs obtained using the simple inverting LT1222 Op-Amp circuit as a power amplifier and off-the-shelf electronics as a pre-amplifier at a pulse length of 57.5 μs.
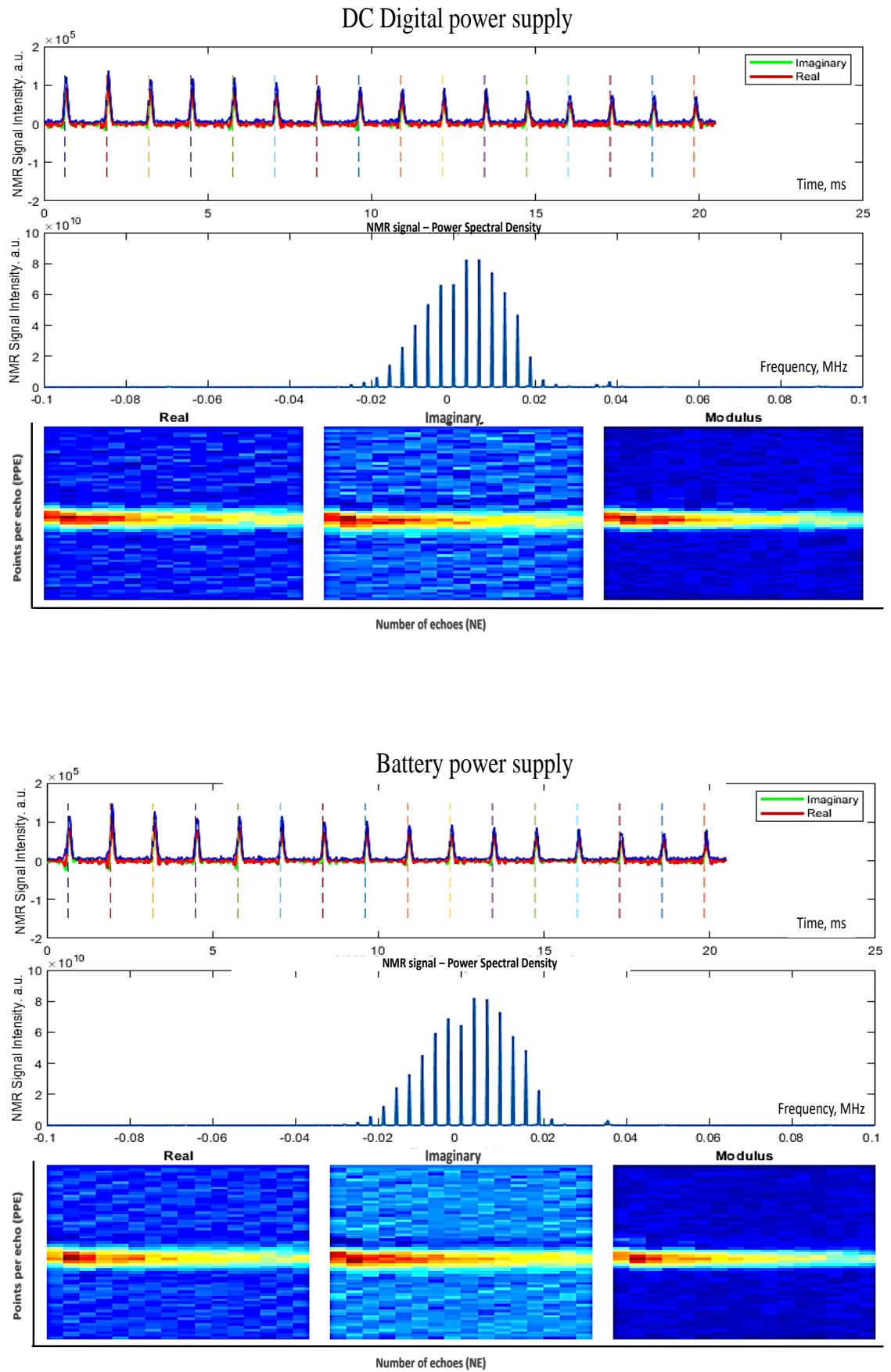
Figure 4.13: NMR signals of an echo train of 16 spin echoes and 64 points per echo were produced using two different power supplies for the inverting Op-Amp circuits; the digital DC power supply and a ± 18 V battery.

The simple inverting Op-Amp circuits exhibited an excellent outcome at frequencies below 1 MHz. The NMR signal gain using this lower power front-end electronics was comparable to that of the NMR signal obtained from the commercial amplifiers. Table 4.2 lists the signal intensities acquired for the different front-end configurations. Additionally, it shows how the 90° pulse duration was affected by the type of the utilised external units amplifiers, regardless the use of the similar NMR probe, static MF, and the sample in all experiments.

Table 4.2: NMR signal intensities for the front-end SpinCore electronics associated with the electronic system.

RF amplifier+Pre-amplifier	Time domain (a.u)	Spectral density domain (a.u)	Pulse length (µs)
TOMCO+two ZFL500LN	$4x10^5$	$2x10^{13}$	5
LT1363+LT1222	$2x10^5$	$6x10^{12}$	40
LT1222+one ZFL500LN	$4x10^5$	$6x10^{12}$	57.5
LT1363 + LT1222 (Digital power)	$2x10^5$	$10x10^{10}$	45
LT1363 + LT1222 (Battery power)	$2x10^5$	$10x10^{10}$	45

A relatively homogeneous magnetic field was used in this study through a laboratory electromagnetic coil to produce the NMR signal information. For applications that required battery power, permanent magnets would be more convenient, but it would result in less homogeneity. This might require a stronger amplification power that can be provided by the LT1363 Op-Amp.

The Op-Amp amplification circuits are an inexpensive external unit that cost less than $20 compared with the off-the-shelf RF electronics components that cost more than $1000 [71]. This is because the Op-Amp can be designed precisely to the required frequency, whereas the capability of commercial electronics is more comprehensive, for which a broader range of the frequency than is required for a specific application and higher power than it requires can be manipulated, which demands a delicate and expensive design of duplexer. Furthermore, as mentioned earlier, the bandwidth of the LT1222 circuit can function as a pre-amplifier and filter for RFs above 1 MHz. Hence, no low-pass filtering is required compared with commercial RF units.

Finally, note that the flexibility and the straightforward construction of the Op-Amp circuit and the hardware and the home-built software could facilitate other potential applications such as in electronics education and biomedical engineering.

4.3 Conclusion

The primary aim of the developed electronic system was a combination with the newly constructed planar magnets. The new planar magnet provides an in-homogeneous field along with the planar coil. Therefore, an optimization of the experimental parameters is required. For example, the 90° pulse duration is expected to be longer, as a trade-off due to probe construction and design [141].

This chapter presents an electronic system successfully operated at a frequency below 1 MHz using a comparatively homogeneous magnetic field for both the static and oscillating frequency fields. Two types of front-end electronics were used: a typical system composed of commercial units and a simple inverting Op-Amp. The external units were associated with the core electronic system (SpinCore), and both provided reliable NMR signal measurements. However, the current hardware system is not portable because the weight of the laboratory electromagnetic coil; it can be utilised as a bench-top spectrometer for different applications.

Chapter 5

NMR-CAPIBarA construction, evaluation, and optimisation

5.1   Introduction

Changes in the values of the NMR relaxation time parameters for the placenta have been reported as early as 1998 [101; 102] utilising clinical MRI. Later research confirmed the 1998 findings and revealed that for both the transverse and longitudinal relaxation times, the relaxation time value reduced as the placental gestational age increased [48; 100]. Further, they showed that these values were lower in the compromised placenta in comparison with the healthy placenta. Thus, this change in relaxation time values during pregnancy could be considered an early indicator of placental disease such as preeclampsia (PE).

Despite this, MRI is not as routine as ultrasound because of the reasons mentioned in Chapter 1, such as cost and availability. Whereas the average price of an MRI scan is over \$2500, an ultrasound image costs approximately \$263 on average [142]. Hence, it is not surprising that the ultrasound technique is employed as a routine scan to monitor the health of the placenta throughout the pregnancy. Although ultrasound imaging is performed at several points during pregnancy, this technique alone is not capable of providing sufficient information about placental diseases at the early stages before they have progressed. Nevertheless, it is a useful technique that can help in locating the placenta with ease. Therefore, developing a simple appliance that can provide relaxation time measurements of the placenta as a supplementary tool to ultrasound could serve as a rapid diagnostic approach, helping to recognise mothers at high risk of PE and monitor them closely.

The low-field unilateral nuclear magnetic resonance (NMR) technique has gained considerable popularity in different applications such as biomedical science and in-situ

patient health monitoring, due to its low cost, portability, and versatility. In these applications NMR experiments such as relaxation time measurements have been performed at a single point in space regardless of the field inhomogeneity and the low SNR [3; 5].

In the light of this, the main aim of the current work is to present the development of a low-field unilateral NMR device called NMR-CAPIBarA: Clinical Assessment of Patients Implemented with Bar magnet Arrays. This chapter describes the hardware construction, evaluation steps, and optimisation. The developed unilateral magnet system is operated at a magnetic field of 18 mT, which corresponds to a frequency of 0.766 MHz. The apparatus comprises an open access magnet that can accommodate pregnant women, where the patient is probed from a single side. Consequently, the placenta can be interrogated by measuring the transverse and longitudinal relaxation times remotely, and at a distance sufficient to reach the anterior placenta of an average pregnancy.

5.2 Planar magnet construction

The focus of this work is on the class of sweet-spot magnets, which produce a homogeneous magnetic field comprising a saddle region. In this region, the gradient of the magnetic field is close to zero. The local homogeneity of the saddle region located along the axis perpendicular to the magnet surface is much larger than that of the sensitive area generated in a high-gradient magnet, such as the NMR-MoUSE [3; 33]. This class of magnets allows a larger sensitive volume to be measured using a fixed RF power and bandwidth. Moreover, the greater uniformity in the magnetic field across the sample reduces the signal attenuation caused by the spin's diffusive motion. This is valuable when measuring a sample with significant free fluids such as human tissue.

Therefore, the planar magnet arrays were constructed using a similar design as proposed by Dabaghyan et al. [5], but with a fewer number of larger magnet blocks. This part of the hardware system was constructed based on the principle of the anti-parallel dipole model [79]. It consists of two equal and oppositely directed dipoles that are spaced apart from each other, and like the NMR-MoUSE, it provides a static magnetic field (B_0) parallel to the magnet surface. This configuration is more convenient for pregnant patients, as the patient can be probed from a single side.

Each magnet array is contained within an acrylic grid, with one layer consisting of a five by two grid of permanent magnets. Each assembly contains 10 cubic N52 neodymium magnets (first4magnets.com, F335-N52-R); each cubic magnet is 50 mm in length, 50 mm in width, and 25 mm in height. Each assembly is 274 mm long, 104 mm wide, and 25 mm high, and the maximum separation between the inner edges of the assemblies is

300 mm. An aluminium frame is used to house and slide the two rectangular magnet arrays. Figure 5.1a illustrates the design of the aluminium frame with the magnets array using the software called SolidWorks, and Figure 5.1b shows a photograph of the constructed planar magnet arrays.

a

b
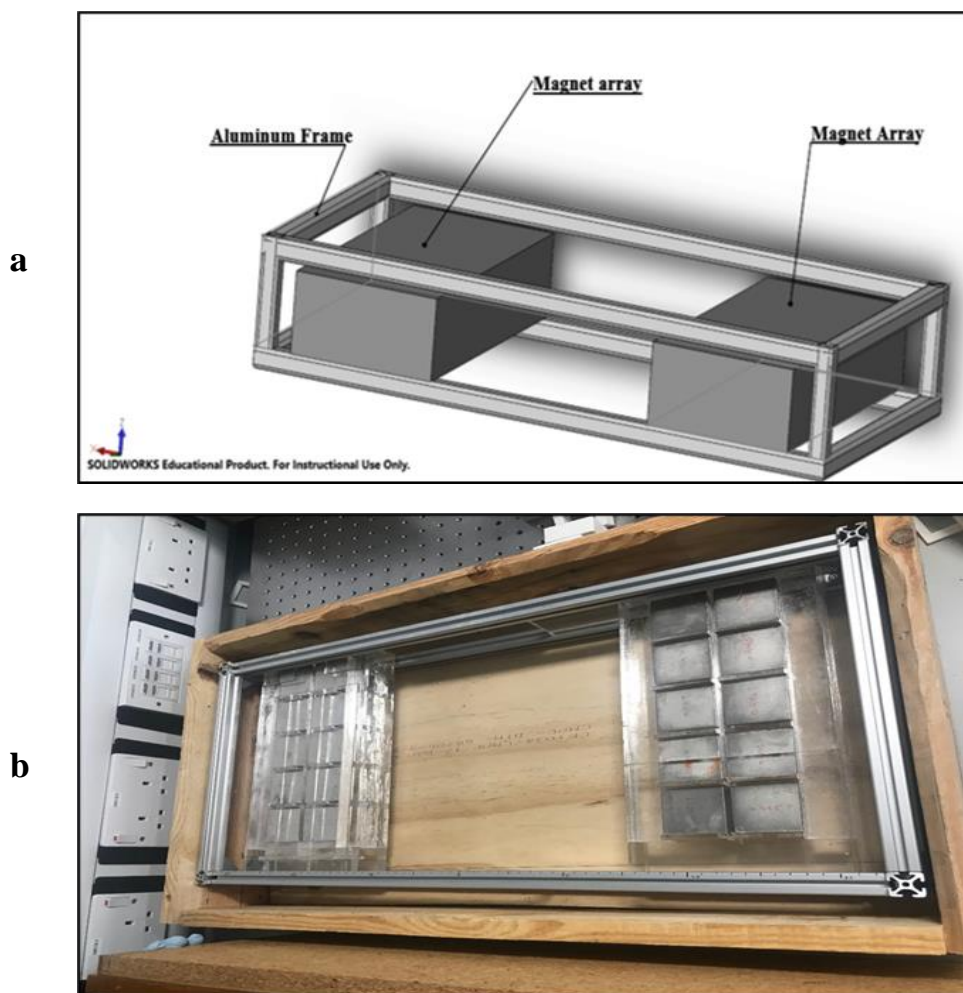
Figure 5.1: a) SolidWorks schematic diagram of the aluminium frame with the magnets arrays. b) The planar magnet after construction.

5.2.1   Theoretical identification of the sweet-spot

Pulyer et al. [79] developed a framework for comparing the relative efficiency and the distance to the saddle point for different dipole magnet configurations. For the model of the anti-parallel dipole, the remote saddle point is generated at a distance equal to (a/2) above and below the central gap of the two dipoles, the magnet arrays, where the dipole is located at the centre of the blocks of the permanent magnet. The distance between the centre of two anti-parallel dipoles is equal to (2a). The existence of a saddle point requires that the aspect ratio of (a/h) should be more than one, where h is the height, the thickness, of the magnet arrays [5]. The effective penetration depth (b) of the saddle point is located at b = (a - h)/2, which is called the sweet-spot. Figure 5.2 shows the geometrical schematic diagram of the anti-parallel permanent magnet arrays, where the most uniform field, the sweet-spot, was theoretically calculated and located at a distance equal to 76 mm from the surface of the magnet arrays.
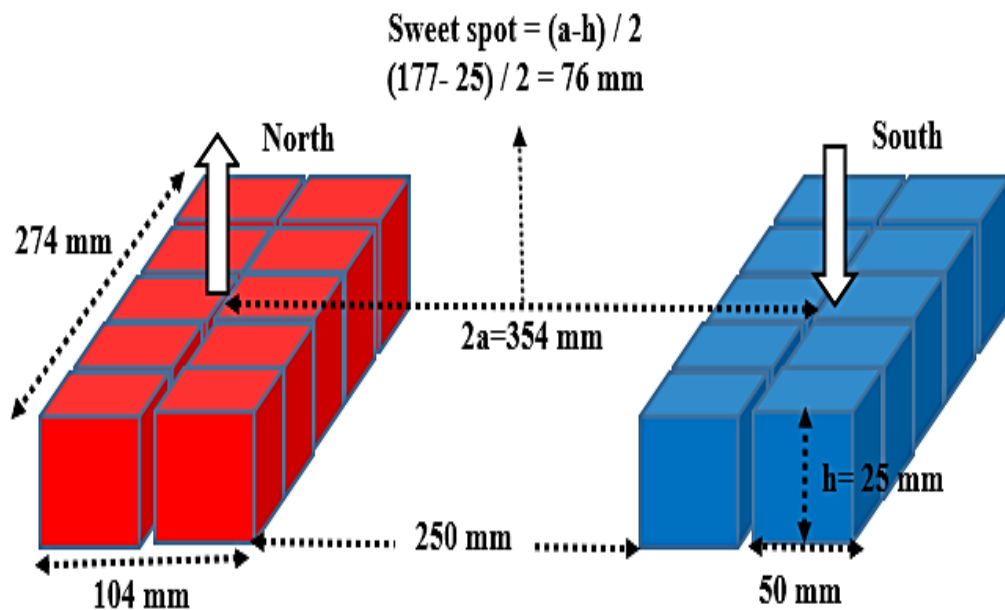
Figure 5.2: Schematic diagram of the constructed anti-parallel planar magnet arrays, the NMR-CAPIBarA, showing the design geometry and the location of the sweet-spot at 76 mm from the surface of the magnet arrays.

5.2.2 Experimental identification of the sweet-spot

Quantitative information on the small variation in the magnetic field over the measuring region is essential to define the most uniform region. Therefore, to define the position of the sweet-spot and the corresponding magnetic field (MF) strength at that position, a mapping for the MF profile was conducted manually at the centre between the two magnet arrays. The equipment utilised for these measurements was a Gauss-meter, the GM08-2476, with a transverse (PT11651) and an axial probe, in addition to a home laser-cut acrylic map sheet which is positioned at different heights from the surface of the magnet arrays, the depth direction. Figure 5.3a shows a photograph of the acrylic map sheet that contains 49 hollow acrylic rods, and Figure 5.3b depicts the position of and the distance between the rods.
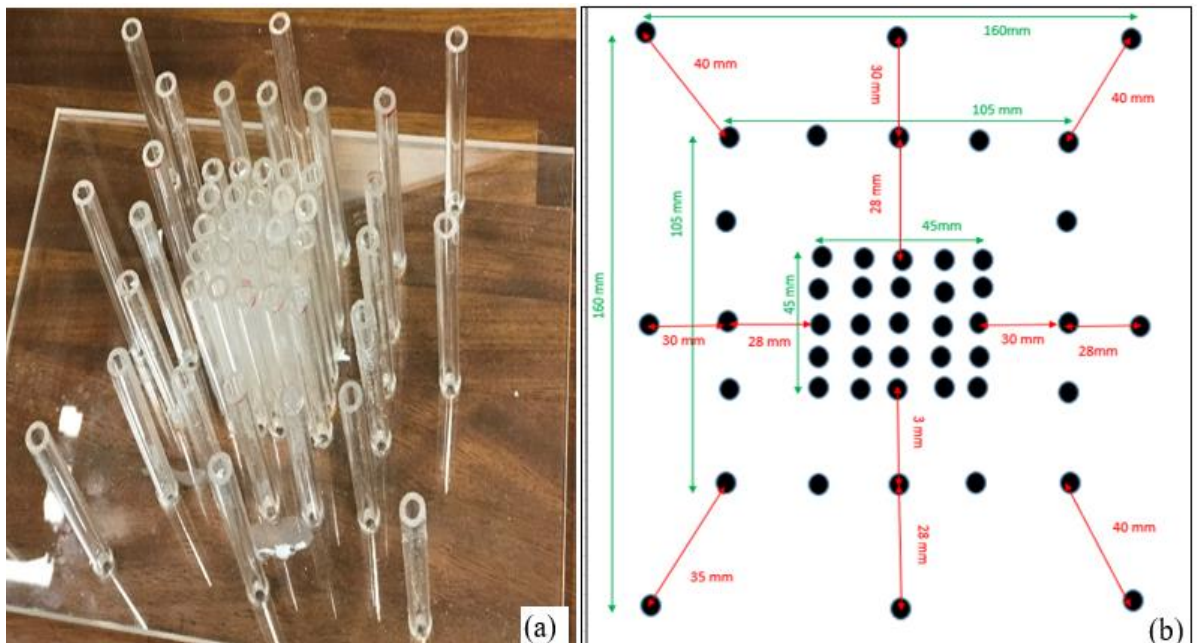
Figure 5.3: (a) Photograph of the acrylic map sheet and (b) schematic diagram for the acrylic map sheet indicating the distance between the rods.

5.2.2.1 Magnetic field mapping inside a metallic box

As an initial step, the magnet arrays were placed inside a metallic box to isolate any external noise (Figure 5.4). The magnetic field that projected above the magnet arrays was measured in the two axes X and Y using the transverse probe after which the measurement was repeated with an axial probe. The two magnet arrays were spaced apart by 250 mm, and all the measurements were conducted at five different heights from the surface of the magnet: 26, 50,74, 98, and 122 mm. The measurements

conducted at the Y-axis were not considered because most readings were zero; this is because the direction of the probe was parallel to the magnetic field.

The average of the three measurements in each hole in the acrylic tube was calculated for both probe types. The data analysis was then conducted in three steps to determine the location of the sweet-spot appropriately and compare it with the theoretical calculation. First analysis was begun by identifying the position of the most homogeneous region in the MF map sheet, which contains the flattest curve at all depths. Second, the depth and the area size that involves less variation in the MF strength was determined. Third, the shape of the homogeneous field at the centre was defined.

Figure 5.4: The metallic box containing the constructed magnet assembly.

To locate the region of the flattest curve for the magnetic field at the previously mentioned distances above the arrays, an analysis was performed on the X-axis data of the rods located along the middle line of the acrylic map sheet from the left to right side. As shown in Figure 5.5, points 1 and 9 represent the MF measurements in the hole of the middle rod, while point 2 represents the average measurements of the three middle rods, as well as those of the other points: 3, 4, 5, 6, 7, and 8. Figure 5.6 shows that the most homogeneous field is located at the centre of the acrylic map sheet for all depths, which represents the central line between the two magnet arrays. Further, the profile across the gap direction exhibits a curve shaped like a soup dish near the magnet surface, at a distance of 26 mm, and flattens out with increasing distance, as seen at a distance of 122 mm, which agrees with other research studies [2].
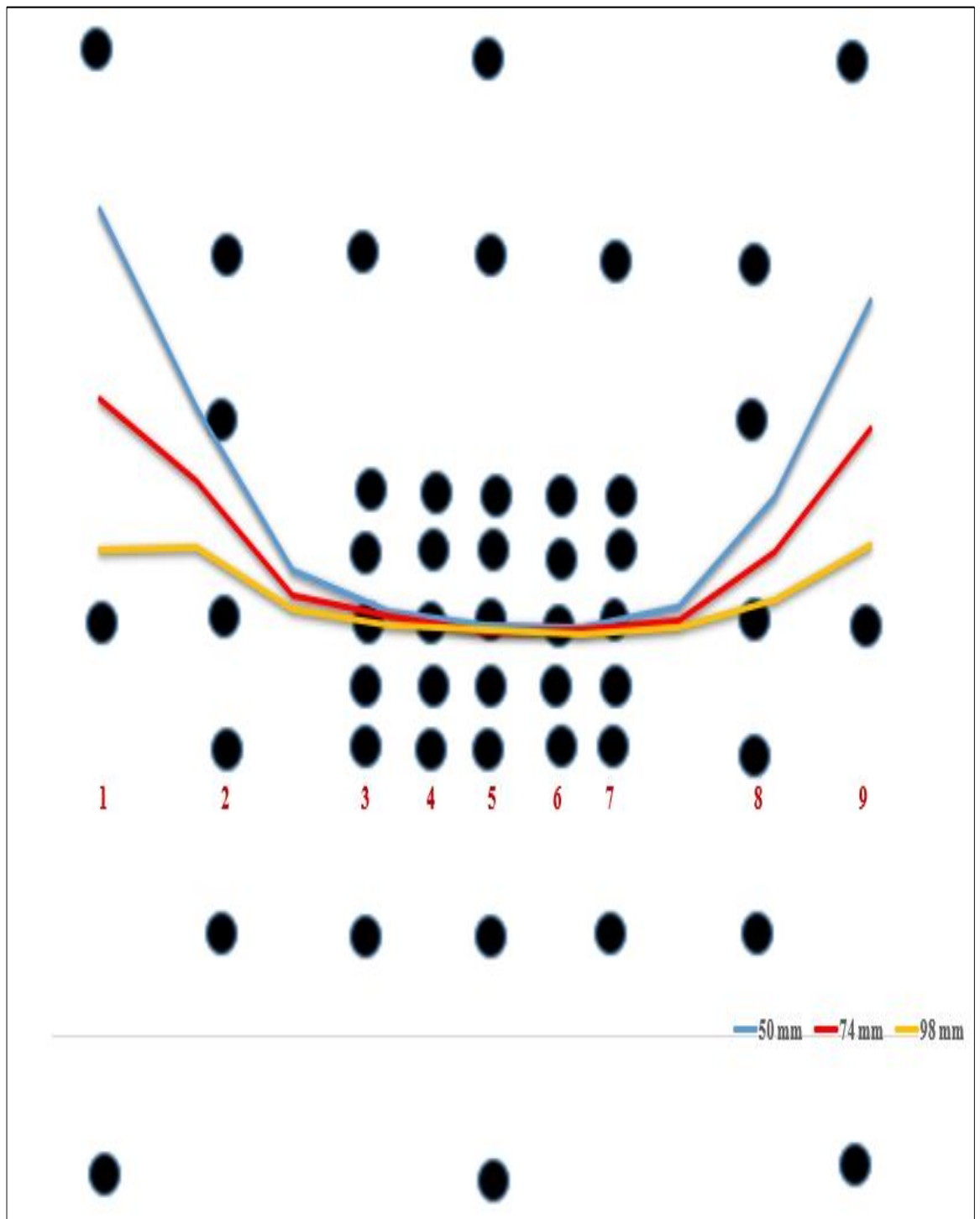
Figure 5.5: Schematic diagram of the magnetic field map sheet that shows the location of the flat curve of the magnetic field. The points from 1 to 9 represent the collated measurements along the centre line, while the coloured curves illustrate the plot of the measured magnetic field at different depths of 50, 74, and 98 mm.

	1	2	3	4	5	6	7	8	9
26 mm	60.40	26.17	15.06	13.33	12.44	12.28	12.82	19.53	40.20
50 mm	46.77	32.34	23.87	22.11	21.60	21.50	22.31	27.39	39.47
74 mm	32.93	28.22	22.77	21.91	21.27	21.38	21.71	24.68	31.03
98 mm	24.83	24.93	22.23	21.56	21.33	21.21	21.46	22.58	25.00
122 mm	16.17	18.07	17.12	16.77	16.71	16.61	16.78	16.92	17.80
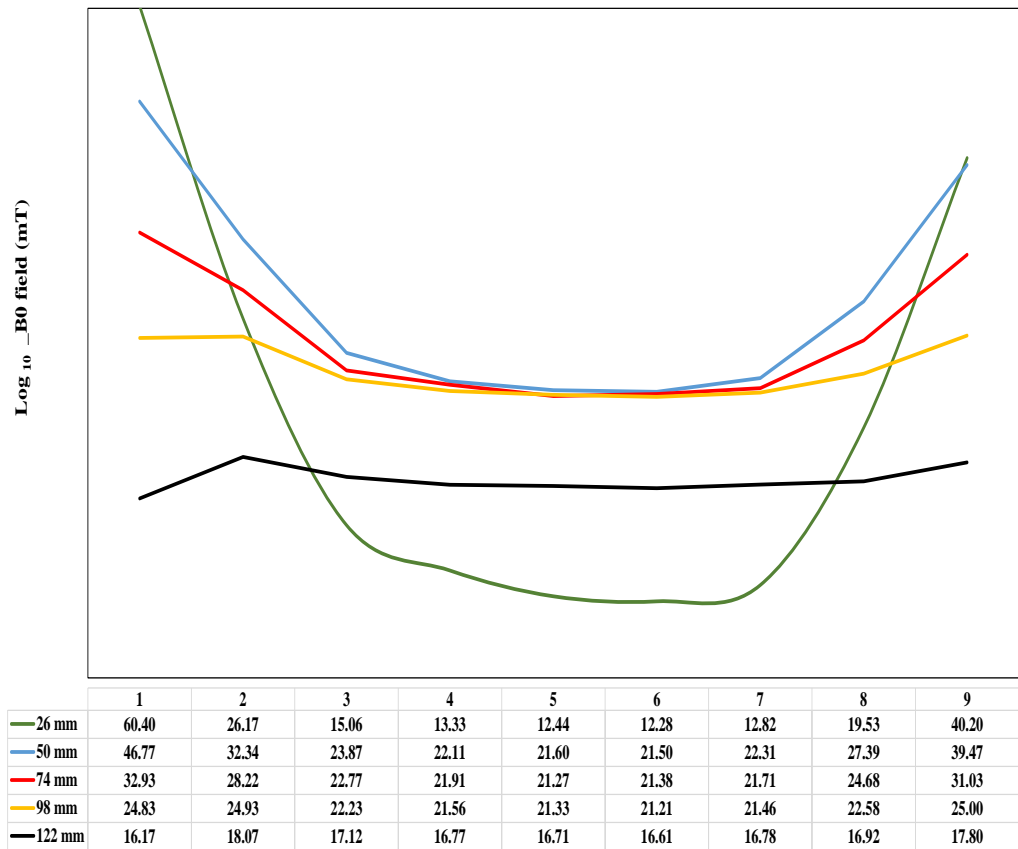
Figure 5.6: Coloured curves for the magnetic field created from the X-axis measurements at five different heights from the magnet arrays. The table lists the averaged value of the strength of the magnetic field at different points (1 to 9) on the acrylic map sheet for each height.

To identify the area of the most homogeneous field and the position of the sweet-spot, five different areas (A) in square millimeters (mm^2) were selected: 25600, 11025, 2025, 1125, and 575 mm^2. Figure 5.7 illustrates the chosen area for each measurement in the acrylic map sheet. The analysis for the data was extracted from the measurements of the MF strength performed on the X-axis using the transverse probe and the axial probe. The average of three measurements in each hole of the acrylic tube was calculated, and then an average value was taken for the selected area from each rod that was included in that region, as shown in Table 5.1 for the transverse probe and in Table 5.2 for the axial probe. This data analysis was repeated for all measurements applied at different heights from the magnet surface.
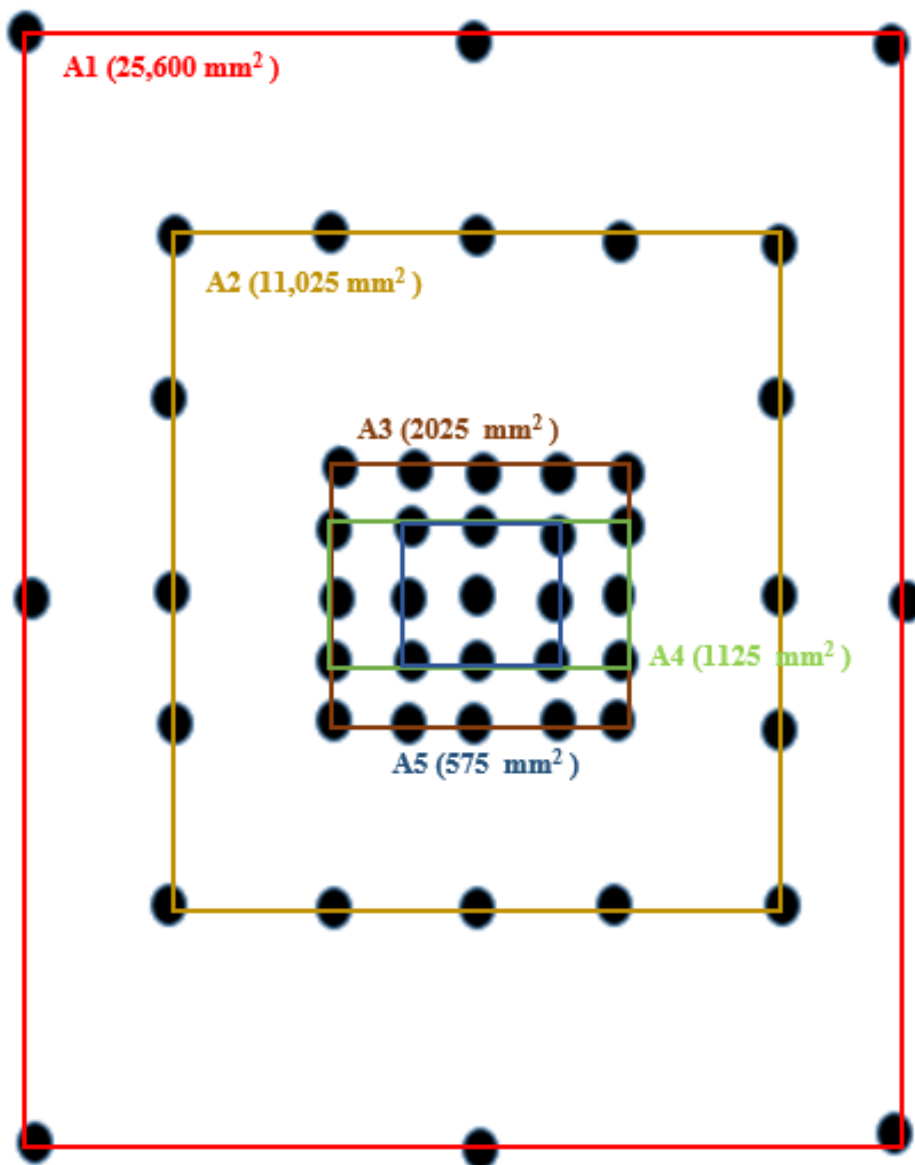
Figure 5.7: Schematic diagram of the various sizes of areas measured in the acrylic map sheet.

Table 5.1: Planar magnet field map measurement inside metallic box on X-axis using the transverse probe.

Depth (mm)	A_1 (25600) (Avg±SD) mT	A_2 (11025) (Avg±SD) mT	A_3 (2025) (Avg±SD) mT	A_4 (1125) (Avg±SD) mT	A_5(575) (Avg±SD) mT
26	37.43±14.26	24.58±4.51	20.00±0.67	20.14±0.68	19.69±0.27
50	34.86±11.35	26.19±4.53	22.23±0.88	22.28±0.90	21.74±0.35
74	26.43±5.65	24.03±3.01	21.75±0.57	21.81±0.57	21.52±0.34
98	22.17±2.667	22.27±1.83	21.49±0.41	21.56±0.39	21.37±0.20
122	15.38±1.45	16.67±1.03	16.80±0.28	16.80±0.24	16.70±0.16

Table 5.2: Planar magnet field map measurement inside metallic box using the axial probe.

Depth (mm)	A_1 (25600) (Avg±SD) mT	A_2 (11025) (Avg±SD) mT	A_3(2025) (Avg±SD) mT	A_4 (1125) (Avg±SD) mT	A_5(575) (Avg±SD) mT
26	8.25±6.31	6.70±3.69	2.20±1.41	2.18±1.44	1.17±0.83
50	5.21±5.06	1.01±0.50	0.66±0.40	0.69±0.41	0.45±0.32
74	10.13±6.78	3.35±2.33	1.15±0.87	1.24±0.86	1.24±0.60
98	10.27±6.68	4.80±2.84	1.45±0.87	1.44±0.89	0.83±0.57
122	9.65±5.88	5.35±3.57	2.50±1.83	2.55±1.85	2.48±1.19

As anticipated, the analysis of the transverse probe along the X-axis showed that the variation in the magnetic field strength decreased with the reduction in the size of the measured area at all depths. For instance, at a depth of 74 mm from the magnet surface, the variation in the magnetic field of area 25600 mm^2 was 5.65 mT in compared to that for the area of 575 mm^2 which was 0.34 mT. Moreover, the intensity of the magnetic field reduced as a function of depth, as can be seen in Figure 5.8. In addition, with a glance at the profile plot across the depth (Z-axis), one can observe that the intensity values of the magnetic field vary less at depths of 50 mm, 74 mm, and 98 mm for the area of 575 mm^2.

Planar magnetic field map using transverse probe for selected areas at different depths
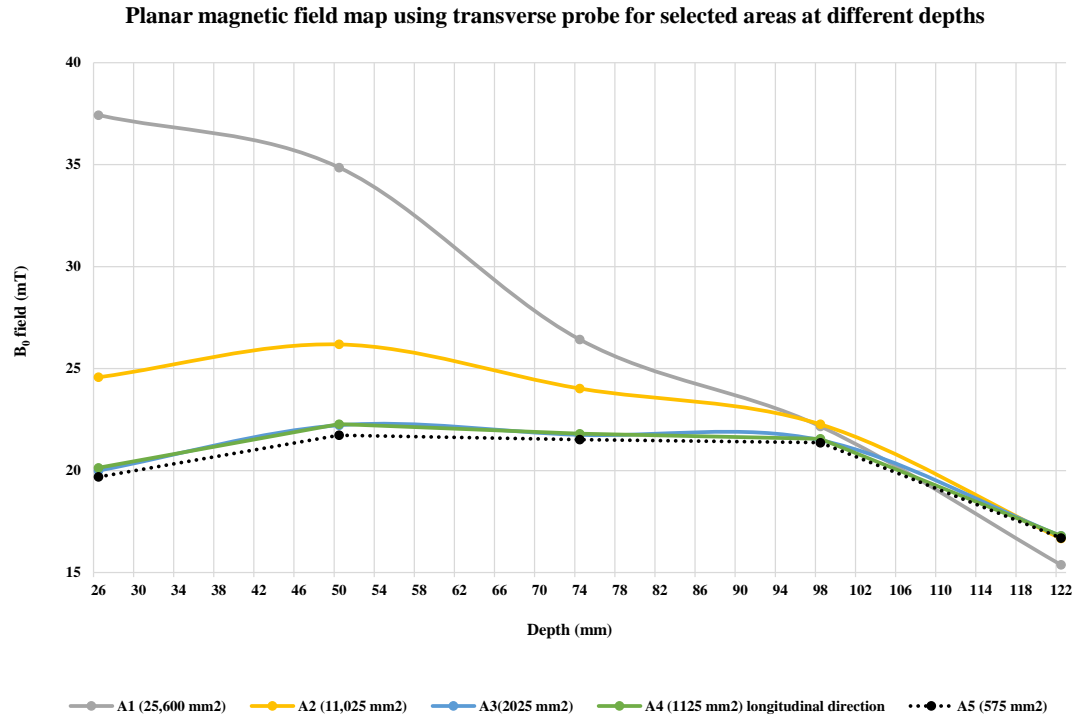
Figure 5.8: Plot of the magnetic field (B_0) profile across the depth (Z-axis) in mm for the various areas in square millimeters. The dot points represent the measurements using the transverse probe along the X-axis at different depths. The straight line connects the measured values.

When comparing the above finding with the data analysis generated from the axial probe in Table 5.2, The results show that the lowest variation in the strength of the magnetic field was at depths of 74 mm and 98 mm from the magnet surface. Besides, this decreases as the area of size decreases. This is in agreement with the theoretical calculation of the sweet-spot, which was 76 mm.

The final study was conducted on the field homogeneity in the central region of the map sheet. The measurements for the area of 1125 mm^2 were analysed by comparing the size of the magnetic field variation when in the longitudinal and transverse directions, as can be seen in Figure 5.9. The data analysis for the transverse probe shows that although the magnetic field strength in both directions was almost similar, the variation in magnetic field value in the transverse direction was higher than that in the longitudinal direction. For the axial probe in Figure 5.10, the results were similar to the transverse probe results in terms of the variation of the magnetic field in the two directions. However, the results were different for the value of magnetic field strength, where the values in the transverse direction were higher than those in the longitudinal direction. Overall, the result indicates the shape of the system's homogeneity, which can be described as a prolate ellipsoid in the centre gap between the magnet arrays.

Planar magnetic field map of the area of 1125 mm² in two directions at different depths

	26	50	74	98	122
Transverse direction	20.14	22.28	21.81	21.56	16.80
Longitudinal direction	19.59	21.71	21.47	21.33	16.71
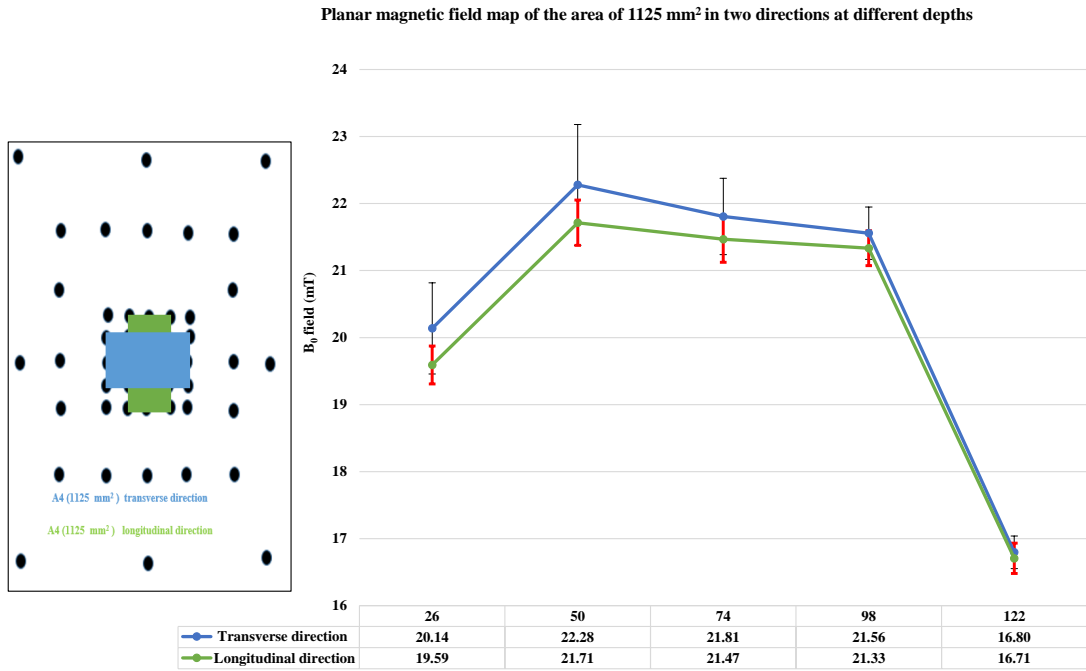
Figure 5.9: Magnetic field profile using the transverse probe to identify the appropriate direction for more homogeneity in the magnetic field by analysing the measured magnetic field strength of area 1125 mm² longitudinally and transversely at different depths from the magnet surface. The error bars indicate the amount of variation in the value of the magnetic field for each direction, and the table represents the magnetic field strength at each depth in both directions.

Planar magnetic field map of the area of 1125 mm² in two directions at different depths

	26	50	74	98	122
Ttransverse direction	20.14	22.28	21.81	21.56	16.80
Longitudinal direction	19.59	21.71	21.47	21.33	16.71
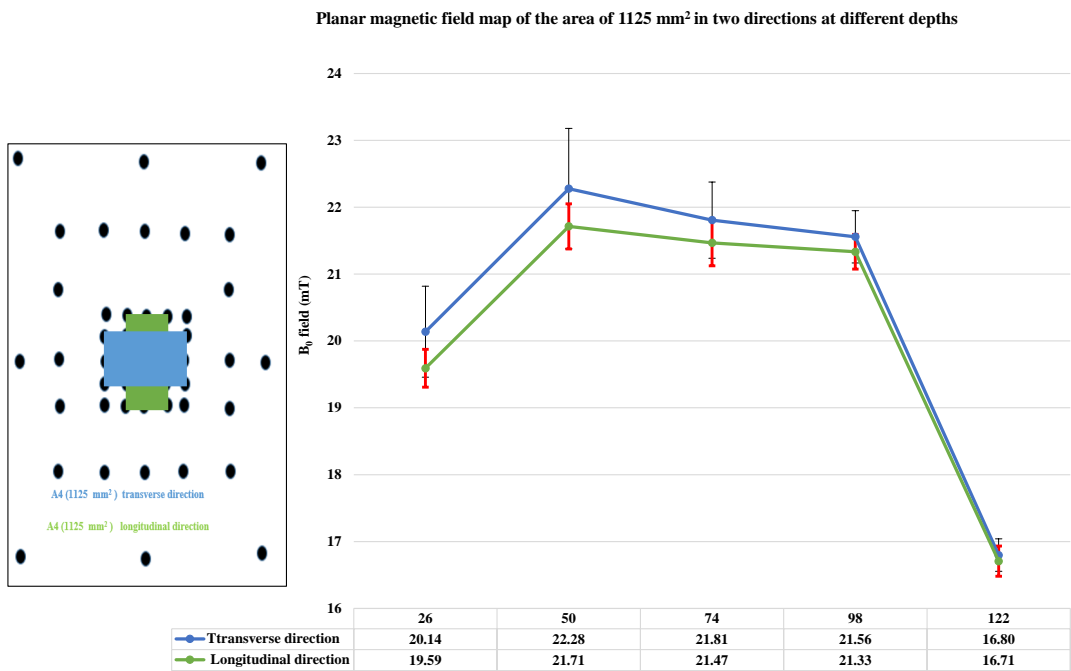
Figure 5.10: Magnetic field profile using axial probe to identify the appropriate direction for more homogeneity in the magnetic field by analysing the measured magnetic field strength of area 1125 mm² longitudinally and transversely at different depths from the magnet surface. The error bars indicate the amount of variation in the value of the magnetic field for each direction, and the table represents the magnetic field strength at each depth in both directions.

5.2.2.2 Magnetic field mapping in a wooden frame

To improve the practical utility of the constructed magnet arrays, the whole assembly was transferred from the closed metallic box into an open wooden frame, as can be seen in Figure 5.11. A magnetic field map measurement was repeated for five different heights from the surface of the magnet: 26, 50, 78, 106, and 134 mm, with a gap of 250 mm maintained between the two magnet arrays.

An average of three measurements at each hole in the acrylic tube was calculated, as shown in Table 5.3 for the transverse probe and in Table 5.4 for the axial probe. Both tables display the average values of the magnetic field strength at different distances from the magnet surface for different area sizes, which are A_1 (25600 mm^2), A_2 (11025 mm^2), A_3 (2025 mm^2), A_4(1125 mm^2) and A_5 (575 mm^2).

Figure 5.11: The wooden frame containing the planar magnet arrays assembly.

Table 5.3: Planar magnet field map measurement in the wooden frame using the transverse probe.

Depth (mm)	A$_1$ (25600) (Avg±SD) mT	A$_2$ (11025) (Avg±SD) mT	A$_3$ (2025) (Avg±SD) mT	A$_4$ (1125) (Avg±SD) mT	A$_5$ (575) (Avg±SD) mT
26	37.45±20.04	18.88±5.76	13.06±1.05	13.19±1.05	12.69±0.51
50	32.88±13.31	21.80±5.26	16.76±1.08	16.86±1.09	16.35±0.49
78	26.11±7.41	21.00±3.52	17.94±0.69	18.00±0.66	17.66±0.36
106	20.04±3.64	18.74±2.11	17.38±0.36	17.43±0.34	17.22±0.16
134	15.41±1.73	15.85±1.06	15.44±0.23	15.48±0.17	15.38±0.12

Table 5.4: Planar magnet field map measurement in the wooden frame using axial probe.

Depth (mm)	A$_1$ (25600) (Avg±SD) mT	A$_2$ (11025) (Avg±SD) mT	A$_3$ (2025) (Avg±SD) mT	A$_4$ (1125) (Avg±SD) mT	A$_5$ (575) (Avg±SD) mT
26	13.35±8.13	10.05±5.63	3.45±2.17	3.39±2.25	1.97±1.33
50	3.75±1.88	4.12±2.02	1.76±1.11	1.72±1.15	0.89±0.67
78	7.00±5.87	1.31±1.11	0.94±0.32	1.00±0.29	1.04±0.14
106	8.73±5.51	3.38±2.38	1.36±1.00	1.42±1.01	1.38±0.65
134	7.71±5.17	4.13±2.46	1.62±1.19	1.67±1.18	1.40±0.92

Similar to the data analysis performed for the magnetic field measurements inside the metallic box, an identical study was applied to the measurements conducted for the assembly in the wooden frame. Before starting the analysis, it had been noticed that the strength of the magnetic field in the wooden frame was lower than that in the metallic box, specifically in the central areas of the map sheet. By contrast, the variation in the magnetic field intensity was very slightly higher for all regions. These outcomes were expected, the reason being the absence of the metallic part beneath the frame of the magnet arrays that directs the magnetic field in one direction, thus increasing the magnetic field intensity. This observation agrees with the results reported by Casanova et al. [3] and has been described in figure 2.14 in chapter 2.

The initial analysis was begun by identifying the region of the flattest curve in the gap between the two magnet arrays. Figure 5.12 displays the magnetic field profile at all depths from the magnet surface and a table that shows the strength of the magnetic field at each depth of the selected points.

	1	2	3	4	5	6	7	8	9
26 mm	60.40	26.17	15.06	13.33	12.44	12.28	12.82	19.53	40.20
50 mm	47.30	28.64	18.83	16.98	16.07	15.97	16.44	22.60	37.60
78 mm	32.80	24.31	19.13	18.12	17.48	17.38	17.90	21.97	31.80
106 mm	23.17	21.56	18.00	17.38	17.12	17.17	17.50	19.74	23.93
134 mm	16.87	17.19	15.67	15.38	15.36	15.41	15.58	16.54	18.03
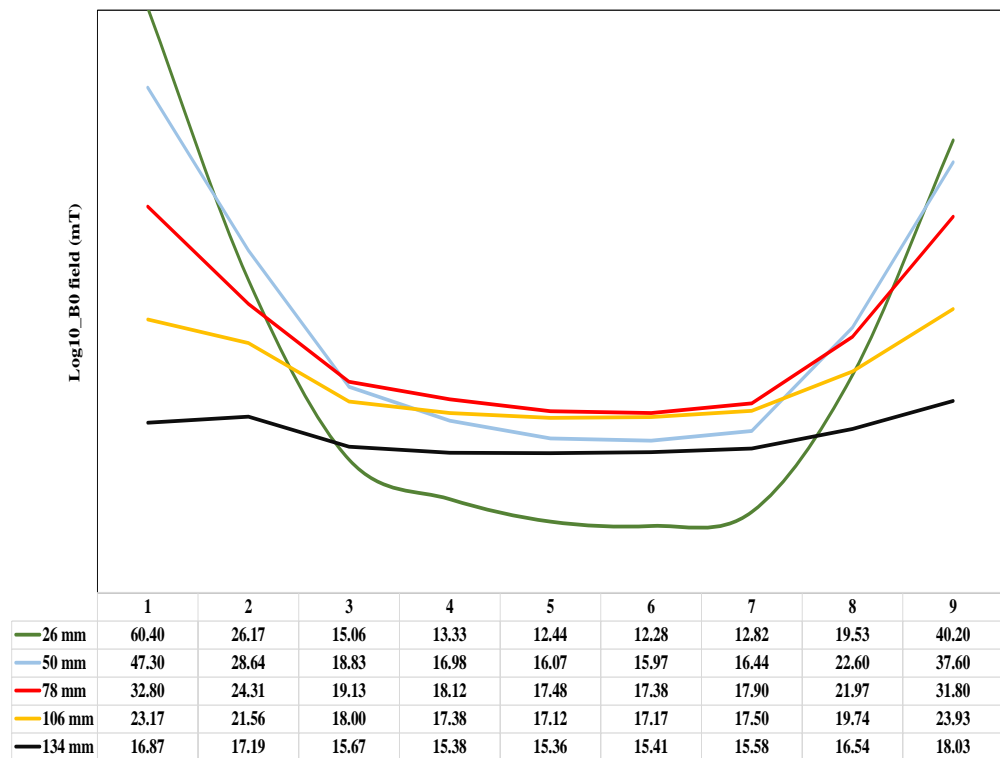
Figure 5.12: Coloured curves produced from the magnetic field map in the wooden frame using the transverses probe measurements at five different heights. The table demonstrates the averaged value of the strength of the magnetic field at different points (1 to 9) on the acrylic map sheet for each height.

The data in table 5.3 exhibit a reduction in the magnetic field strength over greater distances from the magnet surface, with a decrease in the variation of the magnetic field values at greater distances. For example, at a distance of 78 mm the magnetic field in the centre of the map sheet was 17.94 ± 0.68 mT for an area of 2025 mm^2, while it was 15.44 ± 0.23 mT at a distance of 134 mm. Furthermore, and as expected, the magnetic field at the a distance of 134 mm shows less variability. This is due to the lower impact of the static gradient, G_0, on distances far away from the surface.

Figure 5.13 presents the reduction in the magnitude of the static magnetic field (B_0) as a function of the depth for various areas. One can observe that the B_0 magnitude for an area of 25600 mm^2 is reduced dramatically in comparison to other areas. Moreover, the B_0 value at depths of 78 mm and 106 mm has the lowest variations. This outcome is also in agreement with the sweet-spot theoretical calculation and the measurement that was performed inside the metallic box.

The variability of the magnetic field (ΔB_0) was represented through the standard deviation, which was calculated for the magnetic field measurements in Tables 5.3 and 5.4. It was interesting to note that the measurement conducted via the axial probe has shown that the least variability in the magnetic field is at 78 mm depth from the surface (Figure 5.14), which is approximately equivalent to the previous estimation for the depth of the calculated sweet-spot.

Planar magnet field map in the wooden frame at different depths using the transverse probe
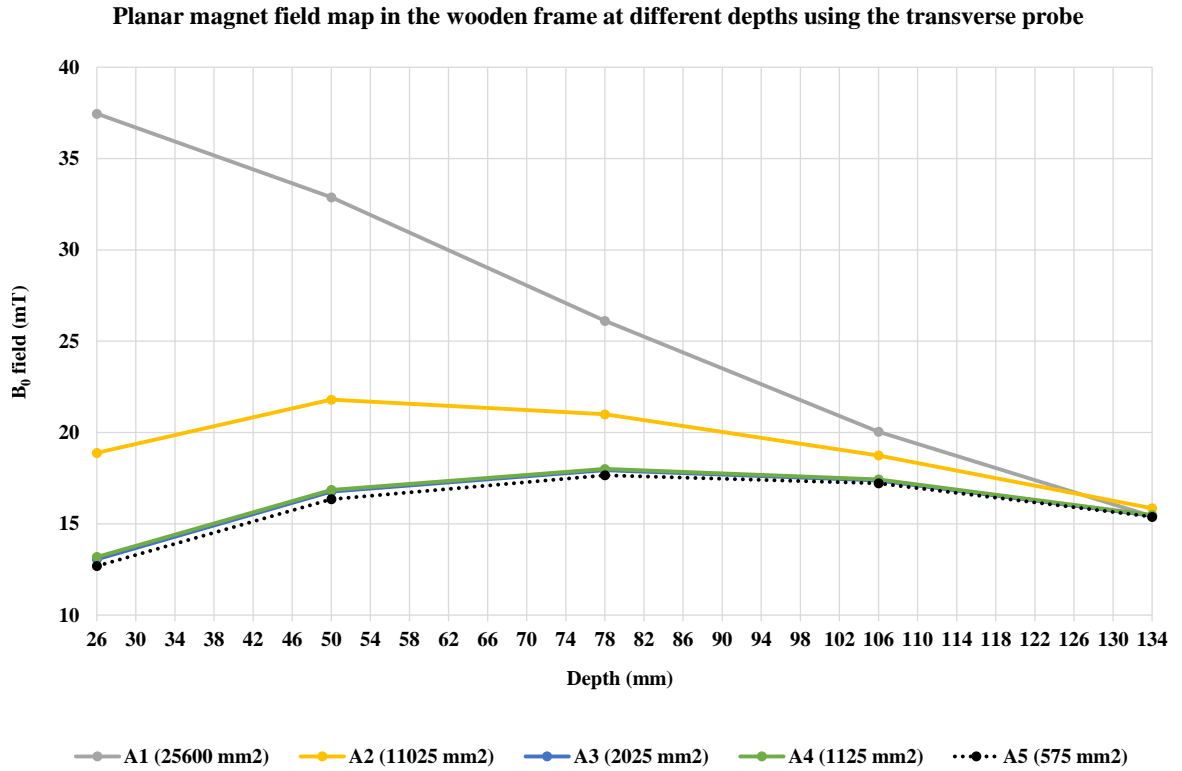
Figure 5.13: Plot of the magnetic field (B_0) profile across the depth direction for the various areas in square millimeters. The dot points represent the measurements carried out by the transverse probe along the X-axis at different depths.

Planar magnet field map in the wooden frame at different depths using the axial probe
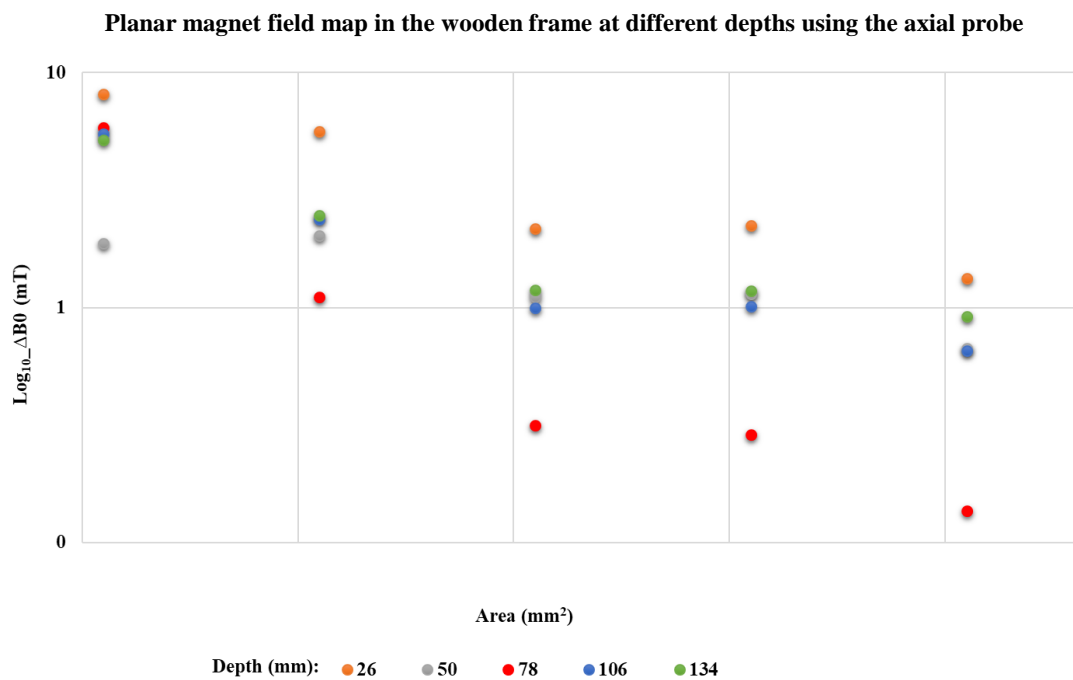
Figure 5.14: Plot shows the logarithmic scale for the variability in the magnetic field (ΔB_0) over the distances from the magnet surface. The coloured circles represent the ΔB_0 amount at each depth.

5.3   Evaluation of the NMR electronic system

This section is devoted to describing the evaluation that was performed to check the compatibility of the developed low-field NMR electronic system in Figure 4.7 of chapter 4 with the constructed planar magnet: the CAPIBarA magnet. The initial evaluation of the assembly was performed inside the metallic box. Later the assembly was transferred to the wooden frame for a second evaluation and an estimation of T_2^{eff} for different materials. Moving the system to a noisy environment is an important step for the developed system to investigate its capability to function as a portable sensor.

5.3.1   Evaluation inside the metallic box

The evaluation was conducted inside the metallic box through an NMR experiment using a solenoid coil as an RF sensor. The reason for using the solenoid coil is to enclose the sensitive volume of the magnet, where most of the sample volume is contained completely. Thus, the spin system will be exposed to a similar applied radiofrequency. The diameter and height of the RF coil were both 15 mm, and it was made up of four layers of 35 turns. The loop was made of Litz wire (500 g, 81 strands of 0.04 mm copper wrapped in silk, 0.67 mm wire diameter). A plastic transparent transfer pipette of 14 mm diameter was filled with olive oil and placed inside the coil. Then the RF coil was placed in a plastic box and connected to a BNC junction (Figure 5.15). This assembly was positioned at the sweet-spot, which is 76 mm from the magnet surface.The resonance circuit was accomplished using the coarse tuning and matching of capacitors. The fine-tuning was achieved by changing the length of the coaxial cable between the duplexer and the capacitors.

Numerous NMR experimental parameters trials were conducted until the NMR signal was obtained at a frequency of 0.915 MHz, which corresponded to a magnetic field of 21.5 mT. The dwell time was 20 μs spaced by an echo time of 1001 μs. The pulse length was 61.66 μs, and the phase shift was 225°. The PPE was 32 points, and the number of echoes was 16. The TR was 250 ms, the power level amplitude was 500 mV, and 1024 averages of the scan number were employed. Figure 5.16 shows the first obtained NMR signal using the CPMG sequence for the low-field NMR system with the CAPIBarA magnet. The reader can clearly see the obtained 16 spin echoes of this run, which is illustrated in the time domain (ms) section, the first part of the MATLAB GUI front panel (CPMG control Software).
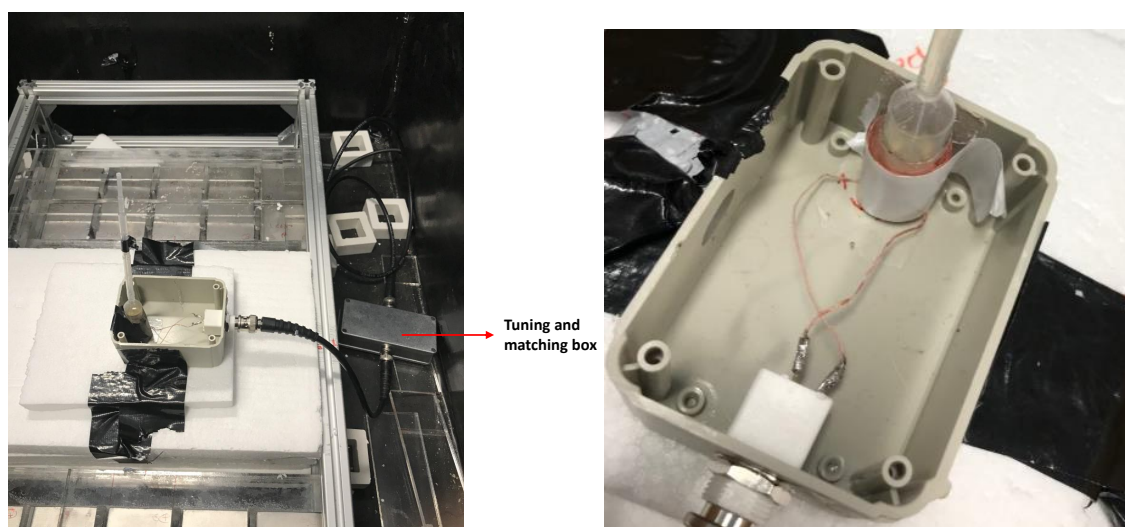
Figure 5.15: Photograph of the 15 mm solenoid coil in a plastic box, and positioned at the sweet spot between the two magnet arrays.
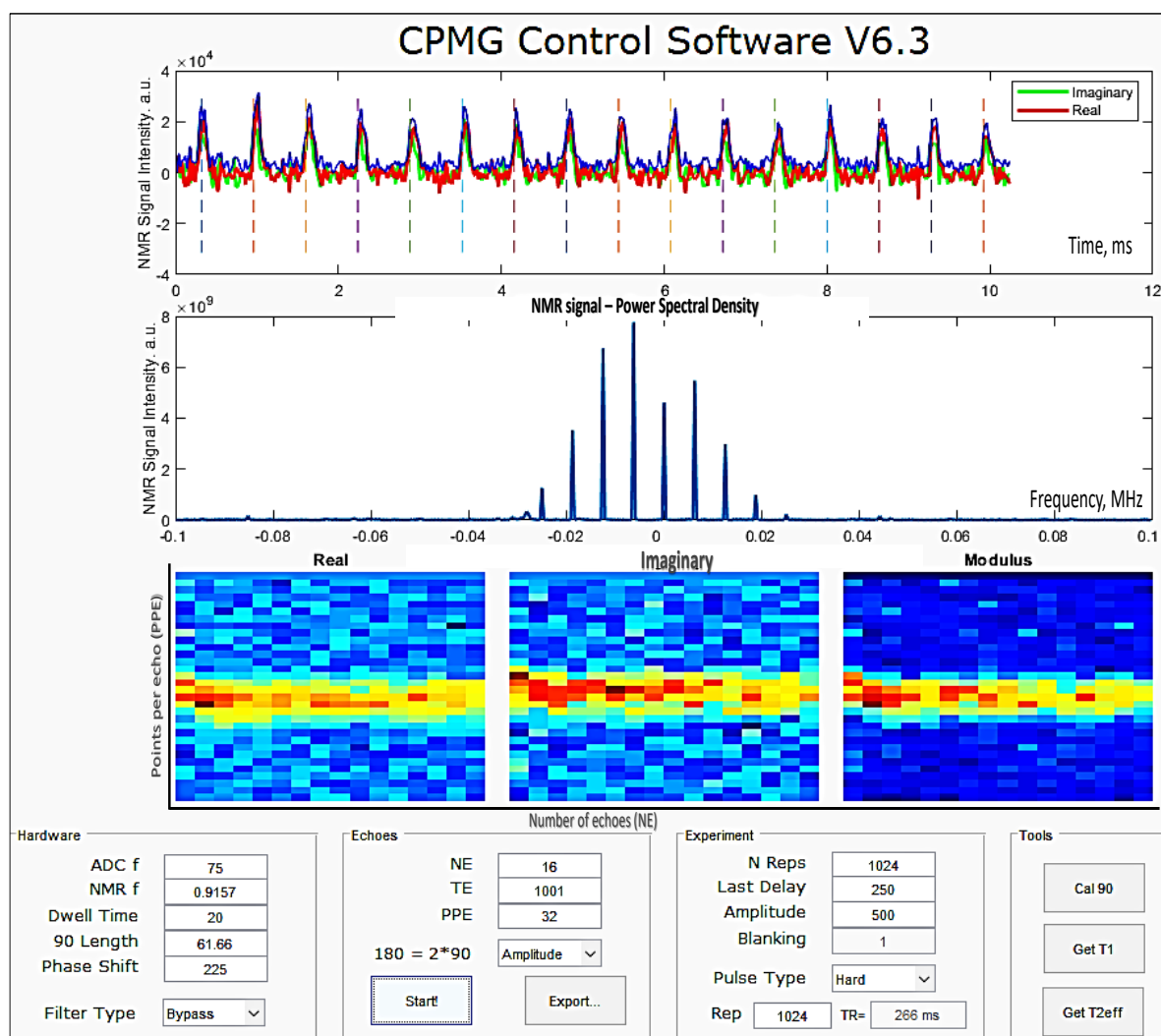
Figure 5.16: NMR signal obtained utilising the inverting Op-Amp as NMR electronic system with the planar magnet inside the metallic box.

Moreover, to improve the performance, a different front-end of the RF power amplifier was introduced, the **mini-circuit ZHL-3A$^+$** (coaxial amplifier, BNC version, 50 Ω medium high power 0.4 to 150 MHz). The DC power required to operate the mini-circuit was 25 V, and the DC digital power supply TENMA was used. Figure 5.17 illustrates the modified circuit. The obtained NMR signal can be found in Appendix AA. The current power amplifier allows the power amplitude value to be raised to 700 mV, and as a consequence, the pulse length was reduced to 15 μs. In addition, the interval time was reduced to 10 μs, and the phase shift changed to 65°.
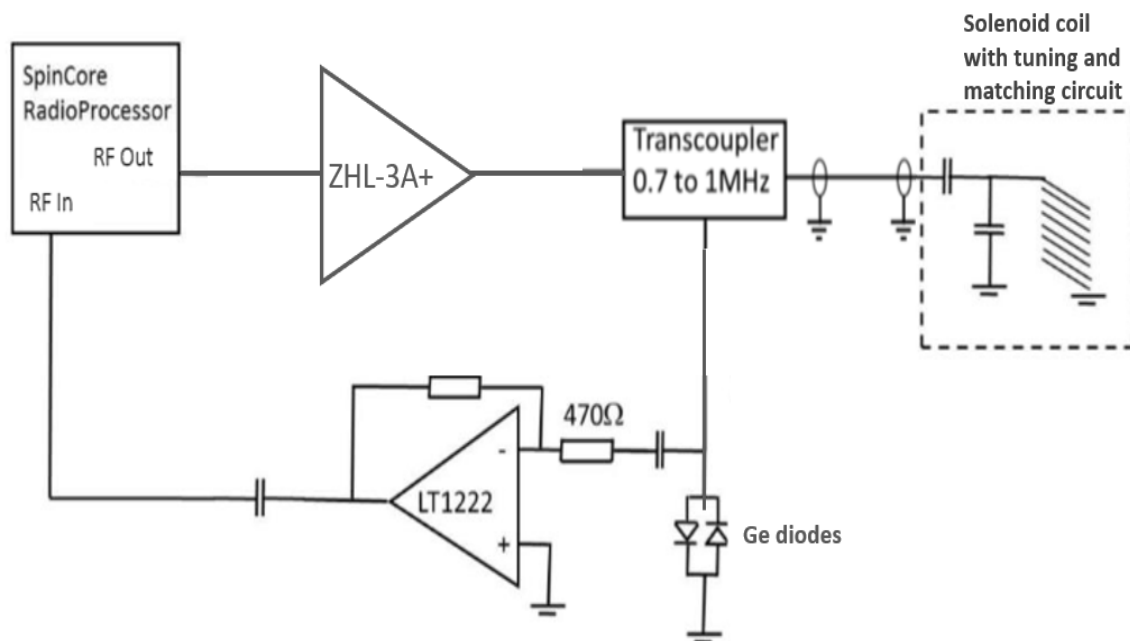
Figure 5.17: Schematic diagram of the modified electronic circuit; the mini-circuit ZHL-3A$^+$ functions as power amplifier and the LT1222 as a pre-amplifier, with the planar magnet.

Significant improvements to the NMR signal intensity by one order of magnitude were observed after modifying the power amplifier. The signal amplitude produced by the inverting Op-Amp LT1363 circuit was 4 x 10^4, while with the mini-circuit ZHL-3A$^+$ was 1 x 10^5. This improvement in the signal was due to the short pulse length which allows a larger volume of the sample to be covered.

Noise measurement was conducted by measuring the NMR signal intensity inside the metallic box with closed and open lids. In each case, the NMR measurements were performed in the presence and absence of the olive oil sample. The results show that in the case of the closed lid, the ratio of the sample inside the coil to no sample was 3.02, while the ratio in the case of the open lid was 2.88. This result demonstrates that there was no significant difference between the open and closed lid of the metallic box in regard to the signal intensity. Therefore, the NMR experiments using the solenoid coil could be conducted for the entire system in the wooden frame.

5.3.2 Evaluation in the wooden frame

After the assembly was transferred to the wooden frame, the NMR experiment was repeated using the 15 mm solenoid coil (Figure 5.18). As noted in the magnetic field mapping section, the magnetic field intensity projected above the magnet arrays was weaker outside the metallic box. Thus, from the measured strength of the magnetic field at the region of interest, the proton resonance frequency in the NMR experiment was changed to 0.744 MHz, which corresponds to 17.48 mT, where the distance between the two magnet arrays was 255 mm. At the same time, the remaining parameters were kept similar. The NMR signal obtained from this experiment is described in Appendix B.
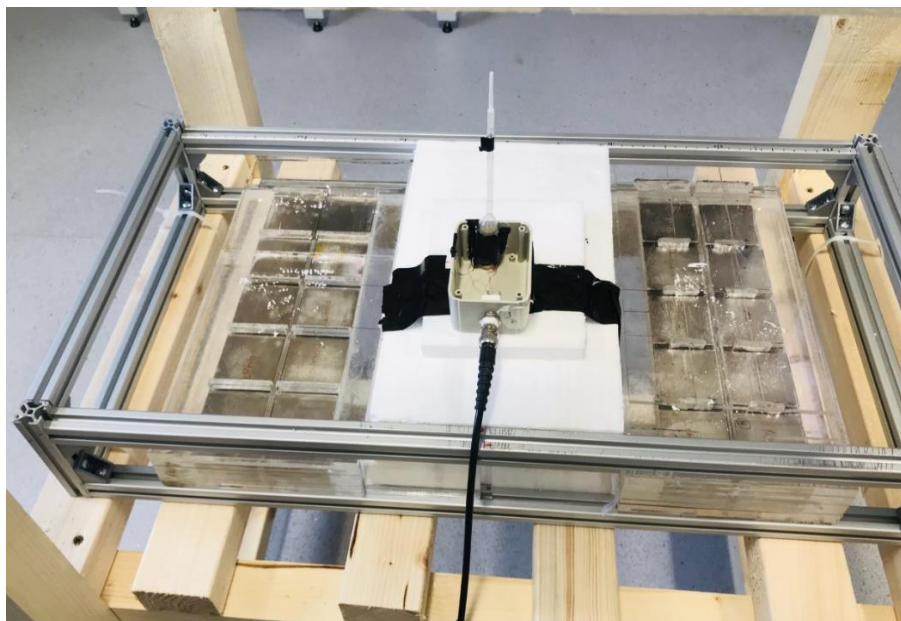
Figure 5.18: Snapshot of the 15 mm solenoid coil over the centre gap between the two magnet arrays at the wooden frame.

Afterwards, to enhance the outwards intensity of the RF coil, thin sheets of copper were placed over the magnet array surface (Figure 5.19b). This shield will reduce the RF coupling to the magnets, and instead RF will couple to the copper, which is highly conductive and thus will help make an electromagnetic circuit and push the RF out of the surface of the coil. In addition, this shield will help reduce the vibration for both the magnet and RF coil, where the eddy current produced by the coil will circulate within the copper shield, not the magnet. Thus, no distortion of the B_0 field will occur, and the RF coil dead time will be reduced after each pulse [34; 142].

It was noted that the measured magnetic field value at the middle of the coil was increased after the addition of the copper sheet (18.2 mT), which corresponds to 774.4 kHz. Therefore, the length of the cables was adjusted, and the tuning circuit frequency was examined by the network analyser, which showed a frequency value of 0.776 MHz at a powered depth of -6.09 dB (Figure 5.19a). Hence, the NMR experiment was repeated for the new set using a similar method and parameters. The reader can find details of the generated NMR signal with two different frequencies after the addition of the copper sheets on the magnet arrays in Appendix C. Figure 5.19e demonstrates the effect of the addition of the copper sheets on the obtained echo train, in which the initial Hahn echo has a similar peak to the subsequent three echoes compared to the obtained echo train before the addition of the copper sheets (Figure 5.19d).
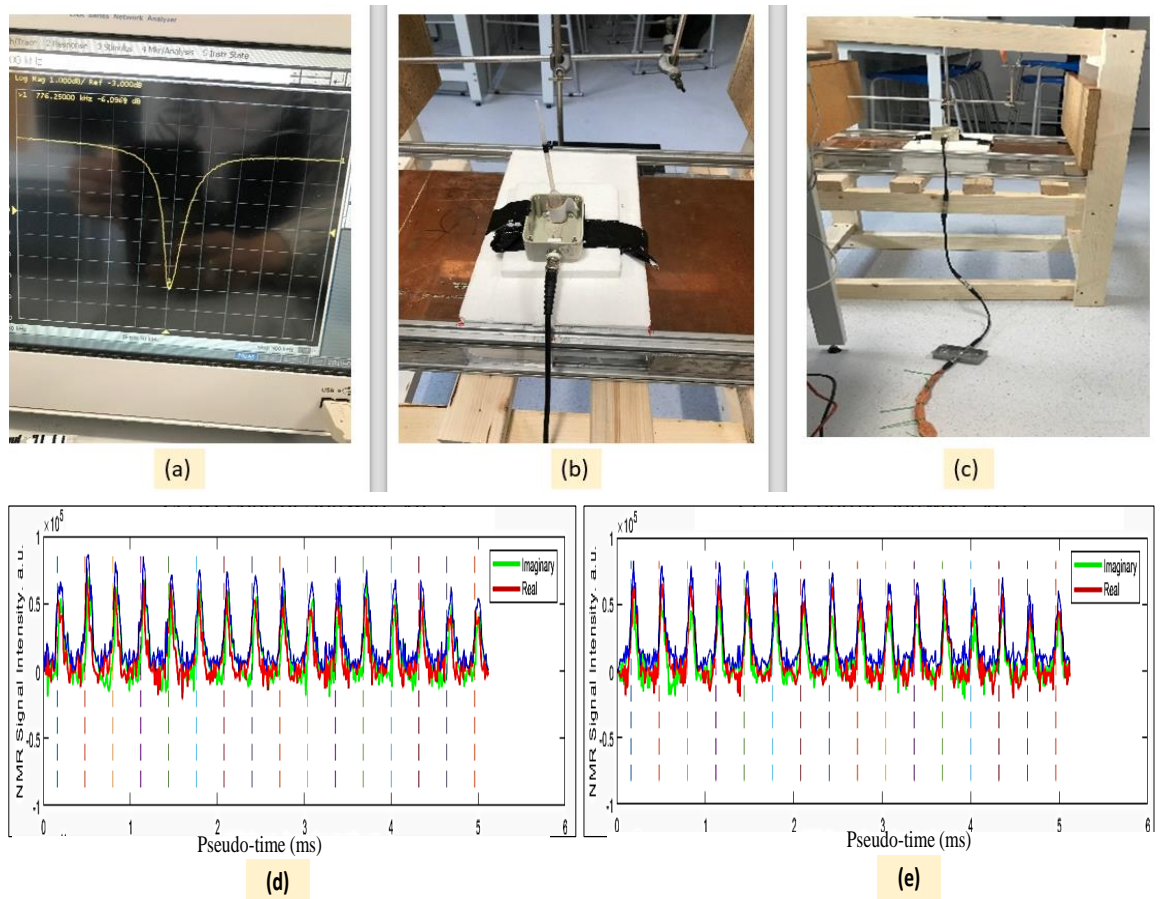
Figure 5.19: Photograph of the copper shield placed above the permanent magnet arrays. Image (a) shows the frequency values for the tuning circuit, (b) copper sheets on the magnet and RF coil positioned at 76 mm from the magnet surface, (c) the entire assembly with the matching and tuning circuit, (d) NMR signal before the addition of the copper sheets, and (e) NMR signal after the addition of the copper sheets.

5.3.3 Time constant estimation (T_2^{eff})

The final extension of the evaluation of the low-field electronic system with the current inhomogeneous static field was to estimate the time constant T_2^{eff} for various materials. Therefore, the experiment for this measurement was conducted by utilising similar front-end electronics and samples that were employed with the EMC laboratory in chapter 4. Thus, the experiment hardware comprised the developed planar magnet as the B_0 source with a gap distance of 250 mm between the magnet arrays, and a solenoid coil of 20 mm diameter as sensor. The solenoid coil is the one that was presented in Figure 4.1 of chapter 4. Careful placement of the middle part of the coil at the sweet-spot plays an essential role in the improvement of the NMR signal, and the measured magnetic field at that position was used for running the experiments. The measured magnetic field was 18.89 mT, which corresponds to 0.804 MHz.

The NMR signals were obtained for all of the tested materials: still smart water, pure sunflower oil, olive oil, 100 mM $CuSO_4$, and 0.1% superparamagnetic (SPIOs). The raw data can be found in Appendix E. T_2^{eff} was estimated from the average of three measurements for each material using the CPMG pulse sequence. Table 5.5 lists the averaged values for the T_2^{eff} of each material with the standard deviation. Furthermore, Figure 5.20 shows the histogram that represents the estimated values for the time constant T_2^{eff} for the two types of static field source: the homogeneous magnetic field produced by the laboratory EMC and the inhomogeneous magnetic field generated by the CAPIBarA magnet. The validation results confirm that the low-field NMR electronic system functioned appropriately with the two types of static magnetic fields. However, the error bar of the estimated T_2^{eff} values for the single-sided magnets is higher than that of the EMC, which is expected, the system can differentiate between the different material compositions.

Table 5.5: Estimated T_2^{eff} values for various materials using the CAPIBarA magnet, which is operated at a magnetic field of 18.89 mT, paired with a solenoid coil of 20 mm diameter.

Material	T_2^{eff} (ms)	$\pm$SD (ms)
$CuSo_4$ (100 mM)	3	0.65
Sunflower oil	31	1
Olive oil	30	2
SPIOs (0.1%)	328	102
Still water	507	209

	CuSo4 100 mM	Sunflower	Olive oil	SPIOS 0.1%	Still water
■ EMC	2	29	31	777	843
■ CAPIBarA magnet	3	31	30	328	507
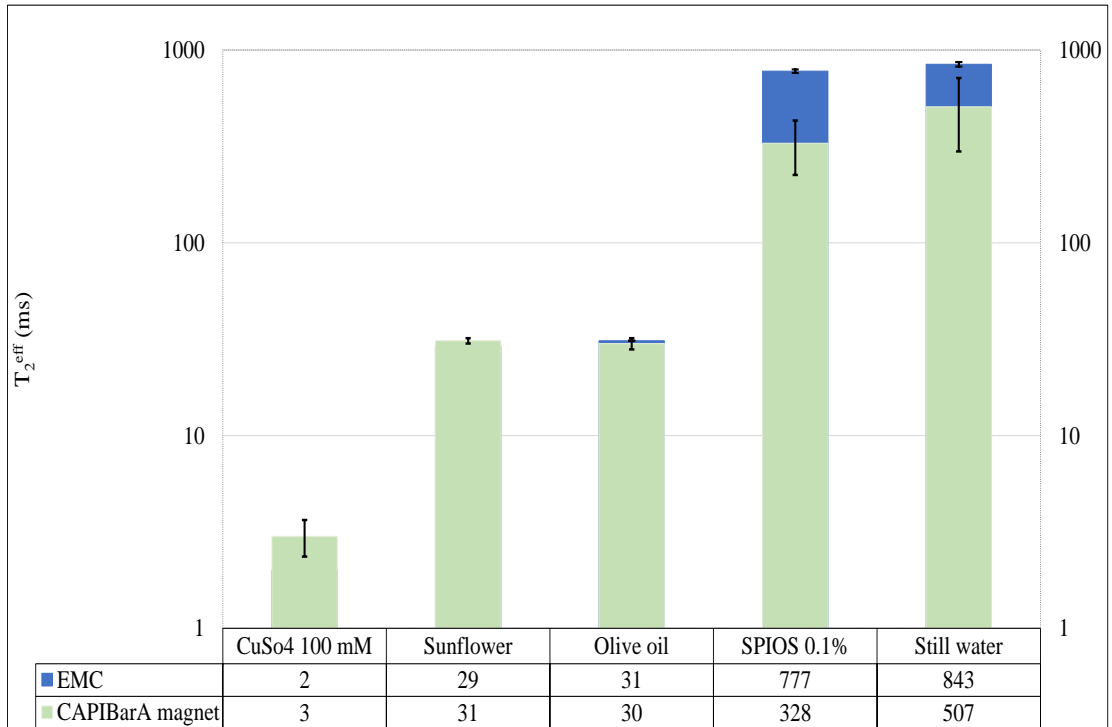
Figure 5.20: Histogram shows the estimated T_2^{eff} values using the laboratory EMC and the CAPIBarA magnet paired with the solenoid coil in a diameter of 20 mm as a sensor. The table lists the T_2^{eff} values for each material.

This section summarises the evaluation performed for the low-field electronic system with the CAPIBarA magnet. The results show that the developed electronic system functions efficiently with the designed planar magnet inside and outside the metallic box. When transferring the magnet from the closed area to the open space, it was essential to re-measure the magnetic field and identify the correct frequency before conducting the experiment. It was also noticed that it is possible to improve the produced NMR signal, as evidenced by the switching of the RF power amplifier (the ZHL-3A$^+$). Furthermore, the T_2^{eff} values were similar to the values generated by the EMC in Chapter 4, except for SPIOS and still water. The main reason is that the value of the employed echo spacing was 2500 μs instead of 5000 μs for EMC. The difference is approximately half.

5.4   Design of the surface coil

This work aims to probe the placenta, which is located at a specific distance from the RF sensor. According to obstetrics research, the overall volume of the PE placenta after delivery is smaller than that of healthy placentas, the values lying between 613 cm^3 and 772 cm^3, respectively [143]. Further, in 2015, other researchers [99] showed that placental volume during the first trimester, which ranged from 11 to 14 gestational weeks, was 50.5 cm^3 for PE while it was 63.6 cm^3 for non-PE cases. Moreover, the overall average thicknesses of the healthy placenta in the second and third pregnancy trimesters using both ultrasound and MRI were 25 $\pm$ 0.05 mm and 29 $\pm$ 0.08 mm, respectively [83]. These studies reported that the PE placenta thickness is smaller than the healthy placenta at all gestational ages. Consequently, in this study, the explored distance that will be employed to investigate the presence of the NMR signal at the region of interest above the sensor surface is 24 mm. This distance represents the position of the anterior placenta for an average pregnancy.

Thus, the RF coil is considered an essential element in the NMR experiment as it defines the sensitivity of the MR sensor. It plays a vital role during the excitation as it perturbs the spin system, the placental tissue, via the application of the B_1 field and detects the NMR signal from each array of volume elements. It is known that the depth of investigation (DOI) does not depend only on the static magnetic field (B_0), but is also determined by the RF oscillating field (B_1), which is generated by the RF coil. Furthermore, the RF coil depth is approximately equal to its inner diameter [3; 34].

Therefore, it is of critical importance to consider the size and the geometry of the RF coil, as they are the keys to control its strength and field homogeneity. This section describes the methodology and methods used for the development of the radiofrequency coil that will be paired with the CAPIBarA magnet.

As noted in Chapter 2, the required RF coil for the sweet-spot magnet should not restrict the size of the sensitive volume. Thus, the RF coil size should be larger than the size of the sensitive volume, which is determined by the 3D spatial variation of the B_0 field. Therefore, the most utilised configuration of the RF coil is the surface or planar coil, as it generates a higher SNR compared to other configurations [3]. Hence, an examination was conducted for various sizes of surface RF sensors that might be capable of detecting NMR signals at a distance of 24 mm. The method employed for this investigation will be explained in the next subsections.

5.4.1 Handmade surface coil

The first coil designed was a handmade surface coil wound as a square loop. It was composed of seven turns of tinned copper wire (18 AGW, Alpha), with an inner diameter of 30 mm by 30 mm and an outer diameter of 67 mm by 67 mm. The copper wire was fixed inside an engraved acrylic sheet and coated by a layer of epoxy resin to effectively match the permittivity, which ensures a sufficient performance (Figure 5.21a). The tested sample was an olive sample filled in a plastic tube of diameter 28 mm and height 15 mm, as shown in Figure 5.21b and 5.21c, which depicts the entire setup. The employed electronic system was the design described in Figure 5.17.
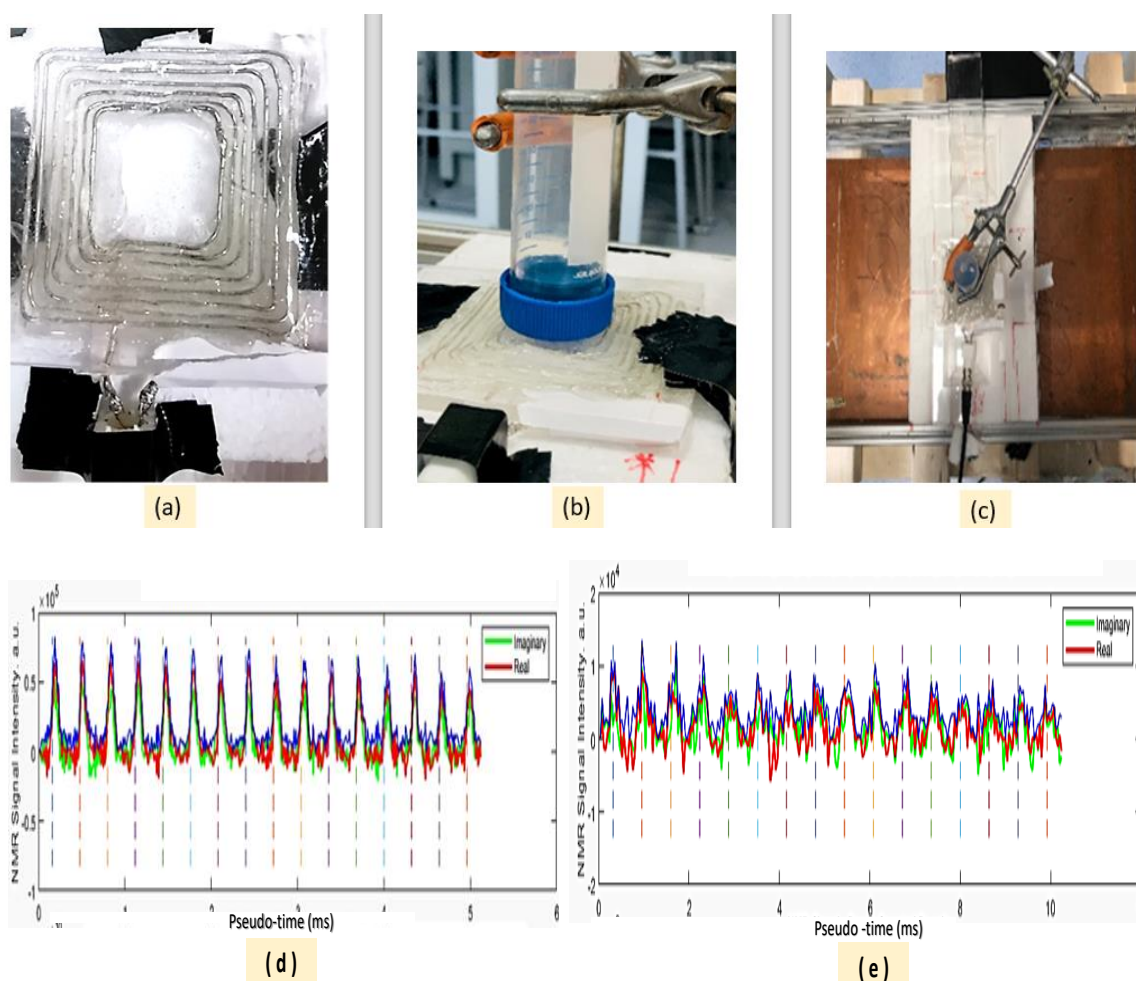

Figure 5.21: (a) Photograph of the handmade surface coil, (b) an olive oil sample in a plastic tube held by an aluminium holder above the surface coil, (c) top view of the entire setup, (d) NMR signal obtained by the 15 mm solenoid coil, and (e) NMR signal obtained by the handmade surface coil.

Due to the epoxy layer, the surface coil was positioned 74 mm from the magnet surface to allow the sample to be located at the sweet-spot (76 mm). Before initiating the NMR experiment, a 90° calibration was performed to find the correct pulse length for the designed planar coil. As anticipated, the pulse duration increased to 138.5 μs. The CPMG experimental parameters were 0.767 MHz for the B_1 frequency with a 125° phase shift, power amplitude of 600 mV, and an average of 1024 scans. The NMR echo signal was acquired using an interval time of 40 μs with 16 points per echo, and the 16 echoes were separated by an echo time of 1000 μs. The produced NMR signal for the handmade coil is illustrated in Figure 5.21e. The reader can observe the effect of the surface coil on the NMR signal, which appears slightly distorted compared to the spin echoes produced by the solenoid coil presented in Figure 5.21d. This distortion in the signal is due to the inhomogeneous B_1 field generated by the surface coil.

A study of the maximum depth that the handmade surface coil can admit was performed by acquiring the NMR signal at various distances from the coil surface. The main element in this study is to secure the sample at the sweet-spot, and later move the coil down by 5 mm at each step. At each distance, a 90° calibration was conducted to realise the optimum pulse duration, besides checking the tuning circuit in the network analyser to ensure the stability of the tuned frequency. The acquired NMR signal at depths of 5 mm and 10 mm can be found in Appendix F. The pulse duration for these depths were 176.6 μs and 185.5 μs, respectively. The dwell time and the echo time for a distance of 10 mm were changed to 70 μs and 1500 μs, respectively.

The acquired NMR signals at 5 mm and 10 mm depths were not of good quality compared to the NMR signal at the surface. Further, it was difficult to observe any NMR signal at a distance greater than 10 mm. The reasons for that could be the prolonged pulse duration, which leads to an insignificant volume. Additionally, there is a limit for the excitation bandwidth determined by the RF circuit bandwidth. Furthermore, this is a handmade coil which owing its imperfect construction might not be able to acquire a sufficient NMR signal at a distance from the coil surface.

From the trials conducted at a depth of 10 mm, it was noticed that with a lower number of points per echo, 8 points, the NMR signal improved at the distance of 10 mm. Besides, a phase shift can be employed, where the real and imaginary components in the time domain are not superimposed on the modulus component.

Despite the challenges faced in acquiring the NMR signal by the handmade surface coil, it gave an insight into the possibility of this type of coil being paired with the CAPIBarA magnet. Additionally, it established a basis for the operating parameters that could be utilised for the next coil design.

5.4.2 PCB coil design and experimental methods

The printed circuit board (PCB) coil is known to enable the manufacturing of sophisticated designs with ease. Moreover, it is reproducible with high efficiency, and also due to its rigidity, it minimises the wire vibration that causes pulse ringdown [34], compared to the handmade coil. All of the PCB coils created in this work were produced utilising milled 75 μm FR4 PCB. Post production, they were coated with a layer of an epoxy resin that was applied to ensure satisfactory performance and effective matching of permittivity. This subsection will present three sizes of the PCB coils that were tested to obtain an adequate NMR signal at a distance of 24 mm above the surface of the coil. At the end of this subsection, the reader will see that the third design successfully provided the desired depth.

5.4.2.1 PCB coil 1

The initial design for the surface coil printed on a circuit board was a double-sided planar rectangular coil (five turns with outer dimensions of 60 mm by 66 mm and inner dimensions of 10 mm by 20 mm), as seen in Figure 5.22a. The circuit frequency was examined with a network analyser, and it was 0.780 MHz with a power depth of -25 dB (Figure 5.22b). The desired operating frequency is 0.767 MHz, and it was gained at the power depth of -11.38 dB in the current tuning circuit. The electronic system utilised is similar to that described in a previous section in Figure 5.17. The sample is the 28 mm diameter olive oil sample that was used with the handmade coil (Figure 5.22c). Further details can be found in Appendix G. The NMR signal was successfully generated after optimising the experimental parameters at the surface of the PCB coil (Figure 5.22e). Again, the reader will readily recognise the difference between the NMR signal produced by the 15 mm solenoid coil (Figure 5.22d), and the one generated by the PCB coil.

Unfortunately, despite the 90° calibration trials and the parameters' optimisation, no NMR signal was observed above a depth of 5 mm. This outcome was anticipated. If the reader compares the present outcome to the capability of the handmade coil in the previous section, the primary reason for the difference is the size of the inner dimensions of the coil, which were 30 mm by 30 mm for the handmade surface coil and 10 mm by 20 mm for the PCB coil. Nevertheless, when comparing the experimental parameters for the NMR signal at the surface of the coil, the reader would appreciate the role of the machined-made coil in improving the sampling interval time and pulse duration.
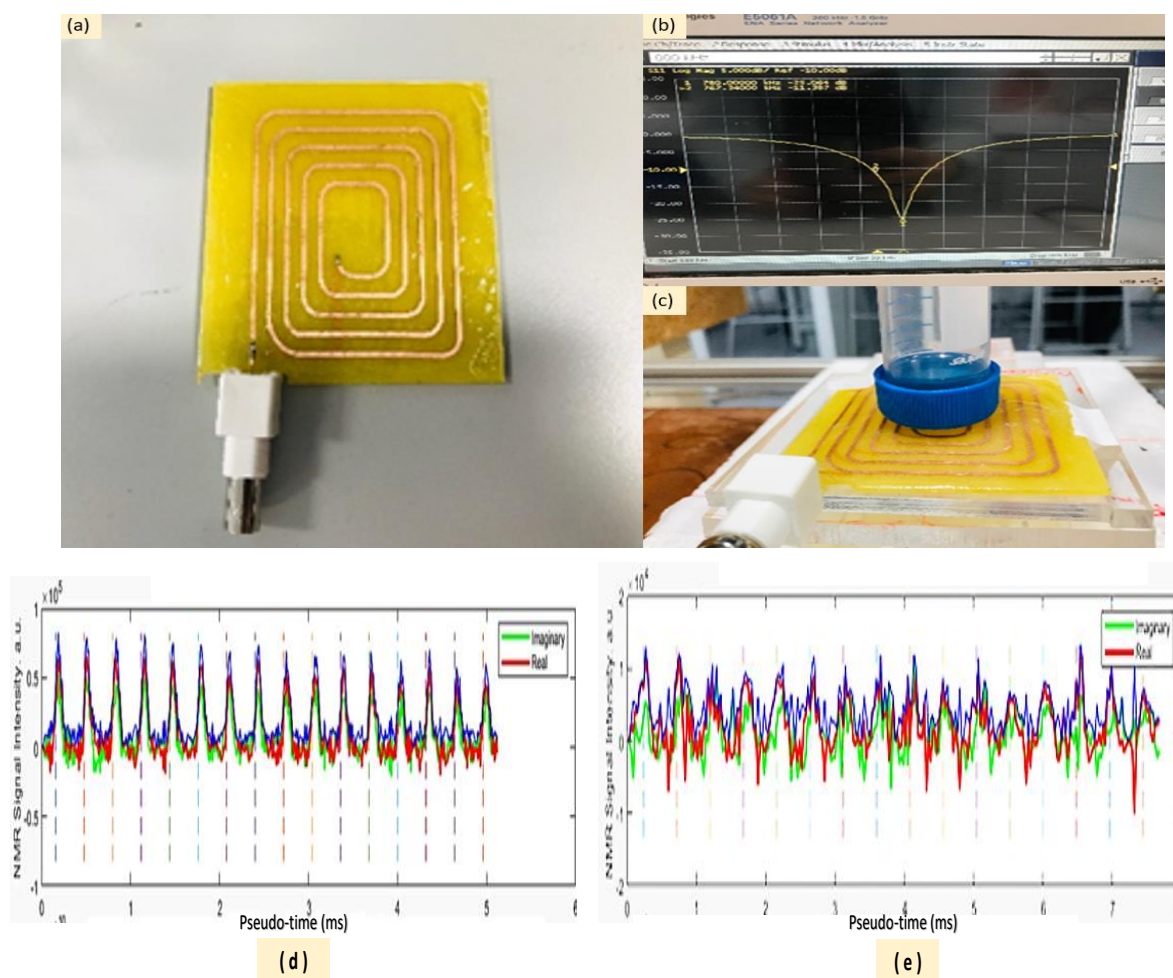
Figure 5.22: (a) Photograph of the PCB coil, (b) snapshot of the network analyser displaying the PCB circuit frequency (c) sample placed on the surface of the coil, (d) NMR signal obtained by the 15 mm solenoid coil, and (e) NMR signal obtained by the PCB coil.

5.4.2.2 PCB coil 2

An improved design of the PCB coil was a double-sided planar square with five turns at a line width of 2 mm and the spacing between the track reduced to 1 mm. The outer dimensions were 66 mm by 66 mm, and the inner dimensions were 40 mm by 40 mm (Figure 5.23a). A network analyser was used to check the circuit tuning frequency, which was 0.756 MHz with a power depth of -11.35 dB (Figure 5.23b). The desired operating frequency, as has been described earlier, is 0.767 MHz, and it was located at a power depth of -9.98 dB. The electronic system utilised and the sample were similar to those described in the above section (Figure 5.23c).

To place the sample at the sweet-spot, a similar method was followed as in the earlier subsections by positioning the PCB coil 74 mm from the magnet surface. The following experimental parameters were employed to acquire the NMR signal: frequency of 0.767 MHz with a pulse duration of 177.5 μs, the echo signals were received at an interval time of 50 μs with 16 points per echo, and the 16 echoes were spaced by 1200 μs. The repetition time was 269 ms, with 512 scans at an amplitude of 600 mV.

Figure 5.23d illustrates the acquired NMR signal at the surface of the PCB coil. The NMR signal obtained at the surface of the PCB coil with two different phase shifts is described in Appendix H.
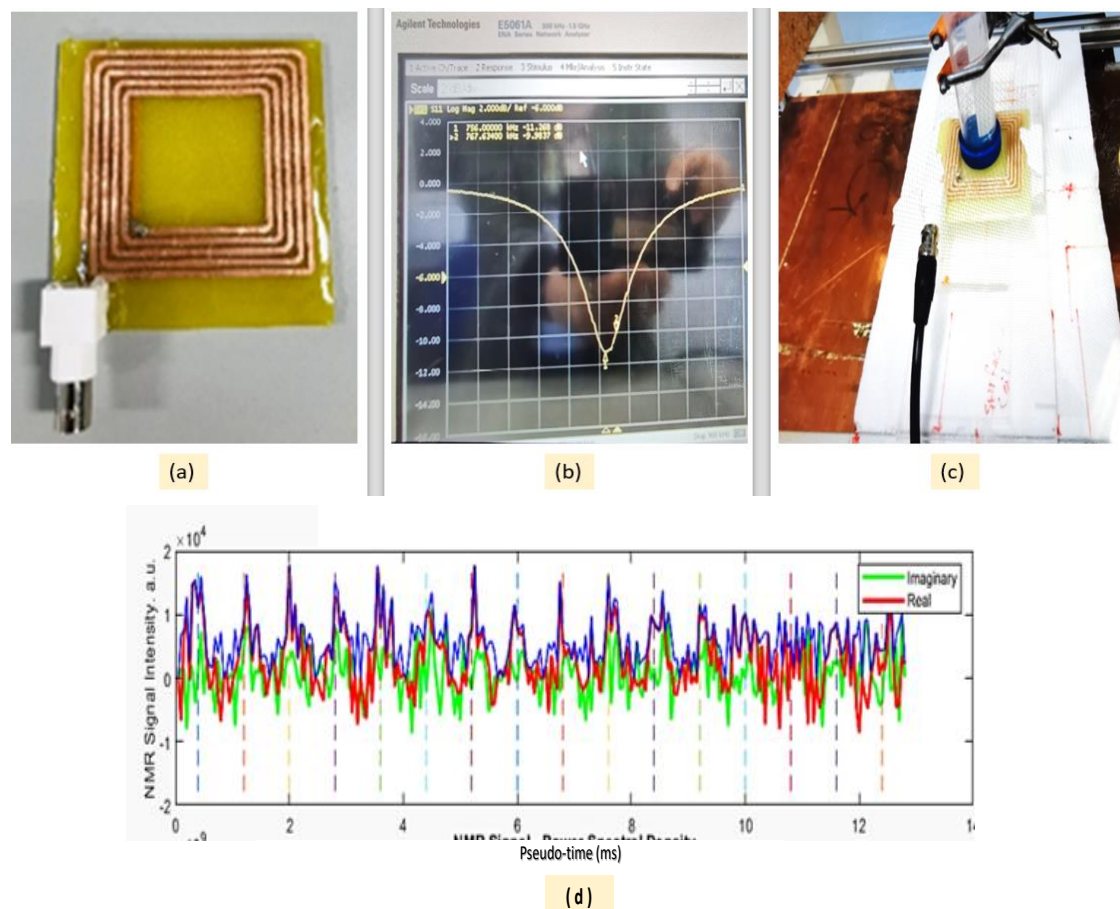
Figure 5.23: (a) Photograph of the square PCB coil, (b) snapshot of the network analyser displaying the PCB circuit frequency and the desired frequency (as a second number), (c) the sample placed at the centre of the surface coil, and (d) NMR signal obtained at the surface of the PCB coil for an olive oil sample of 28 mm diameter.

Multiple 90° calibrations were performed to obtain the optimum pulse duration at 10 mm from the surface of the coil. The NMR signal was relatively obtained at a pulse length of 215 μs. The rest of the experimental parameters were similar to the values utilised for the NMR signal at the surface, except that the number of scans was increased to 1024, the repetition time was 369 ms, and the phase shift was 50°. Details of the acquired NMR signal 10 mm from the PCB square coil can be found in Appendix H.

Although no NMR signal was acquired above the depth of 10 mm, the current system has the potential to improve the SNR. For instance, increasing the number of magnetised spins by enlarging the sample volume to completely fill the inner part of the coil, and also by enhancing of the power depth of the operating frequency.

Therefore, **a larger volume of sample consisting of blocks of Hartley's jelly was investigated**. The length of the block was 82 mm, while the width was 55 mm

and the height was 22 mm. The PCB coil was moved down to 57 mm from the magnet surface to allow the sample to be positioned at the sweet-spot (Figure 5.24a). The first NMR signal obtained for the jelly block utilising similar parameters as for the previous olive oil sample is shown in the time domain section of Figure 5.24b.
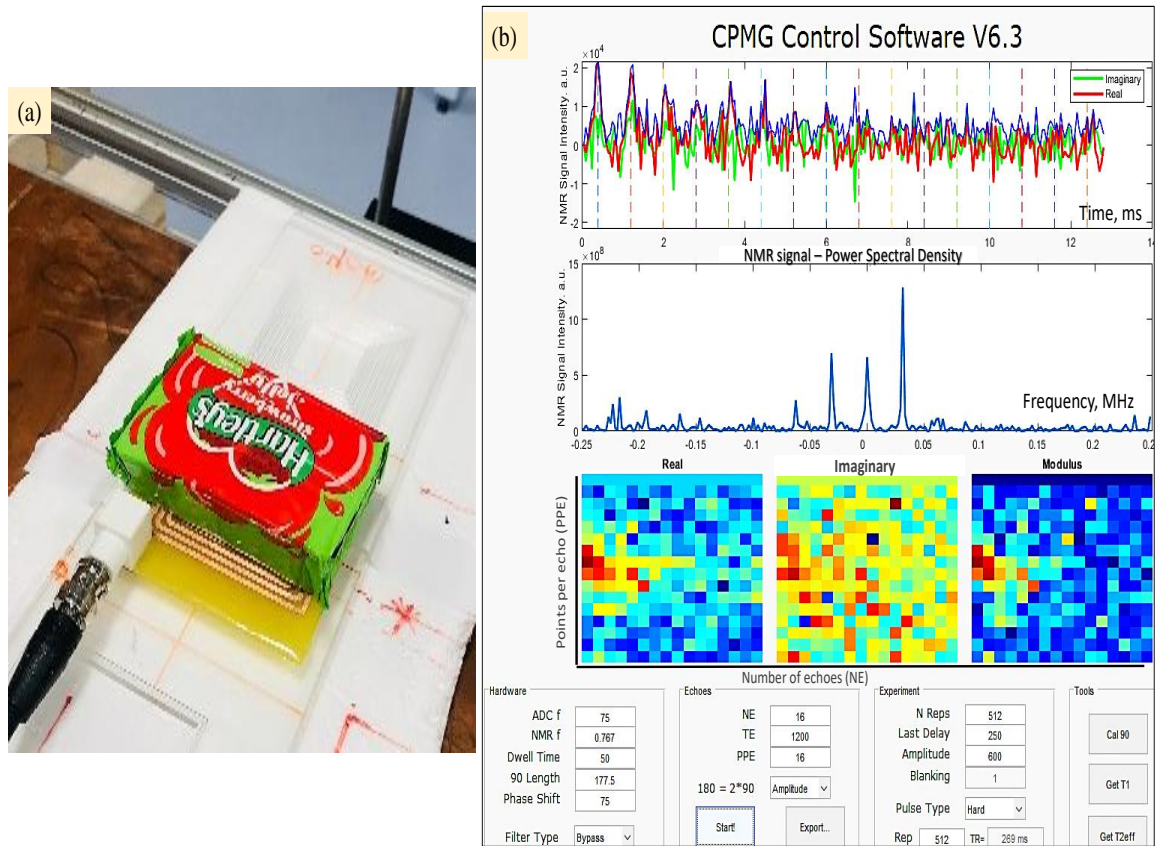

Figure 5.24: NMR signal obtained for one block of Hartley's jelly at the surface of the square PCB coil. Pictures (a) of the jelly block and (b) of the generated NMR signal.

Accordingly, the experimental parameters were optimised for the block of jelly by conducting a 90° calibration. The new pulse durations became 140 μs and 152 μs for sample interval times of 40 μs and 20 μs, respectively. Besides, the number of echoes was reduced to 8 instead of 16 because solid materials have a short T_2, leading to a fast decay, as can be observed in Figure 5.24b. Details of the NMR signal obtained for the jelly block using the optimised parameters can be found in Appendix I.

The NMR signal was acquired for two, three, and four blocks of jelly placed on the top of the square coil surface. All the measurements performed utilised similar parameters as those of the one block assessment. The blocks of jelly were added to determine when the signal will be degraded or distorted and to find the required volume of the polydimethylsiloxane (PDMS), that will be needed to mimic the placenta tissue in the following section. Details of the acquired NMR signal for the different number of jelly blocks can also be found in Appendix I. Further details on enhancing the SNR in the current resonance circuit and obtaining the NMR signal 15 mm from the PCB coil surface can be found in Appendix J.

The NMR signal was attempted to be acquired 22 mm from the PCB coil, but none of the runs for the 90° calibration shows any possible pulse duration that can be utilised for this distance. Consequently, the RF power amplifier (ZHL-3A$^+$) in the electronic system was replaced by the TOMCO (Figure 5.25). This modification in the electronic system was made because of the higher gain of the TOMCO power amplifier compared to the mini-circuit ZHL-3A$^+$: a minimum of 57 dB compared to 24 dB for the mini-circuit. Therefore, it is anticipated that the pulse duration will be reduced with this modification, with TOMCO having a maximum pulse width of 100 ms.
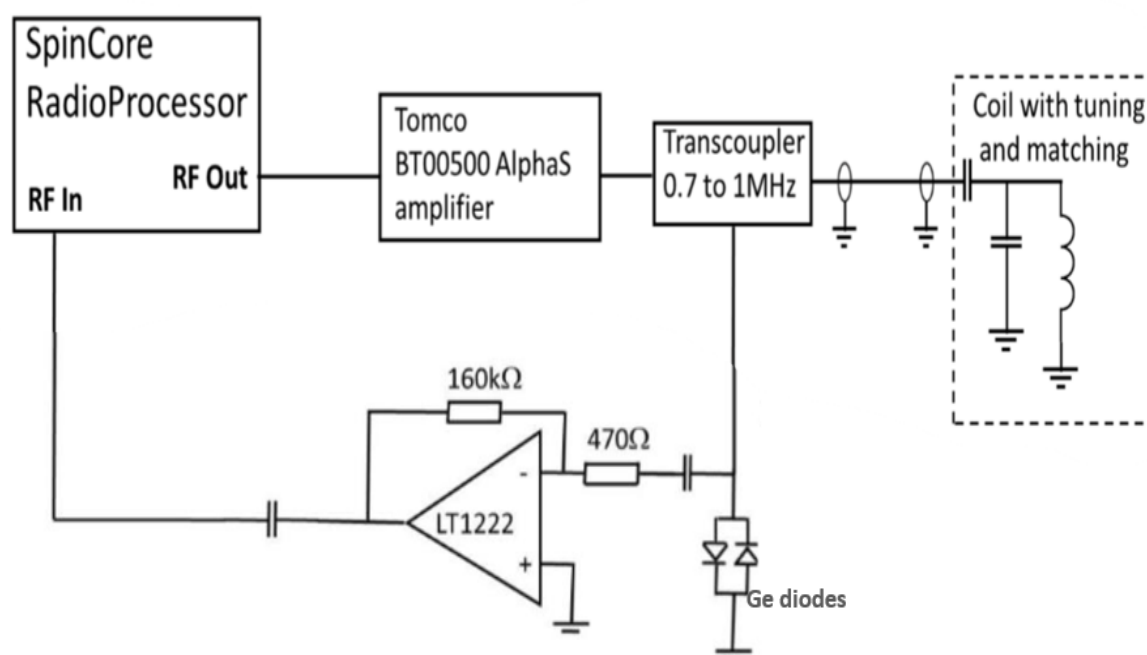
Figure 5.25: Sketch diagram for the electronic system utilising the TOMCO as the RF power amplifier and the simple inverting OP-Amp circuit (LT1222) as pre-amplifier with the CAPIBarA magnet paired with the square PCB coil.

The coil was placed 55 mm from the magnet surface, and the four blocks of Hartley's jelly were placed starting at a distance of 57 mm and ending 145 mm from the sensor surface; thus, the sweet-spot region was involved. A 90° calibration was conducted for the four blocks at the surface of the PCB coil, and it showed a peak at a pulse duration of approximately 25 μs for the two different interval times (10 μs and 5 μs), as shown in Figures 5.26a and 5.26b, respectively. The calibration was run from 5 μs to 50 μs in 10 steps with a power amplitude of 250 mV. The resonance frequency was 0.767 MHz with an interval time of 10 μs for 16 points for each of the 8 echoes spaced by 800 μs. The average number of scans was 512 with a repetition time of 106 ms and a 100° phase shift.

Figure 5.27 shows the NMR signal obtained after using the TOMCO as a power ampli-fier for the square PCB coil paired with the CAPIBarA magnet. Figure 5.27a represents the signal acquired with a dwell time of 10 μs and a pulse duration of 22.5 μs with 55^0 for the phase shift. In contrast, Figure 5.27b shows the signal obtained with an interval time of 5 μs with 25 μs pulse length and a phase shift of 100°. The results show a significant improvement in the shape of the echoes and the signal amplitude, in which the signal intensity was increased by one order of magnitude in comparison to the previous electronic system.
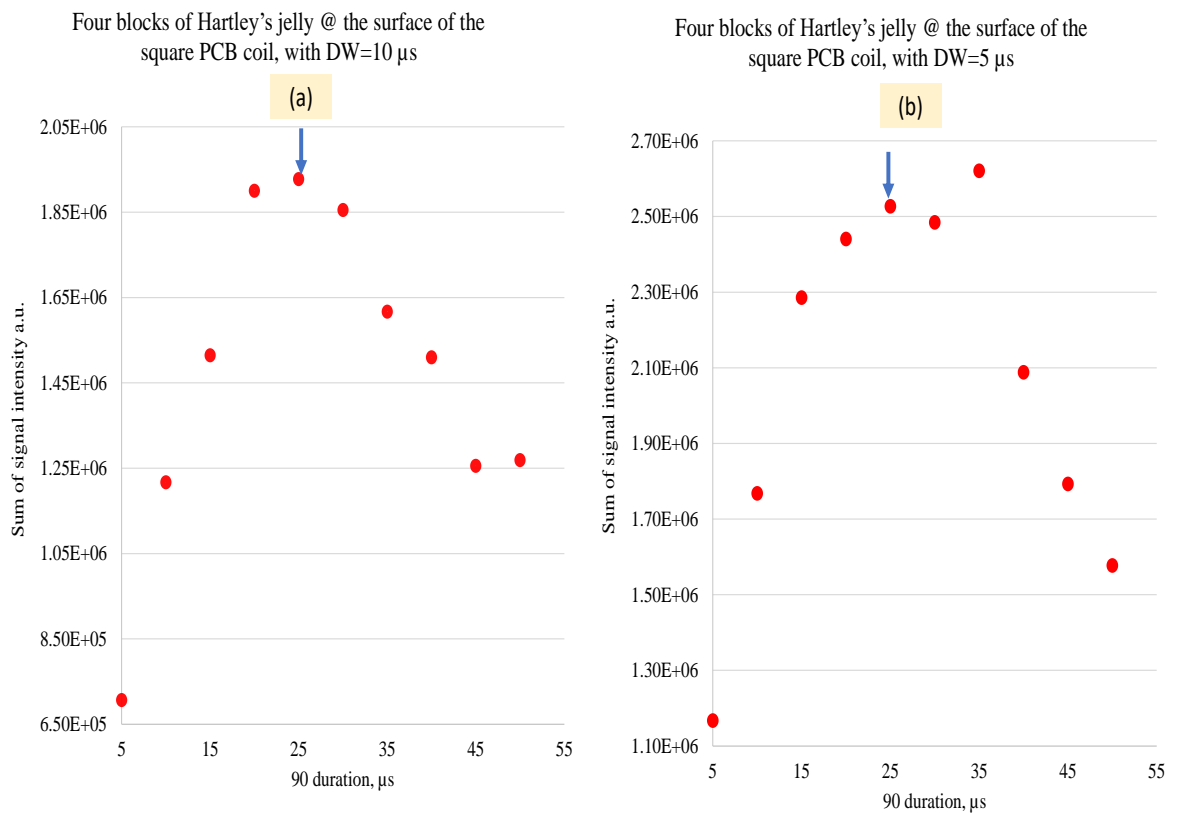

Figure 5.26: 90° calibration for four blocks of jelly at the surface of the PCB coil employing the modified electronic system. Images (a) represents the 90° calibration with 10 μs and (b) the 90° calibration with 5 μs. The higher point in the plot was because of the external noise.
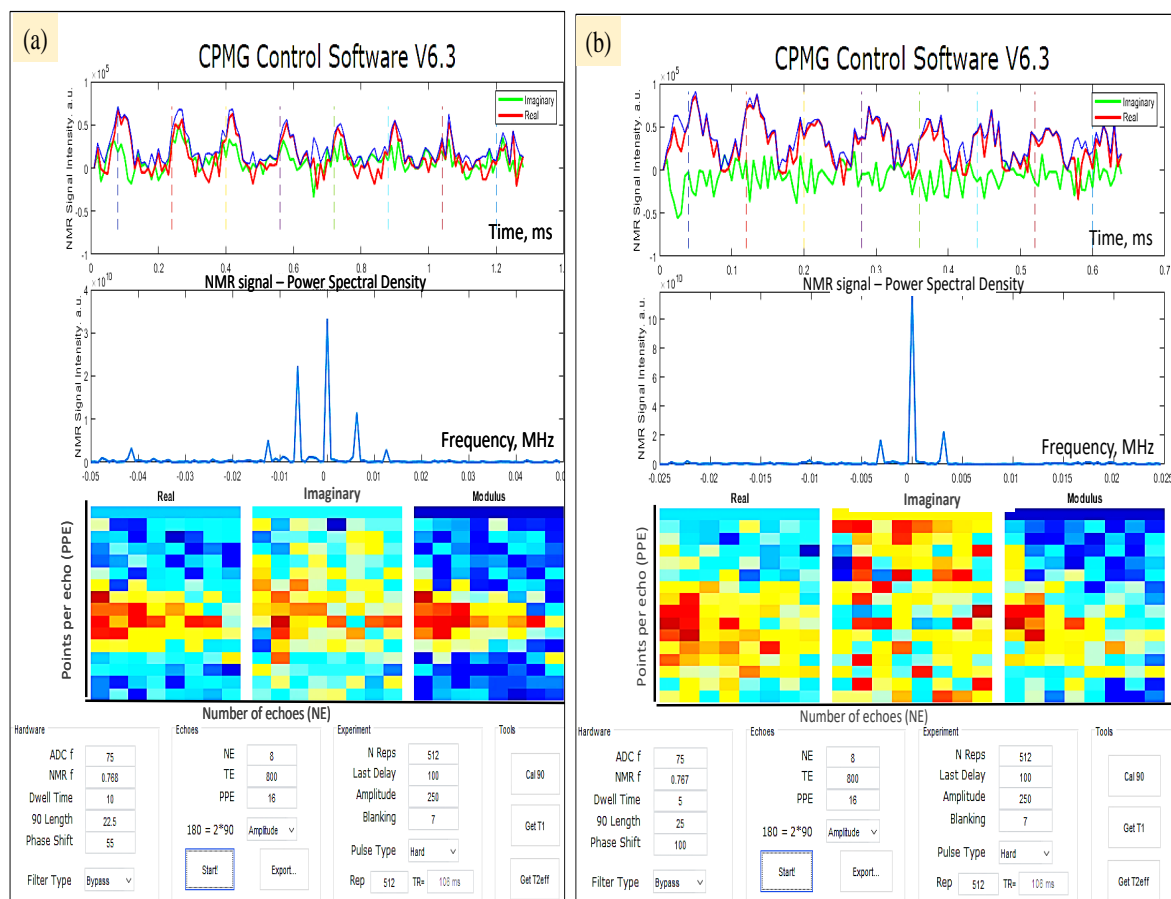
Figure 5.27: NMR signal for jelly blocks at the surface of the PCB coil after utilising the TOMCO power amplifier (a) with interval times of 10 μs and (b) 5 μs.

An experiment was conducted on the **NMR signal at 15 mm distance from the PCB coil**. The coil was 55 mm from the magnet surface. A 15 mm polystyrene foam board was used as a spacer, and three blocks of jelly were positioned over the spacer. The 90° calibration shows that the pulse duration was approximately 45 μs. Therefore, the NMR signal was obtained utilising the previous setting parameters except for the pulse duration, which was 40 μs with an interval time of 10 μs and 1024 average scans.

Furthermore, an attempt was made to acquire the NMR signal at a distance of 22 mm from the PCB coil. The signal was observable, though it was weak. The parameters differed as follows: the pulse length was 60 μs with an interval time of 20 μs with an echoing space of 1500 μs. The average number scans was 2048, and the phase shift was 180°. The obtained NMR signals at distances of 15 mm and 22 mm are described in Appendix K.

Then, to further improve the NMR signal at a depth of 22 mm and above from the sensor, a new PCB coil with a different size was printed, as described in the following subsubsection.

5.4.2.3 PCB coil 3

The final design in this study for the PCB coil was a double-sided planar rectangular coil that was planned as five turns with a line width of 2 mm and 1 mm spacing between tracks. The inner and outer coil lengths were 82 mm and 105 mm, respectively, and the inner and outer coil widths were 40 mm and 67 mm, respectively, (Figure 5.28a). Figure 5.28b shows the top view of the new PCB coil positioned between the two magnet arrays.

As a routine procedure before coating the coil with the epoxy resin, the resonance circuit frequency was checked with a network analyser. It was 0.769 MHz with a power depth of -33.7 dB, while the desired frequency according to the previous subsubsections is 0.768 MHz located at a power depth of - 31.4 dB. The electronic system utilised was the system described in Figure 5.25, and the sample was Hartley's jelly blocks. A 90° calibration was performed from 5 μs to 50 μs for four blocks of jelly on the surface of the coil. The peak of the pulse duration was approximately 20 μs. The experimental parameters for this run were similar to the parameters utilised with the square coil. An image of the setup and the 90° calibration can be found in Appendix L.

NMR signals were produced for the jelly blocks, which were placed at the surface of the rectangular PCB coil, utilising a pulse duration of 22.5 μs for a different number of blocks. The employed experimental parameters were similar to the parameters used to run the 90^0 calibration. Details of the obtained NMR signal can be found in Appendix L.
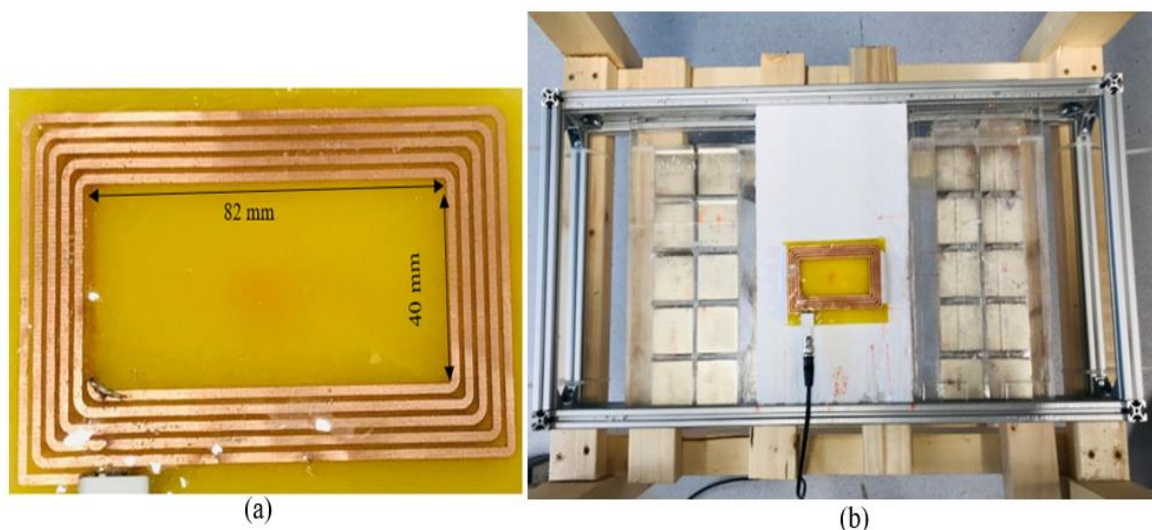

Figure 5.28: Photograph of the rectangular PCB coil, where (a) is the PCB coil coated with a layer of epoxy resin and (b) is the top view for the PCB coil located between the two magnet arrays.

The experimental parameters were optimised to observe the NMR signal 15, 22, 30, and 35 mm from the coil surface utilising three blocks of jelly with a total thickness of 66 mm. Table 5.6 lists these parameters, where the PCB coil was moved down at each depth to ensure that the jelly blocks were always secured at the sweet-spot. The amplitude was similar for all depths, which was 280 mV. Further, the number of points per echo was 16, and the number of echoes was 8. The reader can observe that at depths of 22 mm and 30 mm, different interval times (DW) were applied to acquire the signal, and all these values produced a good NMR signal. From this table, it can be observed that as the distance from the coil surface increased, the pulse length (PL) also increased; this outcome was in agreement with other researchers' findings [3].

Table 5.6: Experimental parameters optimised to obtain the NMR signal from different depths of the rectangular PCB coil utilising three blocks of jelly.

Depth (mm)	PCB Coil position (mm)	Blocks start (mm)	Freq. (MHZ)	DW (μs)	PL (μs)	TE (μs)	Avg scan	PS	TR (ms)
0	55	57	0.767	10	22.5	800	512	55	100
15	55	72	0.768	10	40	800	1024	55	100
22	50	75	0.766	10	52.7	800	2048	55	100
			0.761	20	50	1500	2048	100	80
			0.763	30	52.7	1500	2048	100	100
			0.760	40	50	1800	2048	100	80
			0.761	50	50	2000	2048	100	100
30	39	70	0.763	10	65	800	2048	100	100
			0.765	20	65	1500	3072	100	80
			0.763	40	65	1800	2048	100	80
			0.763	50	63.5	2000	2048	100	80
35	30	67	0.763	50	75	2000	3072	100	80

In general, the surface RF coil exhibits a trade-off between the SNR and the distance from its surface, with the signal intensity decreasing as a function of distance. Therefore, to obtain a clear NMR signal at these depths, the average number of scans was increased, starting with 512 at the coil's surface and reaching 3072 at a depth of 35 mm. An example of the obtained NMR signal at depths of 15, 22, 30, and 35 mm from the surface of the rectangular PCB coil can be found in Appendix L.

To improve the NMR signal at distances of 22 mm and above, there was a need to remove the noisy frequencies outside the desired bandwidth range. Therefore, 1 MHz of low-pass filters were added before and after the Op-Amp's pre-amplifier circuit, as shown in Figure 5.29. Furthermore, the sample was changed to sunflower oil instead of Hartley's jelly because the latter has a short T_2 relaxation time. Further, the amount of noise at a distance from the coil is higher than the T_2^{eff} value of the jelly block, which could potentially be the reason for the poor appearance of the NMR signal at a distance from the coil in the previous experiments.
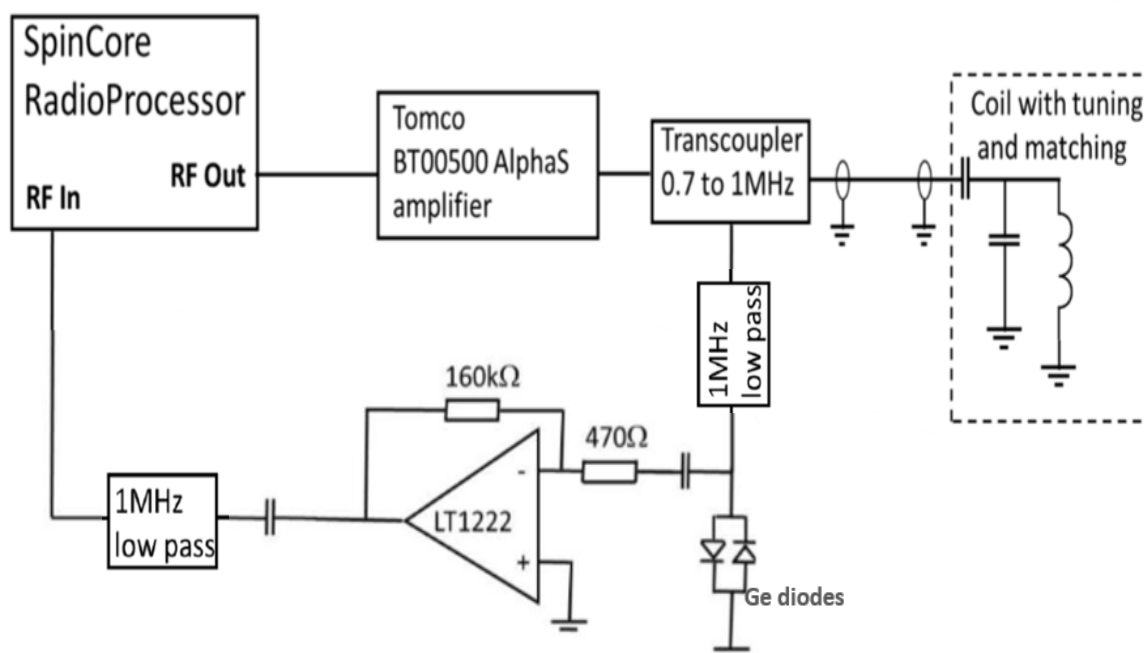

Figure 5.29: Sketch diagram of the electronic system after adding the 1 MHz low-pass filter to the Op-Amp. The CAPIBarA magnet paired with the rectangular PCB coil.

Consequently, the sunflower oil was placed in a plastic container with a total volume of 256 ml (40 mm height and 6400 mm^2 for the length and width). The obtained NMR signal for the sunflower oil at distances of 23 mm and 31 mm from the sensor surface before adding the low-pass filter is described in Appendix M. The obtained NMR signal from the sunflower oil agreed with the previous observation that the short T_2 material is poorly observable at a distance above the depth of 20 mm compared to the longer T_2 material. After the addition of the low-pass filter, a considerably improved NMR signal was observed at depths of 32 mm and 34 mm from the surface of the PCB coil, and the details can be found in Appendix M.

The considerable improvement in the acquired NMR signal at a distance of 34 mm urged us to investigate the possibility of acquiring the NMR signal inside a plastic model (PregnantWomen Model AS30591, anatomystuff.co.uk). Figure 5.30a illustrates the side view of the plastic model without the sample, while Figure 5.30b shows the

NMR signal obtained from the sunflower oil inside the model. The reader can observe the formation of the spin echoes in the time domain section, the first part of the CPMG control panel (Figure 5.30b) compared to the time domain section in Figure 5.30a.
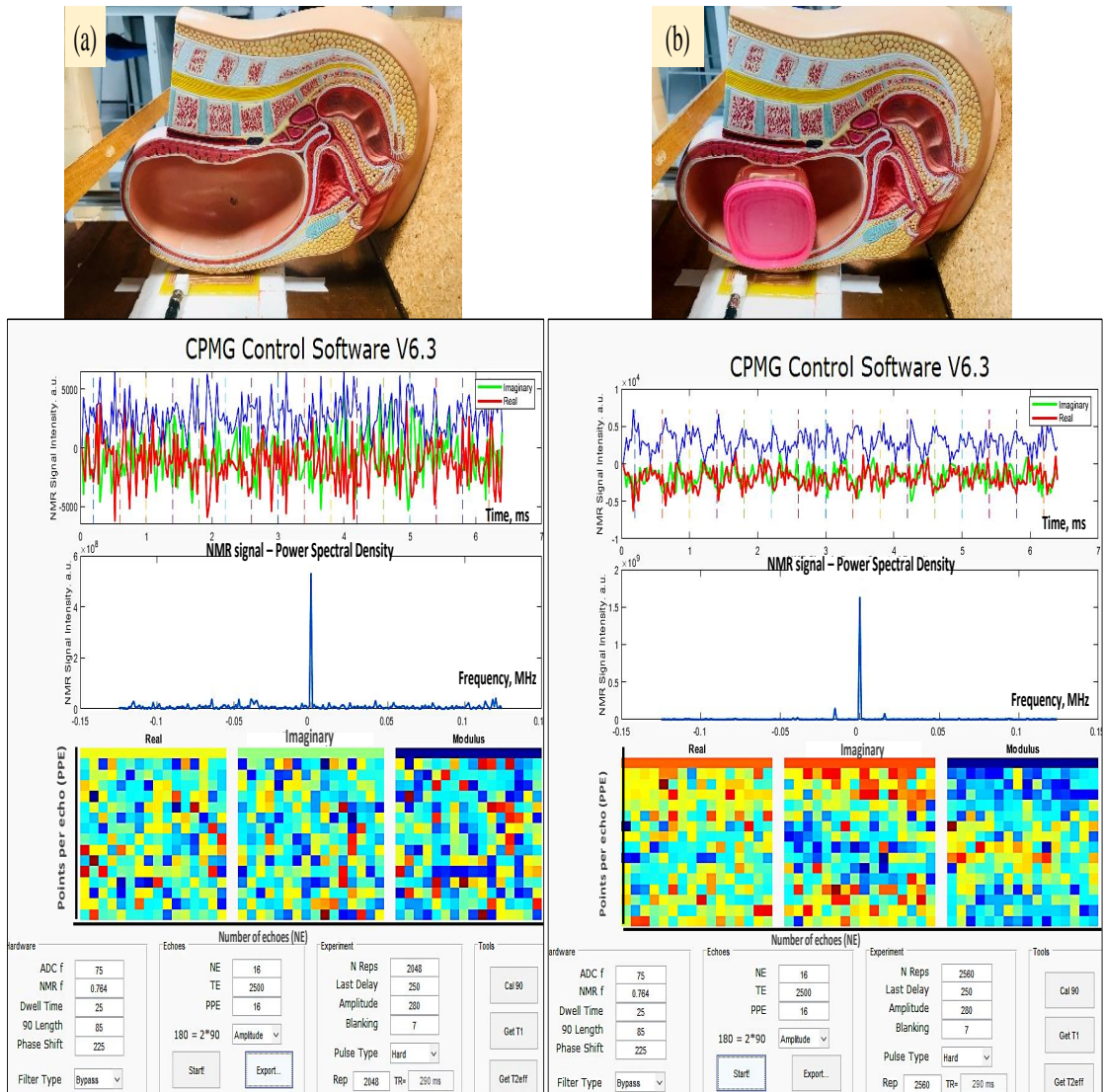

Figure 5.30: NMR signal obtained inside the plastic model of a pregnant women from 256 ml volume of sunflower oil. Image (a) represents the signal without the sample, while image (b) shows the NMR signal inside the model.

The current electronic system exhibits good performance in obtaining the NMR signal up to 35 mm from the PCB coil surface. However, there was a need for dummy echoes in the measurement of the T_2^{eff} relaxation time. It was noticed that for echo times lower than 1000 μs, the first echo dominated and suppressed the appearance of the subsequent echoes, which consequently affected the averaged signal (Figure 5.31a).

Therefore, a dummy echo option was introduced in the dialogue box of the CPMG GUI window, and the outcomes showed a good decay pattern for the points below the echo time of 1000 μs (Figure 5.31b). All of these measurements were performed for the sunflower oil inside the plastic model.
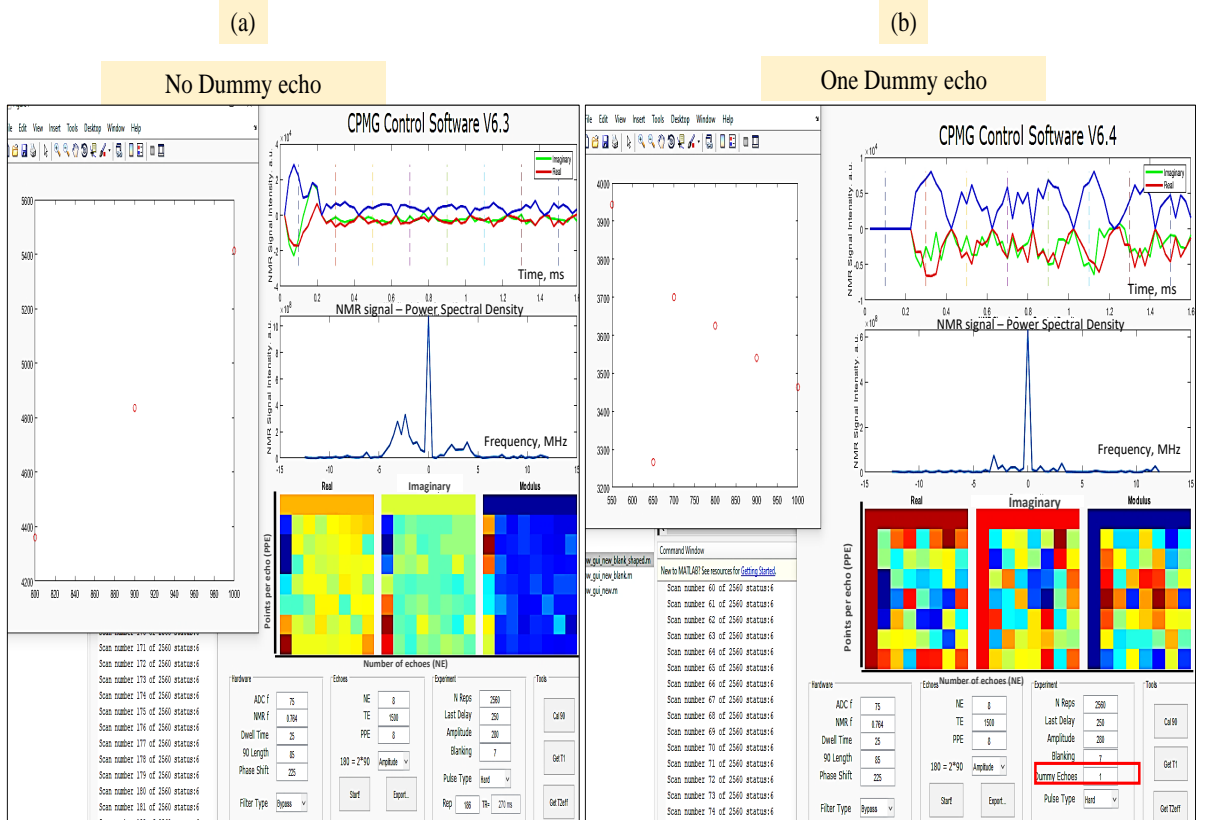
Figure 5.31: The introduction of the dummy echoes option in the CPMG GUI window. Image (a) shows the signal without the dummy echo for an echo time of 1000 μs and the improper appearance of the subsequent echoes that affects the measuring points. Image (b) shows the impact of the dummy echo on the signal at an echo time of 1000 μs and how the subsequent echoes appear correctly with a proper decay pattern for the measured points.

5.5 T_2^{eff} estimation with NMR-CAPIBarA system

Unlike in the very homogeneous field, the decay of T_2^{eff} in the presence of a less homogeneous field as in the presented low-field system is predominant. This is due to the dependency of the T_2^{eff} on parameters that are resulted from the non-uniform fields, such as molecular diffusion, the magnitude of the field gradient, and the echo time. One of the methods that could be utilised to prevent Brownian motion from contributing to the measurement of T_2^{eff} is by measures the integral of the echoes as a function of increasing echo times (TE) as described in [72]. However, with a low-field system such as the current, this technique is considered too prolonged for clinical applications [142].

Thus, the measurement of T_2^{eff} was undertaken by performing a CPMG experiment that included a large number of echoes and the shortest echo width the hardware allowed, to reduce the effect of the molecular motion. This approach in the experiment improves the SNR, and by averaging the scans, the signal is also averaged linearly, whereas the noise scales with the square root of the number of scans; thus, the SNR is dependent on NS$/\sqrt{NS}$.

In this experiment, T_2^{eff} will be estimated for the eight different viscosities of silicone oil that were described in chapter 2. The PDMS viscosities were 300, 600, 900, 2K, 5K, 10K, 15K, and 30K cP. Each sample was placed in a plastic container with a total volume of 128 ml (20 mm height and 6400 mm² for the length and width). A 24 mm polystyrene foam board was used as a spacer between the coil and the sample.

The electronic circuit in Figure 5.29, which employs the simple inverting Op-Amp circuit as a signal pre-amplifier, did not show a proper decay pattern for the T_2^{eff} relaxation time for the PDMS sample (30k cP) that was positioned 24 mm from the PCB coil surface (Figure 5.32). Therefore, the pre-amplifier component was switched to off-the-shelf components, the ones presented as a receive channel in Figure 4.2 of chapter 4. Thus, the final modified electronic system for the current study shown in Figure 5.33, and it was published in this paper [142].
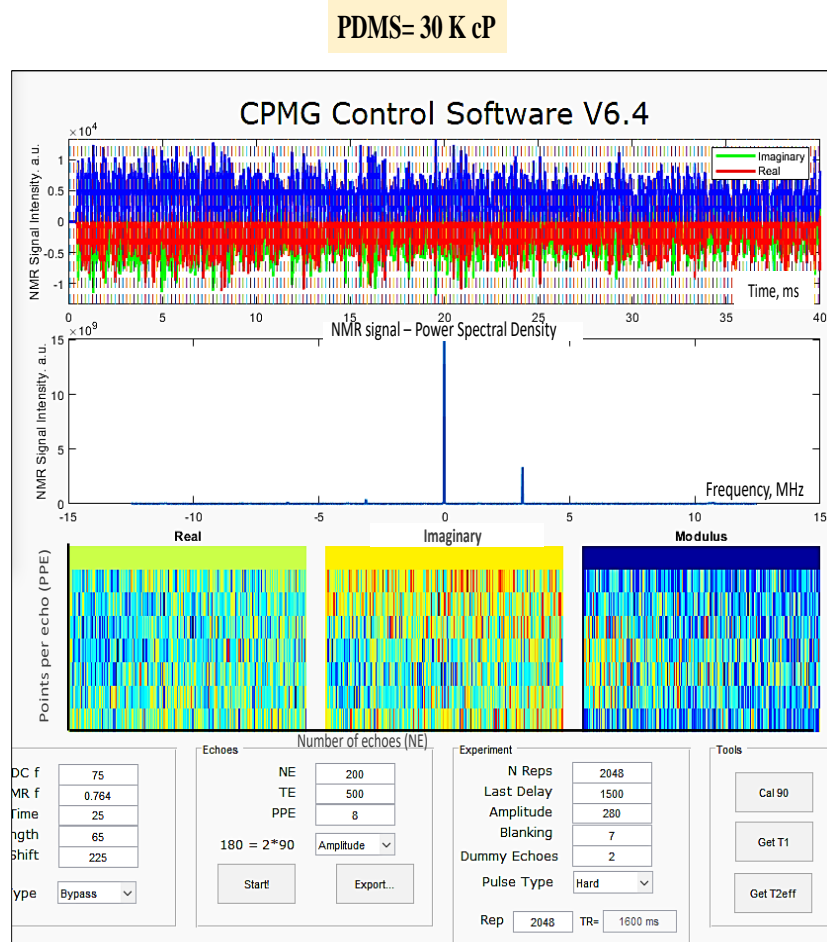

Figure 5.32: Snapshot of the signal decay pattern of the T_2^{eff} relaxation time of the PDMS sample with the Op-Amp circuit used as a pre-amplifier.
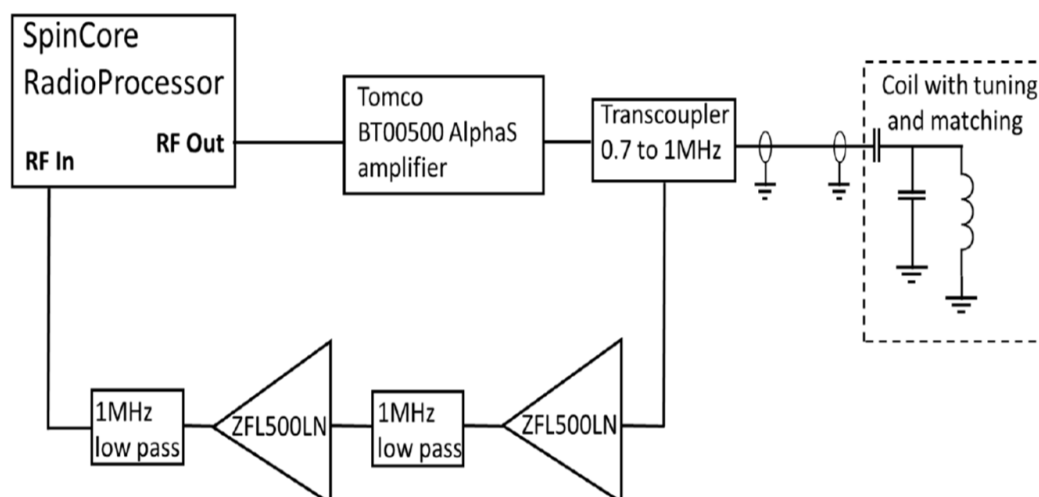
Figure 5.33: Schematic diagram of the electronic system for the NMR-CAPIBarA.

5.5.1 PCB coil sensitivity

The PCB coil sensitivity and pulse duration were evaluated for the modified electronics system. The previous method was followed to evaluate the PCB coil, securing the sample at the sweet-spot and moving the coil down. Thus, for a structured evaluation, the coil will be gradually moved away from the sample surface by 5 mm on each step, starting from the coil surface to a depth of 40 mm.

The sample utilised in the evaluation was sunflower oil placed in a square plastic container and secured 72 mm from the magnet surface. The volume of the sample was 128 ml (20 mm height and 6400 mm^2 for the length and width). The NMR signal was obtained from zero depth to 40 mm, and the experimental parameters employed for this evaluation are listed in Table 5.7. On the other hand, the following parameters were maintained similar at each step of the evaluation: resonance frequency, echo time, number of points per echo, number of echoes, phase shift, reparation time, and amplitude, which were 0.764 MHZ, 2500 μs, 16, 8, 225°, 250 ms and 280 mV, respectively.

The reader can observe that at each measured depth, two sampling interval times were investigated: the 10 μs and 25 μs. It can also be seen that the signal intensity is higher with a dwell time of 10 μs compared to 25 μs, though both interval times were run with similar pulse durations. The signal intensity was obtained at each step by using the T$_2$ option in the GUI window to integrate one point. Snapshots of the CPMG GUI for each depth and dwell time can be found in Appendix N.

Table 5.7: Experimental parameters utilised to obtain the NMR signal at various depths from the rectangular PCB coil with a 128 ml sunflower oil sample.

Depth (mm)	PCB coil position (mm)	DW (μs)	PL (μs)	Scans	Signal intensity (a.u.)
0	72	25	25	2048	11262.77
		10	25	2048	15865.11
5	67	25	25	2048	9680.92
		10	25	2048	14072.19
10	62	25	38.5	2048	8745.65
		10	38.5	2048	10868.74
15	57	25	40	2048	6844.36
		10	40	2048	8487.78
20	52	25	40	2048	5455.63
		10	40	2048	7189.44
		25	50	2048	5771.93
		10	50	2048	7406.49
		25	55	2048	5836.52
		10	55	2048	7019.205
25	47	25	60	2048	4446.79
			65	2048	5575.66
			75	2048	5440.8
		40	65	2048	3326.488
			75	2048	3352.93
30	42	25	75	2048	4140.9
			65	2048	4187.88
			85	2048	4530.311
			72.5	2048	4132.5
		40	75	2048	3063.026
			85	2048	3119.98
35	37	40	85	2048	2867.04
			100	2560	2131.528
		50	85	2048	3029.2
			100	2048	2732.237
			100	2560	2269.62
			75	2560	2173.92
40	32	50	100	2560	2095.41
			90	2560	2104.77
			85	2560	2030.7

Numerous studies have confirmed the negative correlation between signal intensity and depth and the positive relationship between pulse duration and depth. This correlation was also observed in the current experiment, with Figure 5.34 illustrating the reduction in signal intensity as a function of distance. In addition, Figure 5.35 shows the increase in pulse duration as a function of depth.
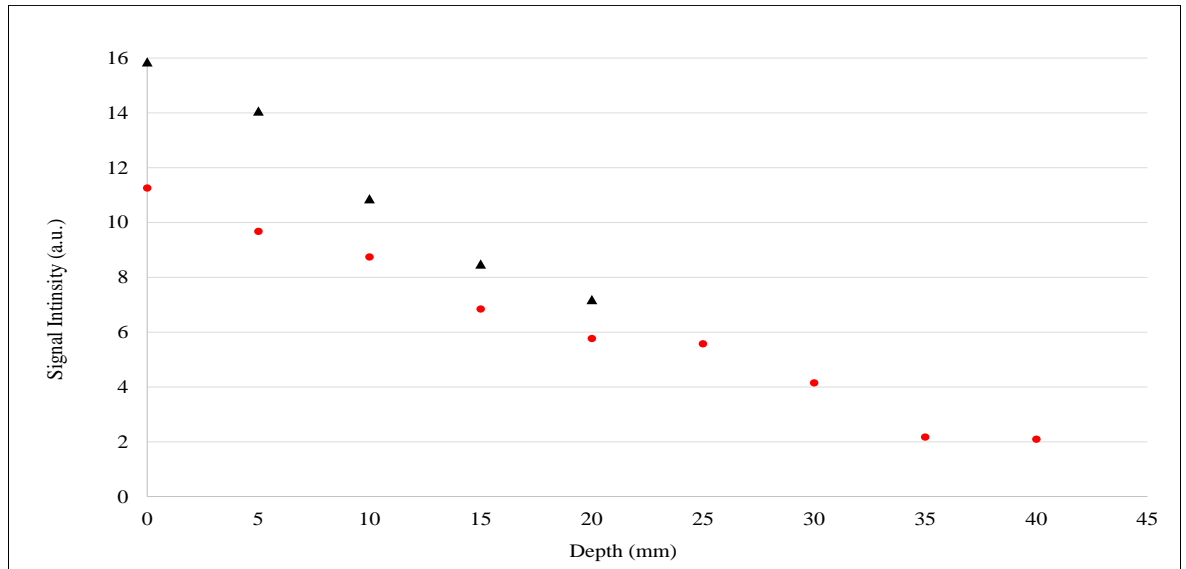

Figure 5.34: Plot shows the inverse relationship between signal intensity and distance from the PCB coil surface. The black triangle represent a dwell time of 10 μs, while the red circle represents a dwell time of 25 μs, except that the last two points obtained with a dwell time of 50 μs.
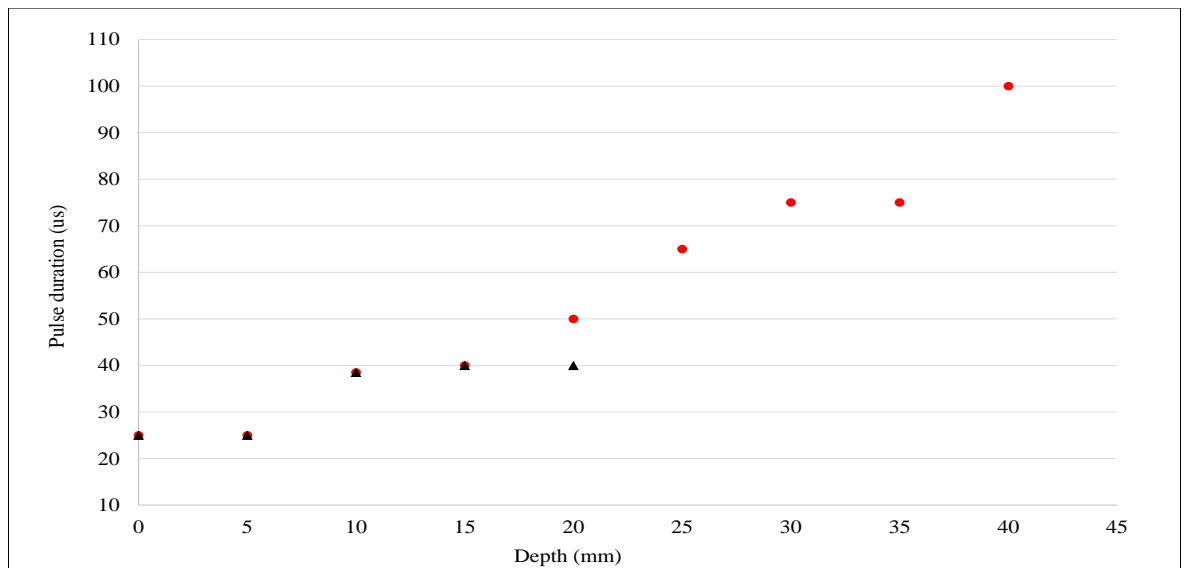

Figure 5.35: Plot shows the relationship between the pulse duration at a distance from the PCB coil surface. The black triangle represent a dwell time of 10 μs, while the red circle represents a dwell time of 25 μs, except that the last two points were obtained with a dwell time of 50 μs.

5.5.2 T_2^{eff} estimation with the solenoid coil

As an intermediate stage between the CAPIBarA system and the MRI scanner, the 20 mm diameter solenoid coil used earlier was utilised as an RF sensor to enclose the magnet sensitive volume. This step reduces the surface coil problems related to the sample filling factor, how much of the coil sensitive volume is filled with sample, and the amount of sample in the inhomogeneous RF fields. The aluminium box was positioned in the centre between the two magnet arrays 48 mm from the magnet surface to ensure that the solenoid coil centre was at the sweet-spot.

The NMR signal was acquired from 256 averages with the pulse duration set to 5 μs for a frequency of 0.804 MHz. The signal was obtained with a dwell time of 10 μs for 8 points over the centre of 250 echoes and 800 μs echo time with a phase shift of 225°. The repetition time was 1200 ms, giving a total experimental time of 5 minutes. The obtained data for the different viscosities of the silicone oils from a CPMG sequence using the solenoid coil can be found in Appendix O.

On some occasions, external or thermal noise disturbed the measurement, and therefore, the MATLAB program calculated the T_2^{eff} value incorrectly. Therefore, the raw data was transferred to the online program (mriToolbox) to extract the value in such cases. The T_2^{eff} values for the silicone oil samples were averaged from three measurements for each viscosity. Table 5.8 lists the averaged estimated T_2^{eff} values with the standard variation.

5.5.3 T_2^{eff} estimation with PCB coil

For the PCB coil, the CPMG sequence parameters are similar to the solenoid coil parameters except for the pulse duration, which was increased to 67.5 μs for a frequency of 0.764 MHz. As a result, the DW time increased to 25 μs, the phase shift became 100°, and the number of averages was increased to 1536, giving a total experiment time of 30 minutes. An example of the data collected for the various silicone oil viscosities measured by the PCB coil is presented in Appendix P. The averaged values for the estimated T_2^{eff} for different viscosities of silicone oils are summarised in Table 5.8.

5.5.4 Sensitive volume

Several parameters control the size of the sensitive volume, such as the uniformity of the magnetic field, the transmission bandwidth, and the receiver chain bandwidth, which in turn, depend on the acquisition time. The more uniform the field is, the larger the volume region will be, while a shorter dwell time and shorter transmit pulses also expand the size of this volume.

These parameters dictate the overall bandwidth of the measurement, and therefore limit the sensitive volume when they are narrow. In the current study, the RF pulse length (t_p) is limiting and excites a bandwidth equal to $1/(4*t_p)$, which was 50 kHz for the solenoid and 3.7 kHz for the PCB coil. These frequencies correspond to 1.2 mT and 88 μT, respectively. These values were employed to determine the volume size over the magnet, for which a home-built three-axis magnetometer based on CYL8405 (ChenYang Gmbh, Finsing, Germany) was utilised to define the area which includes a homogeneous field of these values. For the solenoid coil, the size of the sensitive volume was found to be 209 mm^3, while for the PCB coil it was 60 mm^3. Figure 5.36 shows a graphical approximation of these volumes, where the green ellipsoid area represents the solenoid coil, and the red ellipsoid represents the planar coil [142].
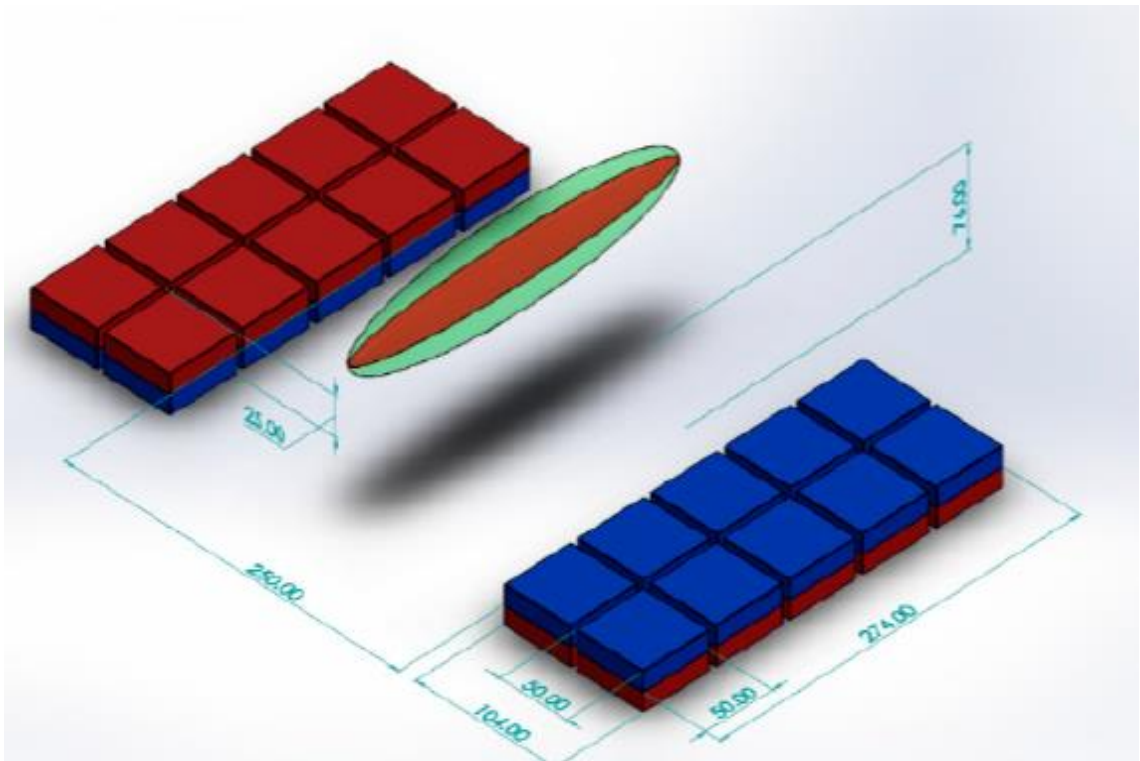

Figure 5.36: Schematic diagram shows an approximation for the sensitive volume of the solenoid coil and the PCB coil at the sweet spot.

5.5.5 T_2^{eff} estimation with PCB coil oriented longitudinally

To explore if the PCB coil direction could improve the SNR, the direction was changed from transverse to longitudinal (Figure 5.37). T_2^{eff} was estimated for all silicone oil viscosities by employing similar experimental parameters that were used with the transverse direction. Details of the obtained data for the effective transverse relaxation time of different viscosities of silicone oils in the longitudinal direction can be found in Appendix Q. Table 5.8 lists the averaged value of three measurements for each viscosity of the silicone oils, which is obtained by utilising the solenoid coil and the PCB coil in two directions, as RF sensors.
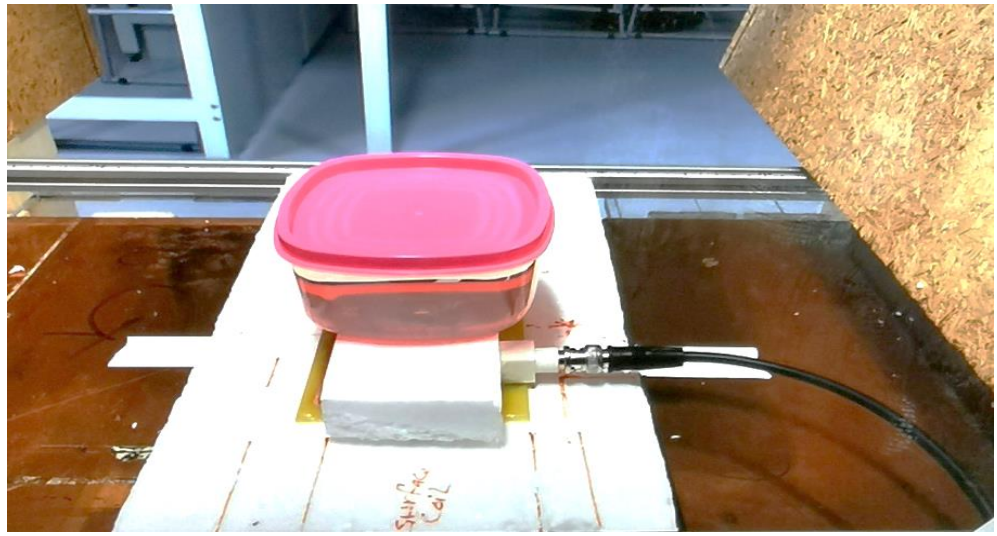

Figure 5.37: Photograph of the PCB coil in the longitudinal position at the sweet-spot.

Table 5.8: T_2^{eff} values for different viscosities of silicone oils, utilising CAPIBarA magnet with the solenoid coil and the two directions of PCB coil.

Silicon oil viscosity (cP)	Solenoid coil $T_2^{\text{eff}} \pm$ SD (ms)	PCB coil transversely $T_2^{\text{eff}} \pm$ SD(ms)	PCB coil longitudinally $T_2^{\text{eff}} \pm$ SD(ms)
300	138.70 ± 21.78	154.59 ± 11.38	160.60 ± 43.72
600	104.31 ± 25.11	107.78 ± 22.79	132.98 ± 19.06
900	84.36 ± 18.75	103.35 ± 11.16	81.84 ± 5.79
2k	74.69 ± 6.70	84.23 ± 10.43	77.49 ± 7.26
5k	69.01 ± 8.72	73.43 ± 1.11	68.05 ± 4.96
10k	56.29 ± 6.36	52.83 ± 8.51	62.82 ± 4.17
15k	47.75 ± 4.87	41.94 ± 9.14	51.69 ± 2.79
30k	38.34 ± 2.17	31.68 ± 5.47	38.40 ± 7.05

It was expected that the error bars for the solenoid coil would be lower than those for the PCB coil owing to its higher B_1 homogeneity and greater filling factor. For coils with sensitive volumes in the same part of the magnetic field, there should be no difference in the T_2^{eff} values because none of the parameters in equation 2.20 are dependent on the coil geometry. However, as Table 5.8 shows, the real measurement demonstrated that although T_2^{eff} did indeed remain unchanged, the error bars of both the solenoid coil and the PCB coil were approximately the same.

Moreover, it was expected that the measurements for the PCB coil in the longitudinal direction would be improved owing to the larger sensitive volume where the B_1 field is orthogonal to the B_0 field in this arrangement, leading to higher SNRs. This is, however, not universally, the case with only half of the silicone oil measurements demonstrating an improved SNR. Similar values for T_2^{eff} were, however, found in each case.

The reduced scatter on the data acquired in the longitudinal versus the transverse orientation (as shown in Appendices P and Q) would, however, support the argument that the, SNR was improved, which would be in agreement with the section of the magnetic field mapping in figures 5.9 and 5.10.

To evaluate the capability of the current system, a correlation relationship between the present system and the MRI scanner was investigated. The T_2^{eff} values which were estimated for the different silicone oil viscosities using the NMR-CAPIBarA were plotted against the reference values produced from the MRI scanner in chapter 3. Figure 5.38 shows the relationship between viscosity and T_2^{eff} for the clinical MRI and the NMR-CAPIBarA with two RF coils: the solenoid and the PCB coil. By contrast, Figure 5.39 illustrates the correlation between the values as determined using these two systems.
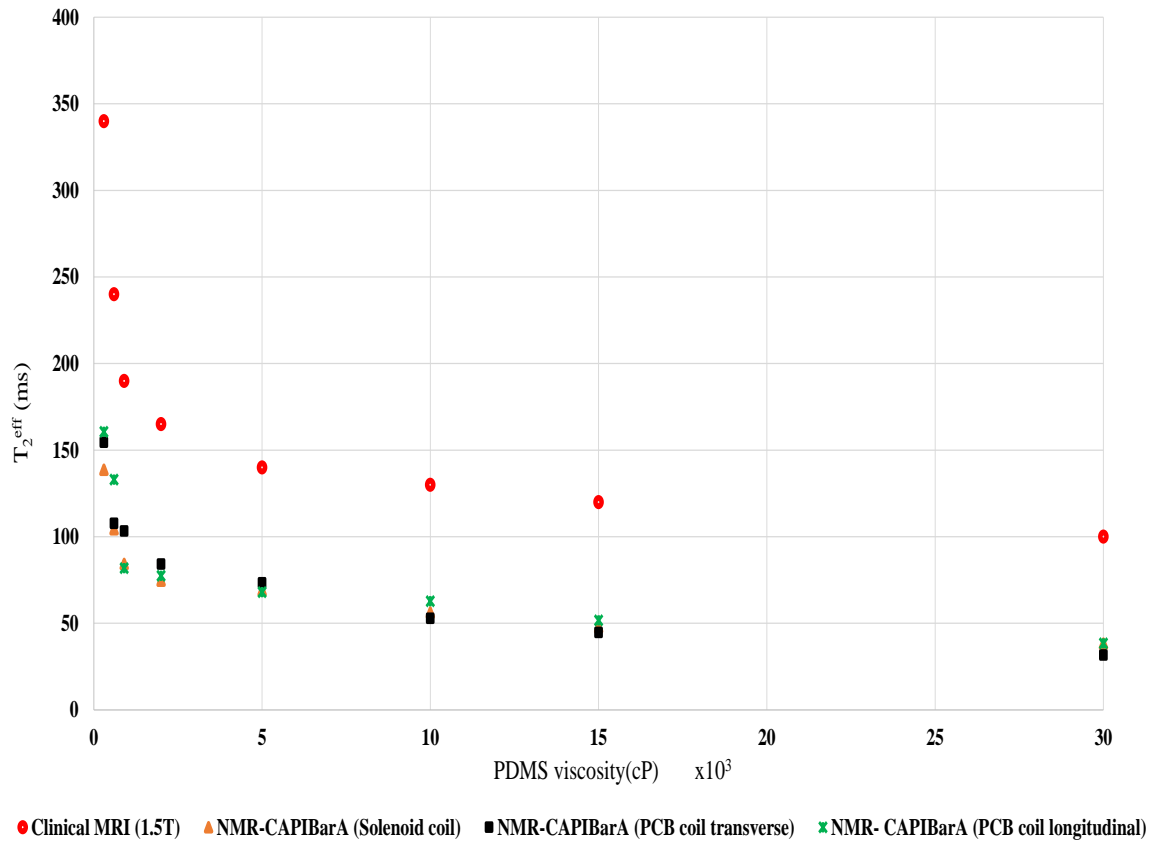
Figure 5.38: Plot presents the estimated T_2^{eff} values as a function of the PDMS viscosity utilising two systems, the clinical MRI and the NMR-CAPIBarA. For the NMR-CAPIBarA, the data obtained with two different RF coils, the solenoid and the PCB in two directions.
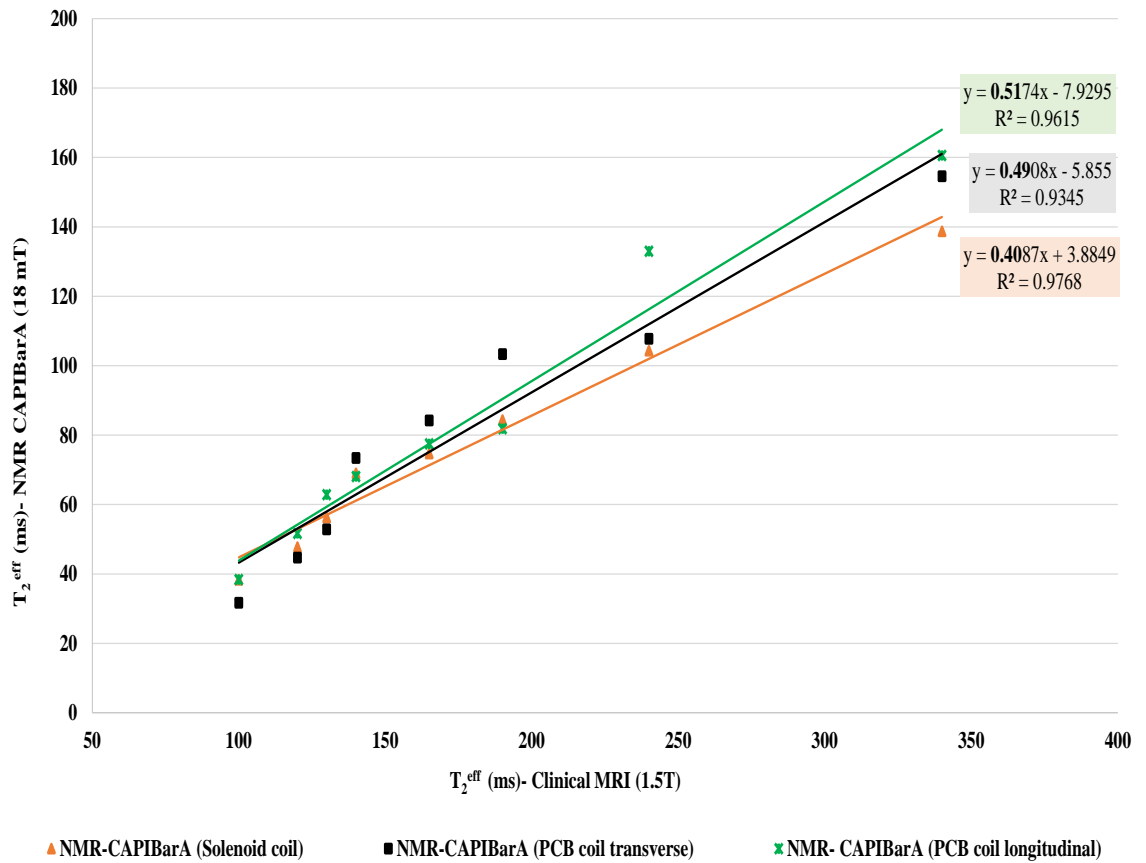
Figure 5.39: Correlation between the T_2^{eff} measurements for the NMR-CAPIBarA system with solenoid and PCB coil and the T_2^{eff} measured with the clinical MRI.

Though the linear coefficient values were not 1 for the two systems (0.4 for the solenoid coil and 0.5 for the PCB coil), the fact that they are linear demonstrates that the NMR-CAPIBarA has clear potential for use in predicting placental health. The data in the Figures in Appendices O, P, and Q for the T_2^{eff} measurements obtained using the PCB coil and the solenoid coil show significant scattering due to the noise. Because the noise distribution for such SNRs is Gaussian, it is not detrimental to the fit and is included as an offset to the baseline. Moreover, collecting several spin echoes per scan without influencing the experiment repetition time provides adequate data point density, allowing a sufficient level of confidence in the fit parameters. The limiting factor in the sensitive volume is the transmit efficiency; however, it could be advantageous for the practical use of the system to produce a small sensitive region that generated good visualisations concurrently with other modalities such as ultrasound imaging.

5.6   Model system for both T_2^{eff} and T_1

This section will present a model system that can shorten both spin-lattice and spin-spin relaxation times by mixing full-fat milk powder with silicone oil. 300 cP PDMS viscosity was selected as the basic viscosity to which a different concentration of milk powder would be added. The reason for this selection is that this viscosity has the highest T_2^{eff} value, and accordingly, the change in the transverse relaxation time will appear more readily. In regard to the spin-lattice relaxation time, the measurement was conducted with a 1.5 T clinical MRI and showed that the T_1 values are similar for all pure viscosities of silicone oil, whose median value was 754.78 ± 8.35 ms, collected from 16 samples of different pure viscosities that ranged from 1k cP to 300k cP. [144] reported a similar value of the T_1 relaxation time for a pure silicone oil tested in a 1.5 T MRI machine in their experiments -779.9 ms- and they also report 986.7 ms in a 3 T machine, where $T_1 \approx \sqrt[3]{B_0}$[123; 144].

The full-fat milk powder was first dissolved in still water and then added to the PDMS. This type of emulsion is unstable and easily breaks down. Therefore, drops of acetone were added to prevent this separation. Later, the whole mixture is placed inside a shaker for sufficient mixing before the experiment. An experiment was conducted on a 1.5 T MRI scanner with this mixture to test the effect of settling on the value of T_2^{eff} and T_1 over the course of time. The plot in Figure 5.40 shows that leaving the sample unmixed for more than 20 minutes will result in a more than 10% change in the T_2^{eff} value, while the T_1 value was less impacted by the separation but still changes.

Five different concentrations of full-fat milk powder were added to the PDMS, all as weight per volume percentage: 0%, 10%, 20%, 33%, and 40%. Table 5.9 presents the preparation for each concentration. All the model systems were placed in a square plastic container similar to the size used in previous experiments.
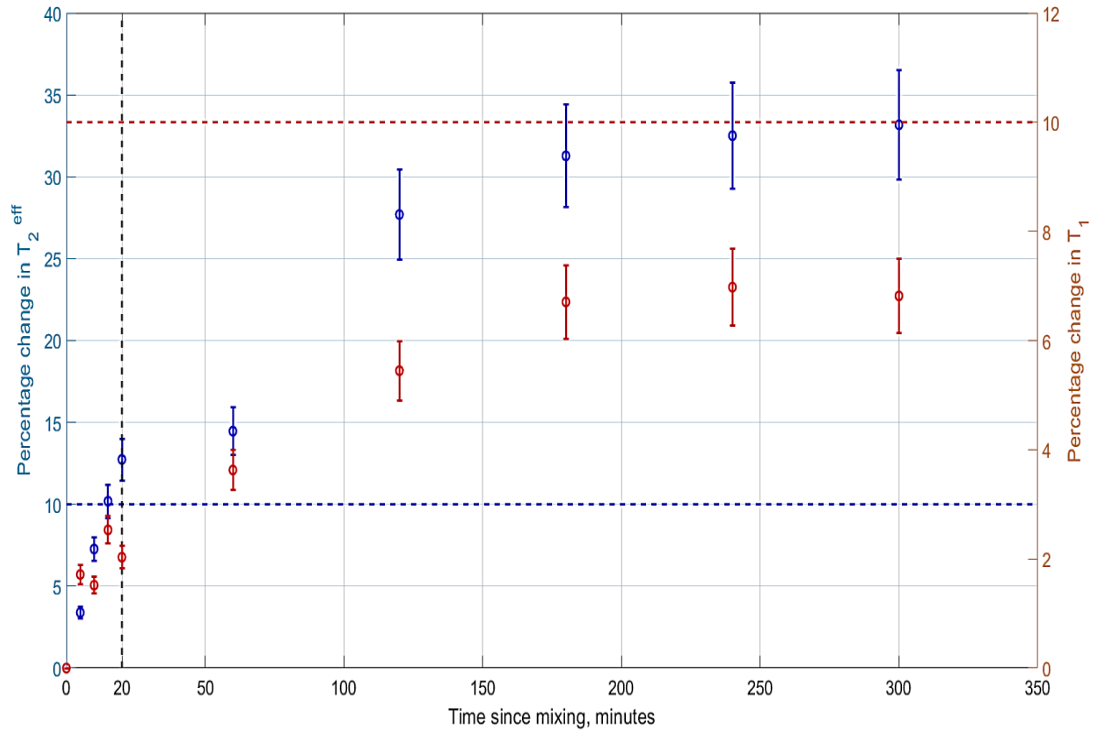
Figure 5.40: Plot presents the impact of the model mixture settling as a percentage over the course of 5 hours on the values of T_2^{eff} and T_1.

Table 5.9: Preparation of the model system components with different concentrations.

Sample concentration% (w/v)	PDMS (300 cP) (ml)	Milk powder (g)	Dissolved in still water (ml)	Total volume (ml)
0	65	0	0	65
10	30	15	120	150
20	30	15	45	75
33	60	60	120	180
50	60	90	120	180
10*	A 35 ml from	33% mixture was diluted	by 80 ml of water	115
20*	A 35 ml from	33% mixture was diluted	by 23 ml of water	58
40	A 60 ml from	50% mixture was diluted	by 15 ml of water	75

In this experiment, for both relaxation time experiments (T_2^{eff} and T_1), the PCB coil was positioned 50 mm from the magnet surface, while the model sample was placed 24 mm from the coil. The experimental parameters for T_2^{eff} were optimised; the resonance frequency was modified to 0.768 MHz with a pulse duration of 65 μs. The echo number was increased to 1000, which increased the repetition time to 1800 ms; the number of averaged scans were reduced to 1024. The rest of the parameters were similar to those described in the previous section. The total experimental time for each model sample was 31 minutes. An example of the obtained data from the CPMG sequence for the different concentrations of model samples is included in Appendix R.

For the T_1 estimation, silicone oil is known to have an exceedingly long T_1 relaxation time [144]. However, the magnitude of the spin-lattice relaxation time is dictated by the strength of the B_0 field. Hence, it was expected for the current low-field NMR system that a maximum T_R value of 1500 ms would be adequate for the measurement. Therefore, the experiment was performed for 12 different points of repetition time: 25, 60, 80, 100, 120, 160, 180, 250, 350, 500, 1000, and 1500 ms, spaced by 800 μs echo time. Each of the 16 echoes was digitised by 16 points at an interval time of 25 μs and a pulse duration length of 65 μs. The average number of scans was 1024. The total experimental time for each model sample was 1.26 hour. A fresh model sample was prepared for concentrations of 20% and 10%. This is due to the highly fluctuating data points generated from the previous diluted samples. The data obtained for the T_1 relaxation time measurements for the different concentrations of the model sample is presented in Appendix S.

Table 5.10 displays the estimated averaged values with the SD of the three measurements that were performed for each modelled sample concentration to obtain the spin-spin and spin-lattice relaxation times. Figure 5.41a and 5.41b demonstrate the reduction in the values of the T_2^{eff} and T_1 relaxation times as the full-fat milk concentration is increased in the sample, respectively.

Table 5.10: T_2^{eff} and T_1 values for different concentrations of the modelled system, milk powder mixed with 300 cP of PDMS oil, utilising the NMR-CAPIBarA system.

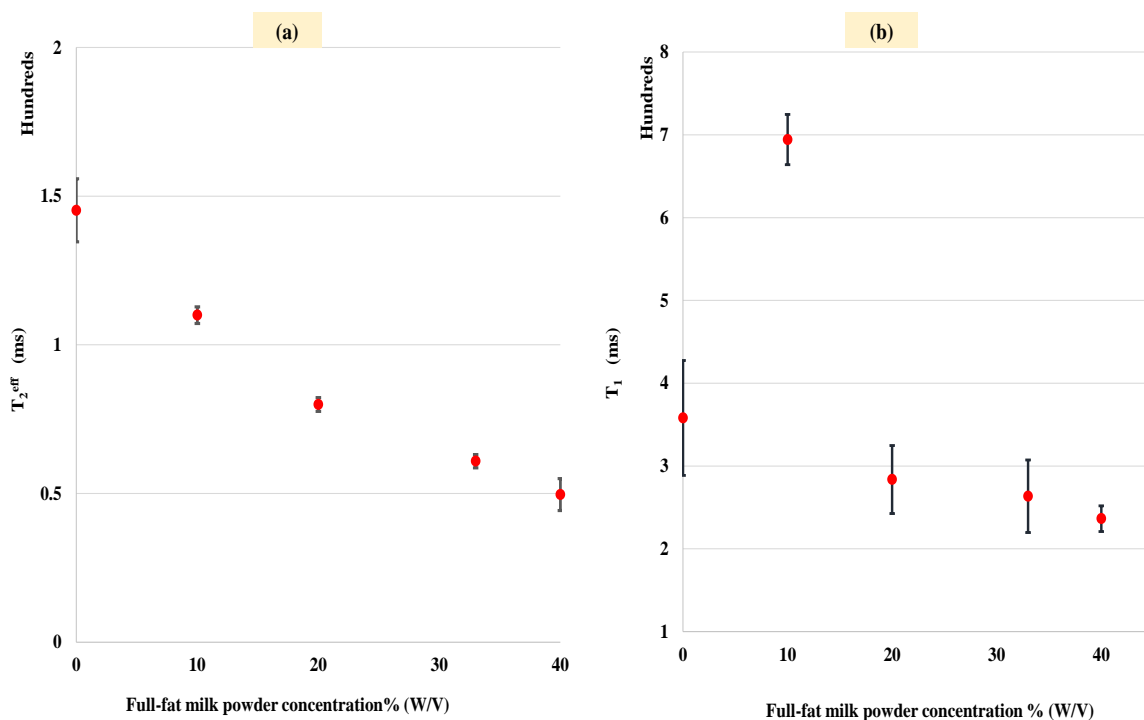| Sample concentration% (w/v)	$T_2^{\text{eff}} \pm$ SD (ms)	$T_1 \pm$ SD (ms)
0	145.23 ± 10.61	358.16 ± 69.39
10	109.98 ± 2.79	694.29 ± 30.31
20	79.93 ± 2.33	283.69 ± 41.04
33	60.87 ± 2.23	263.56 ± 43.83
40	49.64 ± 5.37	236.39 ± 15.57

Figure 5.41: Plots show the inverse proportional relationship of relaxation times to the amount of full-fat milk powder added to the silicone oil. The left-hand shows the sharp reduction in the T_2^{eff} values and the right-hand shows the slight reduction in T_1.

The impact of the large number of echoes in the T_2^{eff} experiment resulted in a significant reduction in variation for the repeated measurements compared to the previous section, which employed 250 echoes. Moreover, the addition of the full-fat milk powder sufficiently shortened the values of the T_2^{eff} relaxation time for the silicone oil with 300 cP viscosity. As shown in Figure 5.40a, the points sharply decreased at higher concentrations of the milk powder. It is noteworthy that the measurement of the relaxation time for the 50% concentration was unsuccessful, as the repeated measurement did not show any changes in the relaxation time, which means that the substances did not mix sufficiently.

By contrast, the spin-lattice relaxation time was not sufficiently influenced by the increased concentration of the milk powder in the silicone oil, specifically after the concentration of 20%. In addition, the variation between the repeated measurements was considerably high, as seen in Figure 5.40b and presented in Table 5.12. The main reasons could be the long experimental time and thermal noise. Moreover, the number of repetition times (12 points) was insufficient and should be higher at the beginning of the curve to build an accurate magnetisation curve. Further, a higher number of average scans could improve the measurement. Of course, all of these parameters are at the expense of the experimental time.

Moreover, the reader will observe that the 10% model sample had a higher value than the pure PDMS, because in the sample preparation method the volume of the dissolved water is approximately four times higher than the amount of the PDMS. The thermal

and system noise causes outlier points in some of the measurements. Therefore, these values were repeated and added to the fit curve, and the T_1 value was re-calculated using the online program (mritoolbox).

5.7 Composite pulse

Usually, the traditional refocusing pulse, the CPMG pulse sequence, does not allow for the greatest SNR achievable in inhomogeneous static magnetic fields. Long time measurement might change the magnetic field gradient due to the instability of the magnetic field caused by temperature drift. The utilisation of refocusing pulses (180°) in the refocusing cycle with RF power limits leads to an error due to the deflection between the axis of the effective refocusing sequence and the magnetisation rotation, which distorts the refocusing phase. To improve the sensitivity of the low-field NMR system, researchers in 1981 [145] found a solution by employing an additional rotation of the magnetisation vector with different phase and duration to correct these unavoidable errors.

The composite pulse is considered an elegant approach to compensate for the imperfection arising from the inhomogeneous B_1 field or the off-resonance effect [146]. The composite pulse consists of a cohort of pulses of varying duration and phase which is used to replace a single pulse with an equal net rotation but for a higher gross tolerance for the imperfections [146; 147]. The inhomogeneity in the applied RF field across the sample volume causes the nuclei to be subject to a different pulse flip angle, notably at the sample periphery. Amendments to the pulse sequences that can tolerate the RF non-uniformity yield a reasonable leeway for the experimentalist to set up the pulse experiments. The off-resonance excitation emerges from the mismatch between the transmitter frequency and the Larmor frequency of the spin.

Therefore, the composite plus was introduced to the pulse sequence in the MATLAB GUI code and was investigated utilising the exact experimental parameters of the hard pulse. To check if an improvement is achieved, a comparison study between hard and composite pulses was conducted. The test was performed by measuring the T_2^{eff} relaxation time for the PDMS of 5k cP viscosity at 24 mm distance from the PCB coil. The PCB coil was placed 50 mm away from the magnet surface in the transverse direction. Echo times of 800, 1500, and 2500 μs were tested, while all the other parameters were the same. Table 5.11 illustrates the applied settings and the averaged value of two measurements for T_2^{eff} estimation for each pulse type.

Table 5.11: T_2^{eff} relaxation time for 5k PDMS oil utilising composite pulse and hard pulse, and the applied experimental parameters 24 mm from the PCB coil.

Pulse type	T_E (μs)	Freq (MHz)	DW (μs)	PL (μs)	NE	Scans	TR (ms)	$T_2^{eff} \pm$ SD (ms)
Composite	800	0.768	25	65	250	1024	1000	71.91±9.07
	1500							71.24±4.75
	2500							50.35±5.64
Hard	800	0.768	25	65	250	1024	1000	58.82.91±3.25
	1500							56.75±5.15
	2500							59.67±0.71

The analysis of the experimental data in Table 5.11 and Figure 5.42 illustrates that the composite pulse exhibits a higher variation between the points of measurements than the hard pulse, which means that a 90° calibration should be conducted to find the optimum pulse duration. However, in a shorter experimental time (20 minutes) with the composite pulse, the T_2^{eff} value of 5k cP was closer to the average value of this viscosity when it was performed with a hard pulse in the transverse direction for 30 minutes. On the other hand, the T_2^{eff} value was lower with a hard pulse. Another reason for the lower value with the hard pulse could be the distance of the PCB coil from the surface of the magnet.
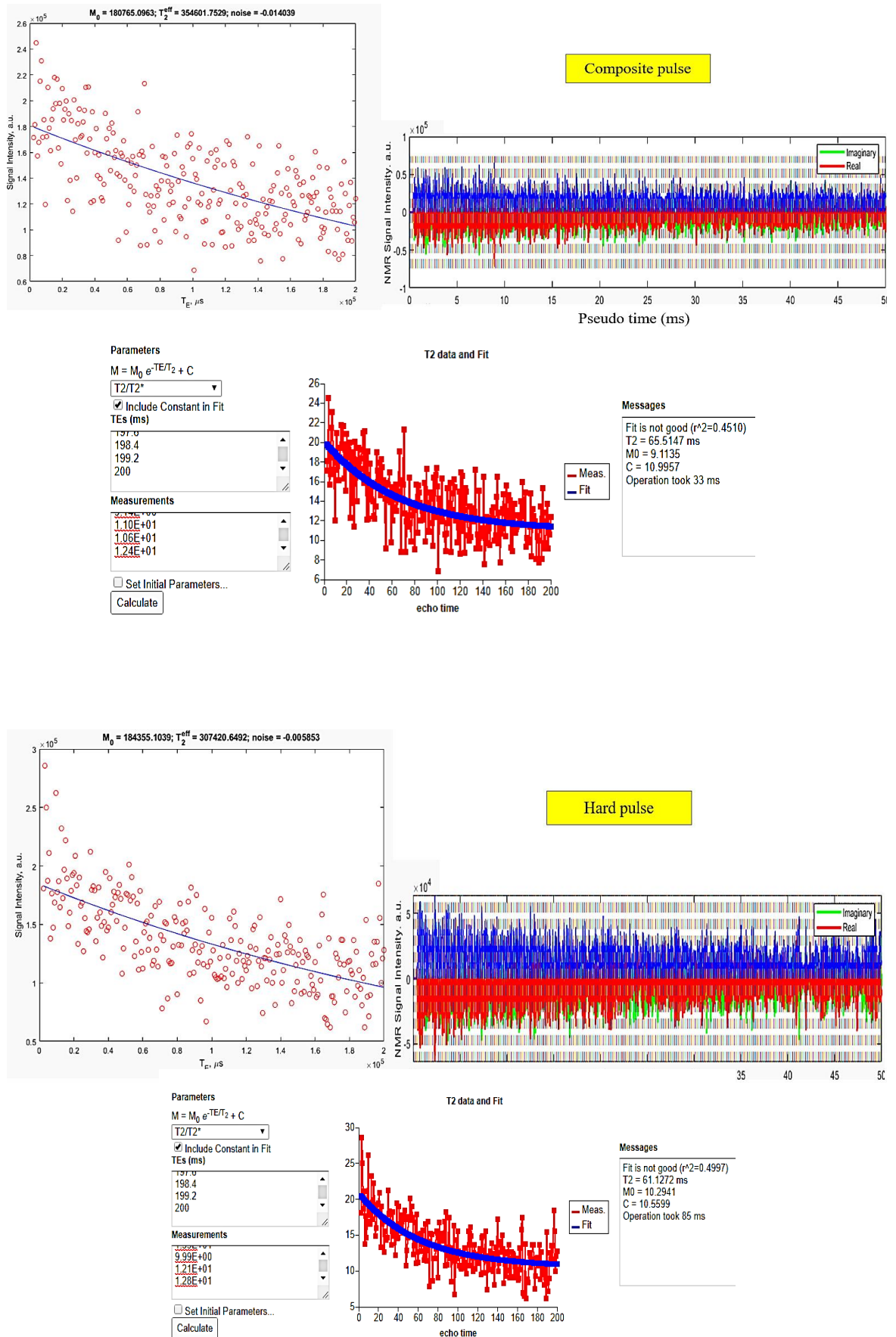
Figure 5.42: T_2^{eff} utilising composite pulse and hard pulse at echo width of 800 (μs). The bottom image is from the online program utilised to produce the fit curve for the data of the T_2^{eff}.

5.8 Discussion

At the beginning of this chapter, the construction of the unilateral magnet was demonstrated, and the magnetic field homogeneity was measured in both closed and open environments. The results obtained from the manual field mapping for the magnetic field exhibited a good agreement with the mathematical calculation of the sweet-spot, which is 76 mm. This agreement has been proved through the data analysis, which illustrates that the lower variability in the magnetic field strength was located at the depths of 74 mm and 82 mm. Additionally, the axial probe was utilised for the field measurement over the depth direction. Although it does not reflect the correct value of the flux density, it revealed that the lowest variation in the magnetic field was at 74 mm and 96 mm inside the metallic box and 78 mm depth in the wooden frame in all of the selected areas of the map sheet. Moreover, the last data analysis conducted to find the direction for the most uniform region of the magnetic field at the centre gap between the two magnets arrays revealed the longitudinal direction, which is in line with other studies [3; 148].

Later, the unilateral magnet was integrated with the low-field electronic system developed in Chapter 4 (Figure 4.7). The outcome of various experiments employed to evaluate the low-field electronic system leads to a considerable improvement in the acquired NMR signal for the sample enclosed by the solenoid coil, both inside the metallic box and at the wooden frame. As demonstrated in previous studies [28], the RF transmitter power amplifier has shown a direct impact on the signal intensity. This has also been observed in this study, where the signal amplitude increased by one order of magnitude by changing the RF power amplifier circuit from the simple inverting Op-Amp (LT1363) of 12 dB gain to the mini-circuit ZHL-3A$^+$ with a gain of 24 dB. This modification allowed the sampling interval time rate to be reduced to half and the RF power amplitude to be raised, which allowed the pulse duration to be reduced. Accordingly, due to the inverse relationship between the size of the excited volume and the pulse duration, the SNR was enhanced by the excitation of a larger volume slice in the sample.

Additionally, the results of the T_2^{eff} experiment in the final part of the evaluation for the low- field electronic system shown in Figure 4.2 confirms the capability of such a system to distinguish between compositions of different materials in the presence of the inhomogeneous B_0 field. As anticipated, the error bar with the non-uniform field (the unilateral magnet) was higher than that with the uniform field (the EMC) because the nuclear spin system magnetised unequally in the presence of an inhomogeneous static field. A larger number of average scans could help reduce this variation in the measurements. Additionally, it was interesting that similar T_2^{eff} values were obtained for all materials except for the still water and the 0.1% SPIOS. This is due to the shorter

echo spacing that was employed (2500 μs) compared to 5000 μs used with the EMC. The longer echo time disturbed the measurement, where the molecular self-diffusion was dominant.

The performance and characteristic of the RF coil dictate the sensitivity of the NMR sensor. The outcomes in Section 5.4 for the different designs of the PCB coil show excellent performance for such coils compared to the handmade surface coil. However, the initial start with the handmade coil was essential to understand the appropriate experimental parameters that could be employed. It is well known that PCB coil is rigid and easy to reproduce accurately [28; 34]. The depth sensitivity of the planar coil is approximately equal to its inner diameter [3; 23; 149]; therefore, different sizes of the PCB coil diameter were manufactured and investigated. Nevertheless, as shown in Table 5.12, the depth of investigation does not depend only on the inner width of the coil; it is also influenced by the gain of the RF power amplifier and the signal receiver circuit (the RF circuit bandwidth).

Table 5.12: Summary of the maximum depth achieved for different planar coil sizes.

Planar coil dimensions (mm)	Depth (mm)	Sample (length X width X height) (mm)	Electronic system
Handmade (30 x 30)	10	Olive oil (28 diam, 15 height)	Figure 5.17
PCB recta.(10 x 20)	5	Olive oil (28 diam, 15 height)	Figure 5.17
PCB square (40 x 40)	10	Olive oil (28 diam, 15 height)	Figure 5.17
PCB square (40 x 40)	15	Jelly block (82 x 44 x 22)	Figure 5.17 + high voltage capacitor
PCB square (40 x 40)	22	Jelly blocks (82 x 44 x 66)	Figure 5.25
PCB recta. (40 x 82)	30	Jelly blocks ((82 x 44 x 66)	Figure 5.25
PCB recta. (40 x 82)	34	Jelly blocks (82 x 44 x 66)	Figure 5.29
PCB recta. (40 x 82)	40	Sunflower oil (80 x 80 x 20)	Figure 5.33

As summarised in the above table, the PCB rectangular (recta.) coil with dimensions of 40 mm by 82 mm exhibited the best overall performance among the other tested surface coils at large distances from the sensor. This was certainly achieved after the gradual modification of the front-end parts in the electronic system. Although the square coil has a width of 40 mm on each side, it did not show satisfactory results at distances beyond 22 mm, unlike the recta. PCB coil. The main potential reason is the receiving circuit channel, where the Op-amp pre-amplifier could not filter the received noise at this height. Therefore, adding the low-pass filter of 1 MHz to the receiving circuit channel in Figure 5.29 boosted the NMR signal for the recta. PCB coil. Moreover, when the pre-amplifier component was switched in the receiver channel

(Figure 5.33) the improvement was substantial. A secondary reason could be the size of the recta. coil, where a larger coil size could reduce the variation in the B_1 field in the region of interest [3].

The results given in Table 5.7 and shown graphically in Figures 5.34 and 5.35 demonstrates three impacts for the distance from the coil surface on the NMR signal intensity. First, the negative correlation pattern between the signal intensity and the coil depth agrees with [3; 28; 32; 34], which were similar to the investigation in this study. The second impact is the positive relationship between the pulse duration and the distance from the sensor. Finally, the reader can observe the reduction in the overall signal intensity with increasing pulse duration. These behaviours are mainly caused by the RF inhomogeneity that spreads the phase across the sensitive volume and distorts the spectrum [28]. Further a spectral bandwidth reduction occurred due to the quality factor of the coil.

The initial estimation of the T_2^{eff} values for the eight viscosities of the PDMS oils was conducted utilising the solenoid coil as an intermediate stage between the constructed unilateral magnet and clinical MRI. As an RF senor, the solenoid coil eliminates two primary issues that reduce the SNR created by the surface coils: the filling factor and the non-uniform RF fields, where the solenoid coil encloses most of the sample within its sensitive volume, thus minimising the B_1 variation across the sample. Interestingly, and according to the obtained results for the solenoid coil and the surface coil in Table 5.8, the error bar was a little lower for the surface coil in the longitudinal direction for half of the silicone oil measurements, which supports the argument that the SNR would be improved in this direction. This improvement is due to the excitation of a larger sensitive volume at the centre of the surface coil, where the RF field was less variant.

Therefore, although the size of the sensitive volume for the solenoid coil is larger than that for the surface coil, 209 mm^3 and 60 mm^3, respectively, they showed an approximately similar value of T_2^{eff} which decayed smoothly as a function of viscosity. This outcome indicates that the surface coil provides adequate information for the different viscosities of the PDMS oils at a distance of 24 mm above the PCB coil. Moreover, the capability of the NMR-CAPIBarA system to replace the high-field system (1.5T MRI) was demonstrated in Figure 5.39. Though the correlation between the two systems was 0.4 for the solenoid coil and 0.5 for the surface coil, the critical attribute is that they are linear. Thus, these results illustrate that the developed NMR-CAPIBarA can work sufficiently over a range of suitable values to predict placental health.

The T_2^{eff} and T_1 relaxation times of the model system showed a perfect outcome for the former, while the latter was not significantly affected by the increased concentration of the full-fat milk powder. This could be due to the level of dependency of these parameters on the B_0 strength and the relaxation mechanism of the spin system. As

was explained in Chapter 2, for the transverse relaxation, spins interact with each other; this internal interaction leads to the loss of phase coherence, and therefore, the transverse magnetisation fades out. Therefore, as these spins increase in the sample, the decay rate will be faster. However, for the longitudinal relaxation, spin dissipates the absorbed energy from the RF pulse at the resonance frequency to the surrounding environment due to the molecular motion. The sample's molecular mobility and size determine the T_1 relaxation rate; slower mobility implies a shorter relaxation time.

In the current study, although the number of nuclei was incremented in the model sample, the T_1 values did not show as significant a reduction as the T_2^{eff} values. Still, the values decrease as a function of viscosity but with an error bar that is considered high. Other researchers have reported that the variation in the T_1 relaxation time values is highly pronounced at low magnetic fields and, if not similar, is higher than the variation in T_2 values and significantly more than the variation in the high magnetic field [150; 151]. This high variation could be due to the long measurement time that the T_1 required compared to the T_2^{eff} measurements, because of which the effect of thermal and external noise could influence the measurements. Additionally, the T_1 relaxation at a low magnetic field allows the magnetisation to transfer from one domain to another during measurement. It then averages the magnetisation of all the samples. Therefore, the different phases are unrecognisable because T_1 relaxation executes on a similar time scale as the spin diffusion process [152]. However, numerous studies show that in a clinical setting T_1 relaxation at low-field provides a better tissue contrast to noise ratio in comparison to the high-field system [151; 153; 154]

The last trial for the enhancement of the NMR signal was conducted by introducing of the composite pulse. However, an improvement was not observable with the tested material (PDMS 5K cP). There are several reasons why the composite pulse was not successful during the first trial. For instance, the composite pulse used might not be suitable for this experiment, as considerable care should be exercised when this type of approach is used with the pulse sequence [146]. Another reason could be that the spectrometer system was not executing this pulse sequence correctly. Moreover, if the investigation starts with a material that has a shorter T_1 and T_2 relaxation time, such as sunflower oil, observation of the improvement would be more straightforward. Besides, a 90° calibration for the new pulse sequence might be needed before starting to acquire the signal. Therefore, a further investigation will be conducted so that this approach will achieve the expected outcome.

One of the essential steps for conducting a successful NMR experiment is to re-measure the magnetic field and identify the correct tuning frequency if needed before conducting any measurements. Furthermore, the limiting factor of the transmission efficiency could be considered an advantage in this work; the corresponding RF pulse at the sensitive volume would generate a small region at the coil centre. Thus, this small spot would

be visualised easily with a concurrent modality such as ultrasound imaging.

At the current time, although the system can reach anterior placentae, there is a piece of evidence in the literature that supports an increased risk of placental disease in this region [155]. Enlarging the space between the magnet arrays could help in reaching the posterior placenta, taking into consideration spine thickness and the drop in field strength that may require additional averaging scans or efficient RF coil designs.

5.9   Evaluation against specifications

The evaluation of the NMR-CAPIBarA is illustrated in Table 5.13, which discusses different specifications proposed in the summary of Chapter 2 to prove the concept of utilising the low-field unilateral NMR system to monitor the health of the placenta during pregnancy in the clinical environment. The specifications include the strength of the operating field, the cost of such a system compared to other imaging modalities, accessibility for pregnant women, the depth of investigation, and the sensitivity.

As shown in Table 5.13, the proposed system satisfies all the criteria that the current application requires. However, the measuring time for an effective transverse relaxation time is considered long for a routine scan.

Table 5.13: Evaluation against specifications of the NMR-CAPIBarA system

Specification	Evaluation
Low magnetic field <20 mT	The system is operated at 18 mT from the magnet surface, which corresponds to 0.766 MHz. This operating frequency provides a safe environment for monitoring pregnant women. The strength of the RF power irradiated compared to the clinical MRI is lower, where the local heat effect is almost negligible. Additionally, the acoustic noise is zero due to the absence of the gradient coil in the system. Therefore, this operating strength does not require a shielding room and can be used in a clinical environment.
Cost-effective	The central part of the system is composed of 20 cubes of ultra-high performance N52 neodymium magnets that are priced approximately $856 [156], and the typical electronic system is priced approximately $16,000 [71; 157; 158], which gives a total cost of approximately $16,856. The proposed system is considered an affordable method in comparison to the 1.5 T clinical MRI scanner, whose starting cost for only the equipment is approximately $325,000 up to above $500,000 depending on the manufacturing company and specification [159]. Furthermore, the hardware value of the current system is also lower than the price of the ultrasound machine, whose cost could start from $6,427 for a low-tier machine up to $128,550 for a high-tier device [160]. Therefore, the presented system should offer an affordable examination cost as a complementary tool for ultrasound imaging.
Open access	It is a single-sided magnet, which is open to accommodate the pregnant woman and the placenta to be probed easily from one side, as demonstrated in Chapter 5 in Figure 5.30 for a pregnant model.
Portable	External noise does not significantly affect the measurement as the experiments were conducted in an open environment, and so the entire system is portable and can be transferred to different sites.
Depth of investigation	The sensor is capable of measuring the NMR signal up to 40 mm from its surface; however, the relaxation time measurements were conducted at 24 mm to ensure a sufficient SNR at that position. This distance is equivalent to the location of the anterior placenta of an average pregnancy.
Sensitivity	The system has the potential to differentiate the signal from noise and effectively measure the T_2^{eff} and T_1 relaxation times. It covers the entire range of the transverse relaxation time from 217 ms to 45 ms, to monitor the health of the placenta presented in previous studies. However, the measurement time, which is 30 minutes, is considered too long for a routine scan in the clinical environment. Although, the T_1 measurement used for the model compound does not mimic the relaxation time of placenta tissue, it shows the system's potential for such an experiment.

5.10 Conclusion

The present study addressed the data analysis for the relaxation time standard to characterise the developed low-field unilateral magnetic resonance system, the NMR-CAPIBarA, which is operated at 18 mT. The data comprises the whole range of the T_2^{eff} relaxation time of the developing placenta mimicked by silicon oils at a distance of 24 mm from the NMR sensor. Additionally, it provides the measurements for both effective transverse and longitudinal relaxation times utilising a model system composed of full-fat milk powder dissolved in PDMS. These measurements were conducted at a depth considered applicable to the anterior placenta but not deep enough to reach the posterior placenta at the current time.

The current time for quantification of the T_2^{eff} relaxation time for pure silicone oil utilising the surface coil is 30 minutes, which is considered long for a routine scan in a clinical environment. However, the experimental parameters employed for the model system compound suggest that there is scope to reduce the experimentation time. Furthermore, the 5 minutes experimentation time achieved with the solenoid coil suggested the possibility of improving the depth of investigation to reach the posterior placenta, despite losing the SNR as a function of depth. Moreover, the magnet homogeneity and the sizeable potential measurement volume help provide a range of locations for viable measurement within the magnet volume. Therefore, it is expected that through adjustments to the design of the magnet array and RF coil, or by improving the composite pulse for example with adiabatic or chirp pulses, ultrasound co-located MR relaxation measurements for the placenta could be performed in vivo by utilising this low-cost system.

Chapter 6

Conclusion and Future work

6.1 Summary of the findings

The work presented in this thesis is a novel approach to monitor pregnant women at high risk of placenta disorders such as PE. This work aimed to develop an affordable NMR system that can measure the range of placental relaxation times presented in previous literature. Based on the outcomes obtained from this research, it can be concluded that the developed low-field NMR-CAPIBarA system is capable of providing these quantitative relaxation time parameters (T_2^{eff} and T_1) at a single point in space. Precisely, these measurements were performed on materials that mimic placental tissue relaxation values at a distance equivalent to the position of the anterior placenta of an average pregnancy, which is 24 mm from the surface of the PCB coil. The full potential of this approach will be achieved when it is ultimately integrated with the ultrasound imaging modality to locate the placenta in vivo. However, this is beyond the scope of this thesis.

With the aim to develop a low-field NMR system, it was essential to set up reference values to characterise the performance of the NMR-CAPIBarA system in Chapter 5. Therefore, Chapter 3 demonstrates two different materials assessed in the high-field system (the 1.5 T MRI) to mimic the placental tissue relaxation time values separately. Results exhibited safe and inexpensive materials that can be utilised to represent T_2^{eff}, which is the silicone oil, and utilising the full-fat milk powder as a novel food substance to shorten the T_1 relaxation time. Various viscosities were employed for both materials to cover the whole relaxation time for the different gestational ages. Both the materials showed an excellent decaying pattern as the viscosity increased in the sample.

Moreover, Chapter 3 shows that the implementation of this novel food substance was effective in shorting the T_1 values in both 1.5 T clinical MRI and 0.3 T MR sensor, where both systems have the same exponential fitting coefficient. This section of the chapter was published in the Multidisciplinary Digital Publishing Institute Proceedings in 2017 [110]. Collectively, the presented results are consistent with those of other researchers, who stated that the MR relaxation times rely on the molecular size and the chemical environment of the nucleus [108; 109].

To decide which electronic system is appropriate for the integration with the constructed unilateral magnet in Chapter 5, the developed electronic system was initially evaluated utilising a homogeneous field for both the static field- EMC, and the oscillating field- the solenoid coil, and is presented in Chapter 4. This chapter demonstrates the employment of two different front-end electronics by means of their attachment to the console of the spectrometer. The first test was performed with the front-end composed of the typical system- the commercial units, and the second test used the simple inverting Op-Amps as cost-effective electronics. The experimental work presented in this chapter showed that both the external units successfully generated NMR signals at a magnetic field of approximately 18 mT, which is below the frequency of 1 MHz. Moreover, the system with commercial units can differentiate between the composition of different materials. Results obtained from the simple design of the Op-Amp electronic circuit provided evidence that we could still obtain excellent outcomes with much lower-power units, which could be suitable for battery-powered applications.

Moreover, because the Op-Amp can be designed precisely to the desired frequency, it is considered an inexpensive external unit compared to the commercial one. It was also interesting to note that the bandwidth of the Op-Amp receiving circuit functioned both as a signal pre-amplifier and a filter for frequencies above 1 MHz, which eliminated the need for a low-pass filter as is the case with commercial units. These findings provide a potential mechanism for the implementation of the Op-Amp in different applications of a low-field NMR system. This part of the chapter produced a published paper in the Multidisciplinary Digital Publishing Institute Proceedings in 2019 [71]. Furthermore, it is noteworthy that with the less homogeneous field as the presently developed permanent magnet, a more robust RF power amplifier is required to produce RF pulses with sufficient flipped angles to flip the spin system.

The development of the NMR-CAPIBarA system is presented in Chapter 5. The progress of such a system was carried out gradually, starting with the magnet array construction until the successful measurement of the T_2^{eff} relaxation time for different viscosities of silicone oil. Moreover, both T_2^{eff} and T_1 for the model system compounds composed of varying concentrations of full-fat milk powder dissolved in silicone oil were measured. In the first section, the sweet-spot position was defined for the current configuration, with reference to the anti-parallel principle inspired by Dabaghyan et

al. [5]. The result obtained from the manual magnetic field mapping was consistent with the calculation method suggested by [79] for the sweet-spot, which was located at 76 mm from the magnet surface. This outcome indicates that the mathematical method could be sufficient to determine the location of the sweet-spot in the future when the distance change between two magnet arrays is demanded. The successive sections illustrate the integration of the low-field electronic system with the NMR-CAPIBarA magnet and the gradual modification of the external units that returned the configuration of the electronic system to the first proposed one, which is the commercial front-end units. Nevertheless, the simple inverting Op-Amp electronic circuit showed an excellent NMR signal for the NMR-CAPIBarA magnet via employing the solenoid coil as a sensor.

The primary issue for the NMR-CAPIBarA system is the inhomogeneous field, which is a common issue with all unilateral NMR systems. Therefore, it was expected that the external units returned to the commercial units, as they are characterised by high voltage gain for both the transmit and receive channels. High voltage gain was essential to enhance the SNR as the measurements were conducted at a distance from the PCB coil surface. However, the feature of the current generation of the operational amplifier, in the simple form of inverting design circuit, is the possibility of increasing the amplifier voltage gain via manoeuvring the value of the resistors. Therefor, this feature requires further investigation to check the circuit gain compatibility with the desired application of the current system.

Moreover, the obtained results showed that the desired depth of investigation, which is 24 mm for the anterior placenta position, depends not only on the magnet configuration but also on the performance and dimensions of the RF coil, in addition to the efficiency of the external units in transmitting the RF pulse and the pre-amplifying of the received signal.

The experiment performed on the model system compound shows the effectiveness of the full-fat milk powder in shorting the relaxation time parameters (T_2^{eff} and T_1), which could be considered the most inexpensive material utilised to suppress the relaxation time for the development of NMR sensors. The final optimisation to enhance the SNR was by introducing the composite pulse to the CPMG sequence; however, no significant improvement was observed. Nevertheless, various studies show the effectiveness of such a pulse. On the other hand, it might prolong the experimental time, as mentioned by another study [147]. Thus, the outcome suggests that further investigation is needed to employ this approach in the present system.

An unavoidable limitation of the method, is the presence of noise. Both external and inherent noises, such as thermal noise, disturb the measurements; and lead to outliers that affect the MATLAB calculation results for the exponential fitting curve. Therefore, to solve this issue, the raw data were transferred to an online program (the

mriToolbox) to produce the correct values of fitting curve parameters.

Moreover, this study lacks data on the T_1 relaxation time, for the full-fat milk powder solution by the NMR-CAPIBarA system, to cover the range of the T_1 relaxation time for the placenta tissue. However, such an experiment will be too long; as demonstrated with the model system compound. The experiment required 1.26 hour at a maximum repetition time of 1500 ms. Consequently, for the full-fat milk powder solution, the measurement time will be seven times that of the model system compound.

In general, the acquired information at a magnetic field strength of 18 mT for different viscosities of silicone oils compared to the 1.5 T clinical MRI outcomes shows the capability of the NMR-CAPIBarA system to provide sufficient relaxation time information covering the placental tissue relaxation time, specifically covering the range of the transverse relaxation time presented in previous literature. This work was published in the Journal of Applied Science in 2020 [142].

6.2   Concluding remarks

The present study demonstrates the successful development of a low-field unilateral NMR system called the NMR CAPIBarA-Clinical Assessment of Patients Implemented with Bar magnet Arrays. This system meets the objectives of this project, and it is characterised as an affordable, portable magnetic resonance relaxometry system operated at a magnetic field of 18 mT. It can measure the effective transverse relaxation time for a various range of pure silicone oils covering the placenta relaxation time presented in previous literature. These measurements have been conducted at an applicable depth to the anterior placenta. The NMR-CAPIBarA system will ultimately combine with conventional ultrasound imaging in vivo to co-locate the MR sensitive volume and then the relaxation properties measured with the MR system. However, this is beyond this project's scope, and this tool, when used in conjunction with the routine ultrasound imaging will improve the predictivity of placenta disease at the early stages of pregnancy. This novel medical early diagnostic approach could possibly identify mothers at high of PE for close monitoring and treatment, consequently giving a better outlook for both mother and foetus.

6.3   Future work

Based on the findings of the present work, recommendations for future studies are listed below:

- The first major challenge to overcome is to reach sufficient depths for the measurement equivalent to the depth of a posterior placenta. In this regard, a detailed study of optimal RF coil designs, possibly with a revised magnet design, is required.

- The second major challenge is making a transverse relaxation time measurement in a sufficiently short measurement time. By investigating shaped, adiabatic, or chirp radiofrequency pulses, the time taken can be significantly reduced compared to that achievable by a standard CPMG pulse sequence.

- This study sets a base for future studies in which the integration between the ultrasound imaging modality and the NMR-CAPIBarA system will be possible as a novel diagnostic approach. The current research has only measured the MR relaxation time at a single point in space. A future study will investigate the combination of the two modalities. Moreover, it would be better to utilise a model of a pregnant woman characterised by a tissue-equivalent material that mimics the real placenta before carrying out measurements for actual cases.

References

[1] D. Capitani, A. P. Sobolev, V. Di Tullio, L. Mannina, and N. Proietti, "Portable nmr in food analysis," *Chemical and Biological Technologies in Agriculture*, vol. 4, no. 1, p. 17, 2017. 1

[2] B. Blümich, J. Perlo, and F. Casanova, "Mobile single-sided nmr," *Progress in Nuclear Magnetic Resonance Spectroscopy*, vol. 52, no. 4, pp. 197–269, 2008. 1, 2, 3, 4, 33, 95

[3] F. Casanova, J. Perlo, and B. Blümich, *Single-Sided NMR*, pp. 1–10. Berlin, Heidelberg: Springer Berlin Heidelberg, 2011. 1, 3, 25, 30, 32, 33, 51, 68, 75, 91, 103, 114, 125, 146, 147, 148

[4] A. Asfour, "Low-field nmr/mri systems using labview and advanced data acquisition techniques," *Practical Applications and Solutions Using Labview TM Software*, pp. 17–40, 2011. 1, 68, 69, 70

[5] M. Dabaghyan, I. Muradyan, A. Hrovat, J. Butler, E. Frederick, F. Zhou, A. Kyriazis, C. Hardin, S. Patz, and M. Hrovat, "A portable single-sided magnet system for remote nmr measurements of pulmonary function," *NMR in Biomedicine*, vol. 27, no. 12, pp. 1479–1489, 2014. 1, 3, 6, 31, 36, 39, 68, 75, 91, 93, 155

[6] J. P. Marques, F. F. Simonis, and A. G. Webb, "Low-field mri: An mr physics perspective," *Journal of magnetic resonance imaging*, vol. 49, no. 6, pp. 1528–1542, 2019. 1

[7] J. Mitchell, L. Gladden, T. Chandrasekera, and E. Fordham, "Low-field permanent magnets for industrial process and quality control," *Progress in nuclear magnetic resonance spectroscopy*, vol. 76, pp. 1–60, 2014. 2

[8] B. Blümich, "Introduction to compact nmr: a review of methods," *TrAC Trends in Analytical Chemistry*, vol. 83, pp. 2–11, 2016. 2, 68

[9] B. Blümich, F. Casanova, and S. Appelt, "Nmr at low magnetic fields," *Chemical Physics Letters*, vol. 477, no. 4-6, pp. 231–240, 2009. 2

[10] R. K. Cooper and J. A. Jackson, "Remote (inside-out) nmr. i. remote production of region of homogeneous magnetic field," *Journal of Magnetic Resonance (1969)*, vol. 41, no. 3, pp. 400–405, 1980. 2

[11] C. G. Masi and M. N. Miller, "Nmr magnet system for well logging," Jan. 5 1988. US Patent 4,717,876. 2

[12] H. J. Vinegar, R. Akkurt, and P. Tutunjian, "Nmr logging of natural gas reservoirs," Mar. 5 1996. US Patent 5,497,087. 2

[13] G. Eidmann, R. Savelsberg, P. Blümler, and B. Blümich, "The nmr mouse, a mobile universal surface explorer," *Journal of Magnetic Resonance, Series A*, vol. 122, no. 1, pp. 104–109, 1996. 2, 29

[14] B. Blümich, P. Blümler, G. Eidmann, A. Guthausen, R. Haken, U. Schmitz, K. Saito, and G. Zimmer, "The nmr-mouse: construction, excitation, and applications," *Magnetic resonance imaging*, vol. 16, no. 5-6, pp. 479–484, 1998. 2

[15] B. Blümich, V. Anferov, S. Anferova, M. Klein, R. Fechete, M. Adams, and F. Casanova, "Simple nmr-mouse with a bar magnet," *Concepts in Magnetic Resonance: An Educational Journal*, vol. 15, no. 4, pp. 255–261, 2002. 2

[16] J. Perlo, F. Casanova, and B. Blümich, "Profiles with microscopic resolution by single-sided nmr," *Journal of magnetic resonance*, vol. 176, no. 1, pp. 64–70, 2005. 2, 29

[17] A. E. Marble, I. V. Mastikhin, B. G. Colpitts, and B. J. Balcom, "An analytical methodology for magnetic field control in unilateral nmr," *Journal of Magnetic Resonance*, vol. 174, no. 1, pp. 78–87, 2005. 2

[18] A. E. Marble, I. V. Mastikhin, B. G. Colpitts, and B. J. Balcom, "A compact permanent magnet array with a remote homogeneous field," *Journal of Magnetic Resonance*, vol. 186, no. 1, pp. 100–104, 2007. 2, 3, 4, 34

[19] "Profile nmr- mouse. [online] available at: http://www.magritek.com/wp-content/uploads/2013/12/mouse-2012-web-1.pdf [accessed 9 feb. 2020]." 3

[20] G. Navon, U. Eliav, D. Demco, and B. Blümich, "Study of order and dynamic processes in tendon by nmr and mri," *Journal of Magnetic Resonance Imaging: An Official Journal of the International Society for Magnetic Resonance in Medicine*, vol. 25, no. 2, pp. 362–380, 2007. 3

[21] F. Heller, A. Schwaiger, R. Eymael, R. Schulz-Wendtland, and B. Blümich, "Measuring the contrast-enhancement in the skin and subcutaneous fatty tissue with the nmr-mouse: a feasibility study," *RoFo: Fortschritte auf dem Gebiete der Rontgenstrahlen und der Nuklearmedizin*, vol. 177, no. 10, pp. 1412–1416, 2005. 3, 30

[22] M. Van Landeghem, E. Danieli, J. Perlo, B. Blümich, and F. Casanova, "Low-gradient single-sided nmr sensor for one-shot profiling of human skin," *Journal of Magnetic Resonance*, vol. 215, pp. 74–84, 2012. 3, 35

[23] E. Rössler, C. Mattea, and S. Stapf, "Feasibility of high-resolution one-dimensional relaxation imaging at low magnetic field using a single-sided nmr scanner applied to articular cartilage," *Journal of Magnetic Resonance*, vol. 251, pp. 43–51, 2015. 3, 30, 147

[24] M. C. Tourell, T. S. Ali, H. J. Hugo, C. Pyke, S. Yang, T. Lloyd, E. W. Thompson, and K. I. Momot, "T1-based sensing of mammographic density using single-sided portable nmr," *Magnetic resonance in medicine*, vol. 80, no. 3, pp. 1243–1251, 2018. 3, 31

[25] L. Brizi, M. Barbieri, F. Baruffaldi, V. Bortolotti, C. Fersini, H. Liu, M. Nogueira d'Eurydice, S. Obruchkov, F. Zong, P. Galvosas, *et al.*, "Bone volume–to–total volume ratio measured in trabecular bone by single-sided nmr devices," *Magnetic resonance in medicine*, vol. 79, no. 1, pp. 501–510, 2018. 3

[26] M. Barbieri, L. Brizi, V. Bortolotti, P. Fantazzini, M. N. d'Eurydice, S. Obruchkov, H. Liu, and P. Galvosas, "Single-sided nmr for the diagnosis of osteoporosis: Diffusion weighted pulse sequences for the estimation of trabecular bone volume fraction in the presence of muscle tissue," *Microporous and Mesoporous Materials*, vol. 269, pp. 166–170, 2018. 3, 33

[27] T. S. Ali, M. C. Tourell, H. J. Hugo, C. Pyke, S. Yang, T. Lloyd, E. W. Thompson, and K. I. Momot, "Transverse relaxation-based assessment of mammographic density and breast tissue composition by single-sided portable nmr," *Magnetic resonance in medicine*, vol. 82, no. 3, pp. 1199–1213, 2019. 3, 13, 15, 16, 17, 18, 19, 31

[28] B. Manz, A. Coy, R. Dykstra, C. Eccles, M. Hunter, B. Parkinson, and P. Callaghan, "A mobile one-sided nmr sensor with a homogeneous magnetic field: The nmr-mole," *Journal of Magnetic Resonance*, vol. 183, no. 1, pp. 25–31, 2006. 3, 33, 146, 147, 148

[29] P. McDonald, P. Aptaker, J. Mitchell, and M. Mulheron, "A unilateral nmr magnet for sub-structure analysis in the built environment: The surface garfield," *Journal of Magnetic Resonance*, vol. 185, no. 1, pp. 1–11, 2007. 3

[30] B. Manz, M. Benecke, and F. Volke, "A simple, small and low cost permanent magnet design to produce homogeneous magnetic fields," *Journal of magnetic resonance*, vol. 192, no. 1, pp. 131–138, 2008. 3

[31] J. Perlo, F. Casanova, and B. Blümich, "Ex situ nmr in highly homogeneous fields: 1h spectroscopy," *Science*, vol. 315, no. 5815, pp. 1110–1112, 2007. 3, 35

[32] S. Utsuzawa and E. Fukushima, "Unilateral nmr with a barrel magnet," *Journal of Magnetic Resonance*, vol. 282, pp. 104–113, 2017. 3, 4, 148

[33] A. Bashyam, M. Li, and M. J. Cima, "Design and experimental validation of unilateral linear halbach magnet arrays for single-sided magnetic resonance," *Journal of Magnetic Resonance*, vol. 292, pp. 36–43, 2018. 3, 4, 91

[34] M. Greer, C. Chen, and S. Mandal, "An easily reproducible, hand-held, single-sided, mri sensor," *Journal of Magnetic Resonance*, p. 106591, 2019. 3, 38, 75, 110, 114, 117, 147, 148

[35] Z. He, W. He, J. Wu, and Z. Xu, "The novel design of a single-sided mri probe for assessing burn depth," *Sensors*, vol. 17, no. 3, p. 526, 2017. 4

[36] F. Kılıç, Y. Kayadibi, M. A. Yüksel, İ. Adaletli, F. E. Ustabaşıoğlu, M. Öncül, R. Madazlı, M. H. Yılmaz, İ. Mihmanlı, and F. Kantarcı, "Shear wave elastography of placenta: in vivo quantitation of placental elasticity in preeclampsia," *Diagnostic and Interventional Radiology*, vol. 21, no. 3, p. 202, 2015. 4, 41

[37] M. Hladunewich, S. A. Karumanchi, and R. Lafayette, "Pathophysiology of the clinical manifestations of preeclampsia," *Clinical Journal of the American Society of Nephrology*, vol. 2, no. 3, pp. 543–549, 2007. 4, 40, 42

[38] J. S. Moldenhauer, J. Stanek, C. Warshak, J. Khoury, and B. Sibai, "The frequency and severity of placental findings in women with preeclampsia are gestational age dependent," *American journal of obstetrics and gynecology*, vol. 189, no. 4, pp. 1173–1177, 2003. 4, 42

[39] L. S. Cox and C. Redman, "The role of cellular senescence in ageing of the placenta," *Placenta*, vol. 52, pp. 139–145, 2017. 4, 41

[40] S. Gandhi, M. Ohliger, and L. Poder, "State-of-the-art imaging of the placenta," *Current Radiology Reports*, vol. 3, no. 12, p. 46, 2015. 4

[41] J. E. Bamfo and A. O. Odibo, "Diagnosis and management of fetal growth restriction," *Journal of pregnancy*, vol. 2011, 2011. 5, 40, 42

[42] C. Cimsit, T. Yoldemir, and I. N. Akpinar, "Strain elastography in placental dysfunction: placental elasticity differences in normal and preeclamptic pregnancies in the second trimester," *Archives of gynecology and obstetrics*, vol. 291, no. 4, pp. 811–817, 2015. 5

[43] H. Park, S. Shim, and D. Cha, "Combined screening for early detection of preeclampsia," *International journal of molecular sciences*, vol. 16, no. 8, pp. 17952–17974, 2015. 5, 42

[44] S. Dekan, N. Linduska, G. Kasprian, and D. Prayer, "Mri of the placenta–a short review," *Wiener Medizinische Wochenschrift*, vol. 162, no. 9-10, pp. 225–228, 2012. 5

[45] S. Davie, W. L. Wong, T. Clapham, D. Angstetra, and R. Narayan, "Could elastography be used in the prediction of morbidly adherent placentation?," *Case reports in obstetrics and gynecology*, vol. 2016, 2016. 5

[46] G. Low, S. A. Kruse, and D. J. Lomas, "General review of magnetic resonance elastography," *World journal of radiology*, vol. 8, no. 1, p. 59, 2016. 5

[47] P. Gowland, "Placental mri," in *Seminars in Fetal and Neonatal Medicine*, vol. 10, pp. 485–490, Elsevier, 2005. 5, 47

[48] I. Derwig, D. Lythgoe, G. Barker, L. Poon, P. Gowland, R. Yeung, F. Zelaya, and K. Nicolaides, "Association of placental perfusion, as assessed by magnetic resonance imaging and uterine artery doppler ultrasound, and its relationship to pregnancy outcome," *Placenta*, vol. 34, no. 10, pp. 885–891, 2013. 5, 48, 52, 90

[49] W. Gerlach and O. Stern, "Der experimentelle nachweis des magnetischen moments des silberatoms," *Zeitschrift für Physik*, vol. 8, no. 1, pp. 110–111, 1922. 12

[50] G. Werth, H. Haffner, and W. Quint, "Continuous stern-gerlach effect on atomic ions," *Advances in Atomic Molecular and Optical Physics*, vol. 48, pp. 191–218, 2002. 12

[51] F. Weinert, "Wrong theory—right experiment: The significance of the stern-gerlach experiments," *Studies in History and Philosophy of Science Part B: Studies in History and Philosophy of Modern Physics*, vol. 26, no. 1, pp. 75–86, 1995. 12

[52] J. Emsley and J. Feeney, "Magnetic resonance, historical perspective," in *Encyclopedia of Spectroscopy and Spectrometry* (J. C. Lindon, ed.), pp. 1232 – 1240, Oxford: Elsevier, 1999. 12

[53] I. Rabi, "On the process of space quantization," *Physical Review*, vol. 49, no. 4, p. 324, 1936. 12

[54] F. Bloch, "Nuclear induction," *Physical review*, vol. 70, no. 7-8, p. 460, 1946. 12

[55] E. M. Purcell, H. C. Torrey, and R. V. Pound, "Resonance absorption by nuclear magnetic moments in a solid," *Physical review*, vol. 69, no. 1-2, p. 37, 1946. 12

[56] T. L. James, "Fundamentals of nmr," *Online Textbook: Department of Pharmaceutical Chemistry, University of California, San Francisco*, pp. 1–31, 1998. 12, 13, 15, 16, 17

[57] D. Weishaupt, V. D. Köchli, and B. Marincek, *How does MRI work?: an introduction to the physics and function of magnetic resonance imaging.* Springer Science & Business Media, 2008. 13, 14, 15, 19, 20, 21, 25

[58] P. J. Hore, *Nuclear magnetic resonance.* Oxford University Press, USA, 2015. 13

[59] T. L. James, "Fundamentals of nmr," *Online Textbook: Department of Pharmaceutical Chemistry, University of California, San Francisco*, pp. 1–31, 1998. 15

[60] S. Zhang and D. Zhao, *Advances in magnetic materials: processing, properties, and performance.* CRC press, 2017. 16, 17, 19, 21

[61] H. B. Caytak, *Signal optimization for unilateral NMR magnet design.* PhD thesis, Carleton University, 2011. 16, 17

[62] Z. Yin, "Magnetic resonance characterization of tissue engineered cartilage via changes in relaxation times, diffusion coefficient, and shear modulus," *Critical Reviews™ in Biomedical Engineering*, vol. 42, 2014. 19, 20, 21

[63] A. M. Torres and W. S. Price, "Common problems and artifacts encountered in solution-state nmr experiments," *Concepts in Magnetic Resonance Part A*, vol. 45, no. 2, p. e21387, 2016. 22, 76

[64] E. L. Hahn, "Spin echoes," *Physical review*, vol. 80, no. 4, p. 580, 1950. 22

[65] H. Y. Carr and E. M. Purcell, "Effects of diffusion on free precession in nuclear magnetic resonance experiments," *Physical review*, vol. 94, no. 3, p. 630, 1954. 22, 23

[66] R. H. Morris, *Advanced design and experimental validation of MRI contrast agents for fluid pressure mapping using microbubbles.* PhD thesis, Nottingham Trent University, 2009. 22, 23

[67] B. A. Jung and M. Weigel, "Spin echo magnetic resonance imaging," *Journal of Magnetic Resonance Imaging*, vol. 37, no. 4, pp. 805–817, 2013. 22, 23

[68] S. Meiboom and D. Gill, "Modified spin-echo method for measuring nuclear relaxation times," *Review of scientific instruments*, vol. 29, no. 8, pp. 688–691, 1958. 23

[69] M. Appel, J. Freeman, D. Pusiol, *et al.*, "Robust multi-phase flow measurement using magnetic resonance technology," in *SPE Middle East Oil and Gas Show and Conference*, Society of Petroleum Engineers, 2011. 24

[70] B. Blumich, *NMR imaging of materials*, vol. 57. OUP Oxford, 2000. 25

[71] N. K. Almazrouei, M. I. Newton, and R. H. Morris, "Operational amplifiers revisited for low field magnetic resonance relaxation time measurement electronics," in *Multidisciplinary Digital Publishing Institute Proceedings*, vol. 42, p. 1, 2019. 25, 81, 82, 84, 88, 151, 154

[72] C. Henoumont, S. Laurent, and L. Vander Elst, "How to perform accurate and reliable measurements of longitudinal and transverse relaxation times of mri contrast media in aqueous solutions," *Contrast media & molecular imaging*, vol. 4, no. 6, pp. 312–321, 2009. 25, 128

[73] J. Keeler, "Understanding nmr spectroscopy (2004)," 2016. 27, 28, 73, 74

[74] H. S. Black, *Modulation theory*. van Nostrand, 1953. 28

[75] A. P. Gaunt, *Towards micro-imaging with dissolution dynamic nuclear polarisation*. PhD thesis, University of Nottingham, 2018. 28

[76] P. Blümler, D. Holland, J. Van Duynhoven, B. Balcom, E. Fukushima, M. Hurlimann, A. Legchenko, N. Sun, M. Espy, A. McDowell, *et al.*, *Mobile NMR and MRI: developments and applications*. Royal Society of Chemistry, 2015. 29

[77] E. Danieli and B. Blümich, "Single-sided magnetic resonance profiling in biological and materials science," *Journal of Magnetic Resonance*, vol. 229, pp. 142–154, 2013. 29, 30, 31

[78] B. Blümich, "Applications in biology and medicine," in *Single-Sided NMR*, pp. 187–202, Springer, 2011. 30

[79] Y. M. Pulyer and M. I. Hrovat, "Generation of remote homogeneous magnetic fields," *IEEE transactions on magnetics*, vol. 38, no. 3, pp. 1553–1563, 2002. 31, 36, 91, 93, 155

[80] J. Perlo, "Magnets and coils for single-sided nmr," in *Single-sided NMR*, pp. 87–110, Springer, 2011. 31

[81] J. Perlo, F. Casanova, and B. Blümich, "Single-sided sensor for high-resolution nmr spectroscopy," *Journal of Magnetic Resonance*, vol. 180, no. 2, pp. 274–279, 2006. 34

[82] P. C. McDaniel, C. Z. Cooley, J. P. Stockmann, and L. L. Wald, "The mr cap: A single-sided mri system designed for potential point-of-care limited field-of-view brain imaging," *Magnetic resonance in medicine*, vol. 82, no. 5, pp. 1946–1960, 2019. 37

[83] T. Victoria, A. M. Johnson, S. S. Kramer, B. Coleman, M. Bebbington, and M. Epelman, "Extrafetal findings at fetal mr: evaluation of the normal placenta and correlation with ultrasound," *Clinical imaging*, vol. 35, no. 5, pp. 371–377, 2011. 39, 44, 114

[84] T. Mayhew, C. Ohadike, P. Baker, I. Crocker, C. Mitchell, and S. Ong, "Stereological investigation of placental morphology in pregnancies complicated by preeclampsia with and without intrauterine growth restriction," *Placenta*, vol. 24, no. 2-3, pp. 219–226, 2003. 40, 42

[85] M. Austdal, L. Tangerås, R. Skråstad, K. Salvesen, R. Austgulen, A.-C. Iversen, and T. Bathen, "First trimester urine and serum metabolomics for prediction of preeclampsia and gestational hypertension: a prospective screening study," *International journal of molecular sciences*, vol. 16, no. 9, pp. 21520–21538, 2015. 40

[86] T. M. Mayhew, "A stereological perspective on placental morphology in normal and complicated pregnancies," *Journal of anatomy*, vol. 215, no. 1, pp. 77–90, 2009. 41, 42

[87] A. H. Schönthal, "Endoplasmic reticulum stress: its role in disease and novel prospects for therapy," *Scientifica*, vol. 2012, 2012. 41

[88] C. Lam, K.-H. Lim, and S. A. Karumanchi, "Circulating angiogenic factors in the pathogenesis and prediction of preeclampsia," *Hypertension*, vol. 46, no. 5, pp. 1077–1085, 2005. 41

[89] M. Egbor, T. Ansari, N. Morris, C. Green, and P. Sibbons, "Pre-eclampsia and fetal growth restriction: how morphometrically different is the placenta?," *Placenta*, vol. 27, no. 6-7, pp. 727–734, 2006. 42

[90] R. O. Bahado-Singh, R. Akolekar, R. Mandal, E. Dong, J. Xia, M. Kruger, D. S. Wishart, and K. Nicolaides, "First-trimester metabolomic detection of late-onset preeclampsia," *American journal of obstetrics and gynecology*, vol. 208, no. 1, pp. 58–e1, 2013. 42

[91] S. Sohlberg, A. Mulic-Lutvica, P. Lindgren, F. Ortiz-Nieto, A.-K. Wikström, and J. Wikström, "Placental perfusion in normal pregnancy and early and late preeclampsia: a magnetic resonance imaging study," *Placenta*, vol. 35, no. 3, pp. 202–206, 2014. 42

[92] J. Miller, S. Turan, and A. A. Baschat, "Fetal growth restriction," in *Seminars in perinatology*, vol. 32, pp. 274–280, Elsevier, 2008. 42

[93] A. Sinha and P. Potdar, "An ultrasonographic study of placental thickness and gestational age in second third trimester," *PARIPEX-INDIAN JOURNAL OF RESEARCH*, vol. 6, no. 8, 2018. 43, 45

[94] T. Tongsong, C. Wanapirak, and S. Sirichotiyakul, "Placental thickness at mid-pregnancy as a predictor of hb bart's disease," *Prenatal diagnosis*, vol. 19, no. 11, pp. 1027–1030, 1999. 43

[95] S. Tanawattanacharoen, S. Manotaya, B. Uerpairojkit, *et al.*, "Ultrasound measurement of placental thickness in normal singleton pregnancy," *Thai J Obstet Gynecol*, vol. 10, p. 73, 2000. 43, 45

[96] T. Tongsong and P. Boonyanurak, "Placental thickness in the first half of pregnancy," *Journal of Clinical Ultrasound*, vol. 32, no. 5, pp. 231–234, 2004. 43

[97] A. J. Lee, M. Bethune, and R. J. Hiscock, "Placental thickness in the second trimester: a pilot study to determine the normal range," *Journal of Ultrasound in Medicine*, vol. 31, no. 2, pp. 213–218, 2012. 44

[98] B. M. Mathai, S. C. Singla, P. P. Nittala, R. J. Chakravarti, and J. N. Toppo, "Placental thickness: its correlation with ultrasonographic gestational age in normal and intrauterine growth-retarded pregnancies in the late second and third trimester," *The Journal of Obstetrics and Gynecology of India*, vol. 63, no. 4, pp. 230–233, 2013. 44

[99] W. Plasencia, E. González-Dávila, A. González Lorenzo, M. Armas-González, E. Padrón, and N. L. González-González, "First trimester placental volume and vascular indices in pregnancies complicated by preeclampsia," *Prenatal diagnosis*, vol. 35, no. 12, pp. 1247–1254, 2015. 45, 114

[100] C. Wright, D. M. Morris, P. N. Baker, I. P. Crocker, P. A. Gowland, G. J. Parker, and C. P. Sibley, "Magnetic resonance imaging relaxation time measurements of the placenta at 1.5 t," *Placenta*, vol. 32, no. 12, pp. 1010–1015, 2011. 46, 47, 52, 90

[101] P. Gowland, A. Freeman, B. Issa, P. Boulby, K. Duncan, R. Moore, P. Baker, R. Bowtell, I. Johnson, and B. Worthington, "In vivo relaxation time measurements in the human placenta using echo planar imaging at 0.5 t," *Magnetic resonance imaging*, vol. 16, no. 3, pp. 241–247, 1998. 46, 47, 90

[102] K. Duncan, P. Gowland, S. Francis, R. Moore, P. Baker, and I. Johnson, "The investigation of placental relaxation and estimation of placental perfusion using echo-planar magnetic resonance imaging," *Placenta*, vol. 19, no. 7, pp. 539–543, 1998. 46, 47, 90

[103] S. Ong, D. Tyler, R. Moore, P. Gowland, P. Baker, I. Johnson, and T. Mayhew, "Functional magnetic resonance imaging (magnetization transfer) and stereological analysis of human placentae in normal pregnancy and in pre-eclampsia and intrauterine growth restriction," *Placenta*, vol. 25, no. 5, pp. 408–412, 2004. 47

[104] L. Kjær, C. Thomsen, O. Henriksen, P. Ring, M. Stubgaard, and E. Pedersen, "Evaluation of relaxation time measurements by magnetic resonance imaging: a phantom study," *Acta Radiologica*, vol. 28, no. 3, pp. 345–351, 1987. 51

[105] M. Bucciolini, L. Ciraolo, and B. Lehmann, "Simulation of biologic tissues by using agar gels at magnetic resonance imaging," *Acta Radiologica*, vol. 30, no. 6, pp. 667–669, 1989. 51

[106] T. Cosgrove, C. Roberts, T. Garasanin, R. G. Schmidt, and G. V. Gordon, "Nmr spin- spin relaxation studies of silicate-filled low molecular weight poly (dimethylsiloxane) s," *Langmuir*, vol. 18, no. 26, pp. 10080–10085, 2002. 51, 55

[107] J. O. Christoffersson, L. Olsson, and S. Sjöberg, "Nickel-doped agarose gel phantoms in mr imaging," *Acta radiologica*, vol. 32, no. 5, pp. 426–431, 1991. 51, 55

[108] N. Bloembergen and L. Morgan, "Proton relaxation times in paramagnetic solutions. effects of electron spin relaxation," *The Journal of Chemical Physics*, vol. 34, no. 3, pp. 842–850, 1961. 51, 154

[109] T. H. Kim, "Pulsed nmr: Relaxation times as function of viscocity and impurities," 51, 154

[110] N. K. Almazrouei, M. I. Newton, E. R. Dye, and R. H. Morris, "Novel food-safe spin-lattice relaxation time calibration samples for use in magnetic resonance sensor development," in *Multidisciplinary Digital Publishing Institute Proceedings*, vol. 2, p. 122, 2017. 51, 57, 61, 154

[111] M. D. Mitchell, H. L. Kundel, L. Axel, and P. M. Joseph, "Agarose as a tissue equivalent phantom material for nmr imaging," *Magnetic resonance imaging*, vol. 4, no. 3, pp. 263–266, 1986. 51

[112] "Copper(ii) sulfate safety data sheet [online] available at: http://datasheets.scbt.com/sc-211133.pdf [accessed: 10- mar- 2020]." 51

[113] "Nickel sulfate safety data sheet [online] available at: https://www.teknova.com/sds/pdfs/n6565.pdf [accessed: 10- mar- 2020]." 51

[114] "Polydimethylsiloxane safety data sheet [online] available at: https://www.exdron.co.il/images/products/files/momentive-element14-pdms-350-e-5-liter-msds.pdf [accessed: 10- mar- 2020]." 51

[115] J. Belloque and M. Ramos, "Application of nmr spectroscopy to milk and dairy products," *Trends in Food Science & Technology*, vol. 10, no. 10, pp. 313–320, 1999. 52

[116] F. Hu, K. Furihata, Y. Kato, and M. Tanokura, "Nondestructive quantification of organic compounds in whole milk without pretreatment by two-dimensional nmr spectroscopy," *Journal of agricultural and food chemistry*, vol. 55, no. 11, pp. 4307–4311, 2007. 52

[117] A. Métais, M. Cambert, A. Riaublanc, and F. Mariette, "Effects of casein and fat content on water self-diffusion coefficients in casein systems: a pulsed field gradient nuclear magnetic resonance study," *Journal of agricultural and food chemistry*, vol. 52, no. 12, pp. 3988–3995, 2004. 52, 64

[118] H. Todt, G. Guthausen, W. Burk, D. Schmalbein, and A. Kamlowski, "Water/moisture and fat analysis by time-domain nmr," *Food chemistry*, vol. 96, no. 3, pp. 436–440, 2006. 52, 64, 66

[119] F.-H. Su, S.-S. Shyu, and Y.-C. Chen, "Nmr properties of poly (dimethyl siloxane) colloids as new contrast agents for nmr imaging," *Polymer international*, vol. 49, no. 7, pp. 787–794, 2000. 52

[120] T. Cosgrove, M. J. Turner, and D. R. Thomas, "The adsorption of polydimethylsiloxane onto silica from the melt," *Polymer*, vol. 38, no. 15, pp. 3885–3892, 1997. 55

[121] "Mri toolbox website. [online] available at: http://www.mritoolbox.com/parameterfitting.htm1 [accessed: 30- oct- 2019]." 62

[122] H. Gudbjartsson and S. Patz, "The rician distribution of noisy mri data," *Magnetic resonance in medicine*, vol. 34, no. 6, pp. 910–914, 1995. 62

[123] R. E. Sepponen, "Low-field mr imaging—development in finland," *Acta Radiologica*, vol. 37, no. 3, pp. 446–454, 1996. 66, 139

[124] A. Mohoric and J. Stepisnik, "Nmr in the earth's magnetic field," *Progress in Nuclear Magnetic Resonance Spectroscopy*, vol. 54, no. 3-4, pp. 166–182, 2009. 68

[125] K. Raoof, A. Asfour, and J. Fournier, "A complete digital magnetic resonance imaging (mri) system at low magnetic field (0.1 tesla)," in *IMTC/2002. Proceedings of the 19th IEEE Instrumentation and Measurement Technology Conference (IEEE Cat. No. 00CH37276)*, vol. 1, pp. 341–345, IEEE, 2002. 68

[126] A. Asfour, "A new daq-based and versatile low-cost nmr spectrometer working at very-low magnetic field (4.5 mt): a palette of potential applications," in *2008 IEEE Instrumentation and Measurement Technology Conference*, pp. 697–701, IEEE, 2008. 68

[127] A. Asfour, "A novel nmr instrument for the in-situ monitoring of the absolute polarization of laser-polarized 129xe," *Journal of Biomedical Science and Engineering*, vol. 3, no. 11, p. 1099, 2010. 68

[128] A. Asfour, K. Raoof, and J.-P. Yonnet, "Software defined radio (sdr) and direct digital synthesizer (dds) for nmr/mri instruments at low-field," *Sensors*, vol. 13, no. 12, pp. 16245–16262, 2013. 68

[129] J. R. Biller, K. F. Stupic, A. B. Kos, T. Weilert, G. A. Rinard, Y. Nakishima, and J. Moreland, "Characterization of a pxi e based low-field digital nmr spectrometer," *Concepts in Magnetic Resonance Part B: Magnetic Resonance Engineering*, vol. 47, no. 1, p. e21350, 2017. 68

[130] "Spincore technologies, inc. radioprocessor 'owner's manual. 2009-2019; [online] available at: http://www.spincore.com/cd/radioprocessor/radioprocessor_manual.pdf [accessed: 10-jan- 2020]." 69, 71, 72, 74

[131] Q. Teng, *Structural biology: practical NMR applications.* Springer Science & Business Media, 2012. 70, 72

[132] R. Popescu, D. Costinel, O. R. Dinca, A. Marinescu, I. Stefanescu, and R. E. Ionete, "Discrimination of vegetable oils using nmr spectroscopy and chemometrics," *Food Control*, vol. 48, pp. 84–90, 2015. 79

[133] Z. Xu, R. H. Morris, M. Bencsik, and M. I. Newton, "Detection of virgin olive oil adulteration using low field unilateral nmr," *Sensors*, vol. 14, no. 2, pp. 2028–2035, 2014. 79

[134] "method for identifying sunflower oil based on linolic or oleic type thereof - google patents2020; [online] available at: http://www.patents.google.com/patent/ru2447434c1/en [accessed: 13-april-2020]." 79

[135] P. M. Santos, F. V. C. Kock, M. S. Santos, C. M. S. Lobo, A. S. Carvalho, and L. A. Colnago, "Non-invasive detection of adulterated olive oil in full bottles using time-domain nmr relaxometry," *Journal of the Brazilian Chemical Society*, vol. 28, no. 2, pp. 385–390, 2017. 79

[136] J. Melville, D. Kim, D. Gygi, and J. Raberg, "Pulse nmr spectroscopy," *University of California, Berkeley. Accessed*, vol. 15, no. 03, p. 2016, 2014. 79

[137] B. Carter and T. R. Brown, *Handbook of operational amplifier applications.* Texas Instruments Dallas, Tex, USA, 2001. 80

[138] "What is an ideal op amp? learningaboutelectronics.com. 2020; [online] available at: http://www.learningaboutelectronics.com/articles/what-is-an-ideal-op-amp.php [accessed: 18-apr-2020]." 80

[139] "Lt1363 data sheet, analog.com. 2020; [online] available at: https://www.analog.com/media/en/technical-documentation/data-sheets/1363fa.pdf [accessed: 19-apr-2020]." 81

[140] "Lt1222 data sheet, analog.com. 2020; [online] available at: https://www.analog.com/media/en/technical-documentation/data-sheets/1222fc.pdf [accessed: 19-apr-2020]." 81

[141] P. A. Keifer, "90° pulse width calibrations: how to read a pulse width array," *Concepts in Magnetic Resonance: an Educational Journal*, vol. 11, no. 3, pp. 165–180, 1999. 83, 89

[142] R. H. Morris, N. K. Almazrouei, C. L. Trabi, and M. I. Newton, "Nmr capibara: Proof of principle of a low-field unilateral magnetic resonance system for monitoring of the placenta during pregnancy," *Applied Sciences*, vol. 10, no. 1, p. 162, 2020. 90, 110, 128, 129, 134, 156

[143] H. S. Kim, S. H. Cho, H. S. Kwon, I. S. Sohn, and H. S. Hwang, "The significance of placental ratios in pregnancies complicated by small for gestational age, preeclampsia, and gestational diabetes mellitus," *Obstetrics & gynecology science*, vol. 57, no. 5, pp. 358–366, 2014. 114

[144] T. W. Skloss, "Method for reducing spin-lattice relaxation time of silicone fluids used in magnetic resonance imaging," Sept. 14 2004. US Patent 6,791,327. 139, 141

[145] M. H. Levitt and R. Freeman, "Compensation for pulse imperfections in nmr spin-echo experiments," *Journal of Magnetic Resonance (1969)*, vol. 43, no. 1, pp. 65–80, 1981. 143

[146] T. D. Claridge, *High-resolution NMR techniques in organic chemistry*, vol. 27. Elsevier, 2016. 143, 149

[147] G. S. Kupriyanova, V. V. Molchanov, E. A. Severin, and I. G. Mershiev, "Composite pulses in inhomogeneous field nmr," in *Magnetic Resonance Detection of Explosives and Illicit Materials*, pp. 137–147, Springer, 2014. 143, 155

[148] S. Anferova, V. Anferov, M. Adams, P. Blümler, N. Routley, K. Hailu, K. Kupferschläger, M. Mallett, G. Schroeder, S. Sharma, *et al.*, "Construction of a nmr-mouse with short dead time," *Concepts in Magnetic Resonance: An Educational Journal*, vol. 15, no. 1, pp. 15–25, 2002. 146

[149] B. Gruber, M. Froeling, T. Leiner, and D. W. Klomp, "Rf coils: A practical guide for nonphysicists," *Journal of magnetic resonance imaging*, vol. 48, no. 3, pp. 590–604, 2018. 147

[150] O. V. Petrov, E. Rössler, C. Mattea, M. T. Nieminen, P. Lehenkari, S. Karhula, S. Saarakkala, and S. Stapf, "Low-field nmr relaxation times distributions and their magnetic field dependence as a possible biomarker in cartilage," in *EMBEC & NBC 2017*, pp. 952–955, Springer, 2017. 149

[151] E. Rössler, C. Mattea, A. Mollova, and S. Stapf, "Low-field one-dimensional and direction-dependent relaxation imaging of bovine articular cartilage," *Journal of Magnetic Resonance*, vol. 213, no. 1, pp. 112–118, 2011. 149

[152] D. Besghini, M. Mauri, and R. Simonutti, "Time domain nmr in polymer science: from the laboratory to the industry," *Applied Sciences*, vol. 9, no. 9, p. 1801, 2019. 149

[153] R. E. Sepponen, J. T. Sipponen, and A. Sivula, "Low field (0.02 t) nuclear magnetic resonance imaging of the brain.," *Journal of computer assisted tomography*, vol. 9, no. 2, pp. 237–241, 1985. 149

[154] J. T. Sipponen, R. E. Sepponen, J. I. Tanttu, and A. Sivula, "Intracranial hematomas studied by mr imaging at 0.17 and 0.02 t," *Journal of computer assisted tomography*, vol. 9, no. 4, pp. 698–704, 1985. 149

[155] S. Zia, "Placental location and pregnancy outcome," *Journal of the Turkish German Gynecological Association*, vol. 14, no. 4, p. 190, 2013. 150

[156] "50 x 50 x 25mm ultra high performance n52 neodymium magnet - 116kg pull, first4magnets®, 2020, [online] available at: https://www.first4magnets.com/square-c36/50-x-50-x-25mm-ultra-high-performance-n52-neodymium-magnet-116kg-pull-p3785#ps_0_3961|ps_1_1066. [accessed: 15- sep- 2020]." 151

[157] "Radioprocessor rf acquisition and excitation system - spincore technologies", spincore.com, 2020; [online] available at: http://spincore.com/products/radioprocessor/radioprocessor.shtml [accessed: 15-sep-2020]." 151

[158] "Low-pass electrical filters, bnc feedthrough, thorlabs.com, 2020; [online] available at: https:https://www.thorlabs.com/newgrouppage9.cfm?objectgroup_id=8613pn=ef508. [accessed: 15- sep- 2020]." 151

[159] "S. rentz, "mri machine cost and price guide", info.blockimaging.com, 2020, [online] available at: https://info.blockimaging.com/bid/92623/mri-machine-cost-and-price-guide. [accessed: 15- sep- 2020]." 151

[160] "How much does an ultrasound machine cost (2020) - lbn medical", lbn medical, 2020; [online] available at: https://lbnmedical.com/ultrasound-price-guide/. [accessed: 15- sep- 2020]." 151

Appendix A

The table lists the results of a preliminary test conducted for different concentrations of full-fat milk powder solution to shorten the T_1 values using 1.5 T MRI with an ankle coil.

Milk concentration %	T_1 (ms)	Standard Deviation ($\pm$ ms)
5	1857	2
11	1571	3
18	1506	3
23	1129	3
38	536	
50	367	
64	348	

The figure shows that the T_1 values decrease with the increase in the milk concentration using 1.5 T MRI with an ankle coil.
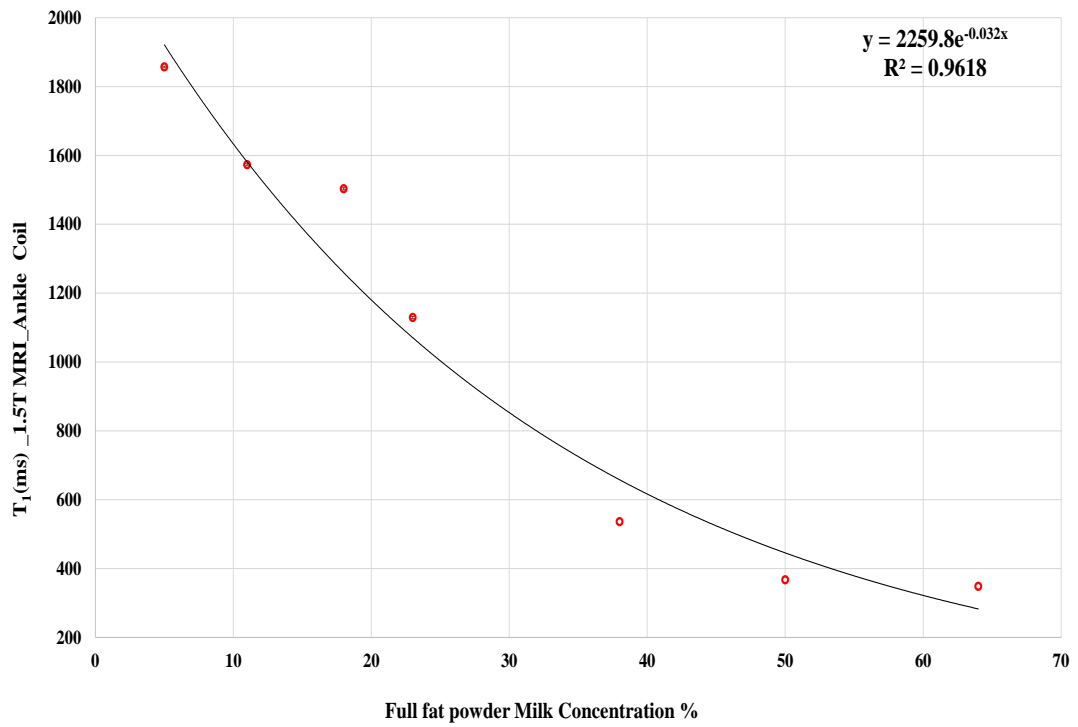
Appendix AA

A screenshot of the obtained NMR signal from the CAPIBarA magnet placed in a metallic box using the mini-circuit ZHL-3A$^+$ as a power amplifier in the front-end electronic system.
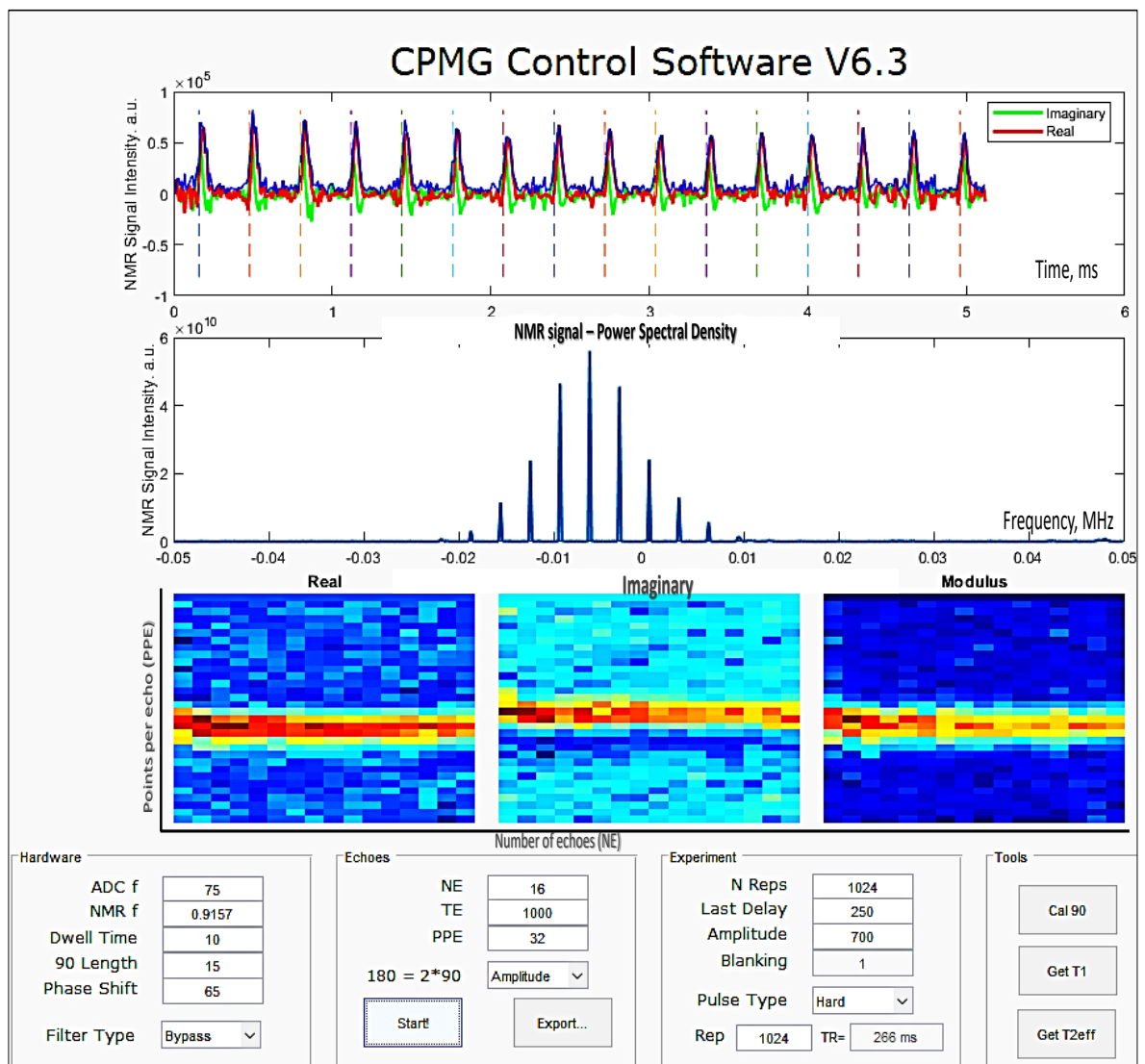
Appendix B

A screenshot of the obtained NMR signal from the CAPIBarA magnet placed at the wood frame using the mini-circuit ZHL-3A$^+$ as a power amplifier in the front-end electronic system.
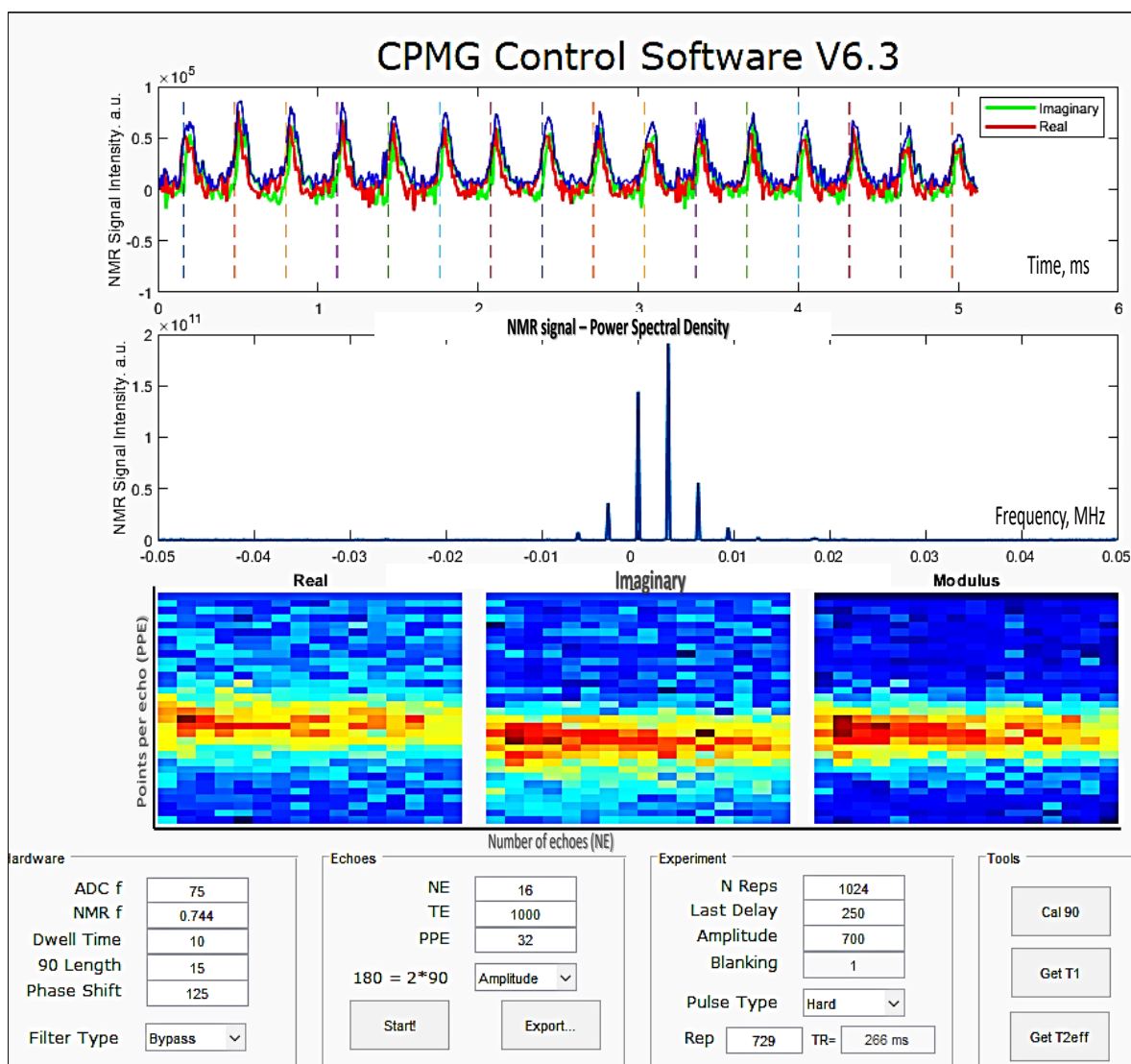
Appendix C

An example for the obtained NMR signals after the addition of copper sheets on the surface of the CAPIBarA magnet arrays. Two frequencies were investigated: the frequency which corresponds to the MF at the middle of the solenoid coil (0.774 MHz) (figure a), and the frequency which the network analyser displayed after adjusting the length of the coaxial cables (0.776 MHz) (figure b). Both frequencies generated an excellent NMR signal.
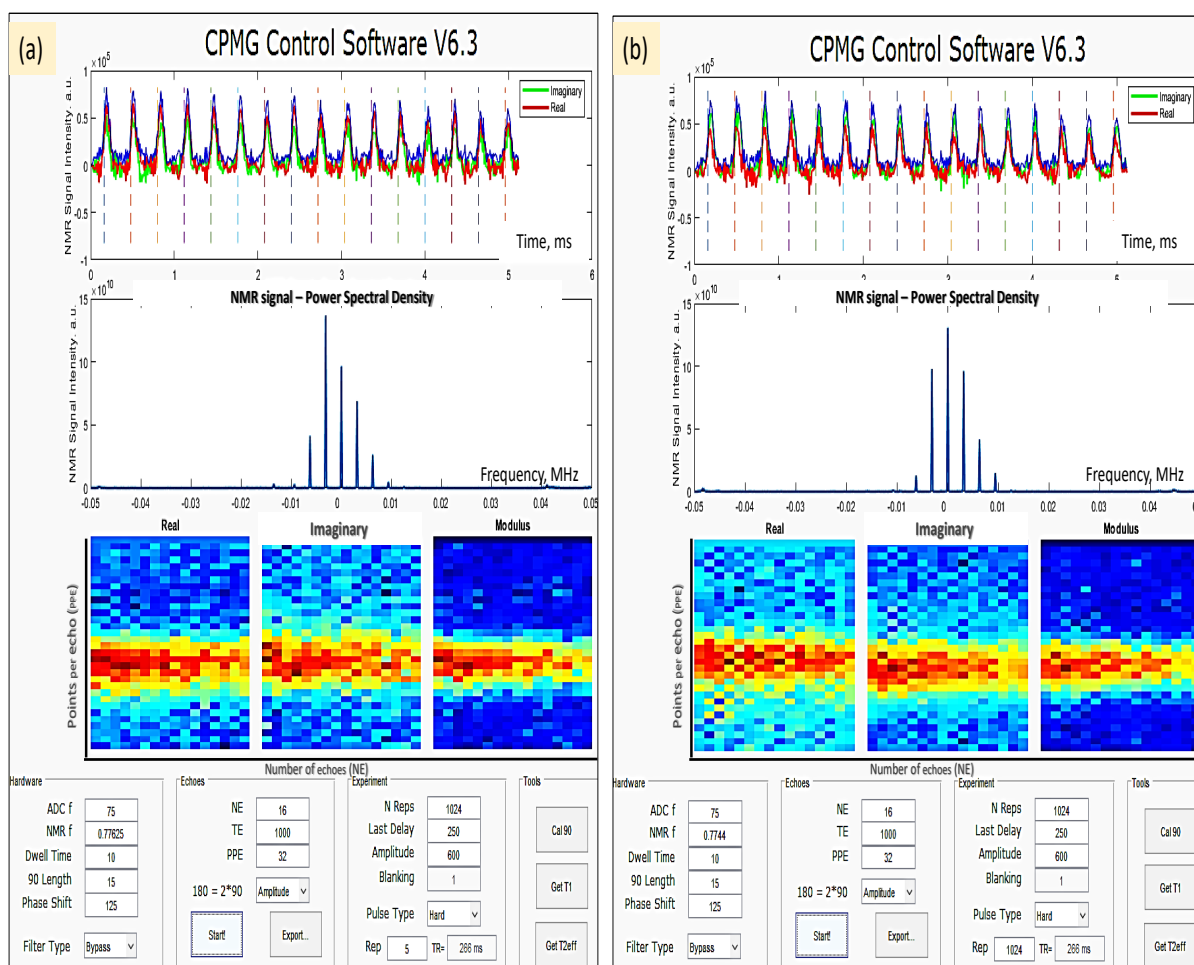
Appendix E

An example of the raw data that was obtained to estimate the T_2^{eff} values from various materials by the CPMG sequence using the MATLAB GUI. Results were obtained using an electronic system composed of the typical front-end electronics, the CAPIBarA magnet as a B_0 source, and the solenoid coil of 20 mm diameter as a detection sensor.
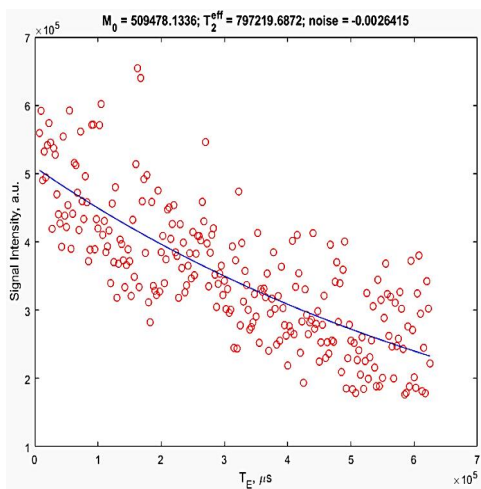
Still water
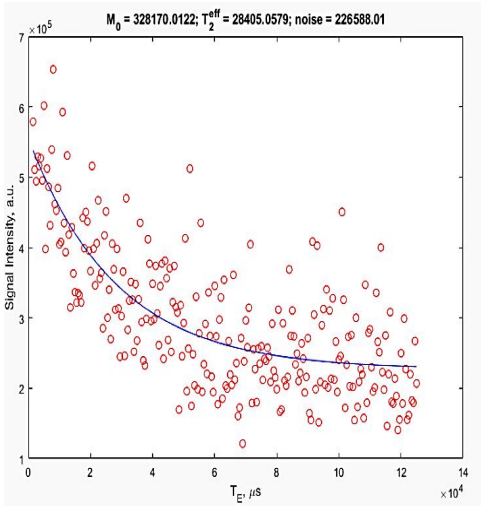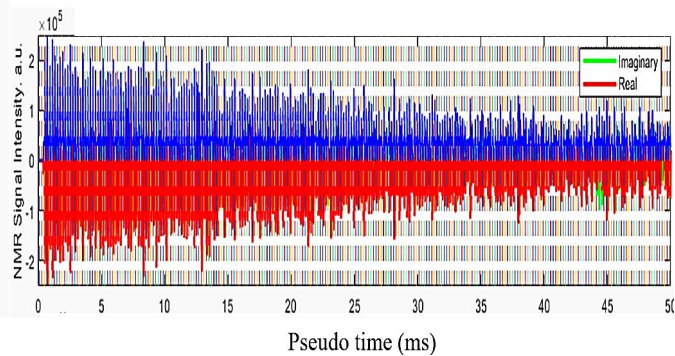
Sunflower oil
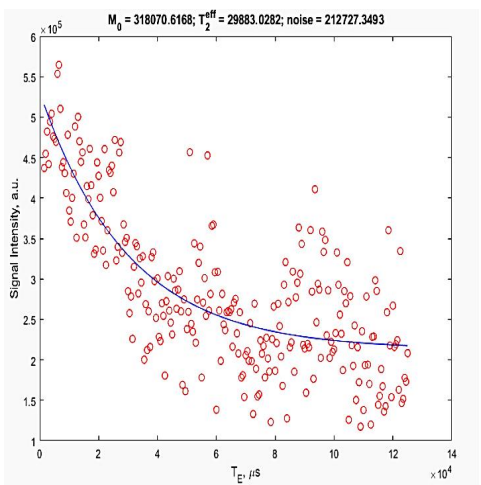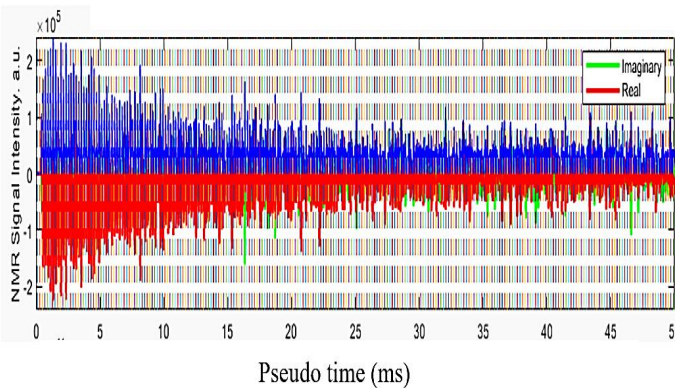
Olive oil
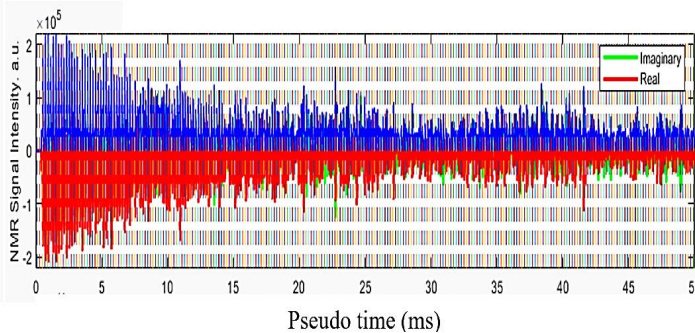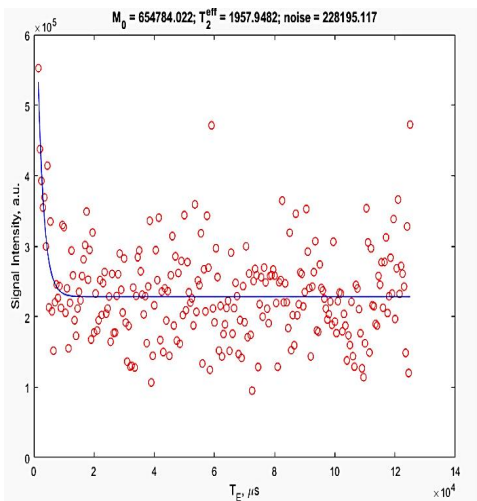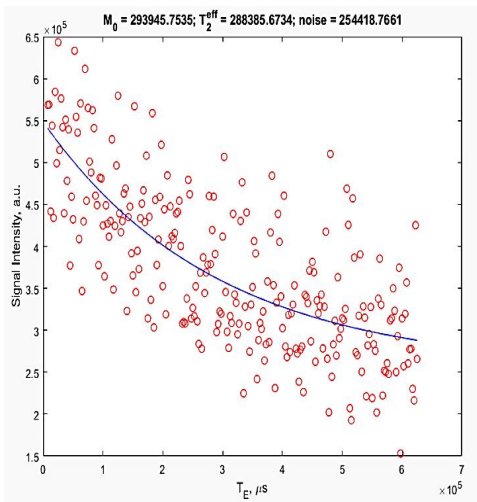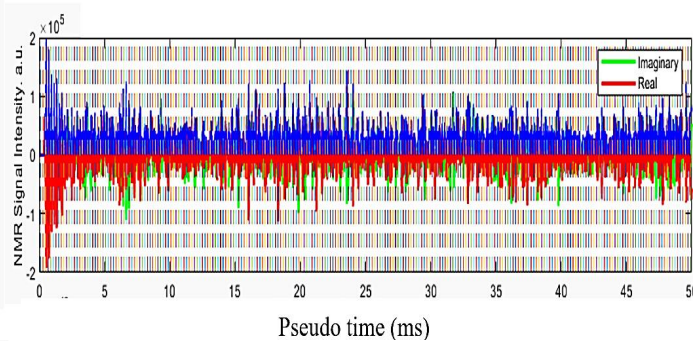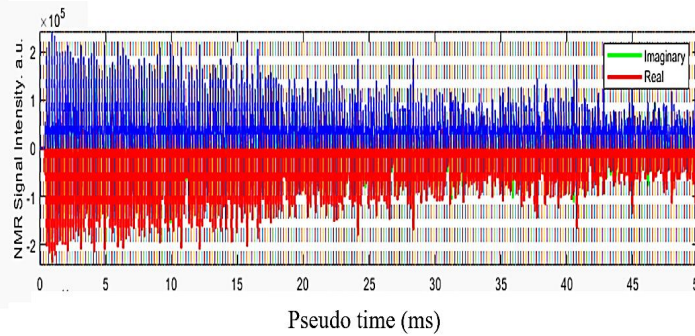
Appendix F

A screenshot for the NMR signal obtained at the surface of the handmade surface coil paired with the CABPIBarA magnet.
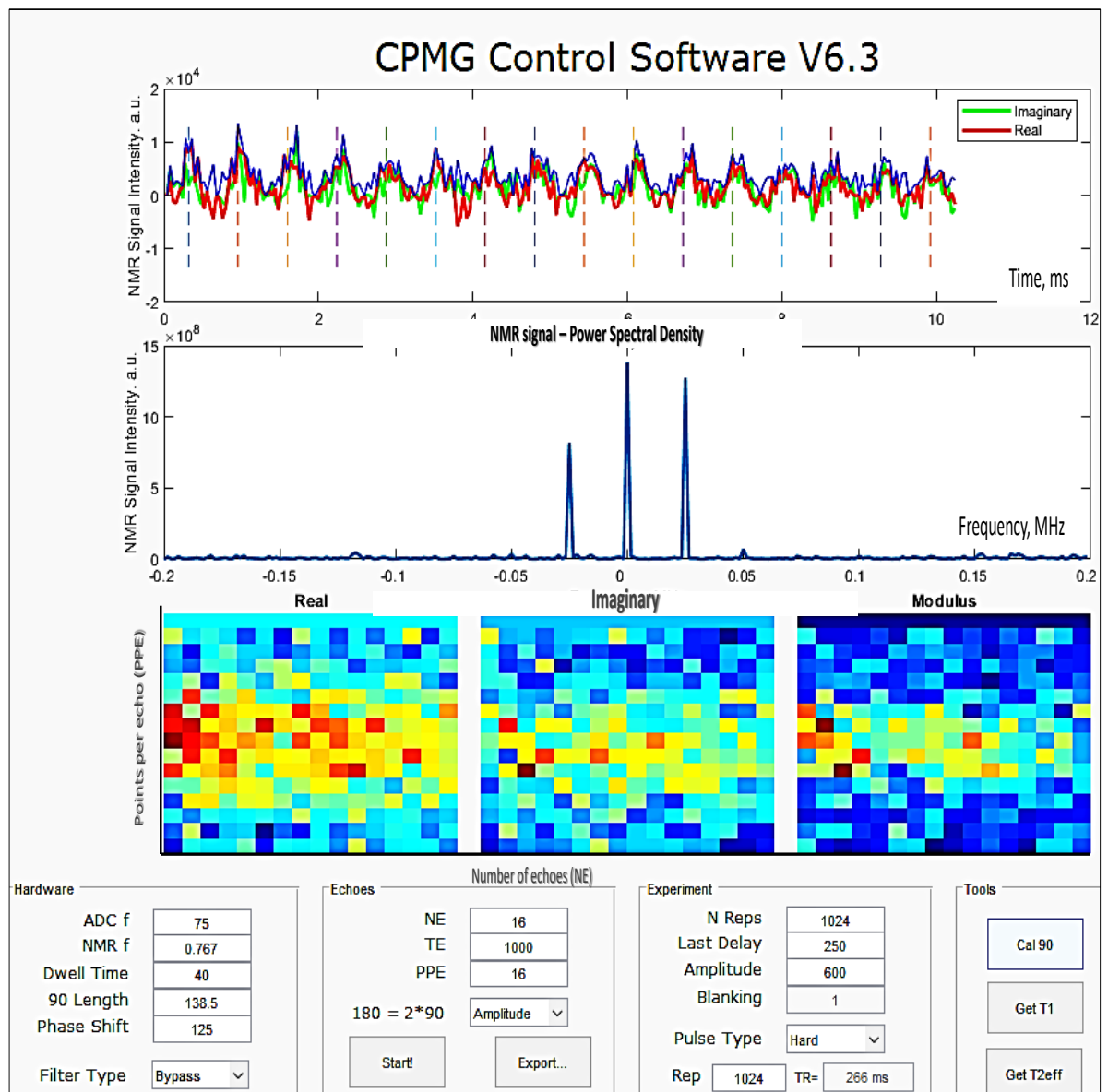
A screenshot for the NMR signal obtained at 5 mm (a) and 10 mm(b) from the surface of the handmade coil paired with the CABPIBarA magnet.
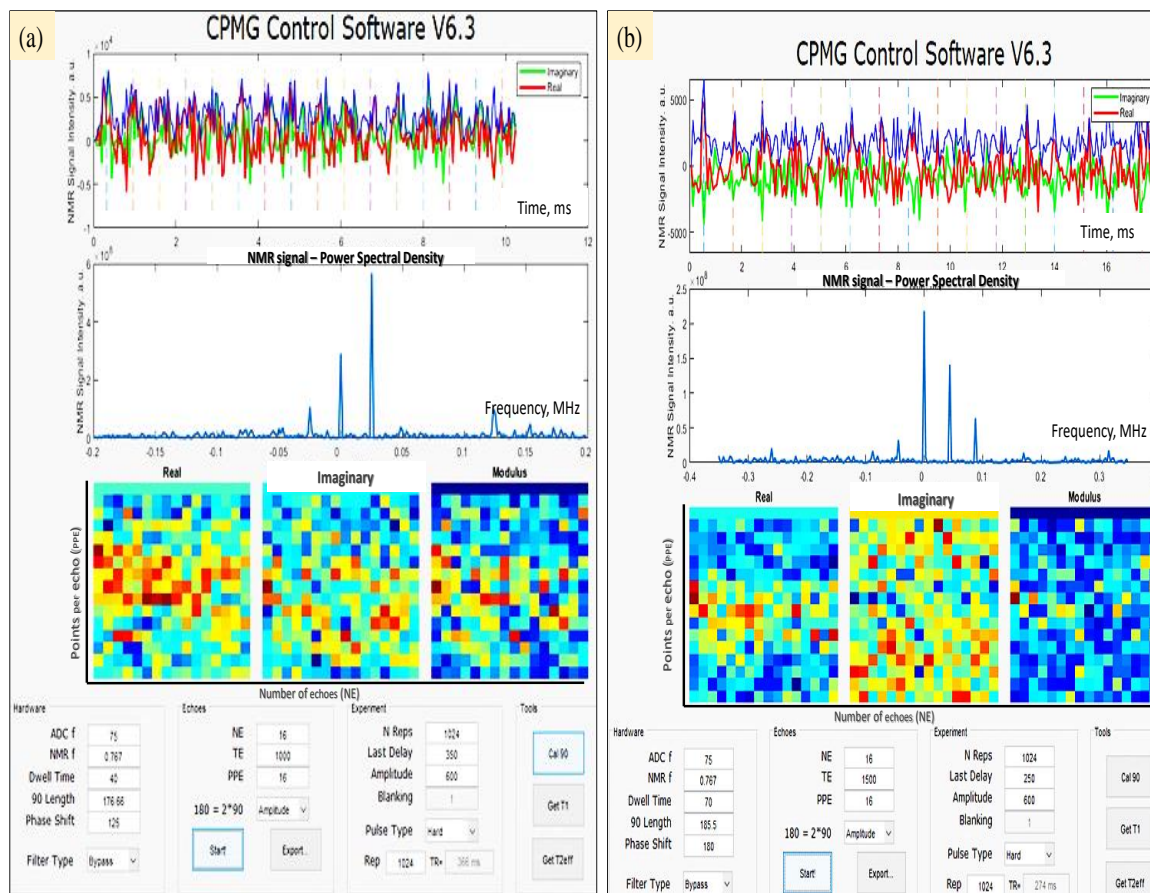
Appendix G

Acquiring of the NMR signal at the surface of the PCB coil with an inner diameter of 10x20 mm^2.

The PCB coil was positioned at 74 mm from the magnet surface to assure sample position at the sweet-spot (76 mm). The initial run of the experiment was performed using similar parameters to the ones employed with the handmade surface coil. The generated NMR signals using these parameters was successful (Figure a).

Thereafter, a 90° pulse calibration was conducted to obtain the optimum pulse duration at the surface of the PCB coil, which was 100 μs. It was observed that this design allows reducing the sampling interval time to 30 μs with an echo time of 800 μs, whereas the other parameters were kept constant. Figure b shows the acquired NMR signal after the parameters optimisation.
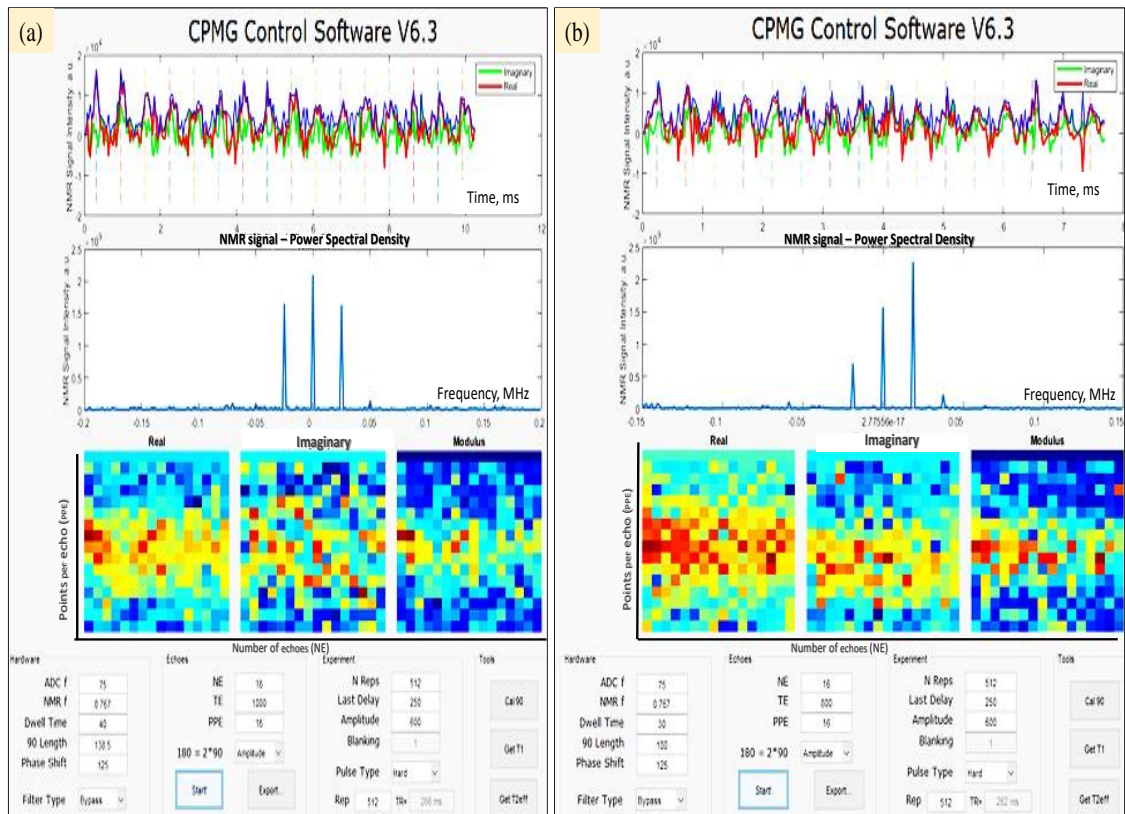
Acquiring of the NMR signal at 5 mm from the surface of the PCB coil with an inner diameter of 10x20 mm^2.

The method described in chapter 5, section 5.4.1, was used to explore the maximum depth for the PCB coil. To find the optimum pulse duration at a depth of 5 mm, several calibrations for the pulse duration were performed, and the most appropriate pulse duration was 160 μs. At this depth, the averages of scans were increased to 1024 to enhance the SNR, and the repetition time increased to 362 ms. The other parameters were kept similar to the experimental parameters at the surface of the coil. Figure (a) shows the positioning of the sample at 5 mm from the coil, and Figure (b) depicts the obtained NMR signal.
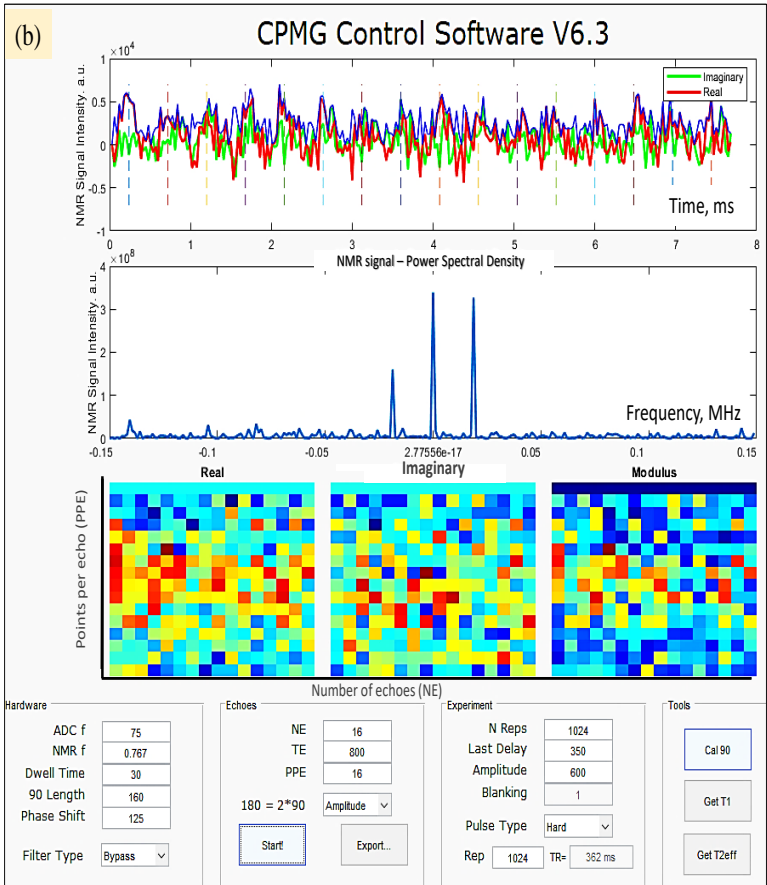
Appendix H

Acquiring of the NMR signal at the surface of the square PCB coil with an inner dimension of 40 mm by 40mm. Figure (a) shows the signal with a phase shift of 125° degree, and figure (b) NMR signal with 75°.
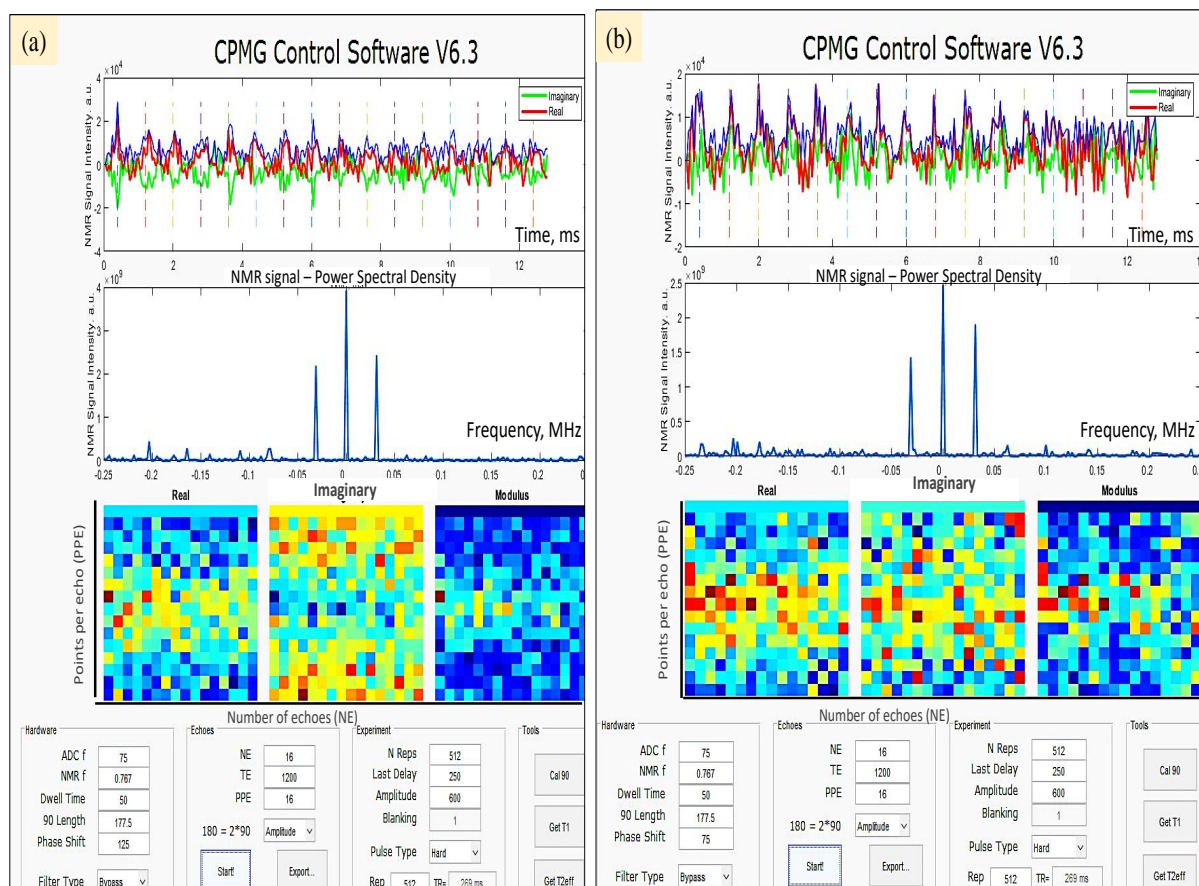
Acquiring of the NMR signal at 10 mm form the surface of the square PCB coil. Figure (a) shows the position of the sample above the coil, and figure (b) shows a screenshot for the obtained NMR signal.
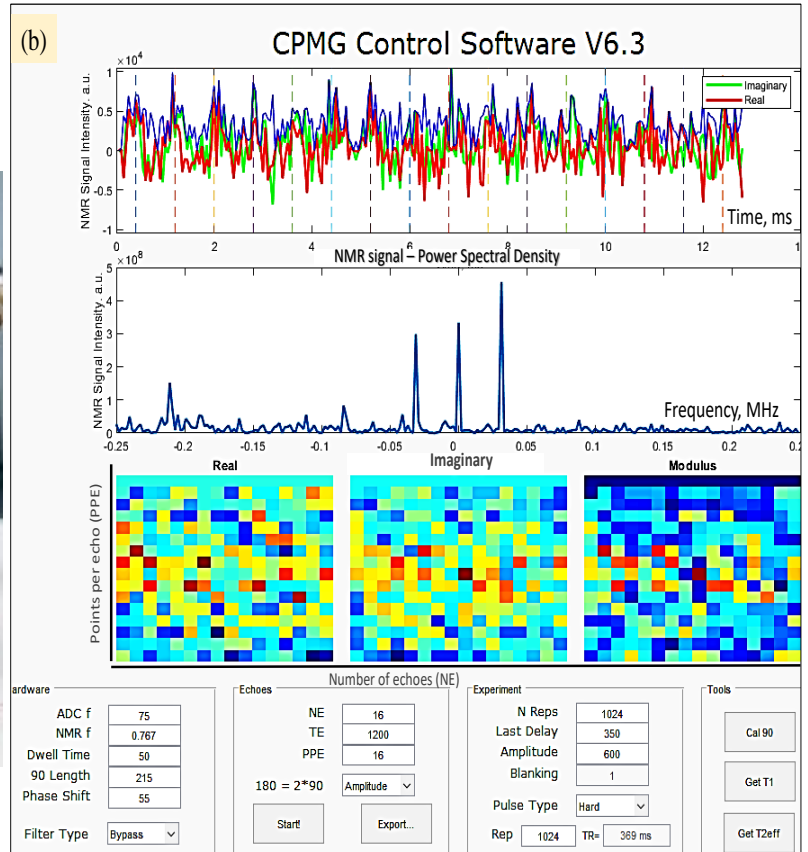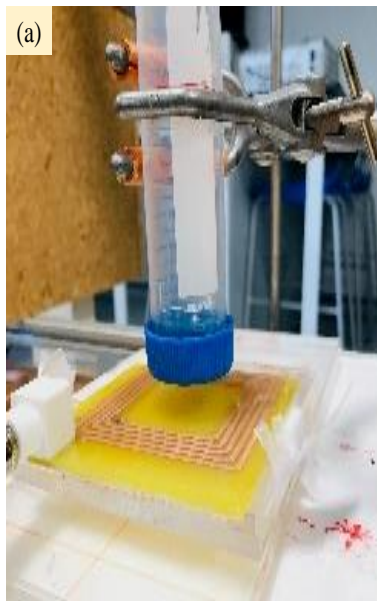
Appendix I

A screenshot for the optimised NMR signal obtained from Hartley's jelly positioned at the surface of the square PCB coil. Left-hand image (a) shows the signal obtained with an interval time of 40 μs, and the right- hand image (b) is the signal with an interval time of 20 μs with 32 PPE.
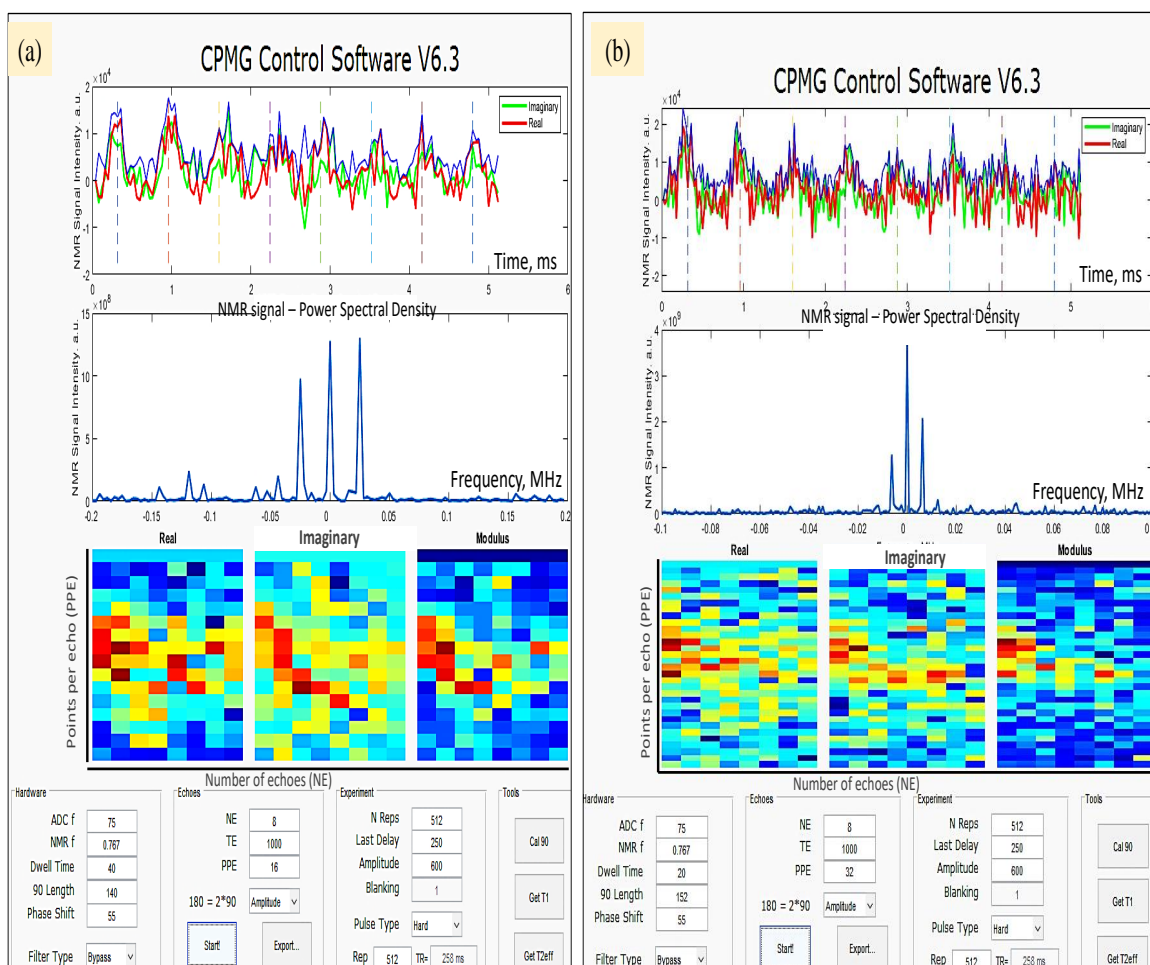
An example for the NMR Signals obtained from several jelly blocks. The images displaying the obtained NMR signals for 2 blocks (a), 3 blocks (b), and 4 blocks (c), respectively.
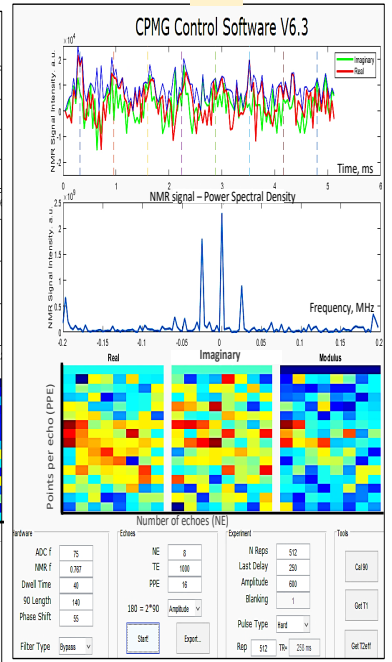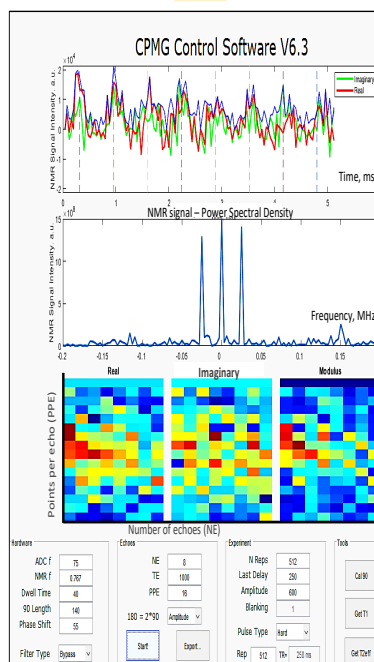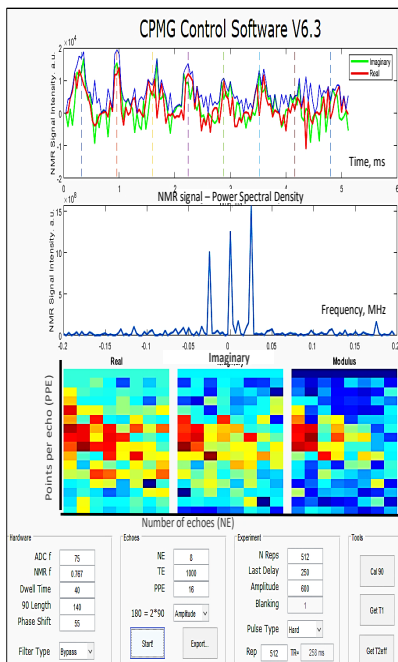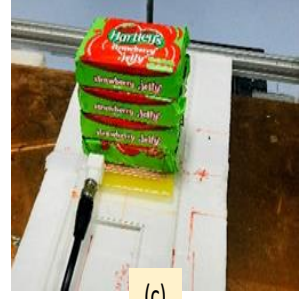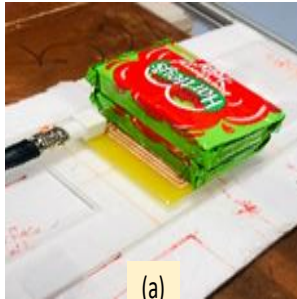
Appendix J

To enhance the power depth at the desired frequency in the current resonance circuit, coarse tuning and matching for the circuit were achieved using AVX high-voltage capacitors, and the fine-tuning was performed by changing the length of the coaxial cables between the duplexer and the capacitors. Thus, the power depth improved to -17.47 dB at the frequency of 0.767 MHz after -9.98 dB. The NMR signal was obtained with a pulse duration of 145 μs with a Dwell time of 50 μs and a phase shift of 100°. The right-hand figure shows the NMR signal acquired for one jelly block after improving the tuning and matching circuit.
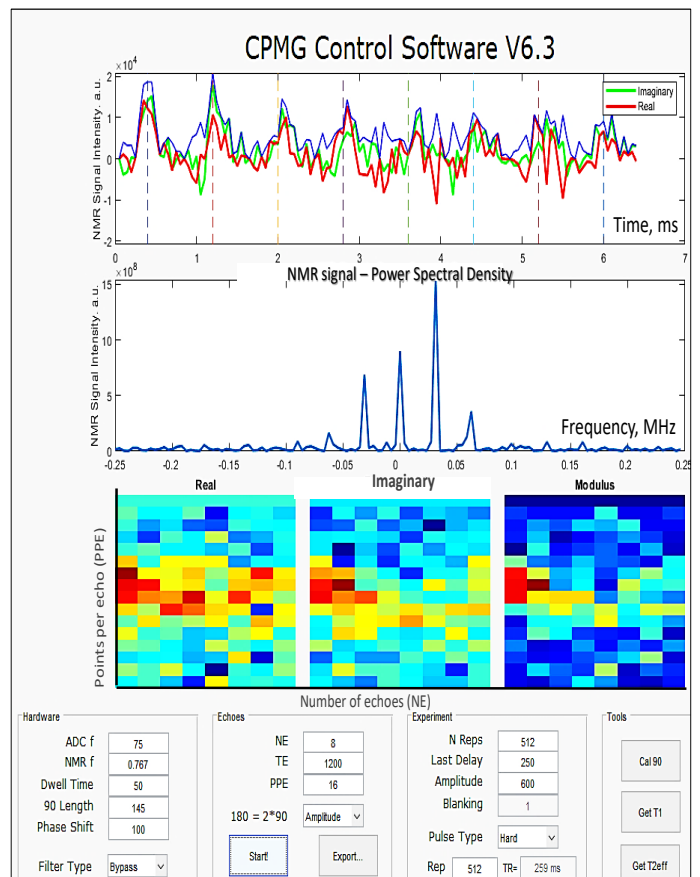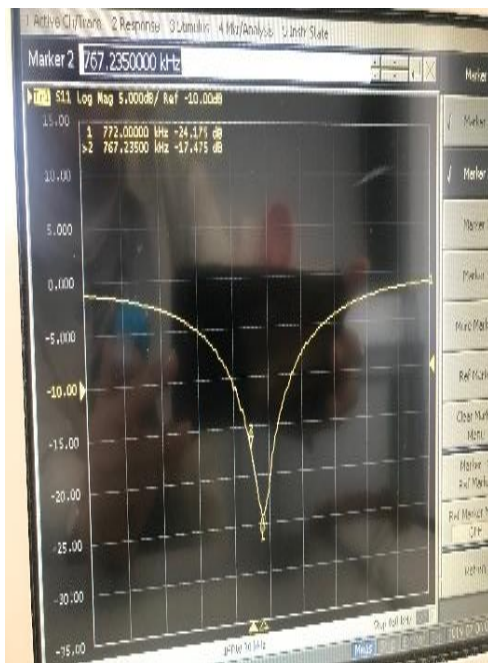
A screenshot of the obtained NMR Signals for several jelly blocks after modifying the tuning and matching circuit .

To assess the effectiveness of adding the high voltage capacitors, NMR signals were obtained for two, three and four blocks of jelly at the surface of the coil (figures (a), (b), and (c)). One can see the improvement in the shape of the produced echoes, specifically with the four blocks of jelly. However, the signal amplitude was similar to the one before the circuit modification, which was 2×10^4, and the pulse duration with sample interval time was prolonged (171 μs) and (50 μs), respectively.
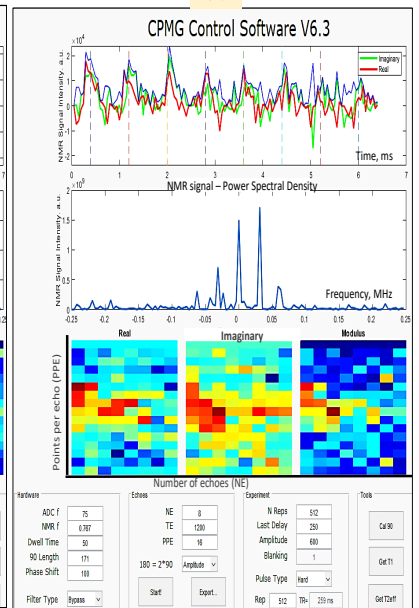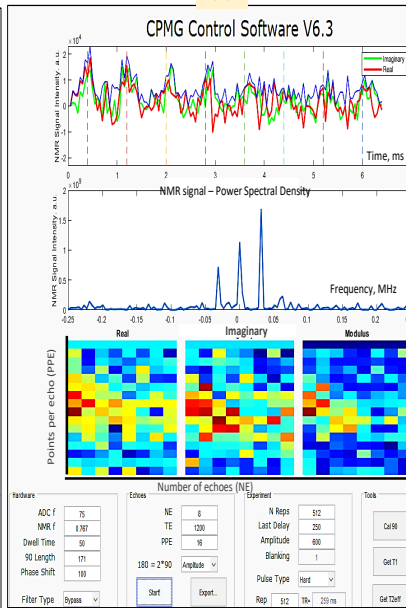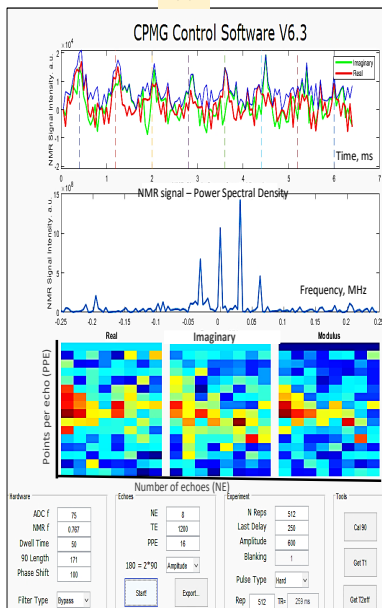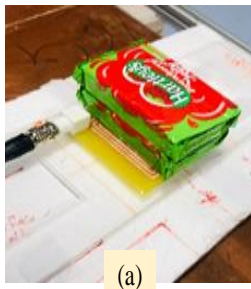
Acquiring of the NMR signals at 15 mm from the square PCB coil.

The NMR signal from one jelly block was investigated at 15 mm from the surface using a spacer of polystyrene foam board (as shown in the top area of the figure). The coil was positioned at a distance of 55 mm from the magnet surface to position the sample at the sweet-spot. Thereafter, the 90° calibration was run with a frequency of 0.768 MHz, and the optimum pulse duration was 223.33 μs. The Dwell time was increased to 70 μs. The lower part of the figure illustrates the acquired NMR signals at 15 mm from the coil surface, in which image (a) represents the signal obtains with a phase shift of 100°, and image (b) with a zero phase shift with a sample, and (c) without sample.
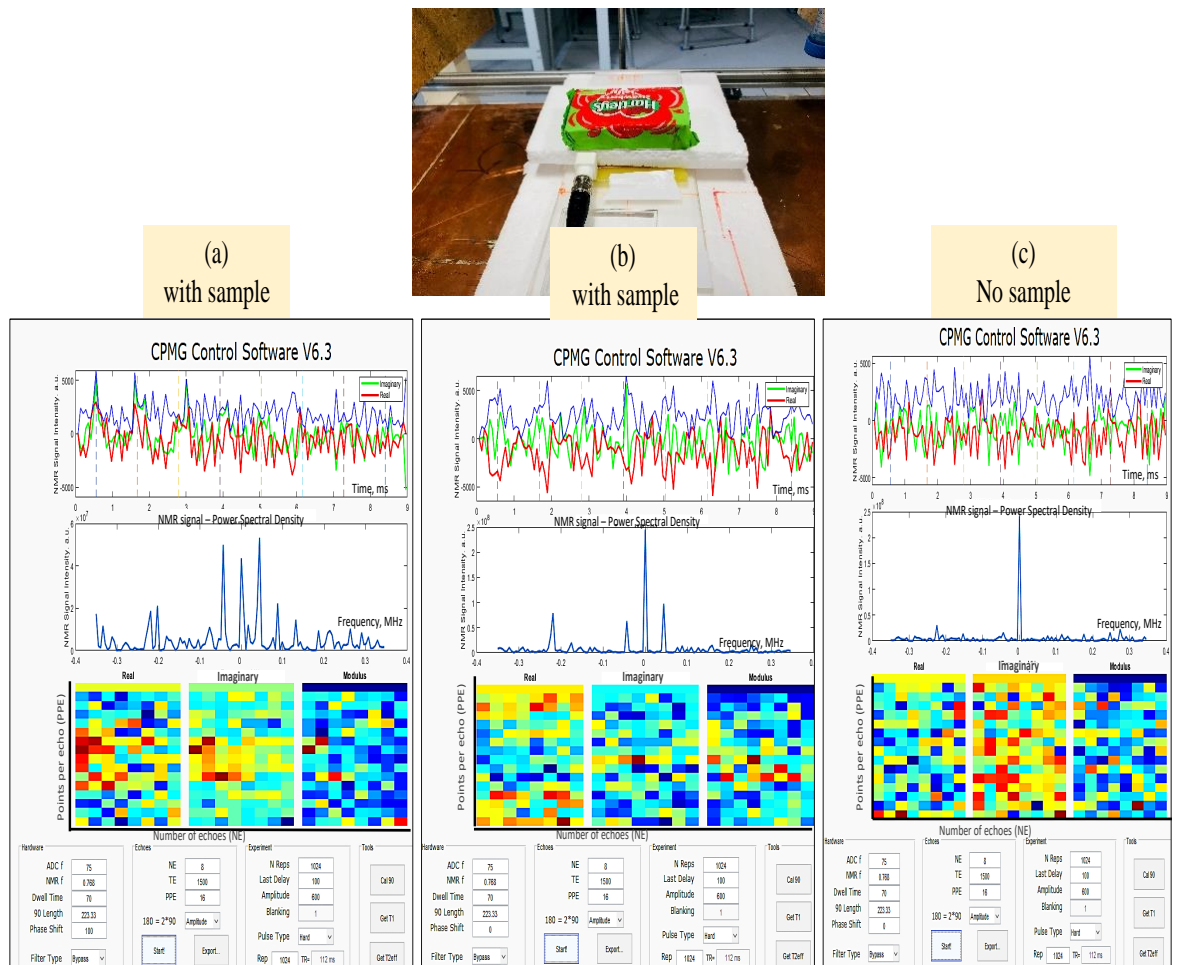
For a better observation of the NMR signal at a distance from the coil surface, it was required for the real and imaginary components to be away from the modules component. As seen in the previous figure, the first image (a) for the NMR signal was available but not observable because of the distortion occurred to the modulus component because of the presence of the real and imaginary parts. Thereafter, when these components were flipped away from the modulus, the signal being more sensible, as in image (b), while image (c) was obtained without a sample to confirm the presence of the NMR signal.

This observation was also being acknowledged in the subsection of the handmade surface coil. Therefore, the chosen value for the phase shift degree shall flip the real and imaginary components or at least one of them away from the modules component. There is no apparent reason, but for all experimental trials that was conducted at a distance from the coil in this study exhibited similar pattern.

Appendix K

A screenshot of the obtained NMR signal from jelly blocks at depth of 15 mm and 22 mm from the surface of the PCB coil using the TOMCO as a power amplifier.
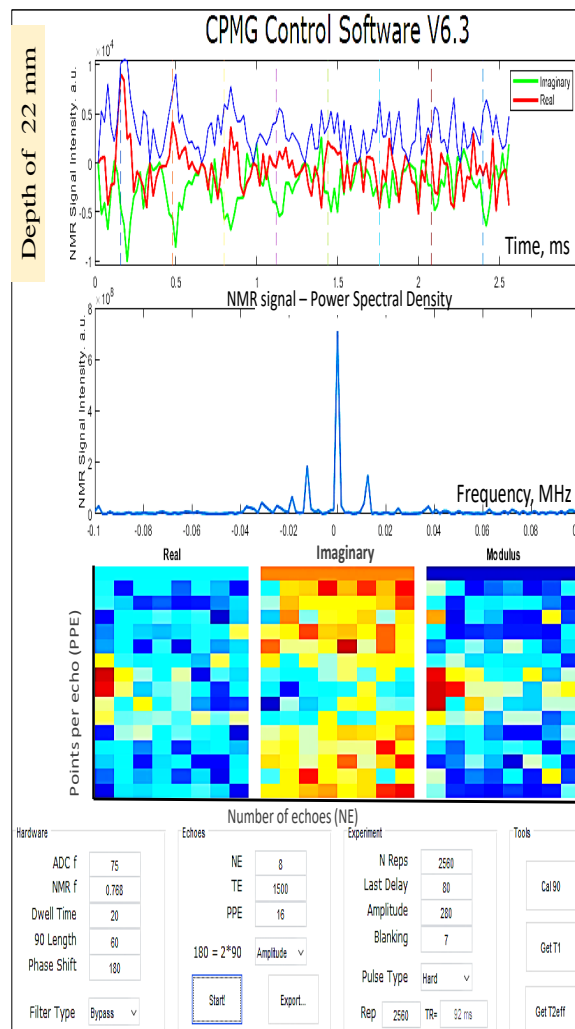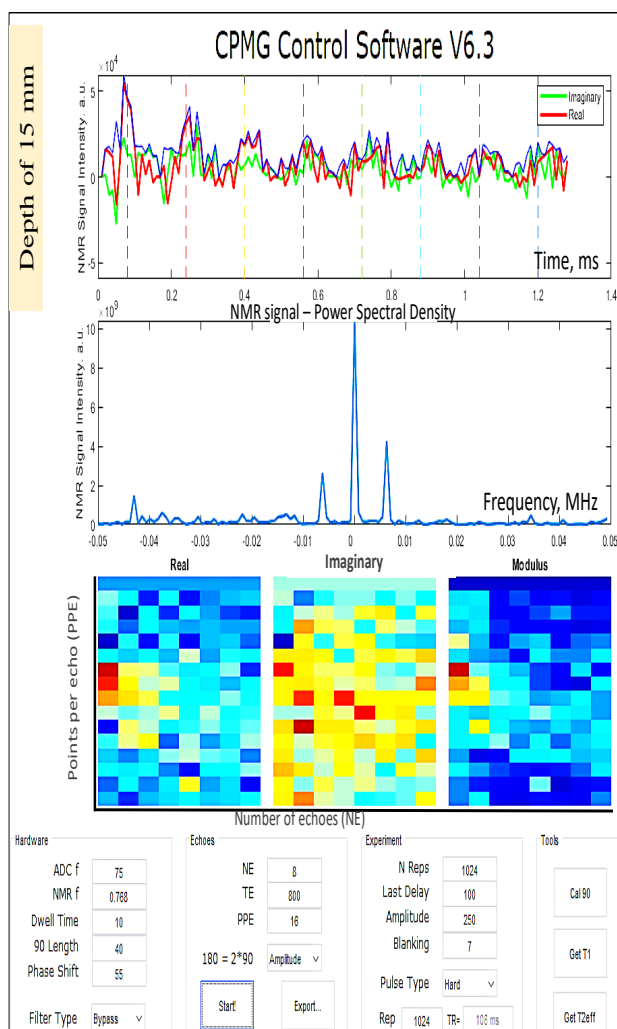
Appendix L

A 90° calibration for the rectangular PCB coil (with an inner dimension of 40 mm by 82 mm) for four jelly blocks positioned at the surface of the PCB coil.

Image (a) illustrates A snapshot for the network analyser showing the frequency for the PCB coil, (b) picture for the jelly blocks used for 90° calibrations, and (c) showing the pulse duration sweep and the blue arrow indicate the produced peak.
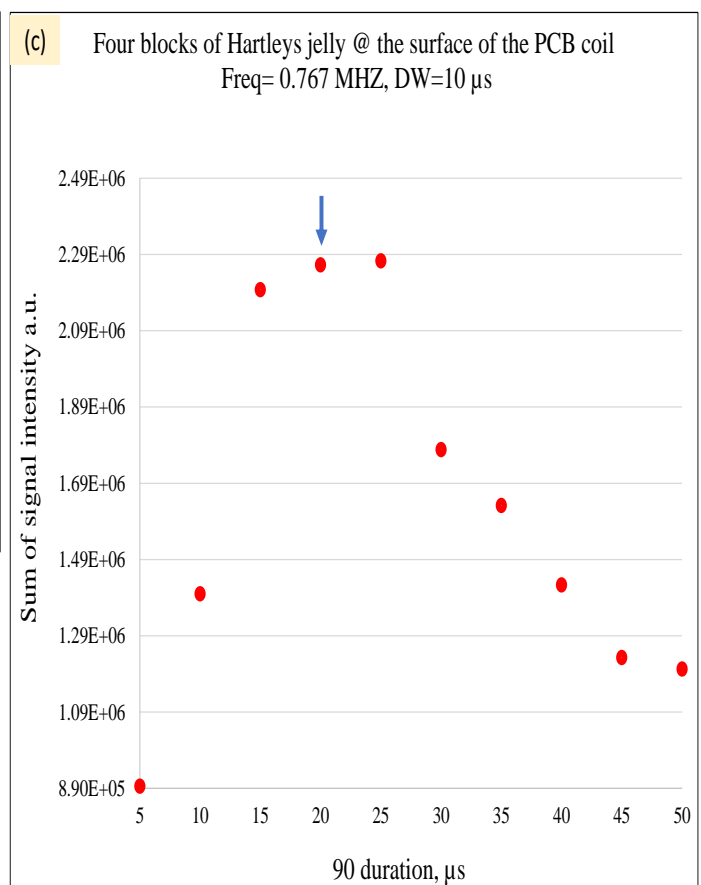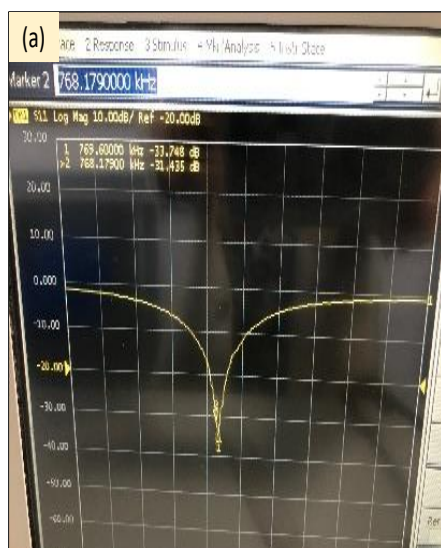
A picture for the generated NMR signal at the surface of the PCB coil for different number of jelly blocks, (a) one block, (b) two blocks (c) three blocks and (d) four blocks.
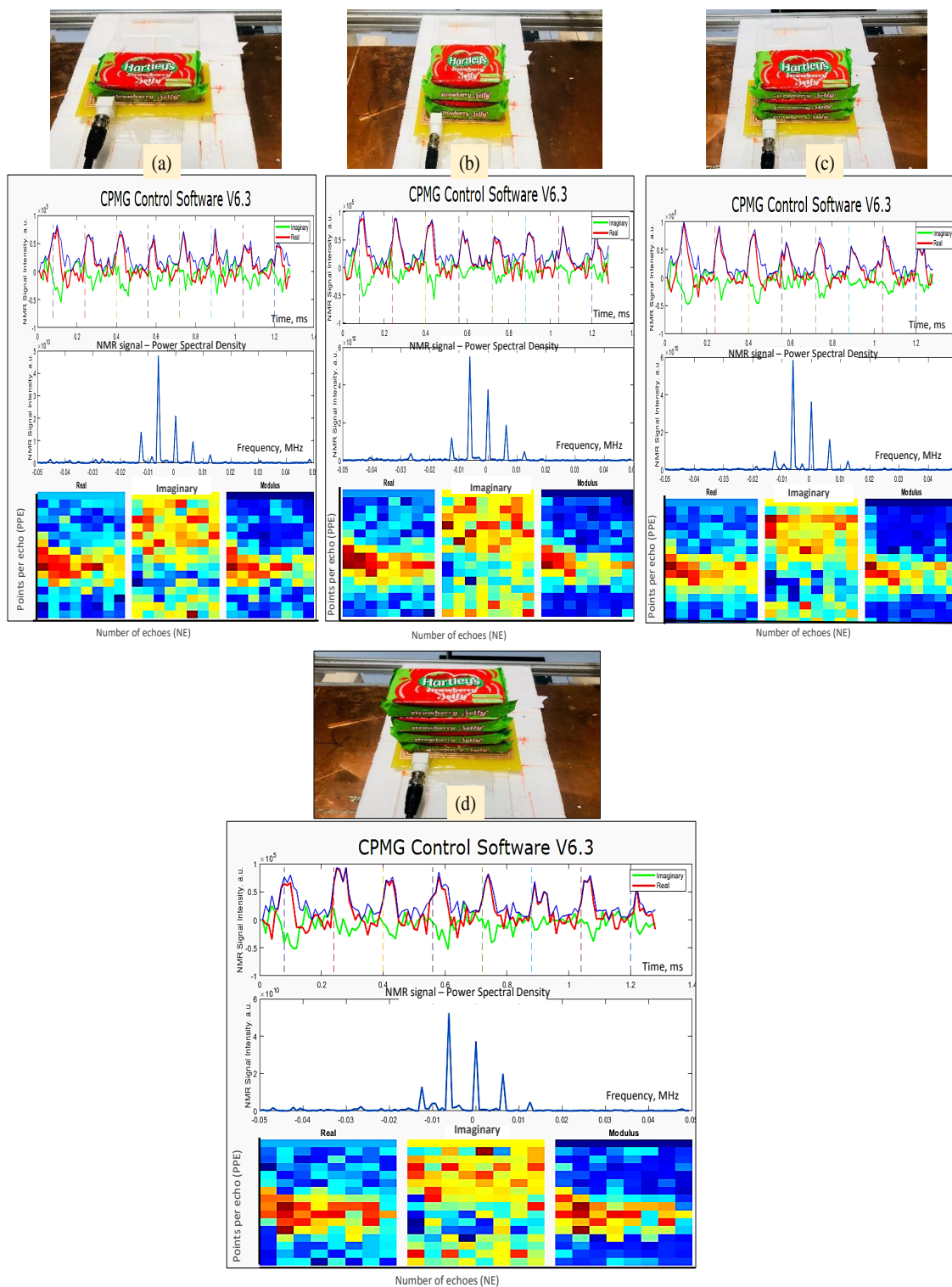
An examples for the NMR signal acquired at depths of 15, 22, 30, and 35 mm from the rectangular PCB coil paired with CAPIBarA magnet.

**Coil at 55 mm from the magnet surface
3 blocks of jelly at 15 mm surface**
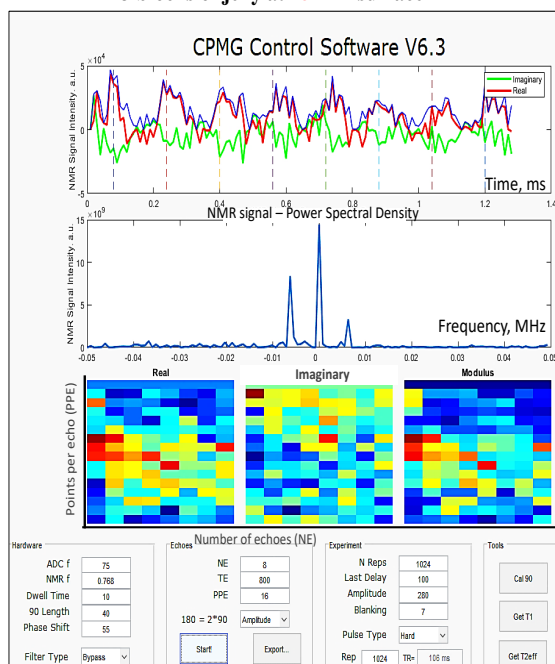
**Coil at 50 mm from the magnet surface
3 blocks of jelly at 22 mm surface:**
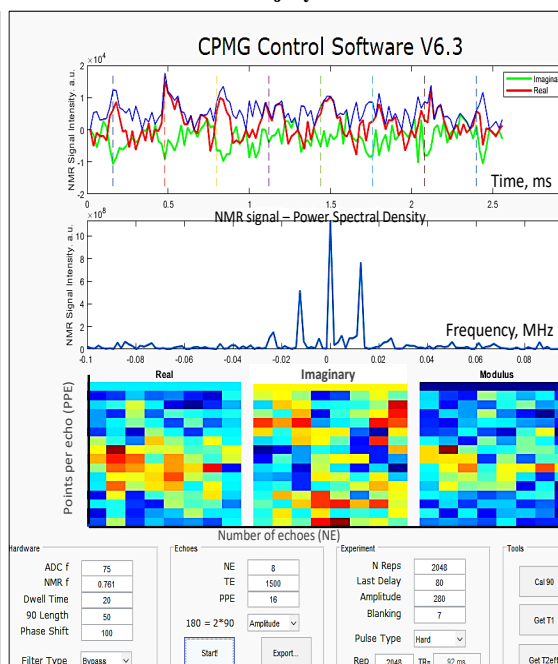
**Coil at 39 mm from the magnet surface
3 blocks of jelly at 30 mm from surface**
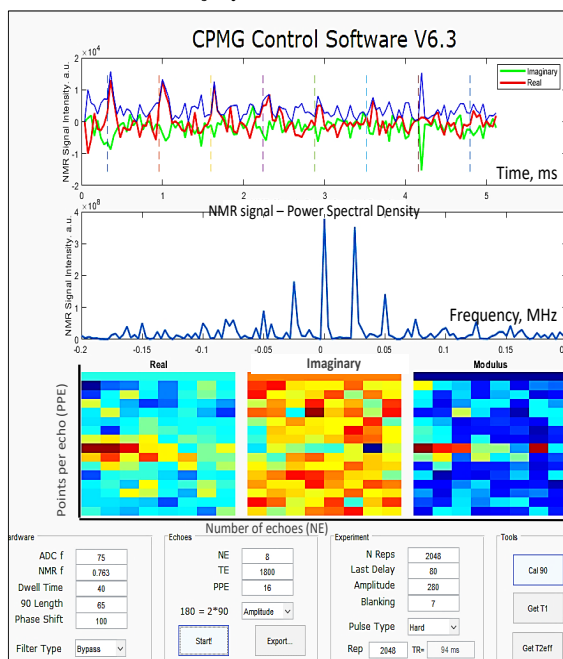
**Coil at 30 mm from the magnet surface
3 blocks of jelly at 35 mm from surface**
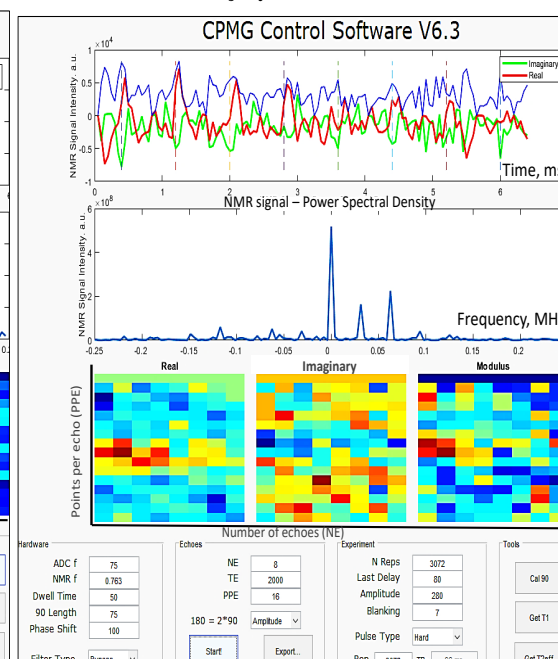
Appendix M

A snapshot of obtained NMR signal from sunflower oil of 256 ml at depths of 23 mm and 31 mm from the PCB coil surface before adding the 1 MHZ low-pass filter to the front-end electronics.
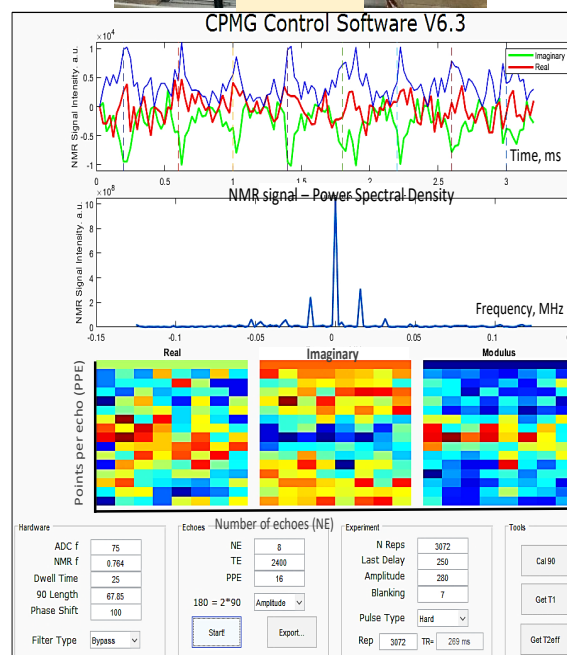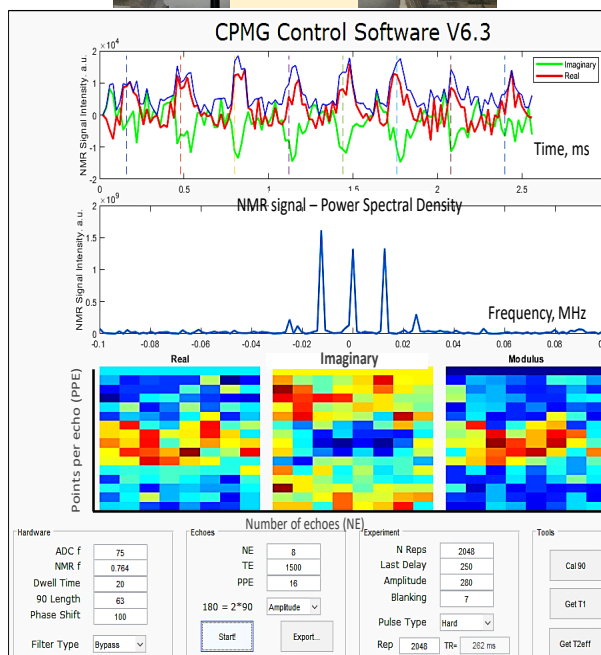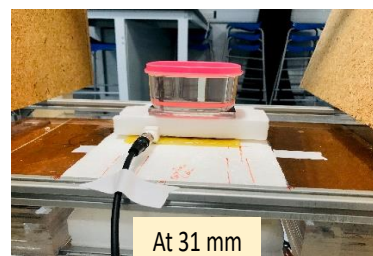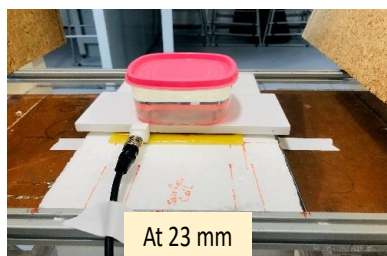
Screenshots of NMR signal obtained from the sunflower oil of 256 ml at distances of 32 mm and 34 mm from the PCB coil surface after adding the 1 MHZ low-pass filter to the front-end electronics.
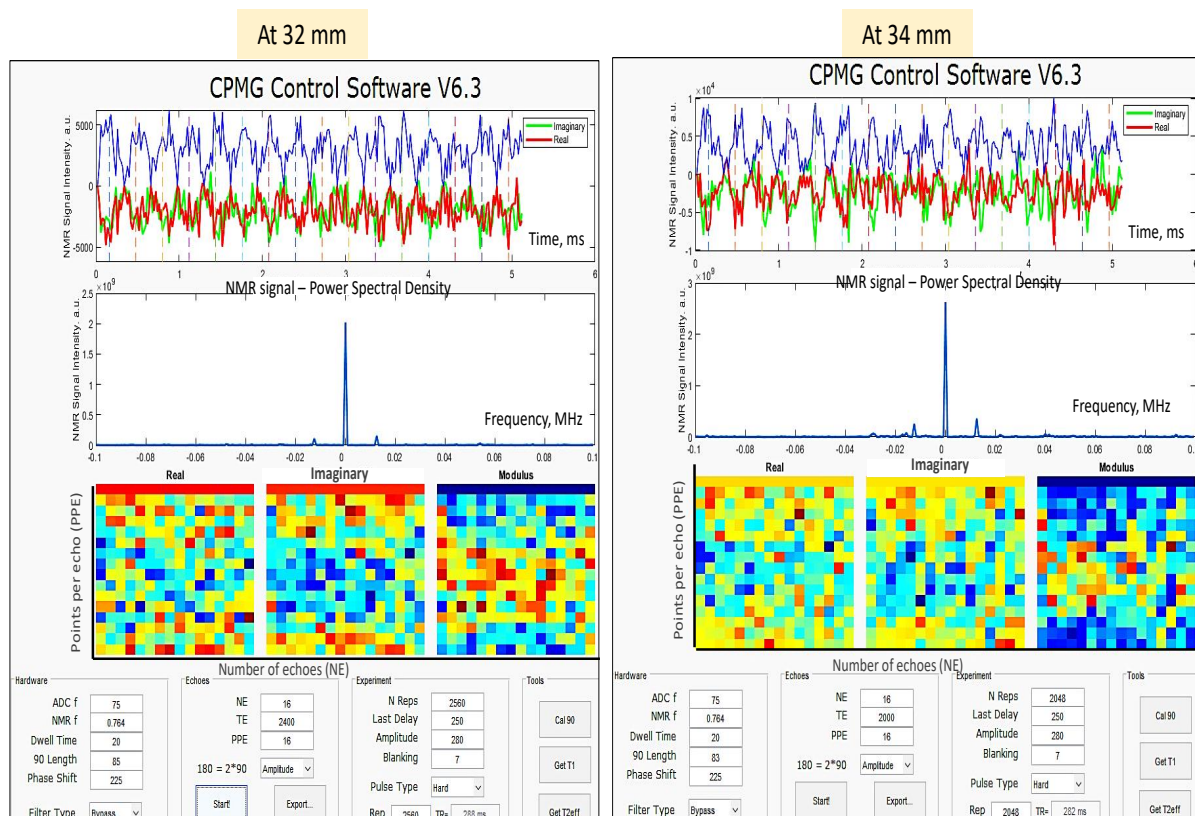
Appendix N

This appendix shows examples of the NMR signals obtained at different depths from the PCB coil starting from zero (at the surface) to 40 mm using two different interval times (Dwell time) at each depth. All measurements were conducted using the sunflower oil of 128 ml. The reader can observe how the shape of the spin echoes starts to be distorted as a function of depth. In addition to the effect of the Dw time on the collected data, the spin echoes' width became narrower.

Depth = 0mm

Dw= 10 μs , PL= 25 μs   Dw= 25 μs , PL= 25 μs

Depth = 5mm

Dw= 10 μs , PL= 65 μs   Dw= 25 μs , PL= 25 μs

Depth = 10mm

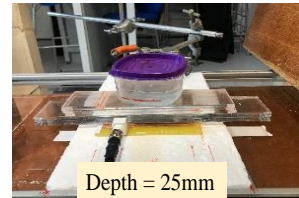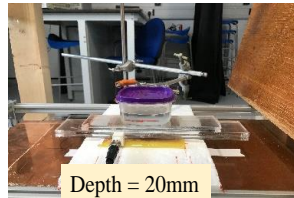Dw= 10 μs , PL= 38.5 μs   Dw= 25 μs , PL= 38.5μs

Depth = 15mm

Dw= 10 μs , PL= 40 μs   Dw= 25 μs , PL= 40 μs

Depth = 20mm

Depth = 25mm

Dw= 10 µs , PL= 50µs Dw= 25 µs , PL= 40µs

Dw= 25 µs , PL= 65 µs Dw= 40 µs , PL= 75 µs

Depth = 30mm

Depth = 35mm

Dw= 25µs , PL= 75µs Dw= 40µs , PL=85µs

Dw= 40µs , PL=100µs Dw= 50µs , PL=100µs
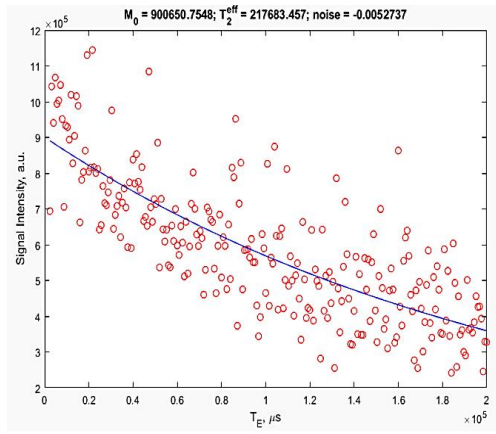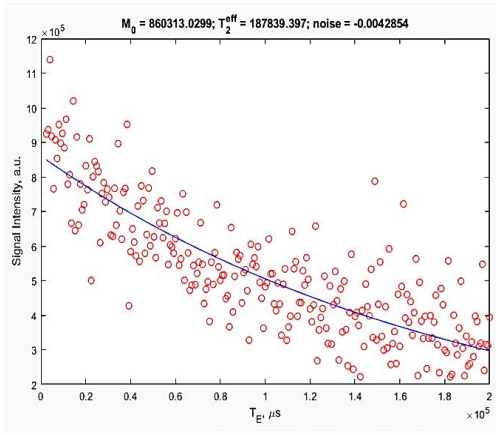
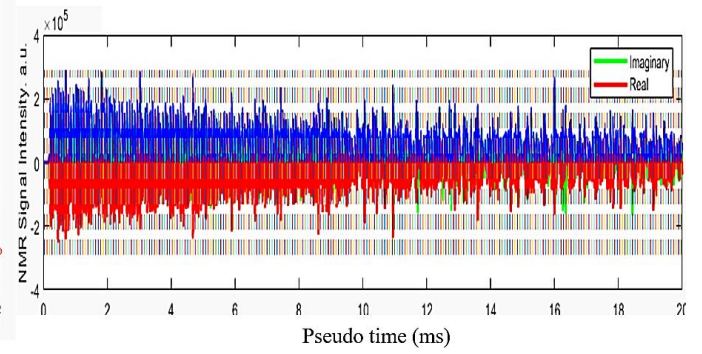

Depth = 40mm

Dw= 50µs , PL=100µs
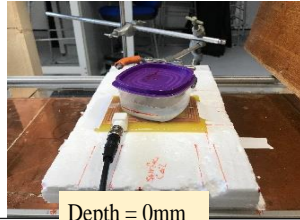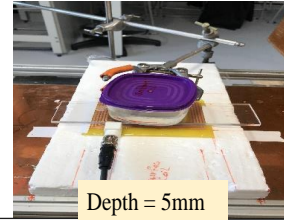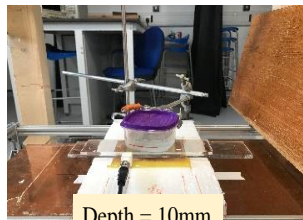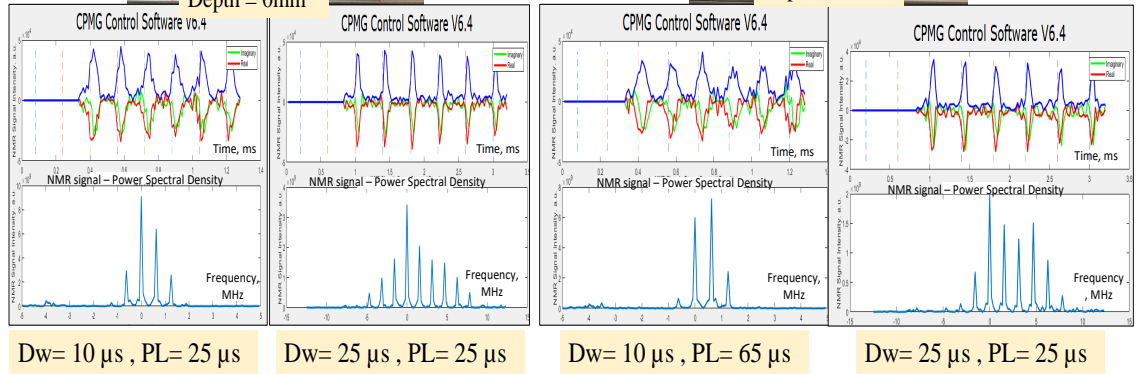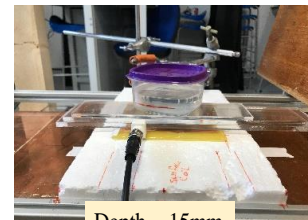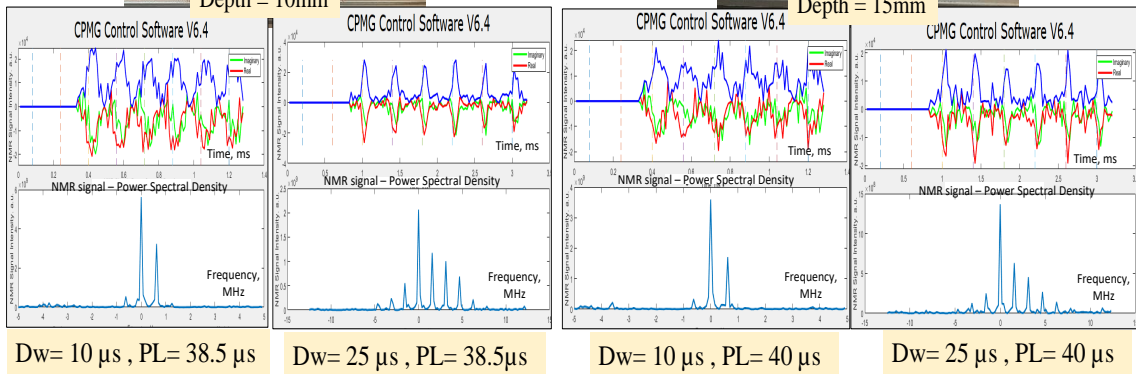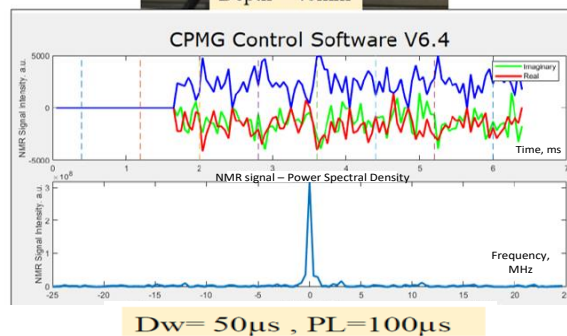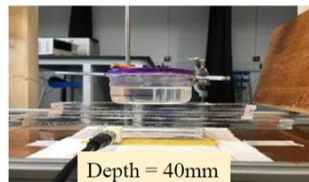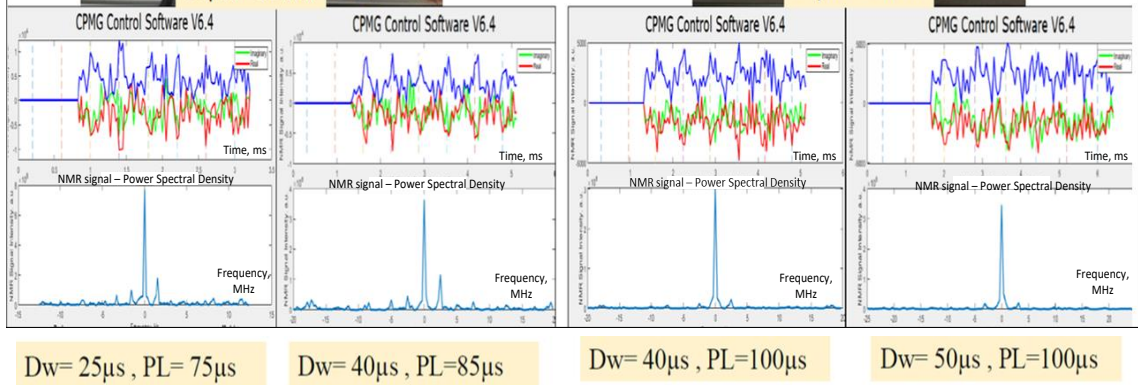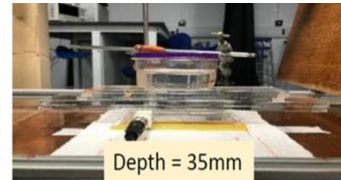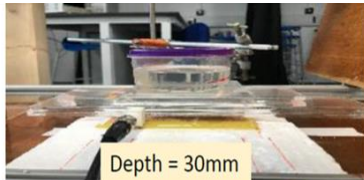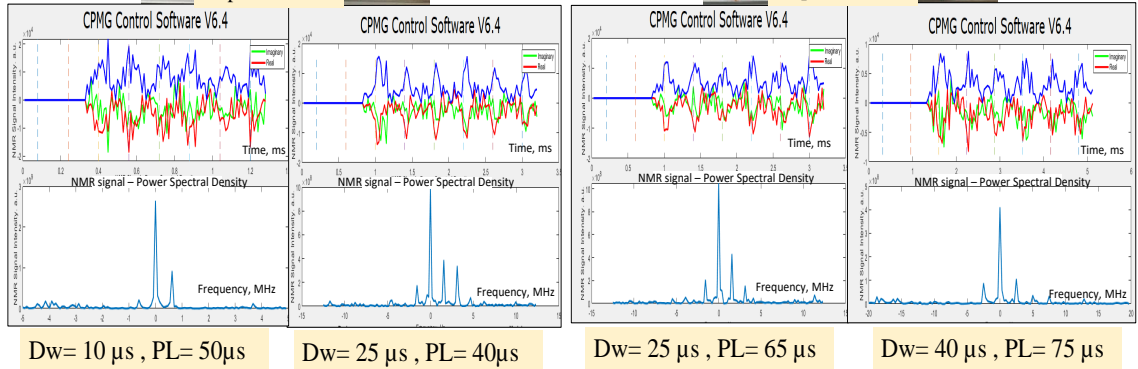
Appendix O

Examples of the collected raw data from different silicone oil viscosities using the CPMG sequence in the MATLAB GUI, in which the solenoid coil was paired with the CAPIBarA magnet as a detector.. The collected raw data were 300, 600, 900, 2k, 5k, 10k, 15k, and 30k cP of silicon oils. The right-hand side of the figure represents the echo train generated by the CPMG sequence. The modulus of the real (red) and imaginary (green) components are represented as a blue overlay. The left-hand side shows the integrals of the produced echoes in a red circle and the fit curve is in blue; the fit parameter is shown above the plot and the T_2^{eff} shows in μs.
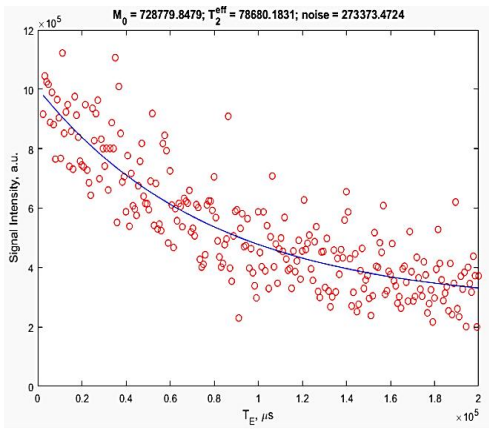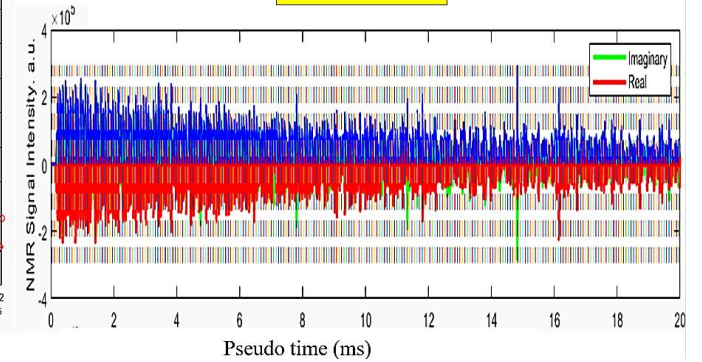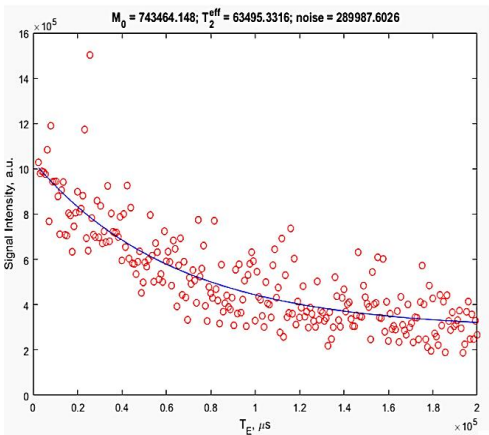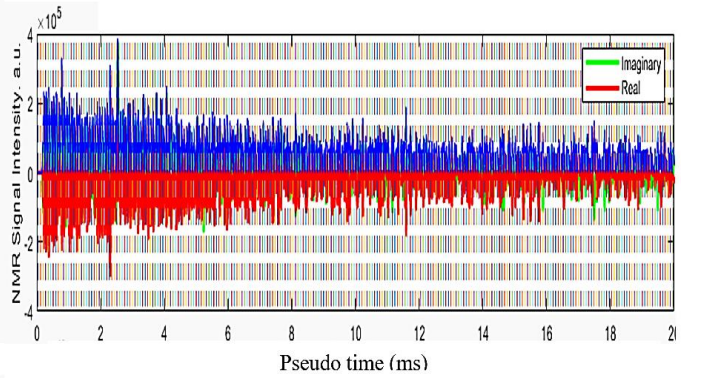
$M_0 = 900650.7548$; $T_2^{eff} = 217683.457$; noise $= -0.0052737$

PDMS = 900 cP

$M_0 = 860313.0299$; $T_2^{eff} = 187839.397$; noise $= -0.0042854$

PDMS = 2k cP

$M_0 = 728779.8479$; $T_2^{eff} = 78680.1831$; noise $= 273373.4724$

PDMS = 5k cP

$M_0 = 743464.148$; $T_2^{eff} = 63495.3316$; noise $= 289987.6026$
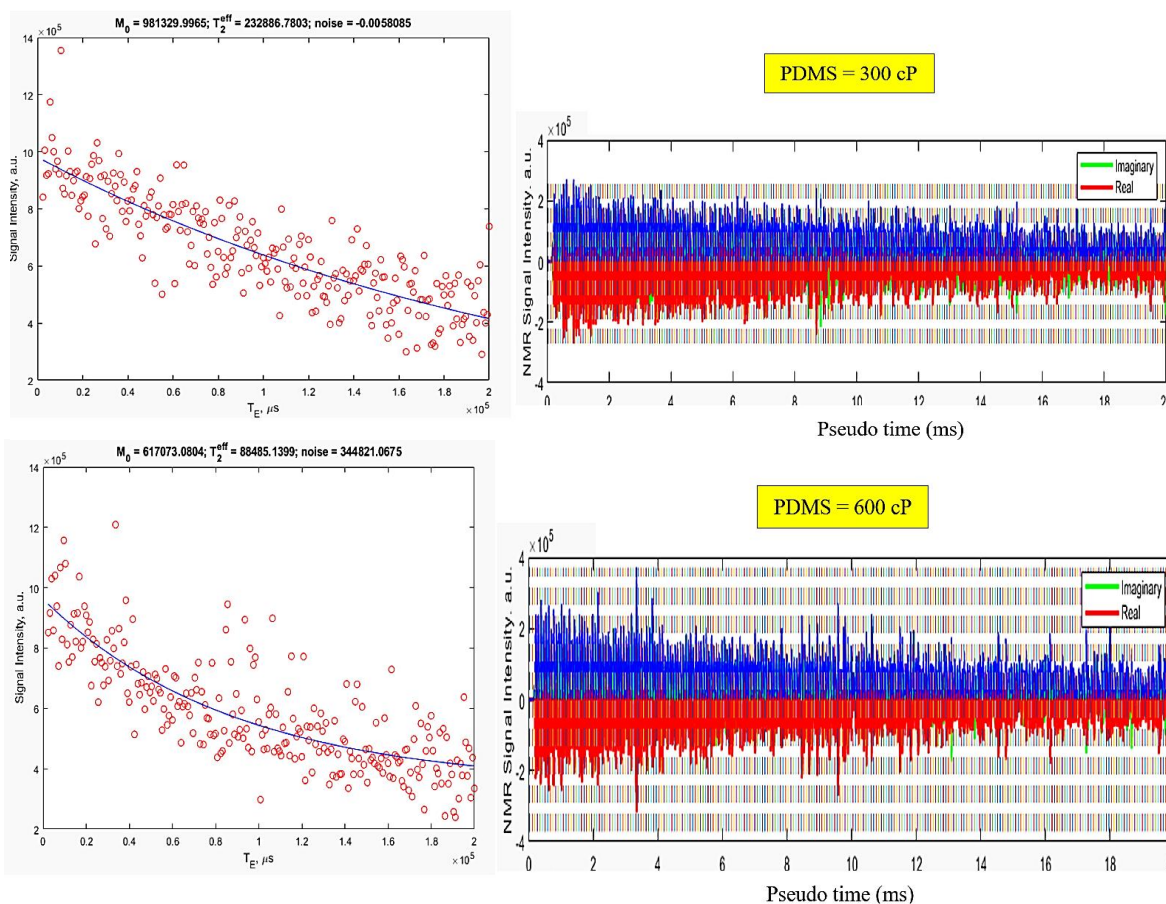
PDMS = 10k cP
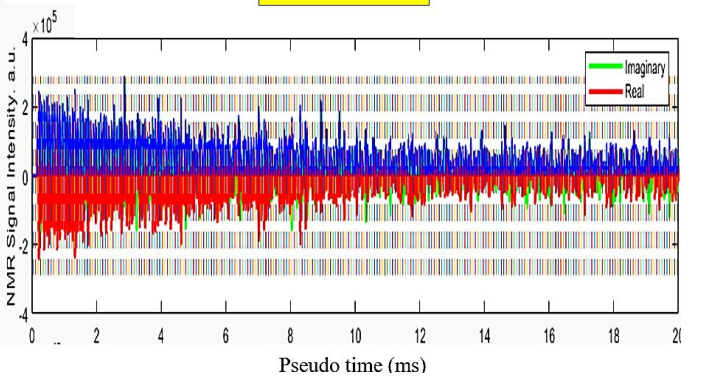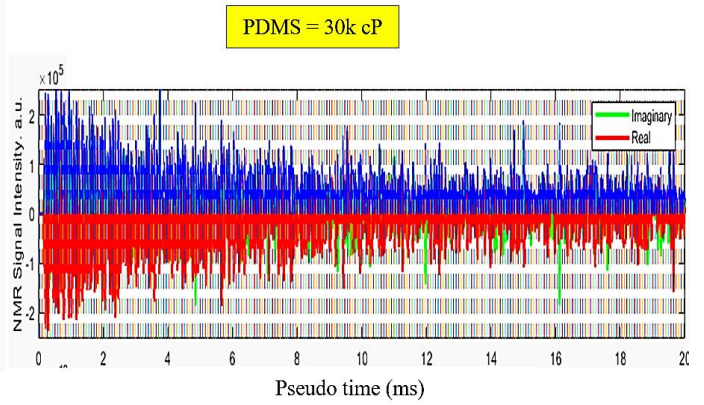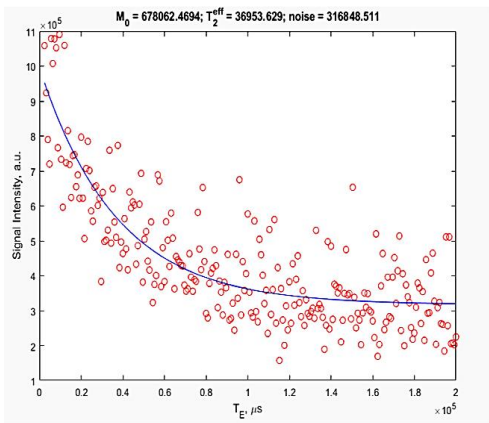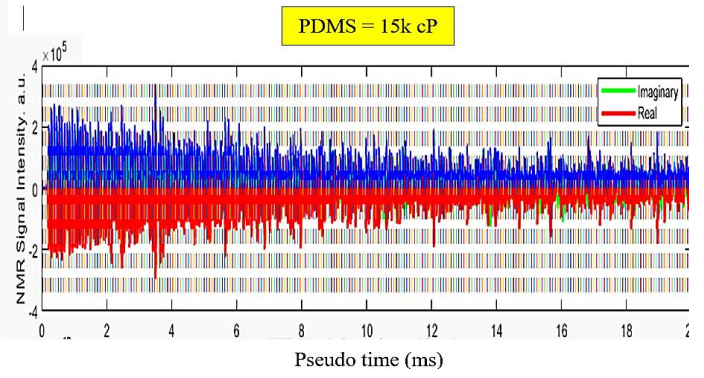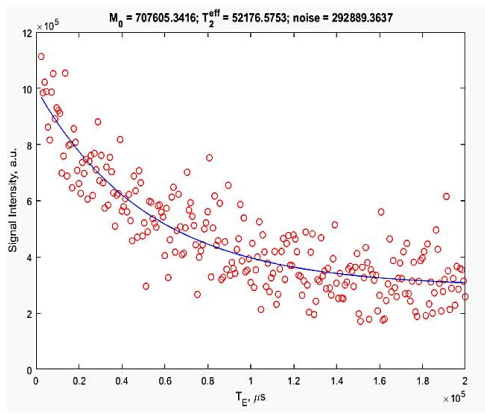
Appendix P

Examples of the collected raw data from different silicone oil viscosities using the CPMG sequence in the MATLAB GUI, in which the PCB coil was paired with the CAPIBarA magnet as a sensor.. T_2^{eff} (μs) data for 300, 600, 900, 2k, 5K, 10K, 15K, and 30k cP of silicon oils are presented. As described in Appendix O, the right-hand part of the image shows the generated echo train, and the left-hand part depicts the integral of the modulus echoes plotted along with the fitting curve.

PDMS = 15k cP

$M_0 = 44559.6915$; $T_2^{eff} = 49713.3115$; noise $= 59431.7566$

PDMS = 30k cP

$M_0 = 35186.639$; $T_2^{eff} = 37421.6636$; noise $= 62130.4868$
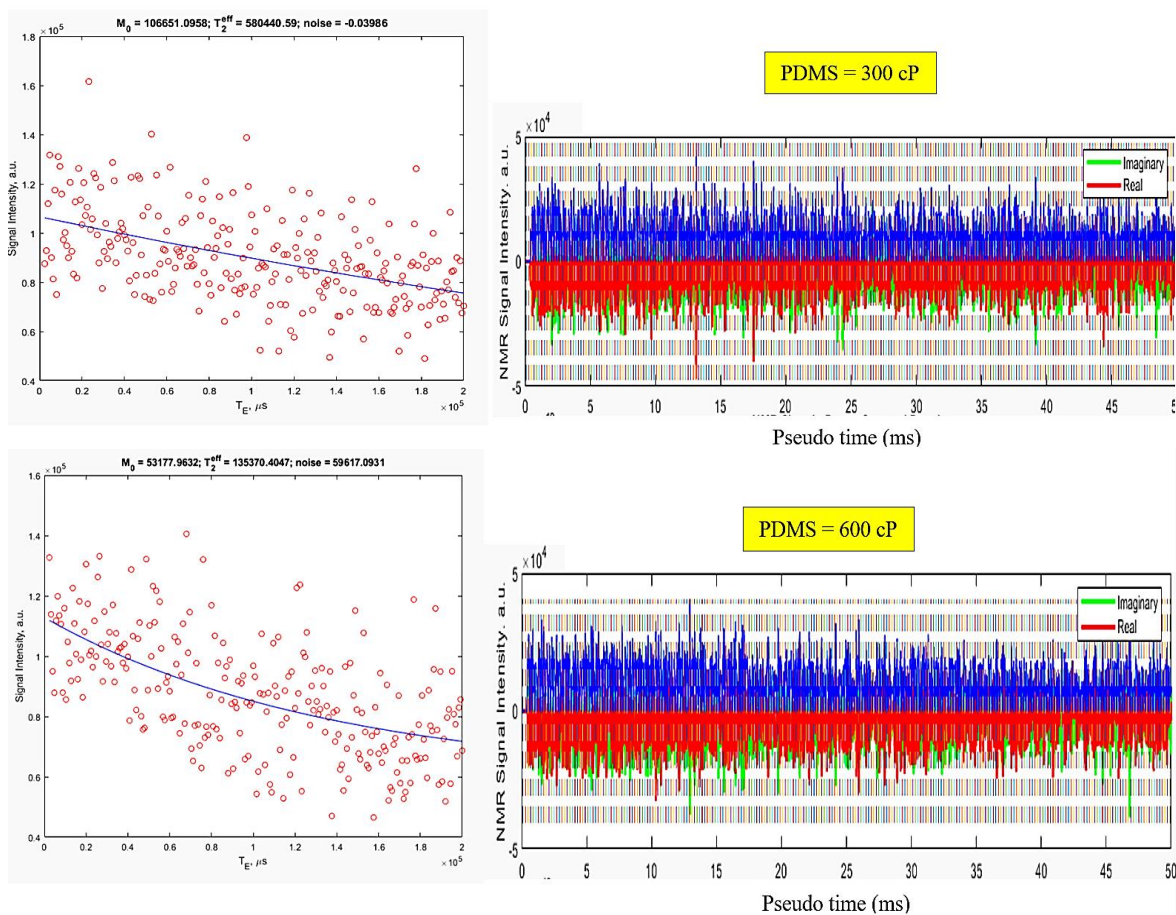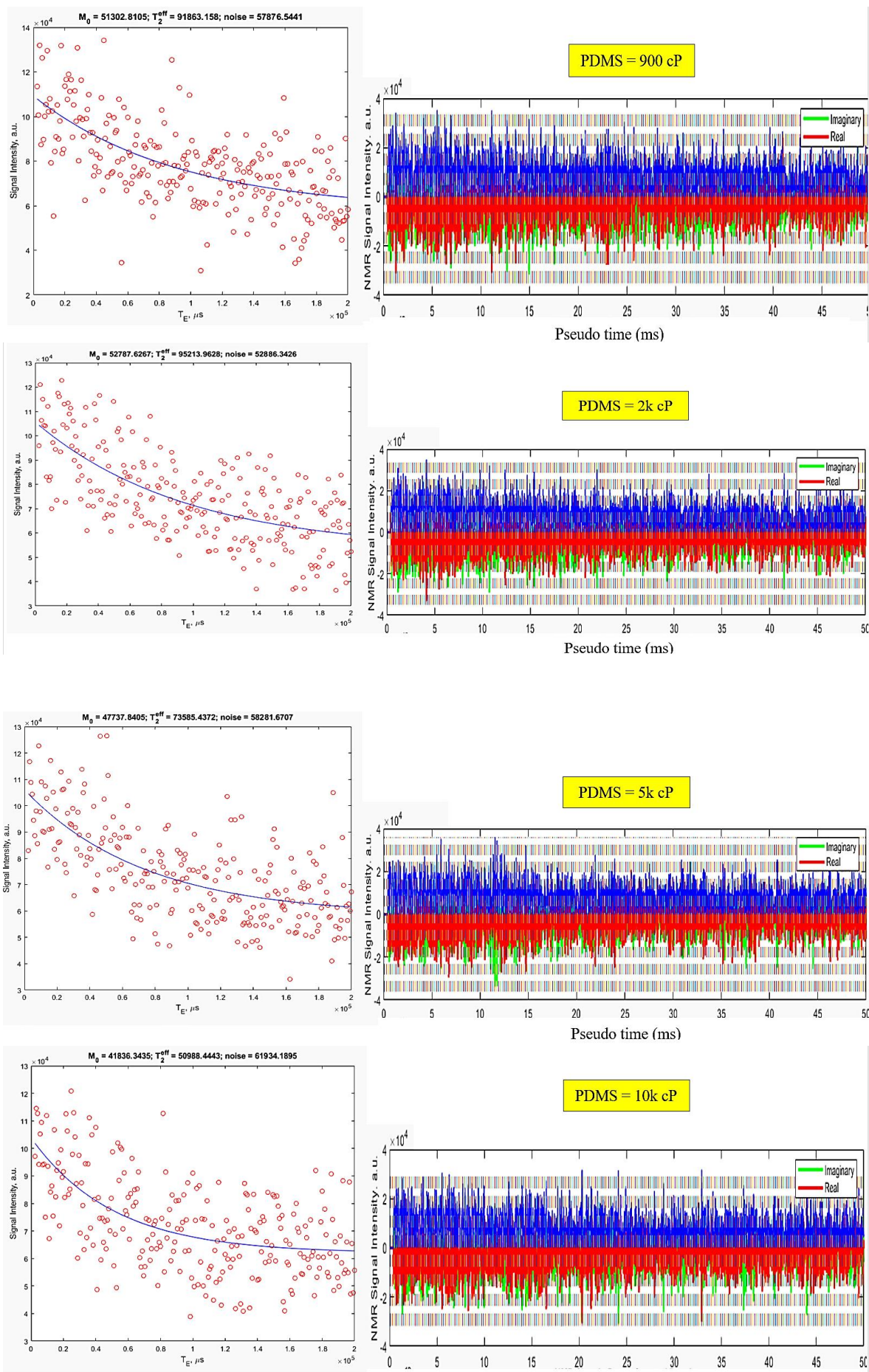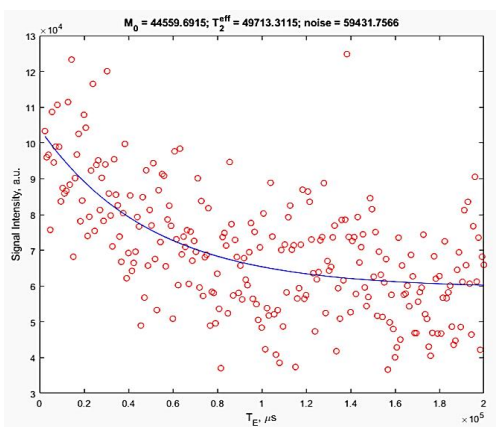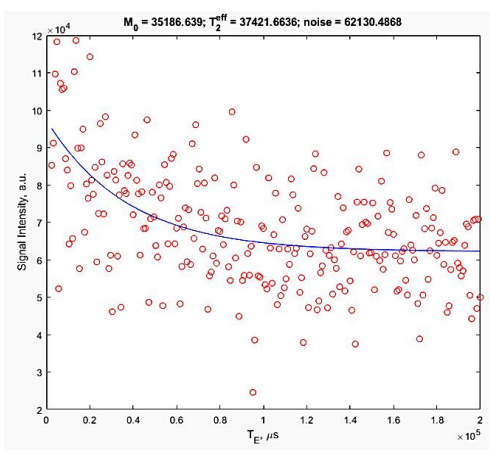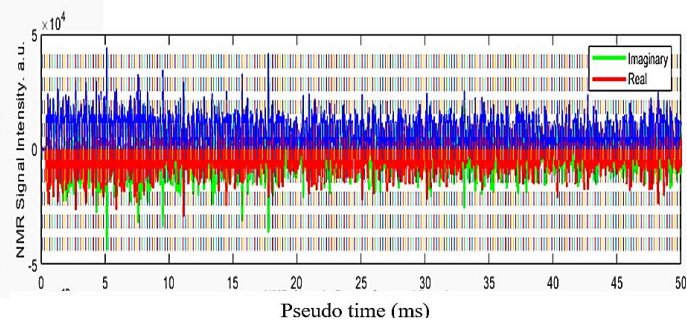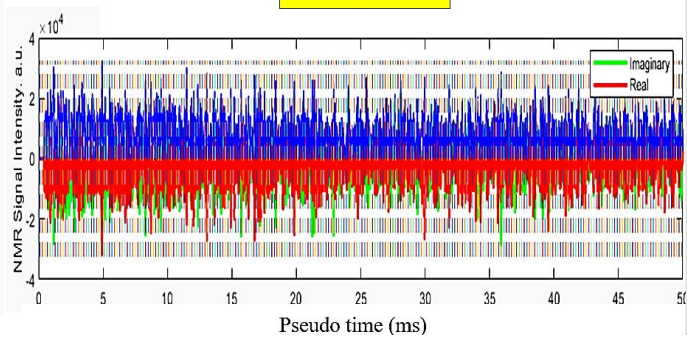
Appendix Q

Examples of the obtained T_2^{eff} (μs) data from the PDMS viscosities of 300, 600, 900, 2k, 5K, 10K, 15K, and 30k cP by placing the PCB coil on the longitudinal direction.
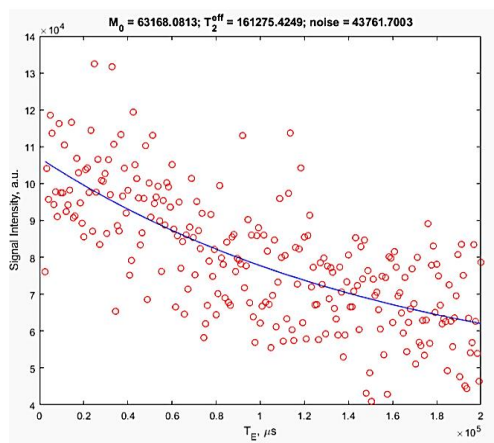
Figures showing NMR signal intensity decay curves (left) and raw NMR signal data (right) for four PDMS viscosities.

Top pair: $M_0 = 62005.8631$; $T_2^{eff} = 89274.9133$; noise $= 48042.7867$ — PDMS = 900 cP

Second pair: $M_0 = 58372.6273$; $T_2^{eff} = 77959.7064$; noise $= 51909.6315$ — PDMS = 2k cP

Third pair: $M_0 = 59470.0878$; $T_2^{eff} = 68205.1459$; noise $= 49473.9032$ — PDMS = 5k cP
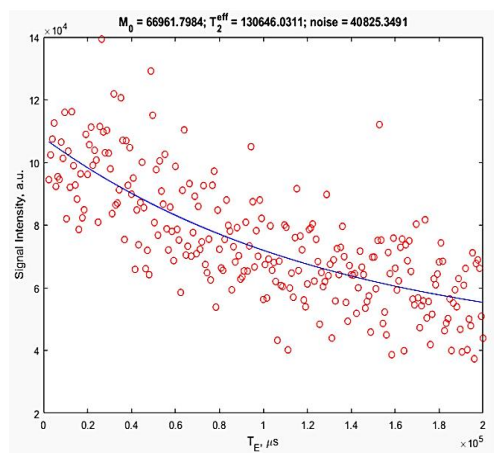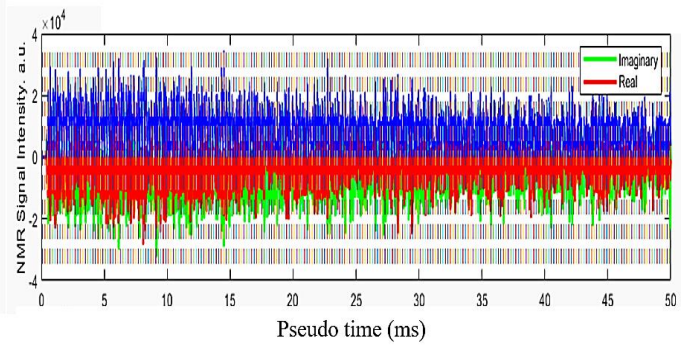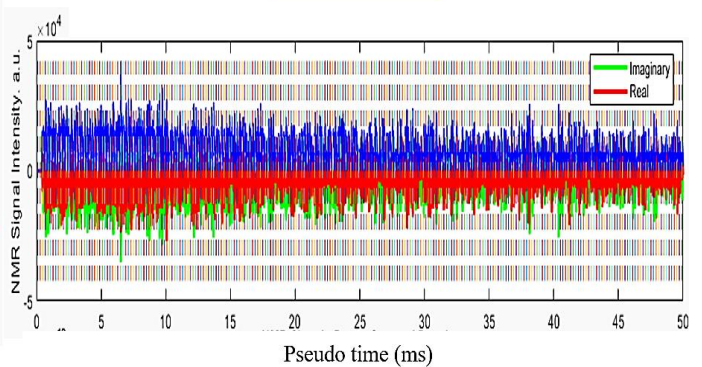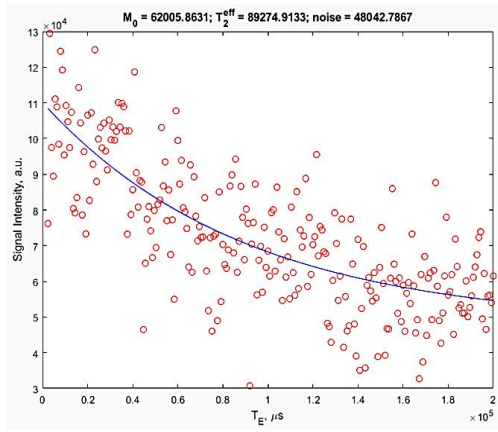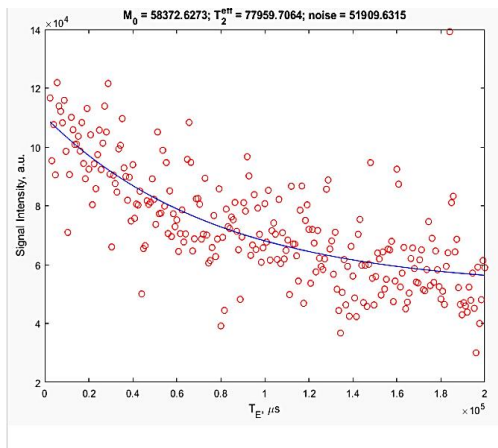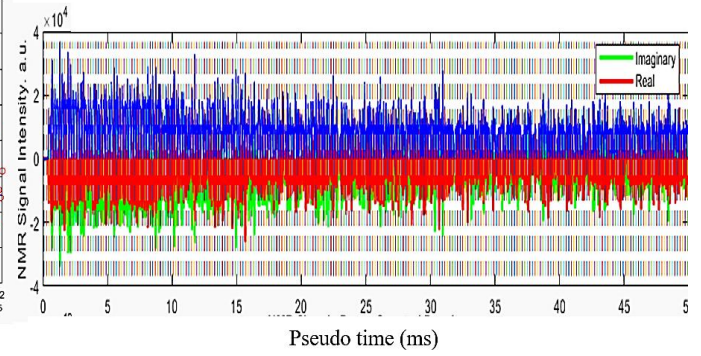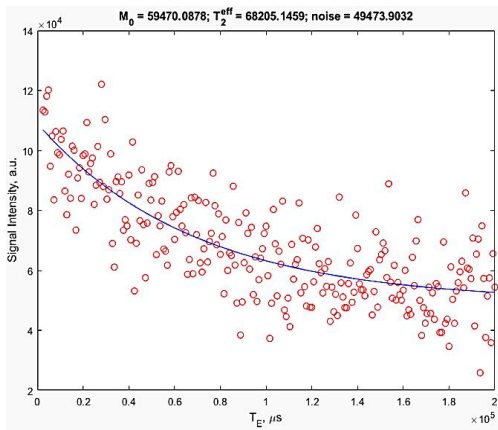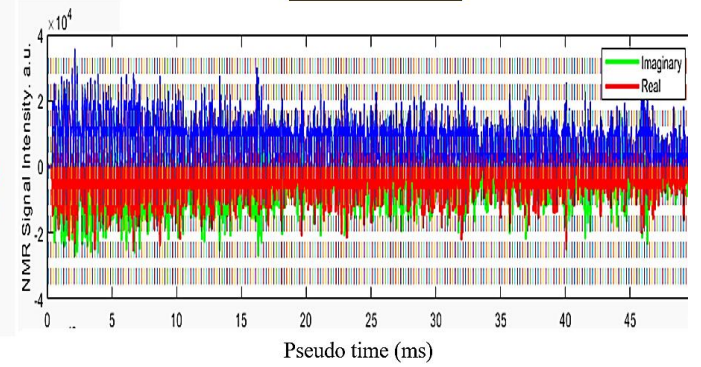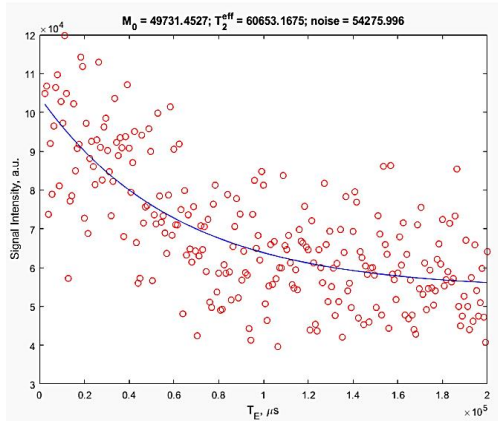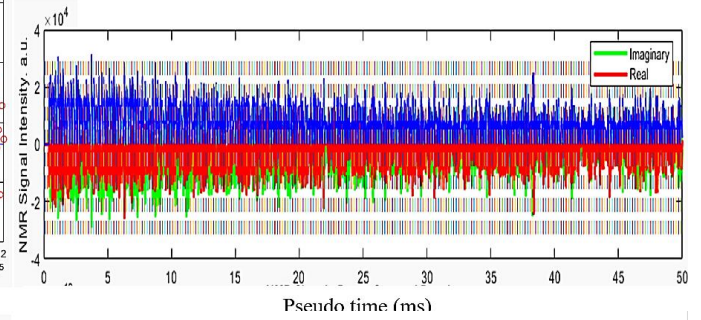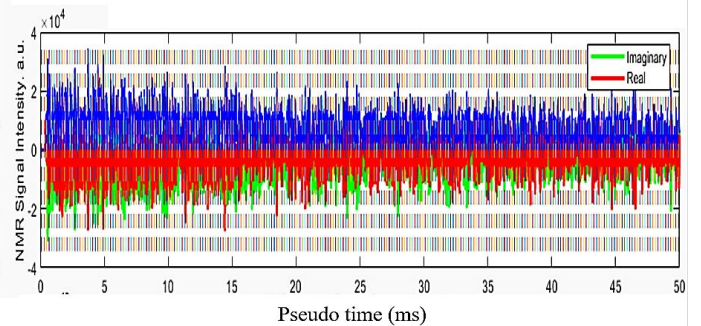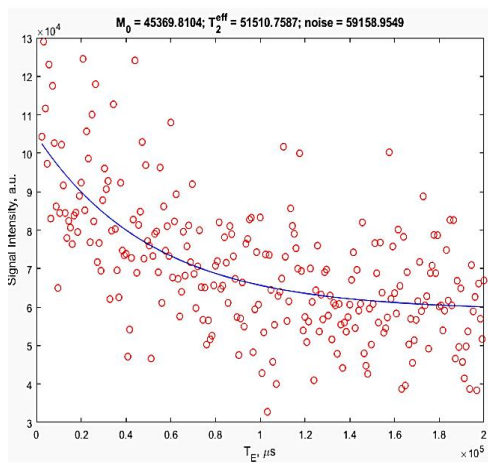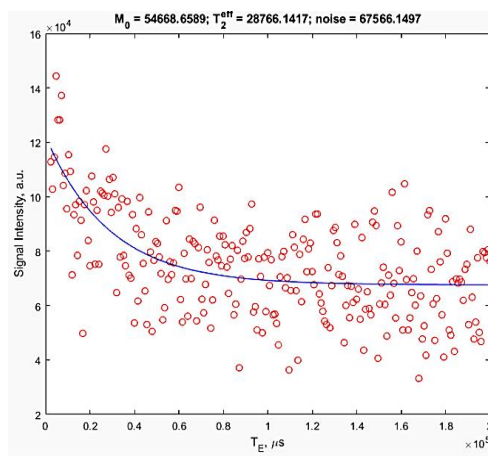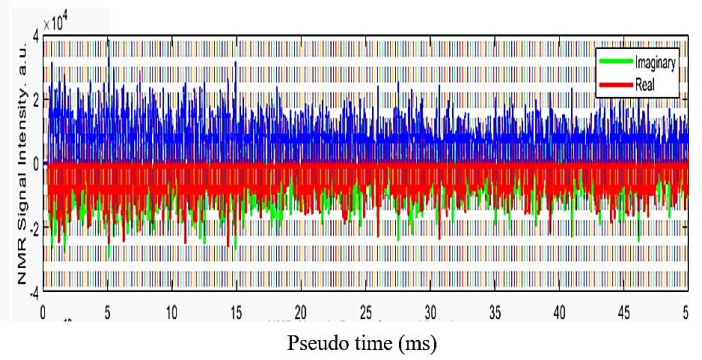
Fourth pair: $M_0 = 49731.4527$; $T_2^{eff} = 60653.1675$; noise $= 54275.996$ — PDMS = 10k cP
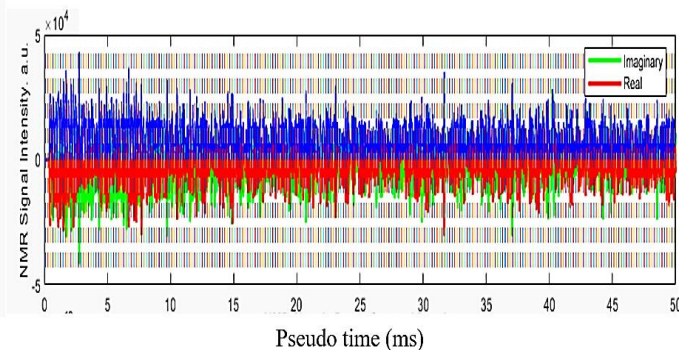
Appendix R

Examples of the obtained T_2^{eff} (μs) data from the different concentrations of the modelled system (milk powder mixed with 300 cP of PDMS oil), which were 0%, 10%, 20%, 33% and 40%.
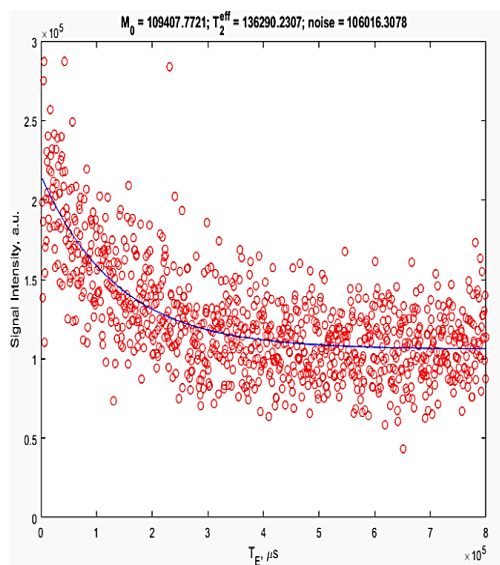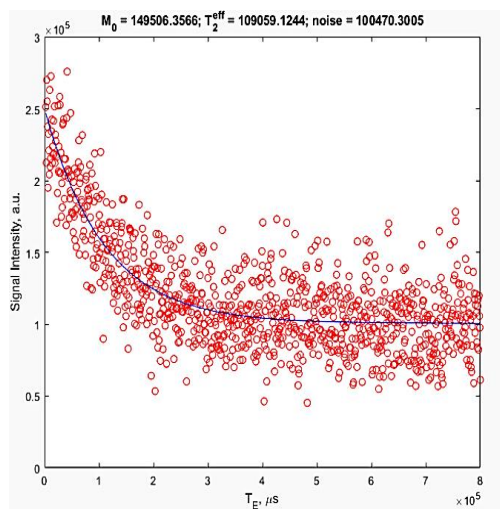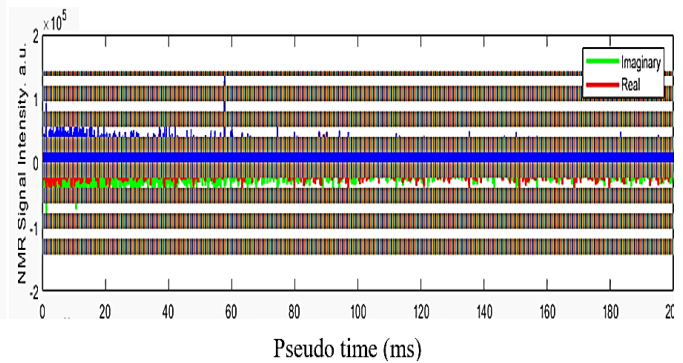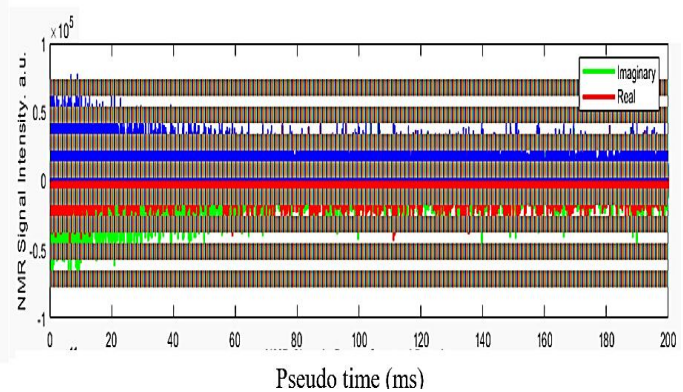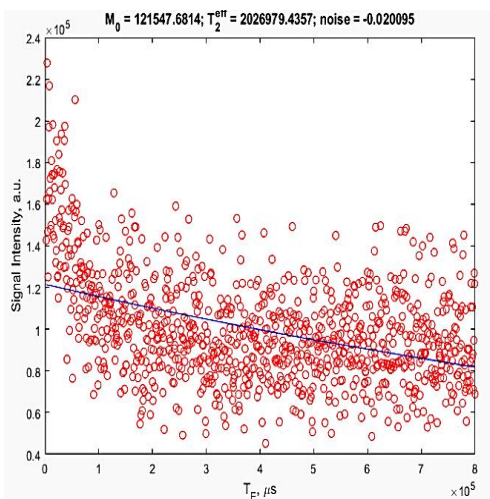
Model system 20% (58 ml)
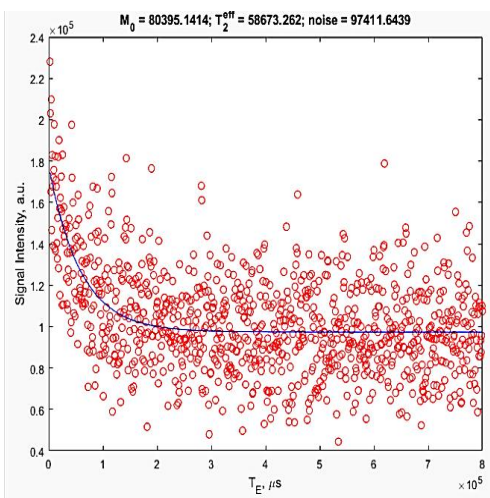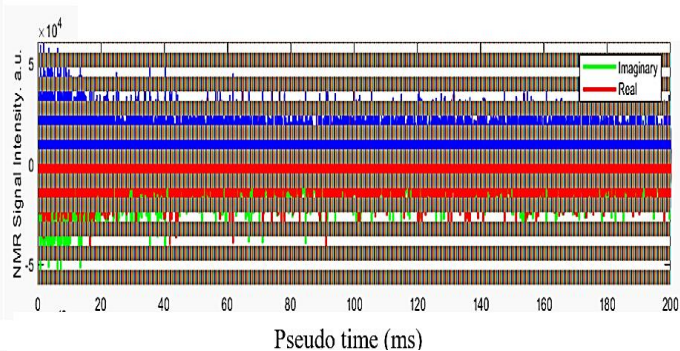
Model system 33% (180 ml)
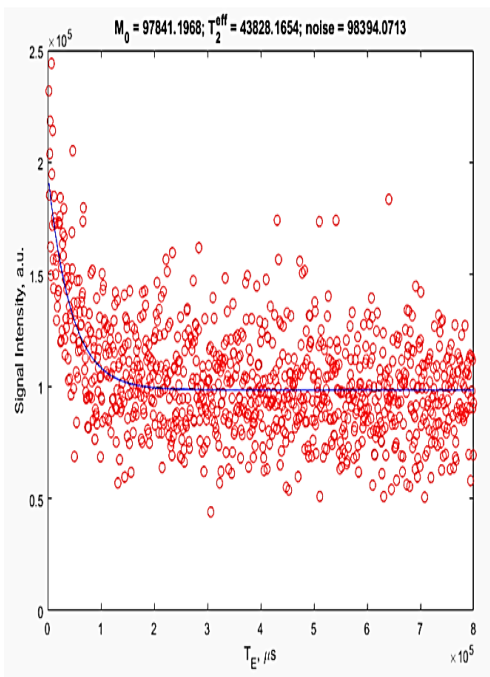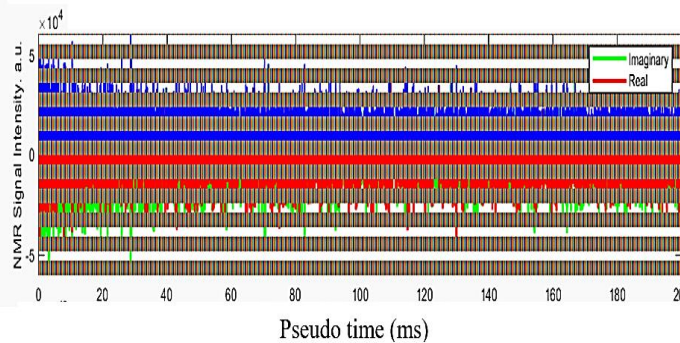
Model system 40% (75 ml)
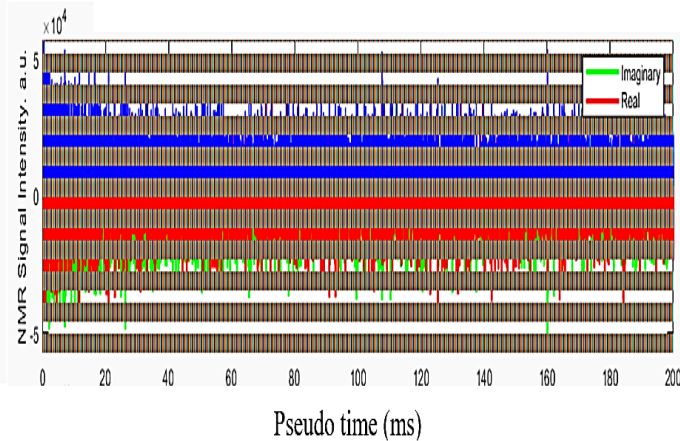
Appendix S

Screenshots of the obtained T_1 (ms) data points from the different concentrations of the modelled system (milk powder mixed with 300 cP of PDMS oil), which are 0%, 10%, 20%, 33% and 40%.

Model system 20% (75 ml)

Model system 33% (180 ml)
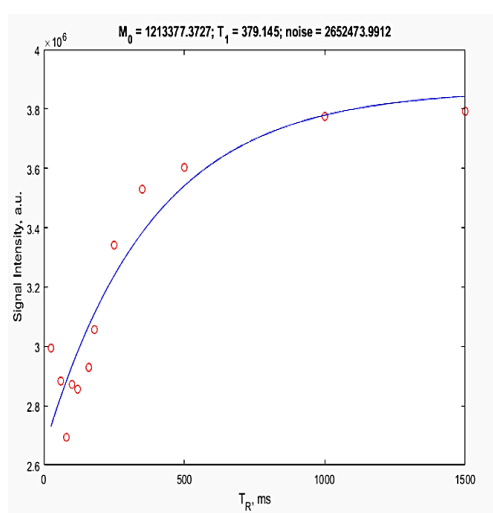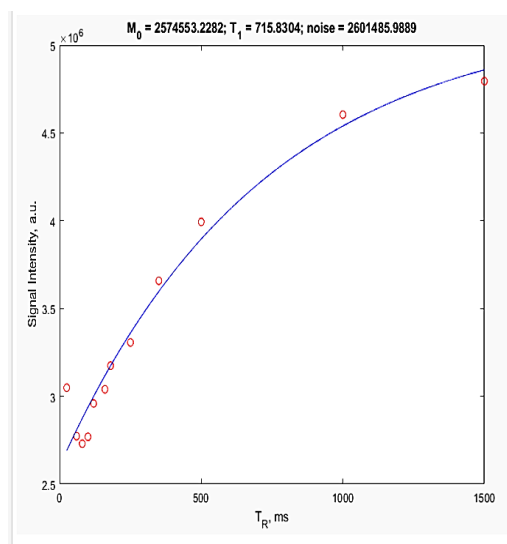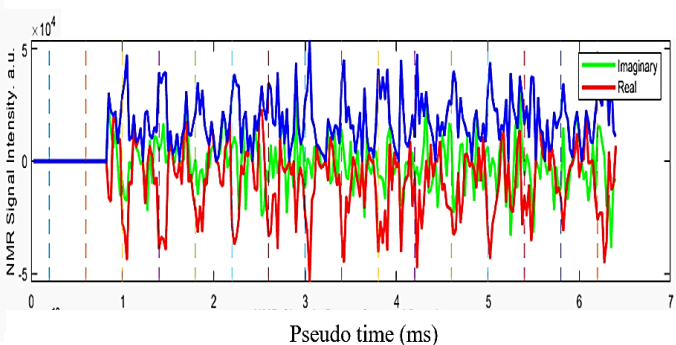
Model system 40% (75 ml)
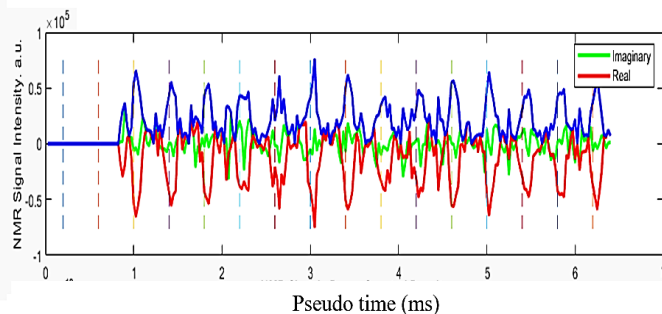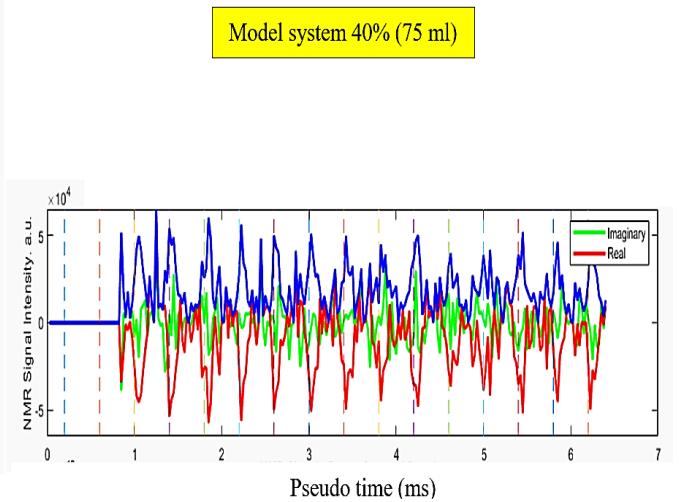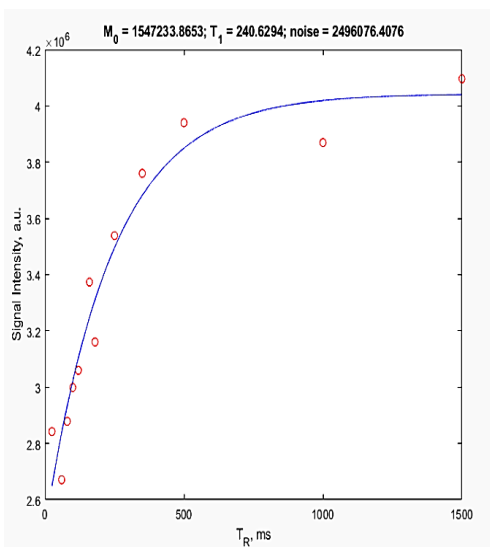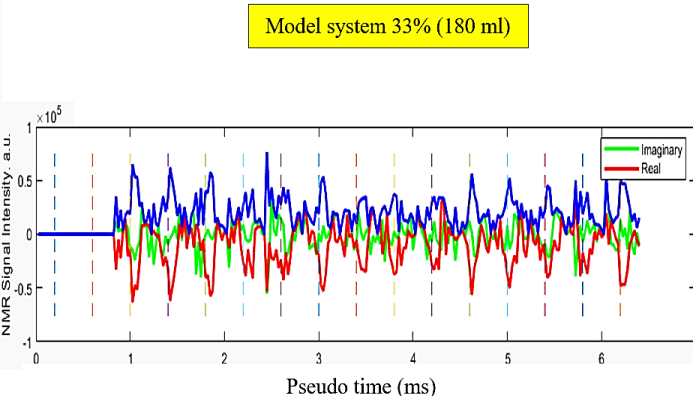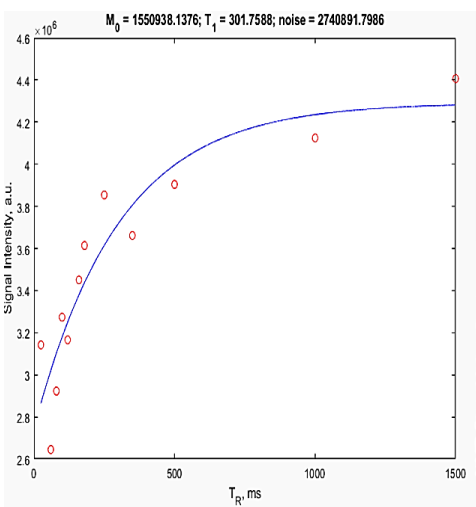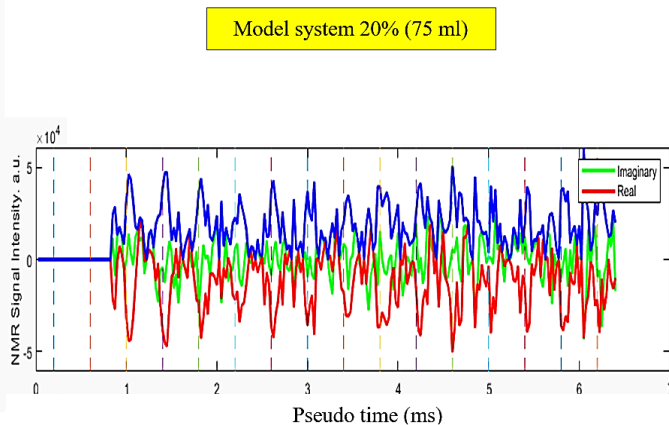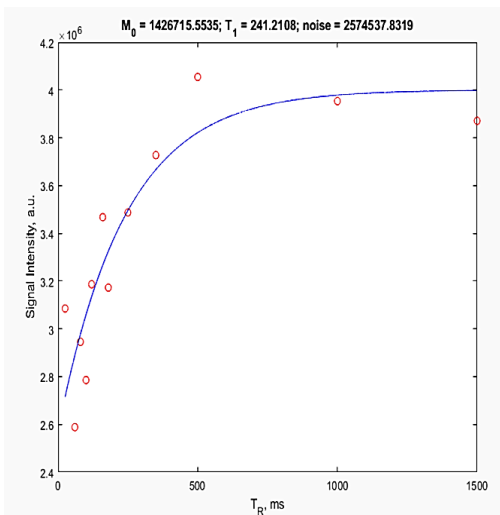
Appendix T

Matlab Code used for CPMG sequence

```matlab
function varargout= CPMG_GUI67(varargin)

% CPMG_GUI67 M-file for CPMG_GUI67.fig
%      CPMG_GUI67, by itself, creates a new CPMG_GUI67 or raises the
existing
%      singleton*.
%7
%      H = CPMG_GUI67 returns the handle to a new CPMG_GUI67 or the
handle to
%      the existing singleton*.
%
%      CPMG_GUI67('CALLBACK',hObject,eventData,handles,...) calls the
local
%      function named CALLBACK in CPMG_GUI67.M with the given input
arguments.
%
%      CPMG_GUI67('Property','Value',...) creates a new CPMG_GUI67 or
raises the
%      existing singleton*.  Starting from the left, property value
pairs are
%      applied to the GUI before CPMG_GUI3_OpeningFunction gets
called.  An
%      unrecognized property name or invalid value makes property
application
%      stop.  All inputs are passed to CPMG_GUI67_OpeningFcn via
varargin.
%
%      *See GUI Options on GUIDE's Tools menu.  Choose "GUI allows
only one
%      instance to run (singleton)".
%
% See also: GUIDE, GUIDATA, GUIHANDLES

% Edit the above text to modify the response to help CPMG_GUI67

% Last Modified by GUIDE v2.5 27-Jan-2020 12:05:08

% Begin initialization code - DO NOT EDIT
gui_Singleton = 1;
gui_State = struct('gui_Name',       mfilename, ...
                   'gui_Singleton',  gui_Singleton, ...
                   'gui_OpeningFcn', @CPMG_GUI67_OpeningFcn, ...
                   'gui_OutputFcn',  @CPMG_GUI67_OutputFcn, ...
                   'gui_LayoutFcn',  [] , ...
                   'gui_Callback',   []);
if nargin && ischar(varargin{1})
    gui_State.gui_Callback = str2func(varargin{1});
end

if nargout
    [varargout{1:nargout}] = gui_mainfcn(gui_State, varargin{:});
else
    gui_mainfcn(gui_State, varargin{:});
end
% End initialization code - DO NOT EDIT

% --- Executes just before CPMG_GUI67 is made visible.

function CPMG_GUI67_OpeningFcn(hObject, eventdata, handles, varargin)
% This function has no output args, see OutputFcn.
```

```matlab
% hObject    handle to figure
% eventdata  reserved - to be defined in a future version of MATLAB
% handles    structure with handles and user data (see GUIDATA)
% varargin   command line arguments to CPMG_GUI67 (see VARARGIN)

% Choose default command line output for CPMG_GUI67
handles.output = hObject;

% Update handles structure
guidata(hObject, handles);

% UIWAIT makes CPMG_GUI67 wait for user response (see UIRESUME)
% uiwait(handles.figure1);

% --- Outputs from this function are returned to the command line.
function varargout = CPMG_GUI67_OutputFcn(hObject, eventdata, handles)
% varargout  cell array for returning output args (see VARARGOUT);
% hObject    handle to figure
% eventdata  reserved - to be defined in a future version of MATLAB
% handles    structure with handles and user data (see GUIDATA)

% Get default command line output from handles structure
varargout{1} = handles.output;

function PPEbox_Callback(hObject, eventdata, handles)
% hObject    handle to PPEbox (see GCBO)
% eventdata  reserved - to be defined in a future version of MATLAB
% handles    structure with handles and user data (see GUIDATA)

% Hints: get(hObject,'String') returns contents of PPEbox as text
%        str2double(get(hObject,'String')) returns contents of PPEbox
as a double

% --- Executes during object creation, after setting all properties.
function PPEbox_CreateFcn(hObject, eventdata, handles)
% hObject    handle to PPEbox (see GCBO)
% eventdata  reserved - to be defined in a future version of MATLAB
% handles    empty - handles not created until after all CreateFcns
called

% Hint: edit controls usually have a white background on Windows.
%       See ISPC and COMPUTER.
if ispc && isequal(get(hObject,'BackgroundColor'),
get(0,'defaultUicontrolBackgroundColor'))
    set(hObject,'BackgroundColor','white');
end

function ADCbox_Callback(hObject, eventdata, handles)
% hObject    handle to ADCbox (see GCBO)
% eventdata  reserved - to be defined in a future version of MATLAB
% handles    structure with handles and user data (see GUIDATA)

% Hints: get(hObject,'String') returns contents of ADCbox as text
%        str2double(get(hObject,'String')) returns contents of ADCbox
as a double
% --- Executes during object creation, after setting all properties.
function ADCbox_CreateFcn(hObject, eventdata, handles)
% hObject    handle to ADCbox (see GCBO)
% eventdata  reserved - to be defined in a future version of MATLAB
```

216

```matlab
% handles    empty - handles not created until after all CreateFcns
called

% Hint: edit controls usually have a white background on Windows.
%        See ISPC and COMPUTER.
if ispc && isequal(get(hObject,'BackgroundColor'),
get(0,'defaultUicontrolBackgroundColor'))
    set(hObject,'BackgroundColor','white');
end

function NMRfbox_Callback(hObject, eventdata, handles)
% hObject    handle to NMRfbox (see GCBO)
% eventdata  reserved - to be defined in a future version of MATLAB
% handles    structure with handles and user data (see GUIDATA)

% Hints: get(hObject,'String') returns contents of NMRfbox as text
%        str2double(get(hObject,'String')) returns contents of NMRfbox
as a double

% --- Executes during object creation, after setting all properties.
function NMRfbox_CreateFcn(hObject, eventdata, handles)
% hObject    handle to NMRfbox (see GCBO)
% eventdata  reserved - to be defined in a future version of MATLAB
% handles    empty - handles not created until after all CreateFcns
called

% Hint: edit controls usually have a white background on Windows.
%        See ISPC and COMPUTER.
if ispc && isequal(get(hObject,'BackgroundColor'),
get(0,'defaultUicontrolBackgroundColor'))
    set(hObject,'BackgroundColor','white');
end

function DTbox_Callback(hObject, eventdata, handles)
% hObject    handle to DTbox (see GCBO)
% eventdata  reserved - to be defined in a future version of MATLAB
% handles    structure with handles and user data (see GUIDATA)

% Hints: get(hObject,'String') returns contents of DTbox as text
%        str2double(get(hObject,'String')) returns contents of DTbox
as a double

% --- Executes during object creation, after setting all properties.
function DTbox_CreateFcn(hObject, eventdata, handles)
% hObject    handle to DTbox (see GCBO)
% eventdata  reserved - to be defined in a future version of MATLAB
% handles    empty - handles not created until after all CreateFcns
called

% Hint: edit controls usually have a white background on Windows.
%        See ISPC and COMPUTER.
if ispc && isequal(get(hObject,'BackgroundColor'),
get(0,'defaultUicontrolBackgroundColor'))
    set(hObject,'BackgroundColor','white');
end
 function ninetybox_Callback(hObject, eventdata, handles)
% hObject    handle to ninetybox (see GCBO)
% eventdata  reserved - to be defined in a future version of MATLAB
% handles    structure with handles and user data (see GUIDATA)
```

```matlab
% Hints: get(hObject,'String') returns contents of ninetybox as text
%        str2double(get(hObject,'String')) returns contents of
ninetybox as a double


% --- Executes during object creation, after setting all properties.
function ninetybox_CreateFcn(hObject, eventdata, handles)
% hObject    handle to ninetybox (see GCBO)
% eventdata  reserved - to be defined in a future version of MATLAB
% handles    empty - handles not created until after all CreateFcns
called


% Hint: edit controls usually have a white background on Windows.
%       See ISPC and COMPUTER.
if ispc && isequal(get(hObject,'BackgroundColor'),
get(0,'defaultUicontrolBackgroundColor'))
    set(hObject,'BackgroundColor','white');
end


function PSbox_Callback(hObject, eventdata, handles)
% hObject    handle to PSbox (see GCBO)
% eventdata  reserved - to be defined in a future version of MATLAB
% handles    structure with handles and user data (see GUIDATA)


% Hints: get(hObject,'String') returns contents of PSbox as text
%        str2double(get(hObject,'String')) returns contents of PSbox
as a double


% --- Executes during object creation, after setting all properties.
function PSbox_CreateFcn(hObject, eventdata, handles)
% hObject    handle to PSbox (see GCBO)
% eventdata  reserved - to be defined in a future version of MATLAB
% handles    empty - handles not created until after all CreateFcns
called


% Hint: edit controls usually have a white background on Windows.
%       See ISPC and COMPUTER.
if ispc && isequal(get(hObject,'BackgroundColor'),
get(0,'defaultUicontrolBackgroundColor'))
    set(hObject,'BackgroundColor','white');
end


function NEbox_Callback(hObject, eventdata, handles)
% hObject    handle to NEbox (see GCBO)
% eventdata  reserved - to be defined in a future version of MATLAB
% handles    structure with handles and user data (see GUIDATA)


% Hints: get(hObject,'String') returns contents of NEbox as text
%        str2double(get(hObject,'String')) returns contents of NEbox
as a double


% --- Executes during object creation, after setting all properties.
function NEbox_CreateFcn(hObject, eventdata, handles)
% hObject    handle to NEbox (see GCBO)
% eventdata  reserved - to be defined in a future version of MATLAB
% handles    empty - handles not created until after all CreateFcns
called


% Hint: edit controls usually have a white background on Windows.
```

```matlab
%       See ISPC and COMPUTER.
if ispc && isequal(get(hObject,'BackgroundColor'),
get(0,'defaultUicontrolBackgroundColor'))
    set(hObject,'BackgroundColor','white');
end


function TEbox_Callback(hObject, eventdata, handles)
% hObject    handle to NEbox (see GCBO)
% eventdata  reserved - to be defined in a future version of MATLAB
% handles    structure with handles and user data (see GUIDATA)

% Hints: get(hObject,'String') returns contents of NEbox as text
%        str2double(get(hObject,'String')) returns contents of NEbox
as a double


% --- Executes during object creation, after setting all properties.
function TEbox_CreateFcn(hObject, eventdata, handles)
% hObject    handle to NEbox (see GCBO)
% eventdata  reserved - to be defined in a future version of MATLAB
% handles    empty - handles not created until after all CreateFcns
called

% Hint: edit controls usually have a white background on Windows.
%       See ISPC and COMPUTER.
if ispc && isequal(get(hObject,'BackgroundColor'),
get(0,'defaultUicontrolBackgroundColor'))
    set(hObject,'BackgroundColor','white');
end


function NRbox_Callback(hObject, eventdata, handles)
% hObject    handle to NRbox (see GCBO)
% eventdata  reserved - to be defined in a future version of MATLAB
% handles    structure with handles and user data (see GUIDATA)

% Hints: get(hObject,'String') returns contents of NRbox as text
%        str2double(get(hObject,'String')) returns contents of NRbox
as a double
% --- Executes during object creation, after setting all properties.
function NRbox_CreateFcn(hObject, eventdata, handles)
% hObject    handle to NRbox (see GCBO)
% eventdata  reserved - to be defined in a future version of MATLAB
% handles    empty - handles not created until after all CreateFcns
called

% Hint: edit controls usually have a white background on Windows.
%       See ISPC and COMPUTER.
if ispc && isequal(get(hObject,'BackgroundColor'),
get(0,'defaultUicontrolBackgroundColor'))
    set(hObject,'BackgroundColor','white');
end


function TRbox_Callback(hObject, eventdata, handles)
% hObject    handle to TRbox (see GCBO)
% eventdata  reserved - to be defined in a future version of MATLAB
% handles    structure with handles and user data (see GUIDATA)

% Hints: get(hObject,'String') returns contents of TRbox as text
% str2double(get(hObject,'String')) returns contents of TRbox as a
double
```

```matlab
% --- Executes during object creation, after setting all properties.

function TRbox_CreateFcn(hObject, eventdata, handles)
% hObject    handle to TRbox (see GCBO)
% eventdata  reserved - to be defined in a future version of MATLAB
% handles    empty - handles not created until after all CreateFcns
called

% Hint: edit controls usually have a white background on Windows.
%       See ISPC and COMPUTER.
if ispc && isequal(get(hObject,'BackgroundColor'),
get(0,'defaultUicontrolBackgroundColor'))
    set(hObject,'BackgroundColor','white');
end

function Ampbox_Callback(hObject, eventdata, handles)
% hObject    handle to Ampbox (see GCBO)
% eventdata  reserved - to be defined in a future version of MATLAB
% handles    structure with handles and user data (see GUIDATA)

% Hints: get(hObject,'String') returns contents of Ampbox as text
%        str2double(get(hObject,'String')) returns contents of Ampbox
as a double

% --- Executes during object creation, after setting all properties.
function Ampbox_CreateFcn(hObject, eventdata, handles)
% hObject    handle to Ampbox (see GCBO)
% eventdata  reserved - to be defined in a future version of MATLAB
% handles    empty - handles not created until after all CreateFcns
called

% Hint: edit controls usually have a white background on Windows.
%       See ISPC and COMPUTER.
if ispc && isequal(get(hObject,'BackgroundColor'),
get(0,'defaultUicontrolBackgroundColor'))
    set(hObject,'BackgroundColor','white');
end

% --- Executes on button press in pushbutton1.
function pushbutton1_Callback(hObject, eventdata, handles)
% hObject    handle to pushbutton1 (see GCBO)
% eventdata  reserved - to be defined in a future version of MATLAB
% handles    structure with handles and user data (see GUIDATA)
    %Get sequence parameters from GUI
        iSpin_Defines;
        get_params;
%Run sequence
        [real_no_clip_res, imag_no_clip_res, tax, dwell_time] =
CPMGPS_GUI_Blank_Composite({get(handles.ADCbox,'String'),
get(handles.PSbox,'String'), get(handles.NMRfbox,'String'),
get(handles.DTbox,'String'), get(handles.ninetybox,'String'),
get(handles.NEbox,'String'), get(handles.TEbox,'String'),
get(handles.NRbox,'String'), get(handles.TRbox,'String'),
get(handles.Ampbox,'String'), get(handles.PPEbox,'String'),
get(handles.blankbox,'String'), shp, dbls, filtert}, handles);
        if(exist('DE'))
            if(DE>0)
                real_no_clip_res(1:(PPE*DE)) = 0;
                imag_no_clip_res(1:(PPE*DE)) = 0;
            end
```

```
            end

axes(handles.axes2)
            comp =
double(real_no_clip_res)+i*double(imag_no_clip_res);
            %Work out spectral x axis
            xax = 1E-8/Spectral_Width/length(comp)*((-
length(comp)/2):((length(comp)/2))-1);
            plot(xax,
fftshift(fft(comp).*conj(fft(comp))/length(comp)), 'LineWidth', 2)
            set(gca, 'XTickLabel', get(gca, 'XTick'));
            title('NMR Signal - Power Spectral Density')
            xlabel('Frequency, MHz')
            ylabel('NMR Signal Intensity. a.u.')
axes(handles.axes3)
            real_no_clip = reshape(real_no_clip_res, PPE, NE);
            imagesc(real_no_clip)
            title('Real')
            axis off


axes(handles.axes4)
            imag_no_clip = reshape(imag_no_clip_res, PPE, NE);
            imagesc(imag_no_clip)
            title('Imaginary')
            axis off


axes(handles.axes5)

imagesc(abs(double(real_no_clip)+i*double(imag_no_clip)))
            title('Modulus')
            axis off


axes(handles.axes1)
            mod_no_clip_res =
reshape(abs(double(real_no_clip_res)+i*double(imag_no_clip_res)),
PPE*NE, 1);
            %work out time axis in ms

tax=((1:length(real_no_clip_res)).*dwell_time).*1E3;
                size((real_no_clip_res))
                size(tax)
                size(imag_no_clip_res)
                plot(tax, imag_no_clip_res, 'g', 'LineWidth', 2)
                hold on
                plot(tax, real_no_clip_res, 'r', 'LineWidth', 2)
                plot(tax, mod_no_clip_res, 'b', 'LineWidth', 1)

                addlines
                 hold off
                legend('Imaginary', 'Real')
                title('NMR Signal - Time Domain')
                xlabel('Time, ms')
                ylabel('NMR Signal Intensity. a.u.')

                do_assigns;
```

```matlab
% --- Executes on button press in pushbutton2.
function pushbutton2_Callback(hObject, eventdata, handles)
% hObject    handle to pushbutton2 (see GCBO)
% eventdata  reserved - to be defined in a future version of MATLAB
% handles    structure with handles and user data (see GUIDATA)

iSpin_Defines;
get_params;

%Function to export the data
[fname, pathname] = uiputfile('*.csv', 'Please select location to save
data...');

fn = strsplit(fname, '.');

floc = [pathname, fn{1}, 'raw.csv'];

tax = evalin('base', 'tax');
imag_no_clip_res = evalin('base', 'imag_no_clip_res');
real_no_clip_res = evalin('base', 'real_no_clip_res');

integs =
sum(reshape(abs(double(real_no_clip_res)+i*double(imag_no_clip_res)),
PPE, NE));

dat = [tax', double(imag_no_clip_res), double(real_no_clip_res),
abs(double(real_no_clip_res)+i*double(imag_no_clip_res))];

csvwrite(floc, dat);

floci = [pathname, fn{1}, 'ints.csv'];

dat = [tau.*(1:NE)', integs'];

csvwrite(floci, dat);


if exist(floc)
    msgbox(['Data writen succesfully to ' floc ' :-)']);
else
    msgbox(['Data write failed to ' floc ' :-{']);
end

 function RepN_Callback(hObject, eventdata, handles)
% hObject    handle to RepN (see GCBO)
% eventdata  reserved - to be defined in a future version of MATLAB
% handles    structure with handles and user data (see GUIDATA)

% Hints: get(hObject,'String') returns contents of RepN as text
%        str2double(get(hObject,'String')) returns contents of RepN as
a double

% --- Executes during object creation, after setting all properties.
function RepN_CreateFcn(hObject, eventdata, handles)
% hObject    handle to RepN (see GCBO)
% eventdata  reserved - to be defined in a future version of MATLAB
% handles    empty - handles not created until after all CreateFcns
called
```

```matlab
% Hint: edit controls usually have a white background on Windows.
%       See ISPC and COMPUTER.
if ispc && isequal(get(hObject,'BackgroundColor'),
get(0,'defaultUicontrolBackgroundColor'))
    set(hObject,'BackgroundColor','white');
end


% --- Executes on button press in Cal_90_Button. - Calibrate 90
function Cal_90_Button_Callback(hObject, eventdata, handles)
% hObject     handle to Cal_90_Button (see GCBO)
% eventdata   reserved - to be defined in a future version of MATLAB
% handles     structure with handles and user data (see GUIDATA)

%Set up the parameters from the interface
    iSpin_Defines;
    get_params;

%Get the range of 90 values from the user with a popup
Nin = inputdlg({'Minimum 90', 'Number of 90s', 'Maximum 90', 'Save
Location'}, 'Please Enter Sequence Parameters...', 1, {'5', '5', '20',
'c:\student\cal90.csv'});
%and convert to numbers
minN = str2num(Nin{1});
maxN = str2num(Nin{3});
NN = str2num(Nin{2});
diffN = ((maxN-minN)/(NN-1));
Ns = minN:diffN:maxN;

%For each of the 90s
for f = 1:NN
    %Get the current value
    N = Ns(f);
    %Update the GUI
    set(handles.ninetybox,'String', num2str(N));
    %Run the sequence
    [real_no_clip_res, imag_no_clip_res, tax, dwell_time] =
CPMGPS_GUI_Blank_Composite({get(handles.ADCbox,'String'),
get(handles.PSbox,'String'), get(handles.NMRfbox,'String'),
get(handles.DTbox,'String'), num2str(N), get(handles.NEbox,'String'),
get(handles.TEbox,'String'), get(handles.NRbox,'String'),
get(handles.TRbox,'String'), get(handles.Ampbox,'String'),
get(handles.PPEbox,'String'), get(handles.blankbox,'String'), shp,
dbls, filtert}, handles);

    %Update the gui plots
    update_plots;

    %Calculate the amplitude of the modulus
    dataout(f) = sum(sum(double(mod_no_clip(floor((PPE/2)-
3):floor((PPE/2)+3), :))));

    %Update the parameters in the base workspace
    do_assigns;

    %Plot a new figure with the results in
    figure(1)
    plot(Ns(1:f)*1E-6, dataout, 'ro')
```

223

```matlab
    xlabel('90 Duration, \mus')
    ylabel('Sum of Signal Intensity, a.u.')

end

 %sanitise the storage information
    [pathname, fname, extname]=fileparts(Nin{4});

    datenow = datestr(datetime('now'), 'yyyy_MM_dd_HH_mm_ss');
    flocs = [pathname, '\', fname, '_', datenow, extname];

    dat = [Ns; dataout];

    csvwrite(flocs, dat');

    if exist(flocs)
        msgbox(['Data writen succesfully to ' flocs ' :-)']);
    else
        msgbox(['Data write failed to ' flocs ' :-{']);
    end

% --- Executes on button press in T1_Button.
function T1_Button_Callback(hObject, eventdata, handles)
% hObject    handle to T1_Button (see GCBO)
% eventdata  reserved - to be defined in a future version of MATLAB
% handles    structure with handles and user data (see GUIDATA)

%Measure T_1
 %Set up the parameters from the interface
    iSpin_Defines;
    get_params;
 %Get the range of rep times from the user with a popup
TRin = inputdlg({'Minimum TR', 'Number of TRs', 'Maximum TR', 'Save
Location'}, 'Please Enter Sequence Parameters...', 1, {'50', '5',
'2000', 'c:\student\T1data.csv'});
minTR = str2num(TRin{1});
maxTR = str2num(TRin{3});
NTR = str2num(TRin{2});
diffTR = ((maxTR-minTR)/(NTR-1));
TRs = minTR:diffTR:maxTR;
TRlist = inputdlg({'TR List'}, 'Please confirm TR Values...', 1,
{num2str(TRs)});
TRs = str2num(string(TRlist));
%sanitise the storage information
[pathname, fname, extname]=fileparts(TRin{4});
%For each of the rep times
for f = 1:NTR
    %Get the current value
    TR = TRs(f);
    %Update the GUI
    set(handles.TRbox,'String', num2str(TR));

 %Run the sequence
 [real_no_clip_res, imag_no_clip_res, tax, dwell_time] =
CPMGPS_GUI_Blank_Composite({get(handles.ADCbox,'String'),
get(handles.PSbox,'String'), get(handles.NMRfbox,'String'),
get(handles.DTbox,'String'), get(handles.ninetybox,'String'),
get(handles.NEbox,'String'), get(handles.TEbox,'String'),
get(handles.NRbox,'String'), num2str(TR),
```

```matlab
        get(handles.Ampbox,'String'), get(handles.PPEbox,'String'),
        get(handles.blankbox,'String'), shp, dbls, filtert}, handles);
            if(exist('DE'))
                    if(DE>0)
                        real_no_clip_res(1:(PPE*DE)) = 0;
                        imag_no_clip_res(1:(PPE*DE)) = 0;
                    end
                end

        %Update the gui plots
        update_plots;

        %Calculate the amplitude of the modulus
        TRdataout(f) = sum(sum(double(mod_no_clip(floor((PPE/2)-
6):floor((PPE/2)+6), :)))));

        %Update the parameters in the base workspace
        do_assigns;

        %Plot a new figure with the results in
        figure(1)
        hold off
        plot(TRs(1:f), TRdataout, 'ro')

        %temporarily store the information
        save('c:\student\T1tmp.mat')

    end

    guess = [max(TRdataout), min(TRs), min(TRdataout)];

    [x, fval, exitflag] = fminsearch(@leastsqs_T1, guess,
    optimset('maxiter', 10000, 'maxfunevals', 10000), TRdataout, TRs);

    size(TRdataout)
    size(TRs)
    size(x)
    size([x, zeros(1, length(TRdataout)-length(x))])
    dat = [TRdataout; TRs]%; [x, zeros(1, length(TRdataout)-length(x))]];

    assignin('base', 'T1fitparams', x);
    assignin('base', 'dat', dat);
    hold on
    plot(min(TRs):.1:max(TRs), abs((x(1).*(1-exp(-
(min(TRs):.1:max(TRs))./x(2)))+x(3))), 'b')
    hold off
    xlabel('T_R, ms')
    title(['M_0 = ' num2str(x(1)) '; T_1 = ' num2str(x(2)) '; noise = '
num2str(x(3))])
    ylabel('Signal Intensity, a.u.')
    %Save results

    %append the datetime
    datenow = datestr(datetime('now'), 'yyyy_MM_dd_HH_mm_ss');
    flocs = [pathname, '\', fname, datenow, extname];

    csvwrite(flocs, dat');

    if exist(flocs)
```

```matlab
        msgbox(['Data writen succesfully to ' flocs ' :-)']);
    else
        msgbox(['Data write failed to ' flocs ' :-{']);
    end


    % --- Executes on button press in T2_Button.
    function T2_Button_Callback(hObject, eventdata, handles)
    % hObject    handle to T2_Button (see GCBO)
    % eventdata  reserved - to be defined in a future version of MATLAB
    % handles    structure with handles and user data (see GUIDATA)
    %Set up the parameters from the interface
        iSpin_Defines;
        get_params;

    TEin = inputdlg({'Minimum TE', 'Number of TEs', 'Maximum TE',
    'Integration Width', 'Save Location'}, 'Please Enter Sequence
    Parameters...', 1, {'1000', '5', '10000', '4',
    'c:\student\T2data.csv'});
    minTE = str2num(TEin{1});
    maxTE = str2num(TEin{3});
    NTE = str2num(TEin{2});
    diffTE = ((maxTE-minTE)/(NTE-1));
    TEs = minTE:diffTE:maxTE;
    TElist = inputdlg({'TE List'}, 'Please confirm TE Values...', 1,
    {num2str(TEs)});
    TEs = str2num(string(TElist));
    wid = floor(str2num(TEin{4})/2);

    %sanitise the storage information
    [pathname, fname, extname]=fileparts(TEin{5});

    %For each of the rep times
    for f = 1:NTE
        %Get the current value
        TE = TEs(f);
        %Update the GUI
        set(handles.TEbox,'String', num2str(TE));
        %Run the sequence
        [real_no_clip_res, imag_no_clip_res, tax, dwell_time] =
    CPMGPS_GUI_Blank_Composite({get(handles.ADCbox,'String'),
    get(handles.PSbox,'String'), get(handles.NMRfbox,'String'),
    get(handles.DTbox,'String'), get(handles.ninetybox,'String'),
    get(handles.NEbox,'String'), num2str(TE), get(handles.NRbox,'String'),
    get(handles.TRbox,'String'), get(handles.Ampbox,'String'),
    get(handles.PPEbox,'String'), get(handles.blankbox,'String'), shp,
    dbls, filtert}, handles);

        if(exist('DE'))
            if(DE>0)
            real_no_clip_res(1:(DE*PPE)) = 0;
            imag_no_clip_res(1:(DE*PPE)) = 0;
            end
        end
        mod_no_clip_res =
    reshape(abs(double(real_no_clip_res)+i*double(imag_no_clip_res)),
    PPE*NE, 1);
        %Update the gui plots
        update_plots;
```

```matlab
        %Calculate the amplitude of the modulus
        TEdataout(f) = mean(mean(double(mod_no_clip(floor((PPE/2)-
wid):floor((PPE/2)+wid), :)))));

        %Update the parameters in the base workspace
        do_assigns;

        %Plot a new figure with the results in
        figure(1)
        hold off
        plot(TEs(1:f), TEdataout, 'ro')

        %temporarily store the information
        save('c:\student\T2tmp.mat')

end


guess = [max(TEdataout), min(TEs), min(TEdataout)];


[x, fval, exitflag] = fminsearch(@T2_fit_offset, guess,
optimset('maxiter', 10000, 'maxfunevals', 10000), TEdataout, TEs);


dat = [TEdataout; TEs]%; [x, zeros(1, length(TRdataout)-length(x))]];


assignin('base', 'T2fitparams', x);
assignin('base', 'dat', dat);
hold on
plot(min(TEs):.1:max(TEs), x(1).*exp(-
((min(TEs):.1:max(TEs))./x(2)))+x(3), 'b')
hold off
xlabel('T_E, ms')
ylabel('Signal Intensity, a.u.')
title(['M_0 = ' num2str(x(1)) '; T_2 = ' num2str(x(2)) '; noise = '
num2str(x(3))])
%Save results

%append the datetime
datenow = datestr(datetime('now'), 'yyyy_MM_dd_HH_mm_ss');
flocs = [pathname, '\', fname, datenow, extname];


csvwrite(flocs, dat');


if exist(flocs)
    msgbox(['Data writen succesfully to ' flocs ' :-)']);
else
    msgbox(['Data write failed to ' flocs ' :-{']);
end

% --- Executes on button press in Diffusion_Button.
function Diffusion_Button_Callback(hObject, eventdata, handles)
% hObject    handle to Diffusion_Button (see GCBO)
% eventdata  reserved - to be defined in a future version of MATLAB
% handles    structure with handles and user data (see GUIDATA)

    iSpin_Defines;
        adc_freq = str2num(get(handles.ADCbox,'String'));
        P1_phase_OS = str2num(get(handles.PSbox,'String'));
        NMR_Frequency = str2num(get(handles.NMRfbox,'String'));
        Spectral_Width = 1/str2num(get(handles.DTbox,'String'))*1E-6;
```

227

```matlab
            pulse_length_90 = str2num(get(handles.ninetybox,'String'))*us;
            pulse_length_180 = 2*pulse_length_90;
            NE = 1;
            set(handles.NEbox,'String', '1');
            tau = str2num(get(handles.TEbox,'String'));
            NR = str2num(get(handles.NRbox,'String'));
            TR = str2num(get(handles.TRbox,'String'));
            Amp = str2num(get(handles.Ampbox,'String'));
            Amp = (.1/115)*Amp;
            PPE = str2num(get(handles.PPEbox,'String'));

            ring = 50;
            shift = 0;

 TRin = inputdlg({'Minimum TE', 'Number of TEs', 'Maximum TE'},
'Please Enter Sequence Parameters...', 1, {'100', '6', '2000'});
minTE = str2num(TRin{1});
maxTE = str2num(TRin{3});
NTE = str2num(TRin{2});
diffTE = ((maxTE-minTE)/(NTE-1));
TEs = minTE:diffTE:maxTE;

for f = 1:NTE
    TE = TEs(f);
    set(handles.TEbox,'String', num2str(TE));
    [real_no_clip_res, imag_no_clip_res, tax, dwell_time] =
CPMGPS_MOUSE_AMPPS_with_amp_func_echo_window_gui_new({get(handles.ADCb
ox,'String'), get(handles.PSbox,'String'),
get(handles.NMRfbox,'String'), get(handles.DTbox,'String'),
get(handles.ninetybox,'String'), get(handles.NEbox,'String'),
num2str(TE), get(handles.NRbox,'String'), get(handles.TRbox,'String'),
get(handles.Ampbox,'String'), get(handles.PPEbox,'String')}, handles);
    axes(handles.axes2)
                comp =
double(real_no_clip_res)+i*double(imag_no_clip_res);
                %Work out spectral x axis
                    xax = 1E-6./Spectral_Width/length(comp)*((-
length(comp)/2):((length(comp)/2))-1);
                plot(xax,
fftshift(fft(comp).*conj(fft(comp))/length(comp)), 'LineWidth', 2)
                title('NMR Signal - Power Spectral Density')
                xlabel('Frequency, Hz')
                ylabel('NMR Signal Intensity. a.u.')
axes(handles.axes3)
                real_no_clip = reshape(real_no_clip_res, PPE, NE);
                imagesc(real_no_clip)
                title('Real')
                axis off

axes(handles.axes4)
                imag_no_clip = reshape(imag_no_clip_res, PPE, NE);
                imagesc(imag_no_clip)
                title('Imaginary')
                axis off

axes(handles.axes5)

imagesc(abs(double(real_no_clip)+i*double(imag_no_clip)))
                title('Modulus')
                axis off
```

```
axes(handles.axes1)
                %work out time axis in ms
                    tax=(1:(length(real_no_clip_res))*dwell_time)*1E3;
                    plot(tax, imag_no_clip_res, 'g', 'LineWidth', 2)
                    hold on
                    plot(tax, real_no_clip_res, 'r', 'LineWidth', 2)
                    hold off
                    legend('Imaginary', 'Real')
                    title('NMR Signal - Time Domain')
                    xlabel('Time, ms')
                    ylabel('NMR Signal Intensity. a.u.')

    dataout(f) =
sum(abs(double(real_no_clip_res)+i.*double(imag_no_clip_res)));
    %dataout(f) =
max(fftshift(fft(comp).*conj(fft(comp))/length(comp)));
    assignin('base', 'dataout', dataout);
    assignin('base', 'TEs', TEs);
    figure(1)
    plot(TEs(1:f)*1E-6, dataout, 'ro')

    start_T2 = 6e-3;
    start_Do = 2e-9;
    start_Mo = dataout(1);
    start_noise = start_Mo/10;

    params = fminsearch('Do_fit',[start_Mo start_T2 start_Do
start_noise],[],dataout,TEs(1:f)*1e-6);
        start_T2 = params(2);
        start_noise = params(4);
        start_Mo = params(1);
        start_Do = params(3);
        params3_array(f) = params(3);
        params2_array(f) = params(2);
        figure(1)
        hold on
        TE_theoretical = 1e-6*(0:(TEs(f)/200):TEs(f));
        plot(TE_theoretical,params(4) + params(1)*exp(-
(1/params(2))*TE_theoretical -
(params(3)*((2.67e8)^2)*((1)^2))*(1/12)*((TE_theoretical).^3)),'k')
        legend(['fitted D_o = ',num2str(params(3))])
        xlabel('T_E (s)')
        ylabel('Hahn echo')

        figure(2)
        clf
        subplot(2,1,1)
        plot(params3_array,'ro')

        xlabel('experiment')
        ylabel('evolution of fitted D_o')

        subplot(2,1,2)
        plot(params2_array,'ko')
         xlabel('experiment')
        ylabel('evolution of fitted T_2')

end
```

```matlab
% --- Executes during object creation, after setting all properties.
function axes1_CreateFcn(hObject, eventdata, handles)
% hObject    handle to axes1 (see GCBO)
% eventdata  reserved - to be defined in a future version of MATLAB
% handles    empty - handles not created until after all CreateFcns
called

% Hint: place code in OpeningFcn to populate axes1


% --- Executes during object creation, after setting all properties.
function axes2_CreateFcn(hObject, eventdata, handles)
% hObject    handle to axes1 (see GCBO)
% eventdata  reserved - to be defined in a future version of MATLAB
% handles    empty - handles not created until after all CreateFcns
called

% Hint: place code in OpeningFcn to populate axes1


 function blankbox_Callback(hObject, eventdata, handles)
% hObject    handle to blankbox (see GCBO)
% eventdata  reserved - to be defined in a future version of MATLAB
% handles    structure with handles and user data (see GUIDATA)

% Hints: get(hObject,'String') returns contents of blankbox as text
%        str2double(get(hObject,'String')) returns contents of
blankbox as a double

% --- Executes during object creation, after setting all properties.
function blankbox_CreateFcn(hObject, eventdata, handles)
% hObject    handle to blankbox (see GCBO)
% eventdata  reserved - to be defined in a future version of MATLAB
% handles    empty - handles not created until after all CreateFcns
called

% Hint: edit controls usually have a white background on Windows.
%       See ISPC and COMPUTER.
if ispc && isequal(get(hObject,'BackgroundColor'),
get(0,'defaultUicontrolBackgroundColor'))
    set(hObject,'BackgroundColor','white');
end

% --- Executes on selection change in Pulse_Type.

function Pulse_Type_Callback(hObject, eventdata, handles)
% hObject    handle to Pulse_Type (see GCBO)
% eventdata  reserved - to be defined in a future version of MATLAB
% handles    structure with handles and user data (see GUIDATA)

% Hints: contents = cellstr(get(hObject,'String')) returns Pulse_Type
contents as cell array
% contents{get(hObject,'Value')} returns selected item from Pulse_Type

% --- Executes during object creation, after setting all properties.

function Pulse_Type_CreateFcn(hObject, eventdata, handles)
% hObject    handle to Pulse_Type (see GCBO)
% eventdata  reserved - to be defined in a future version of MATLAB
```

```matlab
% handles    empty - handles not created until after all CreateFcns
called

% Hint: popupmenu controls usually have a white background on Windows.
%        See ISPC and COMPUTER.
if ispc && isequal(get(hObject,'BackgroundColor'),
get(0,'defaultUicontrolBackgroundColor'))
    set(hObject,'BackgroundColor','white');
end

% --- Executes on selection change in Type_180.
function Type_180_Callback(hObject, eventdata, handles)
% hObject    handle to Type_180 (see GCBO)
% eventdata  reserved - to be defined in a future version of MATLAB
% handles    structure with handles and user data (see GUIDATA)

% Hints: contents = cellstr(get(hObject,'String')) returns Type_180
contents as cell array
%        contents{get(hObject,'Value')} returns selected item from
Type_180

% --- Executes during object creation, after setting all properties.
function Type_180_CreateFcn(hObject, eventdata, handles)
% hObject    handle to Type_180 (see GCBO)
% eventdata  reserved - to be defined in a future version of MATLAB
% handles    empty - handles not created until after all CreateFcns
called

% Hint: popupmenu controls usually have a white background on Windows.
%        See ISPC and COMPUTER.
if ispc && isequal(get(hObject,'BackgroundColor'),
get(0,'defaultUicontrolBackgroundColor'))
    set(hObject,'BackgroundColor','white');
end

% --- Executes on selection change in FilterType.
function FilterType_Callback(hObject, eventdata, handles)
% hObject    handle to FilterType (see GCBO)
% eventdata  reserved - to be defined in a future version of MATLAB
% handles    structure with handles and user data (see GUIDATA)

% Hints: contents = cellstr(get(hObject,'String')) returns FilterType
contents as cell array
%        contents{get(hObject,'Value')} returns selected item from
FilterType

% --- Executes during object creation, after setting all properties.
function FilterType_CreateFcn(hObject, eventdata, handles)
% hObject    handle to FilterType (see GCBO)
% eventdata  reserved - to be defined in a future version of MATLAB
% handles    empty - handles not created until after all CreateFcns
called

% Hint: popupmenu controls usually have a white background on Windows.
% See ISPC and COMPUTER.
if ispc && isequal(get(hObject,'BackgroundColor'),
get(0,'defaultUicontrolBackgroundColor'))
    set(hObject,'BackgroundColor','white');
end
```

```matlab
% --- Executes on button press in EMCheck.
function EMCheck_Callback(hObject, eventdata, handles)
% hObject    handle to EMCheck (see GCBO)
% eventdata  reserved - to be defined in a future version of MATLAB
% handles    structure with handles and user data (see GUIDATA)

% Hint: get(hObject,'Value') returns toggle state of EMCheck
axes(handles.axes1)

addlines

% --- Executes on button press in T2eff_Button.
function T2eff_Button_Callback(hObject, eventdata, handles)
% hObject    handle to T2eff_Button (see GCBO)
% eventdata  reserved - to be defined in a future version of MATLAB
% handles    structure with handles and user data (see GUIDATA)

iSpin_Defines;
get_params;

 %Run sequence
[real_no_clip_res, imag_no_clip_res, tax, dwell_time] =
CPMGPS_GUI_Blank_Composite({get(handles.ADCbox,'String'),
get(handles.PSbox,'String'), get(handles.NMRfbox,'String'),
get(handles.DTbox,'String'), get(handles.ninetybox,'String'),
get(handles.NEbox,'String'), get(handles.TEbox,'String'),
get(handles.NRbox,'String'), get(handles.TRbox,'String'),
get(handles.Ampbox,'String'), get(handles.PPEbox,'String'),
get(handles.blankbox,'String'), shp, dbls, filtert}, handles);
        if(exist('DE'))
            if(DE>0)
                real_no_clip_res(1:(PPE*DE)) = 0;
                imag_no_clip_res(1:(PPE*DE)) = 0;
            end
        end

axes(handles.axes2)
            comp =
double(real_no_clip_res)+i*double(imag_no_clip_res);
            %Work out spectral x axis
            xax = 1E-8/Spectral_Width/length(comp)*((-
length(comp)/2):((length(comp)/2))-1);
            plot(xax,
fftshift(fft(comp).*conj(fft(comp))/length(comp)), 'LineWidth', 2)
            set(gca, 'XTickLabel', get(gca, 'XTick'));
            title('NMR Signal - Power Spectral Density')
            xlabel('Frequency, MHz')
            ylabel('NMR Signal Intensity. a.u.')
axes(handles.axes3)
            real_no_clip = reshape(real_no_clip_res, PPE, NE);
            imagesc(real_no_clip)
            title('Real')
            axis off

axes(handles.axes4)
            imag_no_clip = reshape(imag_no_clip_res, PPE, NE);
            imagesc(imag_no_clip)
            title('Imaginary')
            axis off
```

```
axes(handles.axes5)

imagesc(abs(double(real_no_clip)+i*double(imag_no_clip)))
                title('Modulus')
                axis off

axes(handles.axes1)
                mod_no_clip_res =
reshape(abs(double(real_no_clip_res)+i*double(imag_no_clip_res)),
PPE*NE, 1);
                %work out time axis in ms

tax=((1:length(real_no_clip_res)).*dwell_time).*1E3;
                    size((real_no_clip_res))
                    size(tax)
                    size(imag_no_clip_res)
                    plot(tax, imag_no_clip_res, 'g', 'LineWidth', 2)
                    hold on
                    plot(tax, real_no_clip_res, 'r', 'LineWidth', 2)
                    plot(tax, mod_no_clip_res, 'b', 'LineWidth', 1)

                    addlines

                    hold off
                    legend('Imaginary', 'Real')
                    title('NMR Signal - Time Domain')
                    xlabel('Time, ms')
                    ylabel('NMR Signal Intensity. a.u.')

                    do_assigns;


mod_no_clip_res =
reshape(abs(double(real_no_clip_res)+i*double(imag_no_clip_res)),
PPE*NE, 1);
integs =
sum(reshape(abs(double(real_no_clip_res)+i*double(imag_no_clip_res)),
PPE, NE));

if DE>0;
    TEs = (DE+1:NE).*tau;
    integs = integs(DE+1:end);
else
    TEs = (1:NE).*tau;
end

guess = [max(mod_no_clip_res), min(tau*NE/3), min(mod_no_clip_res)];

disp(size(TEs));
disp(size(mod_no_clip_res));

[x, fval, exitflag] = fminsearch(@T2_fit_offset, guess,
optimset('maxiter', 10000, 'maxfunevals', 10000), integs, TEs);
 dat = [(1:NE).*tau, integs]%; [x, zeros(1, length(TRdataout)-
length(x))]];

assignin('base', 'T2fitparams', x);
assignin('base', 'dat', dat);
```

```matlab
figure(105)
plot(TEs, integs, 'ro')
hold on
plot(min(TEs):.1:max(TEs), x(1).*exp(-
((min(TEs):.1:max(TEs))./x(2)))+x(3), 'b')
hold off
xlabel('T_E, \mus')
ylabel('Signal Intensity, a.u.')
title(['M_0 = ' num2str(x(1)) '; T_2^e^f^f = ' num2str(x(2)) '; noise
= ' num2str(x(3))])
%Save results

%append the datetime
% datenow = datestr(datetime('now'), 'yyyy_MM_dd_HH_mm_ss');
% flocs = [pathname, '\', fname, datenow, extname];
%
% csvwrite(flocs, dat');
%
% if exist(flocs)
%     msgbox(['Data writen succesfully to ' flocs ' :-)']);
% else
%     msgbox(['Data write failed to ' flocs ' :-{']);
% end

% --- Executes on button press in Mystery_Button.
function Mystery_Button_Callback(hObject, eventdata, handles)
% hObject    handle to Mystery_Button (see GCBO)
% eventdata  reserved - to be defined in a future version of MATLAB
% handles    structure with handles and user data (see GUIDATA)

function TR_Disp_Callback(hObject, eventdata, handles)
% hObject    handle to TR_Disp (see GCBO)
% eventdata  reserved - to be defined in a future version of MATLAB
% handles    structure with handles and user data (see GUIDATA)

% Hints: get(hObject,'String') returns contents of TR_Disp as text
%        str2double(get(hObject,'String')) returns contents of TR_Disp
as a double

% --- Executes during object creation, after setting all properties.
function TR_Disp_CreateFcn(hObject, eventdata, handles)
% hObject    handle to TR_Disp (see GCBO)
% eventdata  reserved - to be defined in a future version of MATLAB
% handles    empty - handles not created until after all CreateFcns
called

% Hint: edit controls usually have a white background on Windows.
%       See ISPC and COMPUTER.
if ispc && isequal(get(hObject,'BackgroundColor'),
get(0,'defaultUicontrolBackgroundColor'))
    set(hObject,'BackgroundColor','white');
end
```

```matlab
function DummyEch_Callback(hObject, eventdata, handles)
% hObject    handle to DummyEch (see GCBO)
% eventdata  reserved - to be defined in a future version of MATLAB
% handles    structure with handles and user data (see GUIDATA)

% Hints: get(hObject,'String') returns contents of DummyEch as text
% str2double(get(hObject,'String')) returns contents of DummyEch as a
double


% --- Executes during object creation, after setting all properties.
function DummyEch_CreateFcn(hObject, eventdata, handles)
% hObject    handle to DummyEch (see GCBO)
% eventdata  reserved - to be defined in a future version of MATLAB
% handles    empty - handles not created until after all CreateFcns
called


% Hint: edit controls usually have a white background on Windows.
%       See ISPC and COMPUTER.
if ispc && isequal(get(hObject,'BackgroundColor'),
get(0,'defaultUicontrolBackgroundColor'))
    set(hObject,'BackgroundColor','white');
end
```